PhD-FSTM-2024-016
Faculty of Science, Technology and Medicine

DISSERTATION

Defense held on 22/02/2024 in Luxembourg

to obtain the degree of

DOCTEUR DE L'UNIVERSITÉ DU LUXEMBOURG

EN PHYSIQUE

by

Himanshu Phirke

Born on 3 September 1994 in India

UNDERSTANDING INHOMOGENEITIES AND CARRIER DYNAMICS IN MIXED-HALIDE PEROVSKITES VIA STEADY-STATE AND TIME-RESOLVED PHOTOLUMINESCENCE IMAGING

Dissertation defense committee

Dr. Alex Redinger, dissertation supervisor

Professor, Université du Luxembourg

Dr. Thomas Kirchartz

Professor, University Duisburg-essen & Research Center Jülich

Dr. Philip Dale, Chairman

Professor, Université du Luxembourg

Dr. Thomas Unold

Hemholtz Zentrum Berlin

Dr. Torsten Granzow, Vice Chairman

Luxembourg Institute of Science and Technology

Contents

List of Figures

Acronyms and Symbols

List of acronyms

AFM Atomic force microscopy

AM Air Mass

AM-KPFM Amplitude modulation KPFM

CB Conduction Band

CCD Charged coupled device

CPD Contact potential difference

CW Continuous wave

EDX Energy-Dispersive X-Ray spectroscopy

ETL Electron transport layer

FM-KPFM Frequency modulation KPFM

FTO Fluorine doped tin-oxide

GS Glass side

HIM Helium-Ion Microscopy

HLI High level injection

HOPG Highly-Oriented Pyrolitic Graphite

HTL Hole transport layer

KPFM Kelvin probe force microscopy

LLI Low level injection

PCE Power conversion efficiency

PL Photoluminescence

PSC Perovskite solar cells

PS Perovskite side

SEM Secondary Electron Microscopy

SIMS Secondary Ion Mass Spectroscopy

VB Valence Band

WF Work function

List of Symbols

α Absorption coefficient

D_n Diffusion constant

FF Fill factor

Φ Work function

ϕ Photon flux

J_{SC} Short-circuit current

λ Wavelength

μ_{qfls} Quasi-fermi level splitting

Q_e^{lum} Photoluminescence quantum yield

S_n Surface recombination velocity

$\tau_{\mathbf{bulk}}$ Bulk lifetime

$\tau_{\mathbf{diff}}$ Differential lifetime

τ_{eff} Effective lifetime

$\tau_{\mathbf{surf}}$ Surface lifetime

V_{OC} Open-circuit voltage

Abstract

The Photoluminescence (PL) technique, recognized for its non-destructive and rapid data acquisition attributes relative to other techniques, is pivotal in characterizing photovoltaic materials, especially perovskite absorbers. Quantifying lateral inhomogeneities is gaining interest in the Perovskite solar cells (PSC) community. This thesis harnesses a hyperspectral PL imaging system that has been calibrated to absolute photon numbers to spatially resolve key optoelectronic parameters such as the optical band gap, PL quantum yield, and quasi-Fermi level splitting, rather than relying on conventional averaged measurements. A critical investigation is conducted on the use of pulsed lasers, demonstrating that high repetition frequency pulsed lasers can yield comparable results to Continuous Wave (CW) lasers. A meticulous study is performed on absorbers of high-efficiency 22%-24% $(FAPbI_3)_{0.97}(MAPbBr_3)_{0.03}$ perovskite solar cells, uncovering spatial heterogeneities. These are characterized by luminescence variations, pinholes, and chemical inhomogeneity which is common in solution-processed perovskites, potentially affecting device performance. To decode the underlying causes of these heterogeneities, point Energy-Dispersive X-Ray spectroscopy (EDX) and high-resolution Secondary Ion Mass Spectroscopy (SIMS) measurements are employed, revealing elemental variations originating from partial perovskite stack. Furthermore, high-resolution SIMS mapping exposes micrometer-scale regions lacking the organic component (FA^+) and Br, yet rich in Pb and I, indicating PbI species. Such chemical variation then also affects the luminescence property of the absorber, showing spots of high and low emission.

Apart from chemical heterogeneity, the partial perovskite stack features a stripes pattern that is a consequence of spin coating the TiO_2 layer. Due to this, the charge extraction is spatially modulated by the TiO_2 thickness. A detailed study of these stripes has been conducted in Chapter 5 of this thesis. When the measurement system is simple, such as an absorber layer on glass, interpretation of the luminescence measurement is easy. This thesis then discusses the complexities introduced by the electron transport layer in interpreting time-resolved luminescence measurements, such as quenching, transport, and interface re-

combination. To distinguish carrier dynamic processes for the perovskite layer in contact with the transport layer and using established models and simulation from literature, I employed transient PL measurements at Low level injection (LLI) using two geometries: one with illumination from the top surface of the perovskite and the other with illumination from the back interface. Assumptions of a Lambert-Beer generation profile allow the dissection of surface and interface recombination processes, as well as charge transfer mechanisms to the extraction layer. These insights are pivotal for future advancements in transport layer improvement as such methodology serves as a quality check of the interface as well as the surface.

Addressing surface heterogeneity, the thesis explores strategies, including the use of laser polishing on a CsMAFA perovskite surface, to achieve a smoothed surface with reduced heterogeneity as well as better Spiro-OMeTAD deposition. Atomic force and Kelvin probe force microscopy validate the reduced roughness and work function post-laser treatment. Reduction of surface work function means that the absorber will have better energy level alignment with the transport layer as well as enhanced charge collection. The thesis also ventures into the realm of perovskite film thickness modulation through laser ablation, a novel approach to tailoring absorber layer thickness for enhanced optoelectronic properties. This thesis offers insights into state-of-the-art perovskite absorbers, elucidating the intricate interplay between the perovskite and adjacent layers. It underscores the transformative impact of imaging techniques in understanding and refining the dynamic behavior of perovskite materials in response to interfaces.

Introduction

As humanity faces escalating energy demands amidst the depletion of conventional energy sources, the search for alternative solutions has intensified. In 2021, global energy consumption surged, reaching levels comparable to pre-pandemic times, with an estimated consumption of $595 \cdot 10^{18}$ Joules [1]. The Centre for Global Development (CGD) underscores this trend, indicating a clear correlation between electricity consumption and the human development index [2]. This suggests that as less-developed nations progress, the global energy demand is likely to rise even more. This implies that the rising trend of energy consumption

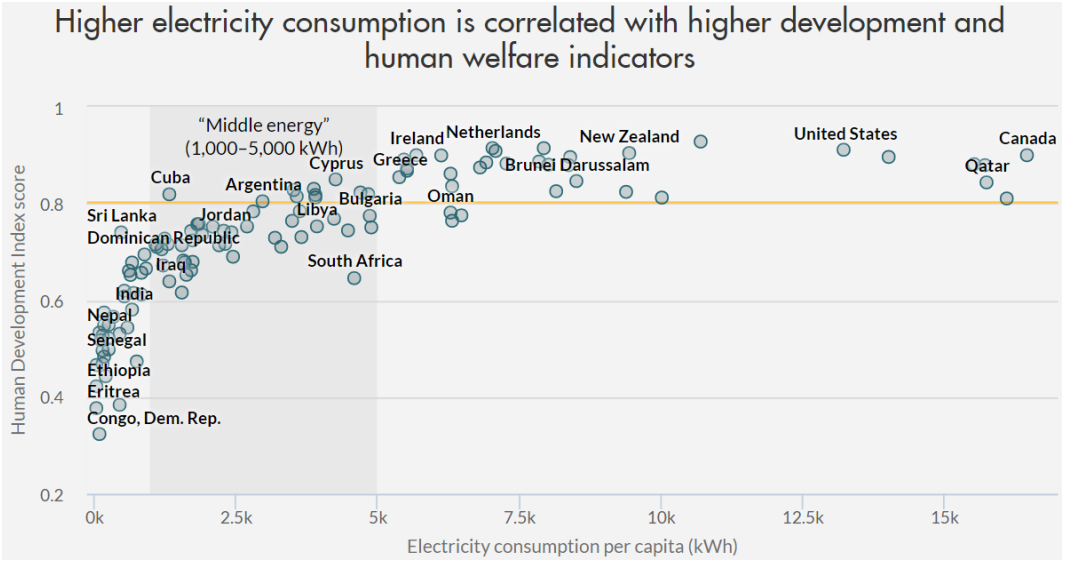

Figure 1: Plot of human development index vs electricity consumption per capita of different countries. This plot shows that countries moving towards developed status consume more electricity.[2]

will become even more pronounced as less-developed countries become more developed. The increase in energy usage is occurring alongside growing concerns about the environmental impacts of burning fossil fuels, particularly their role in the greenhouse effect and global climate change. The reality of global warming is undeniable, with the global average surface temperature already having risen by about 1 degree Celsius compared to pre-industrial levels. Prof.

Petteri Taalas, the Secretary-General of the World Meteorological Organization, highlights the seriousness of the situation by stating that the severe weather conditions experienced by millions of people in July are a clear indication of the impact of climate change. He considers this as a preview of the challenges that lie ahead and emphasizes the urgent need to decrease greenhouse gas emissions. Prof. Taalas emphasizes that taking action to address climate change is not a luxury but a necessity. The current scientific consensus affirms that global

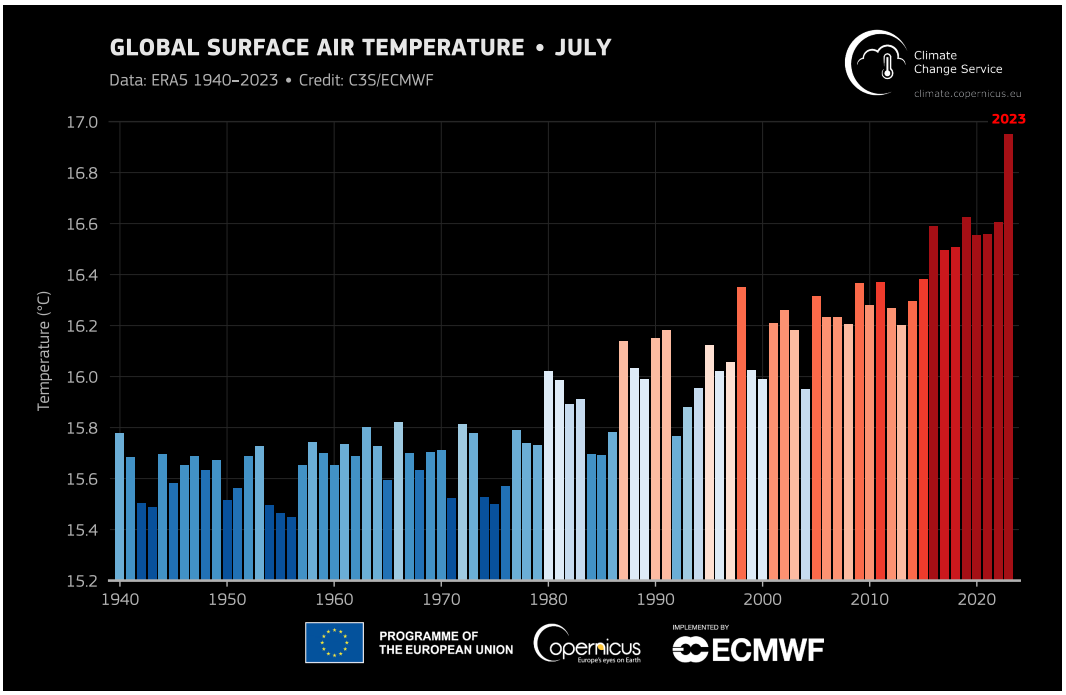

Figure 2: The surface air temperature for all July months from 1940 to 2023 has been globally averaged. Cooler-than-average years are represented by shades of blue, while warmer-than-average years are shown by shades of red. The data used is sourced from the Copernicus Climate Change Service [3]

.

warming is not occurring naturally; rather, it is primarily driven by the excessive burning of fossil fuels for human needs, leading to an increase in atmospheric CO_2 levels. As a result, there is a strong desire to generate electricity from environmentally friendly sources.

Solar energy is an alternative source that can be harnessed using solar cells and solar thermal technologies [4]. Our Sun emits $3.8 \cdot 10^{23}$ kW of power, of which approximately $1.8 \cdot 10^{14}$ kW is intercepted by Earth [5]. The Sahara Desert, located in Africa, provides an optimal location for the collection of solar energy due to its daily exposure to 12 hours of sunlight. Spanning an expansive area of 9.2 million square kilometers [6], it would take only 1.1% of the total area of the Sahara to meet the global power demand of 18.5 TW,

assuming an 18% efficiency in solar energy conversion. However, this is not feasible due to the large amount of power lost in transmitting electricity around the world. Moreover, the current technology does not allow for the global energy demand to be completely met by electricity, as solar-powered aircraft are still far from being commercially available. Solar cells, also known as photovoltaic cells, are semiconductor devices that transform sunlight into electricity. They are used in a variety of ways, from powering small electronics to large-scale power plants to space applications. Solar cells are a key technology for addressing the global energy crisis and reducing our reliance on fossil fuels. For optimal performance, solar cells are designed to absorb a broad range of energies aligning with the spectrum of solar radiation. Most of the Sun's irradiance, or the amount of light energy per unit area, is between 250-2500 nm, with a peak in the visible region (400-700 nm) as seen in Figure 3. This means that the absorber material used in solar cells should absorb as much light in the visible region of the solar spectrum as possible as well as its other layers should efficiently transport the generated charge carriers. The general principle of solar cells is that when sunlight is absorbed by the semiconductor material, photons with sufficient energy can excite electrons, elevating them to a higher energy state. This creates electron-hole pairs within the semiconductor. If these pairs are separated by a built-in electric field, the free electrons can be directed towards an external circuit, generating an electric current, which can then be harnessed as electricity [7]. The photovoltaic effect, first experimentally demonstrated by Edmond Becquerel in 1839, is the physical process by which energy radiation is converted to electrical energy [8]. The design of an efficient solar cell or module requires understanding the sun's emitted light, light-absorbing semiconductor materials, various layers taking part in the transport of excited charge carriers, long-term stability as well as the cost of production.

The sun's energy, originating from hydrogen-to-helium reactions in its core, is emitted from its cooler outer layer at approximately 5772 K. The sun's spectrum is described by Planck's law [9]:

$$\rho(E) = \frac{8\pi}{h^3 c^3} \cdot \frac{E^3}{\exp\left(\frac{E}{k_B T}\right) - 1} \tag{1}$$

Planck's law describes the spectral density ρ of the photons emitted by a black body radiation which is in thermal equilibrium at a given temperature T. k_B is the Boltzmann constant, c is the speed of light in vacuum and h is the Plank's constant. As sunlight traverses the atmosphere, it undergoes scattering and absorption, altering its intensity. The intensity of sunlight is affected by the angle of incidence, which is quantified by the air mass number. The Air Mass (AM) represents the distance that light travels in the atmosphere, divided by the shortest distance it could have traveled. It measures the decrease in light power when it

passes through the atmosphere and is absorbed by air, moisture, and dust. AM is defined as:

$$\text{Air Mass} = \frac{1}{\cos(\theta)} \tag{2}$$

For standardizing solar panel comparisons, AM1.5 is utilized, representing sunlight at a 48° angle and intensity of $1000\,\mathrm{W/m^2}$ [10]. The solar irradiance for AM1.5G, where G means Global, can be seen in figure 3. The majority of photovoltaic energy conversion relies

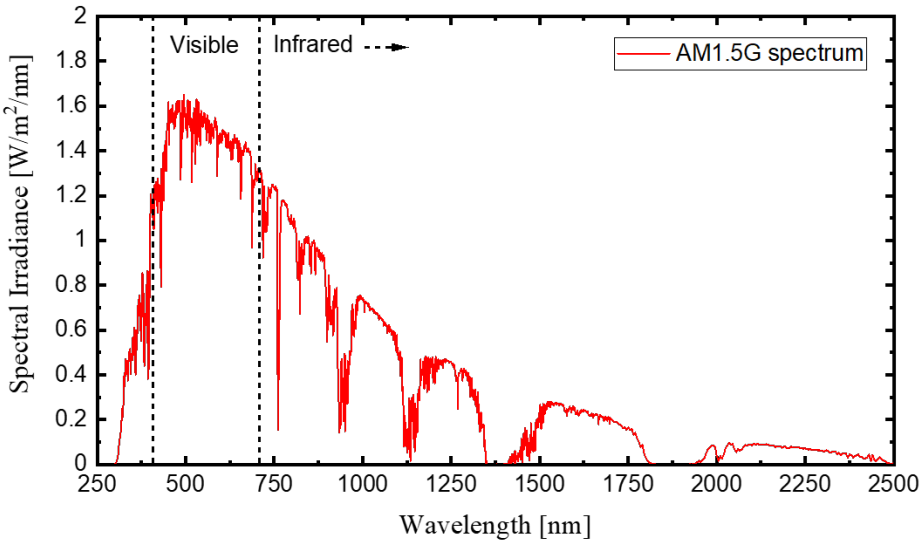

Figure 3: Spectral distribution of solar radiation with AM1.5G. The dotted line represents the range of visible region of the solar spectrum

on the use of semiconductor materials in the form of a p-n junction. Semiconductors are characterized by their distinctive electrical property that allows them to modify their level of conductivity based on external influences such as temperature changes, introduction of impurities or illuminating with light. For a given solar spectrum, the maximum achievable efficiency of a photovoltaic material is related to the bandgap of the material. The bandgap energy of a semiconductor is the energy difference between its valence band, where electrons are bound to atoms, and its conduction band, where electrons are free to move and conduct electricity. This bandgap determines the range of photon energies the semiconductor can absorb, and it is influenced by the atomic structure and the chemical bonding within the crystal lattice. To generate charge carriers, the incident photons need to have enough energy to overcome the bandgap energy. By introducing minuscule amounts of impurities, termed as *dopants*, their conductivity can be drastically modified, even when dopant concentrations are as sparse as parts per billion. Solar cells, essentially large diodes tailored for light absorption,

are rooted in p-n junction devices. Upon photon (light) absorption, electrons move from the Valence Band (VB) to the Conduction Band (CB), forming electron–hole pairs [11]. The recombination of these pairs releases energy, classified as radiative or non-radiative based on whether the energy is emitted as a photon or heat [12] respectively. The detailed balance method, introduced by Shockley and Queisser [13] and later expanded by Tiedje *et al.* [14], offers a way to determine the peak efficiency of photovoltaic devices. It assumes:

1. Infinite mobility ensuring carrier collection irrespective of generation location.

2. Photons with energy equal to or surpassing the band gap are completely absorbed.

The Shockley and Queisser efficiency limit is attained by utilizing the principle of detailed balance to the photon flow entering and leaving the semiconductor. The highest attainable efficiency is reached in the absence of non-radiative recombination, with all produced carriers being either gathered as current in the leads (if in contact) or recombined (if no external leads or electrodes are connected) in which case resulting in the emission of a single photon for each electron-hole pair.

Solar cells are categorized into three generations based on their development timeline, materials, and fabrication techniques. First-generation cells are primarily mono-crystalline or polycrystalline silicon wafer-based. Second-generation cells utilize thin films like amorphous Silicon, Cadmium Telluride, and Copper Indium Gallium Selenide (CIGS). Among these, CIGS stands out for its performance, currently achieving efficiencies up to 23.60% [15]. Third-generation cells aim for cost-effectiveness, either through enhanced efficiency, as seen in multi-junction cells and quantum dots, or reduced fabrication costs, as in dye-sensitized solar cells (DSSCs), quantum dot-sensitized solar cells (QDSSCs), organic photovoltaics, and perovskite solar cells (PSCs). However, challenges persist: organic cells face efficiency constraints due to material disorder and low light absorption [16, 17], while DSSCs grapple with limited dye-sensitizers and device instability. Metal halide perovskites (MHPs) have emerged as promising materials in photovoltaic research, well known for their superior optoelectronic properties, such as robust optical absorption and extended carrier lifetime.

In this thesis, I will dive deep into understanding the perovskite absorber layer in contact with the charge extraction layer. Chapter 1 will discuss the basic background knowledge necessary to understand the following chapters. In this chapter, the focus will be given to semiconductor basics and important terms and definitions that will occur frequently in this thesis. After the semiconductor basics, a brief introduction to the perovskite solar cell will be given. This will talk about the different composition, structures, architecture as well as photo-physics of the perovskite solar cell. A state-of-the-art perovskite solar cell as well as

a powerful technique; PL spectroscopy and Imaging, which showcases the research from the past decade to current advancements. This will help readers introduce themselves to the physics behind the perovskite solar cell, its history, and current status.

Chapter 2 then explains the sample information and experimental techniques in detail used in this thesis for measurements. Primarily the thesis focuses on PL imaging but other complementary techniques such as Secondary Electron Microscopy (SEM), EDX, Helium-Ion Microscopy (HIM), SIMS as well as profilometer that played an important role in correlating and analyzing the study. A full detailed description of the PL imaging system will be discussed in separate Chapter 3.

Chapter 3 introduces the custom-built hyperspectral PL imaging system. The chapter begins by discussing the essential components of the system. Following the component discussion, the chapter focuses on the optimization and calibration process. To ensure accurate quantitative data and analysis, it is necessary to calibrate the system spectrally and in terms of absolute-photon number. This chapter will delve into the calibration procedure. While the system can provide us with measured data, it has limitations. Therefore, we must externally process the measured data and images. This is where the data analysis procedure comes into play. This section of Chapter 3 aims to provide the reader with a comprehensive understanding of the general data analysis approach used throughout this thesis.

Chapter 4 introduces the utilization of the PL imaging system, alongside chemical characterization techniques discussed in Chapters 2 and 3, to investigate the perovskite stack. PL is a valuable method for examining the optoelectronic properties of the perovskite absorber and charge extraction layer. This chapter will specifically concentrate on examining unpassivated perovskite on the mesoporous TiO_2 layer acting as the ETL. The objective is to comprehend the non-uniformity observed in the luminescence measurement, and establish a correlation with the chemical characterization, despite the difference in length scale. Additionally, time-resolved PL will be implemented to comprehend the dynamics of charge carriers when optically excited in the presence of an ETL.

In Chapter 5, I will extensively explore the perovskite stack discussed in Chapter 4. Our focus will be on investigating the non-uniformity resulting from the deposition process of the charge extraction layer on the perovskite absorber. I will present a comprehensive analysis of time-resolved transient photoluminescence (PL) to examine the changes in decay time caused by the mesoporous structure beneath the perovskite layer. This analysis is crucial for understanding the implications of using spin-coating, a commonly employed technique for depositing both the perovskite and extraction layers. If I observe any variations in

luminescence or charge extraction, as demonstrated in this study, it could potentially hinder the efficiency of the device.

Chapter 6 discusses the approaches to address the inhomogeneity issue, namely passivation and a novel technique involving the utilization of a low-energy laser to enhance the surface. Through the utilization of PL and complementary AFM/KPFM, I will demonstrate the significant enhancement of optoelectronic properties and overall efficiency of the solar cell through passivation. Additionally, I will explore the impact of laser light on the optical properties, morphology, and Work function (WF) of the perovskite absorbers by employing a Caesium-doped absorber with a low-energy UV laser.

Chapter 7 integrates the thesis as a summary with a few take-home messages.

It is crucial to note that the perovskite samples utilized in this thesis were obtained from various research groups. The specific groups will be acknowledged when discussing each sample. The primary focus of this thesis is to characterize the perovskite stack received from these research groups through a collaborative effort, with the aim of comprehending its optoelectronic properties.

Chapter 1

Background and State of the art

In this section, I delve into the concepts of carrier generation and recombination in semiconductor material. Generation refers to the creation of electron-hole pairs, while recombination denotes their annihilation. Deviations from thermal equilibrium can alter the concentrations of electrons (n) and holes (p) in a semiconductor. For instance, a temperature surge can amplify the thermal generation rate of these carriers, leading to time-dependent concentration changes until a new equilibrium is achieved. External stimuli, like photon influx from light, can also induce a non-equilibrium state by generating carriers. To grasp these processes, we focus on direct band-to-band generation and recombination.

1.1 Semiconductor basics

1.1.1 Intrinsic semiconductor

Semiconductor material that does not have impurities added to it to change the carrier concentrations is called an intrinsic semiconductor. In a semiconductor, two types of charge carriers can contribute to a current, the electron, and the hole. Since the number of electrons present in the conduction band and the number of holes present in the valence band determines the current, it is then important to know the density of these charge carriers. This involves rigorous mathematical derivations but we will try to keep it easy so that it is relevant and easy to follow. At thermal equilibrium, the electron concentration in the conduction band is given by:

$$n_0 = \int_{E_C}^{E_C^{top}} D(E)F(E)\,dE \tag{1.1}$$

where E_C and E_C^{top} represents the bottom and top of conduction band respectively. The density of states $D(E)$ is approximated by density of electrons near the bottom of the

conduction band for low carrier densities and temperatures. Thus $D(E)$ can be written as;

$$D(E) = M_C \frac{\sqrt{2}}{\pi^2} \frac{m_n^{3/2}(E - E_C)^{1/2}}{\hbar^3}$$

M_C is the number of equivalent minima in the conduction band and m_n is the effective mass for electrons [18]. The probability of an energy level being occupied is a strong function of temperature and energy and is given by the Fermi-Dirac distribution function,

$$F(E) = \frac{1}{1 + \exp\left(\frac{E - E_F}{kT}\right)}$$

where E_F is the Fermi energy level. Thus, using the $D(E)$ and $F(E)$, with evaluation of integral, equation 1.1 can be written as,

$$n_0 = 2\left(\frac{2\pi m_n kT}{h^2}\right)^{3/2} \exp\left(-\frac{E_C - E_F}{kT}\right) = N_C \exp\left(-\frac{E_C - E_F}{kT}\right) \tag{1.2}$$

where k is the Boltzmann constant, T the absolute temperature, h the Planck's constant and N_C is the effective density of states in the conduction band and is given by,

$$N_C = 2\left(\frac{2\pi m_n kT}{h^2}\right)^{3/2}$$

The Fermi energy level E_F is a concept derived from Fermi-Dirac statistics. It denotes the electron's chemical potential at zero Kelvin and is commonly referred to as the topmost filled energy level of electrons in a solid at this temperature. Electrons, being fermions, cannot occupy the same quantum states due to the Pauli exclusion principle. Therefore, at absolute zero, they fill the lowest energy states, forming a "Fermi sea" of electron energy levels. The Fermi level is the surface of this sea, where no electrons have enough energy to surpass it. Similar derivation can be used to find the number of holes p_0 in the valence band with N_V as the effective density of the state of holes, which is given as,

$$p_0 = N_V \exp\left(-\frac{E_F - E_V}{kT}\right)$$

where N_V is the effective density of states in the valence band given as,

$$N_V = 2\left(\frac{2\pi m_p kT}{h^2}\right)^{3/2}$$

with m_p as the effective mass of the hole.

In an ideal intrinsic semiconductor, the number of electrons in the conduction band is equal to the number of holes in the valence band, that is $n_0 = p_0 = n_i$ and n_i is the intrinsic carrier concentration. Therefore, the product $n_0 p_0$ will give us:

$$n_0 p_0 = n_i^2 = N_C N_V \exp\left(\frac{-E_g}{kT}\right)$$

$$n_i = \sqrt{N_C N_V} \exp\left(\frac{-E_g}{2kT}\right) \tag{1.3}$$

where E_g is the band gap of the semiconductor given as $E_C - E_V$. Thus if the band gap of a material is known together with the electron and hole density of states (N_C, N_V), one can calculate the intrinsic carrier concentration. The Fermi level's location can be calculated from the equations above. As the number of electrons and holes (n_0, p_0) are the same in intrinsic semiconductors, the Fermi level will be in the middle of the band gap assuming the effective masses of the electrons and holes are equal.

$$E_F = \frac{1}{2}(E_V + E_C) + \frac{1}{2}kT \ln\left(\frac{N_V}{N_C}\right) \tag{1.4}$$

From the definitions of the N_C and N_V, equation 1.4 can be written as,

$$E_F = \frac{1}{2}(E_V + E_C) + \frac{3}{4}kT \ln\left(\frac{m_p}{m_n}\right)$$

The first term, $\frac{1}{2}(E_C + E_V)$, is the midgap energy. If $m_p > m_n$, the intrinsic Fermi level will be slightly higher than the midgap energy, and if $m_p < m_n$, it will be slightly lower than the midgap energy.

1.1.2 Extrinsic semiconductor

A semiconductor that has had its electron and hole concentrations deliberately changed from their natural, intrinsic levels by the addition of impurities, known as dopants, is referred to as an extrinsic semiconductor. The electrical, optical, and structural properties of intrinsic semiconductors, which have low conductivity and low concentrations of charge carriers, can be altered by the addition of dopants. One type of carrier, either electron or hole, will predominate in extrinsic semiconductors. When the density of electrons is greater than that of holes, the semiconductor is called n-type. When the density of holes is greater than that of electrons, it is called a p-type semiconductor. For an n-type semiconductor, where $n_0 > p_0$, electrons are referred to as majority carriers and holes are minority carriers. Similarly for a p-type semiconductor, where $p_0 > n_0$, holes are the majority carrier and electrons are the minority carrier. If we consider n-type semiconductor in which N_D is the concentration of donor atoms and $N_D >> n_i$, then $n_0 = N_D$ and $p_0 = \frac{n_i^2}{N_D}$. This shows that the number of minority carriers decreases as some of the extra electrons added by doping the material will occupy the empty spots (i.e. holes) in the VB, thus lowering the number of holes. The Fermi energy level in a semiconductor changes as the electron and hole concentrations change. This is illustrated in figure 1.1. By adding and subtracting the intrinsic fermi energy E_{Fi} to the exponential component of equation 1.2, the thermal equilibrium electron and hole

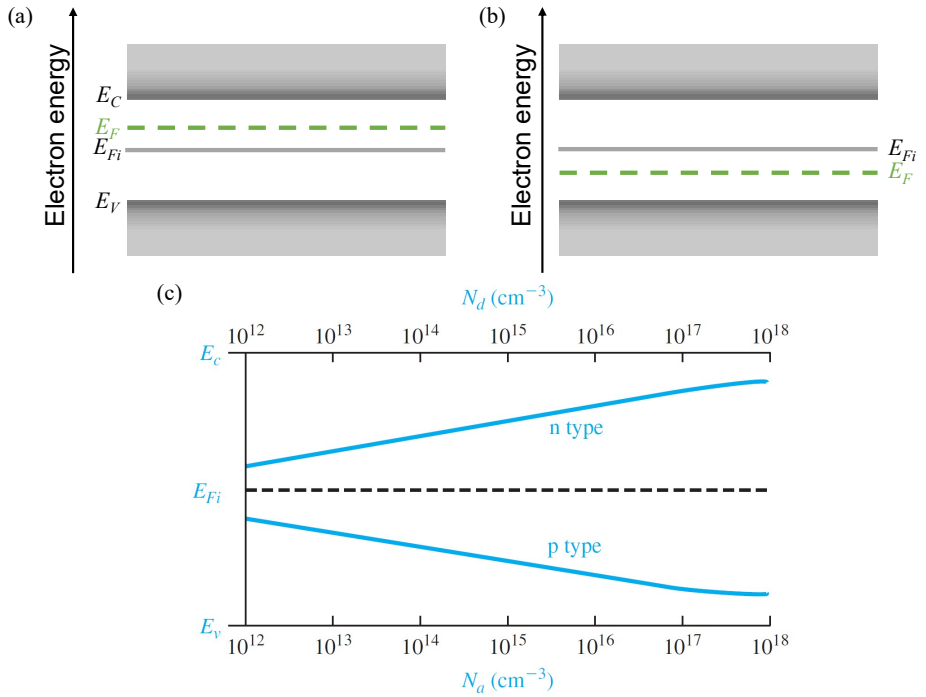

Figure 1.1: The location of the Fermi level is determined by the relative concentrations of donors and acceptors in a semiconductor material. In the case of an n-type material, where the donor concentration N_D is greater than the acceptor concentration N_A ($N_D > N_A$), the Fermi level is closer to the conduction band. On the other hand, in a p-type material, where the acceptor concentration N_A is greater than the donor concentration N_D ($N_A > N_D$), the Fermi level is closer to the valence band. The position of the Fermi level can be described as a function of both the donor and acceptor concentrations. These relationships are illustrated in plots adapted from the book "Semiconductor Physics and Devices" by Donald Neamen.[19]. As the doping level increases, the Fermi energy level moves closer to the conduction band for the n-type material and closer to the valence band for the p-type material.

concentration will now be written as:

$$\begin{aligned} n_0 &= n_i \exp\left(\frac{E_F - E_{Fi}}{kT}\right) \\ p_0 &= n_i \exp\left(\frac{E_{Fi} + E_F}{kT}\right) \end{aligned} \tag{1.5}$$

where the intrinsic carrier concentration n_i is given as;

$$n_i = N_C \exp\left(\frac{-(E_C - E_{Fi})}{kT}\right)$$

The detailed derivation can be found in Semiconductor Physics and Devices by Donald Neamen[19]. For an n-type semiconductor $E_F > E_{Fi}$ and for p-type semiconductor $E_F < E_{Fi}$. However, the product $n_0 p_0 = n_i^2$ will remain constant. Solving equation 1.5 for $E_F - E_{Fi}$

give us:

$$E_F - E_{Fi} = kT \ln\left(\frac{n_0}{n_i}\right) \tag{1.6}$$

This equation tells us that the difference between the Fermi level and the intrinsic Fermi level is a logarithmic function of donor concentration. If the net effective donor concentration is zero, then $n_0 = n_i$ and $E_F = E_{Fi}$. A similar equation can be derived for p-type semiconductor given as:

$$E_{Fi} - E_F = kT \ln\left(\frac{p_0}{n_i}\right) \tag{1.7}$$

1.2 Perovskite solar cells

1.2.1 Definition and Composition

The name "perovskite" is used to describe materials that have the same crystal structure as calcium titanate ($CaTiO_3$) [20]. This mineral was first identified by Gustav Rose in the Ural mountains in 1839 and was named after the Russian mineralogist L. Perovski [21]. Generally, perovskites have a chemical formula of ABX_3, where A and B are cations of different sizes with A being larger than B, and X is an anion [22]. The ideal cubic unit crystal cell of perovskite is composed of three main groups; a monovalent cation (A) such as methylammonium (MA^+) or formamidinium (FA^+); a bivalent metallic cation (B) such as lead (Pb^{2+}) or tin (Sn^{2+}), and a halide anion (X) such as iodine (I^-) or chloride (Cl^-) or bromide (Br^-). The structure of perovskite can be seen in figure1.2. The two most commonly used and widely researched perovskite absorbers for solar cells are methylammonium lead iodide ($CH_3NH_3PbI_3$) commonly referred to as MAPI and formamidinium lead iodide ($HC(NH_2)_2PbI_3$ commonly referred as FAPI. The stability and structure of perovskites are determined by two essential parameters: the octahedral factor (μ) and the tolerance factor (t) [24]. The tolerance factor is conceptualized as the ratio of the bond lengths of A−X to B−X in an ideal solid-sphere model and is mathematically represented as:

$$t = \frac{R_A + R_X}{\sqrt{2}(R_B + R_X)} \tag{1.8}$$

where R_A, R_B, and R_X symbolize the ionic radii of the A, B, and X ions, respectively [25]. Concurrently, the octahedral factor, μ, is defined as the ratio of the ionic radius of the divalent cation (R_B) to the anion (R_X). To preserve the 3D structure, the cation radius at the A-site should be less than 2.6 Å according to Goldschmidt's tolerance factor [26]. Additionally, 3D perovskite materials are recognized for their cost-effective and straightforward low-temperature fabrication (approximately 100°C) [27, 28, 29], significant defect

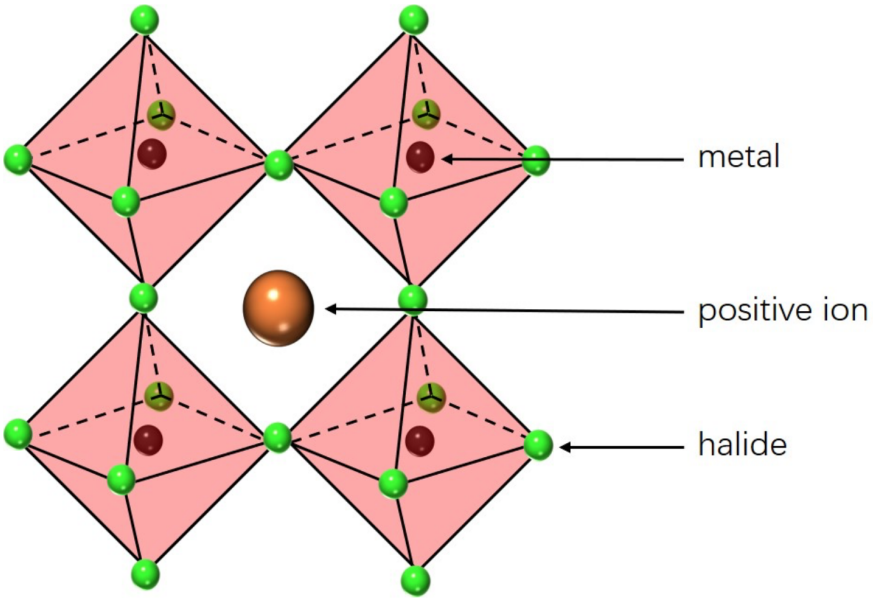

Figure 1.2: ABX_3 Perovskite crystal structure. The image has been taken from Okinawa Institute of Science and Technology Graduate University [23] licensed under a Creative Commons Attribution (CC BY 4.0)

resilience [30, 31], and exceptional diffusion length (beyond 1 µm) [32, 33]. The adaptability of perovskite components has also spurred extensive compositional studies, notably concerning monovalent cation components. One of the main features of perovskite materials is the ability to tune their bandgap by changing the BX_3 part of the perovskite atomic structure by changing the halide composition [34]. For example, MAPI with a bandgap of $1.53eV$ to MAPBr with a bandgap of $2.3eV$ was achieved by tuning the composition of type $MAPb(I_{1-x}Brx)_3$, giving a continuum of different bandgaps. [35]. The use of multi-cation mixtures like MA, FA, Cs, and Rb has set the foundation for highly efficient and durable solar cells [36, 37, 38, 39]. This is complemented by research into halide component blending, including I, Br, and Cl [40, 41, 39, 42].

1.2.2 Architecture and working principle

A Perovskite Solar Cell (PSC) typically consists of a glass substrate with a transparent conductive contact, an ETL, a perovskite layer, a Hole transport layer (HTL), and a conductive contact. Depending on the order of the layers, the cell structure can be either standard or inverted. Figure 1.3 shows the generic structure of the standard and inverted PSC. In a conventional arrangement, the ETL is put on the conductive glass, followed by the perovskite layer, HTL, and the metallic contact. In an inverted setup, the HTL is initially put

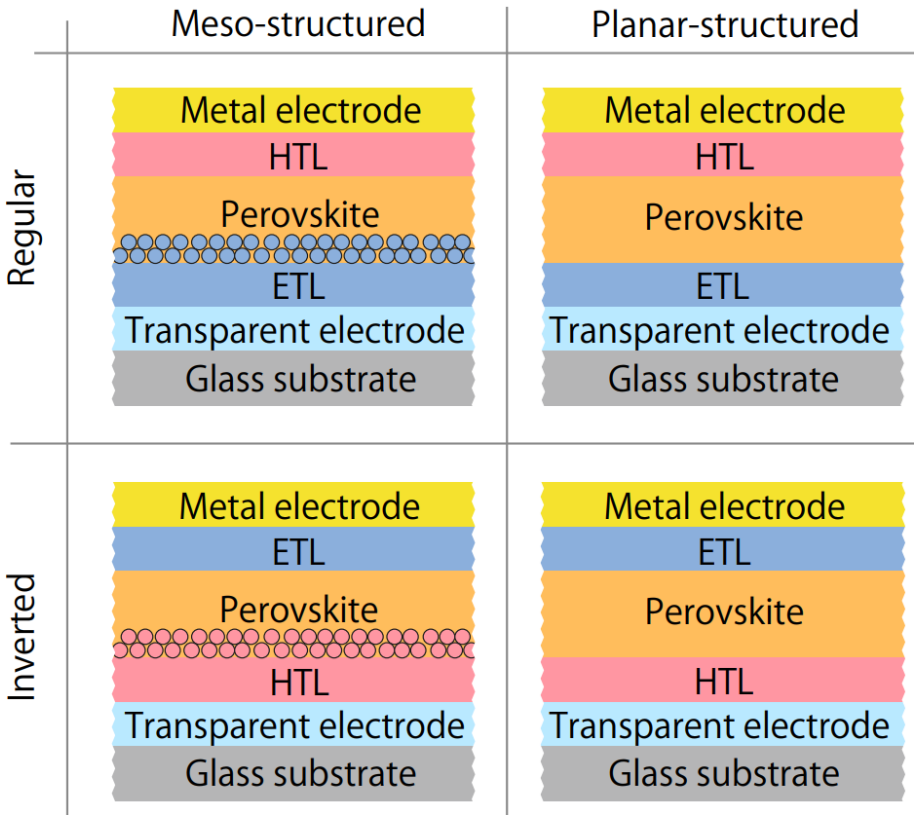

Figure 1.3: This figure showcases the four common configurations of perovskite solar cells: the regular mesoporous structure, regular planar structure, inverted mesoporous structure, and inverted planar structure. The ETL and HTL are denoted as well. The figure has been taken from Kanemitsu et.al [43]

on the conductive glass substrate, followed by the perovskite, ETL, and the metallic contact. Light passes through the transparent contact and goes through the ETL/HTL, reaching the perovskite layer where it is absorbed. The two assemblies can be categorized as mesoscopic and planar cells. The mesoscopic perovskite devices consist of a mesoporous layer, whereas the planar structure comprises entirely of planar films. Both mesoscopic and planar architectures have been documented in previous studies [44, 45]. The mesoporous layer is used because it increases the contact area with perovskite, improving the electron extraction [46].

When light is absorbed by the perovskite material, electron-hole pairs, also known as excitons, are created. These pairs have binding energy that is lower than the thermal energy (25meV), causing them to quickly separate into electrons and holes [47]. The electrons and holes are then pulled to the ETL and HTL, respectively, due to an inherent electric field. The selection of the ETL material ensures that its conduction band is lower than the conduction band level of the perovskite. On the other hand, the HTL has a valence band that is higher than the perovskite's valence band. This specific energy alignment allows for the transport

of electrons to the ETL and holes at the HTL. The energy band schematic can be seen in figure1.4.

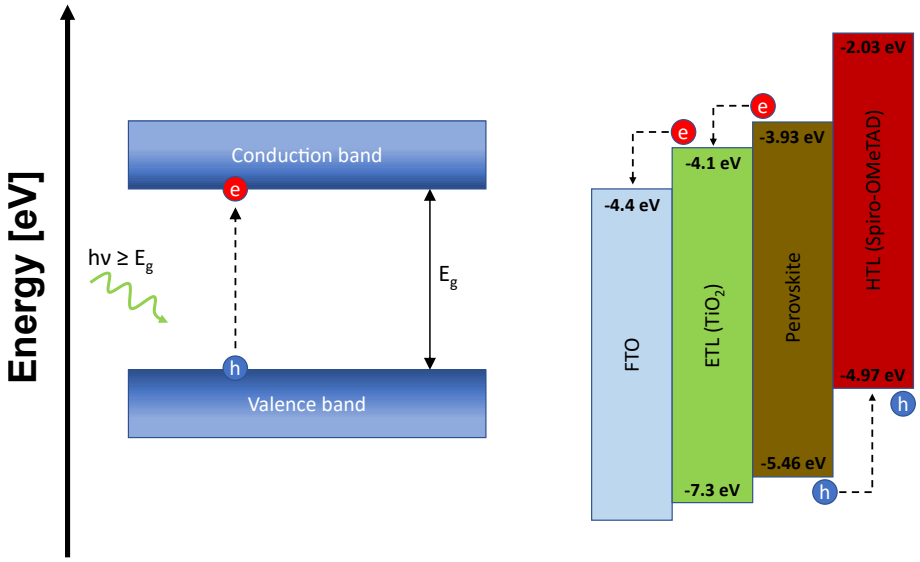

Figure 1.4: Schematic of light absorption and charge excitation by semiconductor absorbing material (left). On the right is the schematic of the layer stack indicating energy levels with respect to vacuum level before they are connected. The numbers represent the energy level of the conduction band and valence band edges relative to the vacuum.

For efficient charge extraction in the external circuit, the contact materials must be selected so that the contact collecting electrons have an energy level lower than the ETL, while the contact collecting holes have an energy level higher than the HTL valence level. The presence of a positive step in the conduction band (energy level of extraction layer being more than the absorber energy level), often referred to as a "spike", can be beneficial for the solar cell [48]. This mechanism aids in the separation of charge carriers, thereby reducing the interface recombination rate. Similarly, a step in the valence band can serve as a hurdle for holes. The splitting of the quasi-Fermi levels for electrons and holes, known as quasi-Fermi level splitting, is indicative of the presence of a photovoltage. Effective charge separation results in the quasi-Fermi level for electrons in the conduction band nearing the conduction band edge, while the quasi-Fermi level for holes in the valence band approaches the valence band edge. A greater splitting signifies a higher potential photovoltage for the solar cell. The electrical and optical characteristics of each layer have a major influence on charge transportation, thus determining the ultimate efficiency of the perovskite solar cell. The first certified perovskite solar cell, created by EPFL, was featured in the NREL solar cell efficiency chart in 2014 which had an efficiency of 14.1%. Since then, the steep increase of the PSC efficiency and research has been remarkable, as can be seen in figure1.5. Increasing

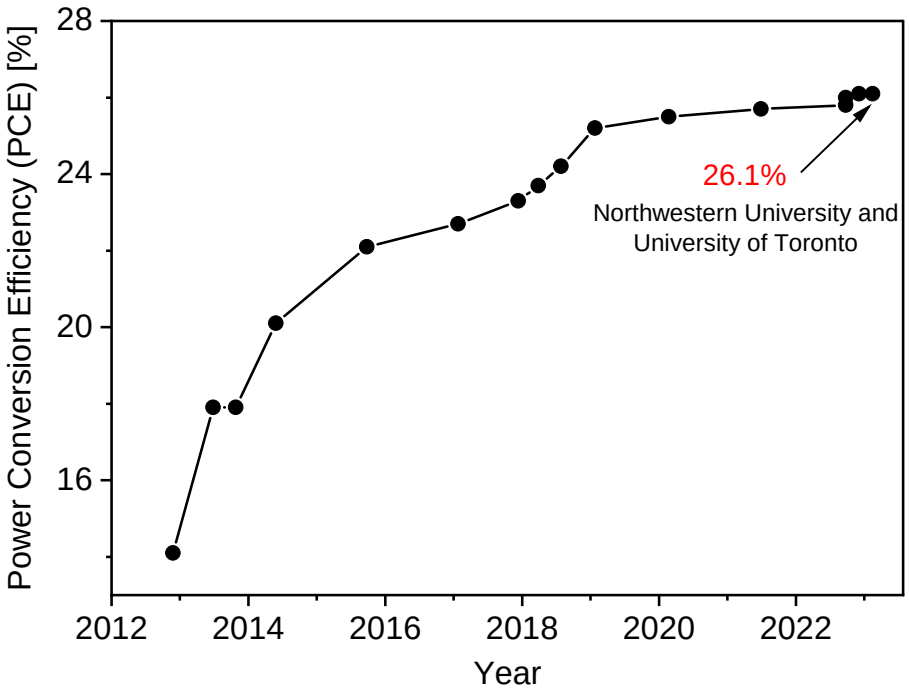

Figure 1.5: Power Conversion Efficiency (PCE) of perovskite solar cell for last 10 years. The current efficiency record stands at 26.1%. The data is taken from the NREL efficiency chart [15]

the Power conversion efficiency (PCE) is more associated with improving every layer of the solar cell device. The generation of electron and hole pairs which will be transported toward the electrodes, points at two optimization processes: improving the intrinsic properties of the absorber material, which is mainly related to defects density, and improving the transport of the charge carriers towards the electrodes by carefully selecting the extraction layers.

1.2.3 Properties and Challenges on Perovskite solar cells

The efficiency of solar cells is governed by their absorption, transport properties, carrier lifetime, and selectivity of charge extraction layers [49]. The literature is abundant with studies on the high quality and light absorption characteristics of perovskite absorbers[50]. Due to its excellent absorption, the current debate in the community is more focused on the transport properties. Different groups around the world measure different values of diffusion coefficient or carrier mobility even though the composition is similar [51]. Mobility and diffusion are important parameters for perovskites as they govern the time that it takes the generated charge carriers to travel across the thickness of the layer. It was shown in the literature that charges transport from the top to the bottom of the films after photo-excitation from the top surface takes a few tens of nanoseconds [52]. This information is

important when analyzing the transient PL data as it can help distinguish the diffusion mechanism from the recombination within a few tens of nanosecond time scales.

Lead-halide perovskites show a soft lattice structure [53], and high reactivity to water, atmosphere, and sunlight making their stability a big challenge[54]. Although self-healing of crystal after exposure to light was evidenced by Ceratti et al. [55]. The scientific community still lacks a complete understanding of the relationship between doping and defect density in the perovskite layer. Perovskites are generally known for their tolerance towards defects. In comparison to other semiconductors, perovskites like MAPI have demonstrated remarkably long Shockley-Read-Hall (SRH) lifetimes, indicating that defects have a lesser detrimental effect on perovskites compared to other inorganic semiconductors. [56, 57, 58]. Few other possibilities for defect tolerant behavior of perovskites would be densities of defects being low [59] or the capture cross-section of the defect state being low which would also lead to longer lifetime [60]. Apart from defects, perovskites are very difficult to extrinsically dope [61].

Transport layer selectivity for the perovskite layer is also a big topic of discussion [62]. Optimizing band alignment and, the chemical and opto-electronic nature of the layer at the interface of perovskite is still questioned. These subjects have been tackled by passivation strategies at the interfaces using 2d perovskites [63], self-assembled monolayer (SAM) deposition, or oxide layer encapsulation. Two main challenges of the perovskite solar cells are upscaling and stability over time.

1.2.4 Evolution and Current state of perovskite solar cells

In 2009, the inaugural photovoltaic device utilizing hybrid organic-inorganic perovskites (HOIPs) was introduced by Kojima *et al.* [64]. They employed methylammonium lead iodide ($CH_3NH_3PbI_3$, $MAPbI_3$) and methylammonium lead bromide ($CH_3NH_3PbBr_3$, $MAPbBr_3$) as the sensitizing agents to construct dye-sensitized solar cells (DSSCs) with a liquid electrolyte [64]. Due to the modest power conversion efficiencies (PCEs) of approximately 3% and the limited stability of the device, HOIP-based light absorbers garnered minimal interest. However, by 2012, a transition from a liquid electrolyte to a solid-state hole transport material (HTM) led to a significant enhancement in the PCE of $MAPbI_3$-based solar cells. The HTL in this study was the Spiro-OMeTAD, which resulted in a solar cell efficiency of 9.7%. This breakthrough had a significant impact on perovskite-sensitized solar cells, as it not only increased efficiency but also greatly improved the device's lifespan. The Spiro-OMeTAD layer successfully endured a long-term stability test of approximately 500 hours

without any encapsulation [65]. This groundbreaking discovery marked the dawn of the advanced perovskite solar cells (PSCs) era, igniting the global "perovskite fever" [66, 67]. In 2013, Burschka *et al.* achieved a notable efficiency of 15% by employing a 2-step sequential deposition method and constructing the cell with a planar design [68]. This approach involved an initial deposition of a PbI_2 layer, subsequently followed by the deposition of CH_3NH_3I, rather than co-processing both materials. This specific configuration resulted in a high short-circuit current density (Jsc) of 20 mA/cm^2, attributed to the formation of a dense and uniformly distributed perovskite layer [68]. Progressing to 2014, Im *et al.* developed $MAPbI_3$-based solar cells utilizing a two-step solution process [69]. By meticulously controlling the dimensions of the $MAPbI_3$, they optimized light absorption and augmented charge transport. Their findings indicated that the size of the cuboid was influenced by the MAI solution concentration and the duration for which PbI_2 was exposed to MAI before spin coating. This research endeavor culminated in an enhanced perovskite solar cell (PSC) boasting an efficiency of 17.01% [69]. In 2015, Giordano *et al.* endeavored to enhance the electronic characteristics of the mesoporous TiO_2 layer (m-TiO_2) by incorporating Li. This strategic addition culminated in a device that not only showcased superior performance but also achieved a power conversion efficiency (PCE) of 19.3%. The Li-doped m-TiO_2 layer exhibited improved electronic properties, primarily attributed to the accelerated electronic transport. This enhancement was a consequence of the diminished electronic trap states. Notably, the device demonstrated an almost negligible hysteresis loss, measuring less than 0.3% [70]. In 2016, Bi *et al.* proposed an innovative technique for perovskite film production, enhancing its electronic properties by incorporating a polymer [71]. By leveraging poly($CH_3C(O)OCH_3$) (PMMA) to optimize the growth and nucleation processes, they realized a PCE of 21.6%. Subsequently, Yang *et al.* explored the use of multiple cations, inclusive of FA, combined with a mixed halide anion for the absorber layer [72]. Their method of integrating an iodide solution into the organic cation solution effectively reduced the prevalence of deep-level defect states. This defect engineering approach culminated in efficiencies of 22.1% for smaller scale devices and 19.7% for a 1 cm^2 cell. A significant milestone was reached in 2018 when a team from the Chinese Academy of Sciences reported an unparalleled PCE of 23.3%. The peak efficiency of single-junction silicon solar cells was surpassed by a tandem architecture combining Perovskite and Silicon, achieving a power conversion efficiency (PCE) of 28% [73]. The efficiency of the single-junction perovskite solar cell (PSC) was elevated to 23.7%. By meticulously crafting a high-quality perovskite layer, a high open-circuit voltage (V_{oc}) proximate to the bandgap was realized, ensuring minimal

recombination loss [74]. Owing to relentless research endeavors over the subsequent years, PSCs have witnessed a remarkable evolution, currently, the certified efficiency marks 26.1% [15] from the University of Toronto and Northwestern University.

The journey of perovskite solar cells (PSCs) has been remarkable, yet there are still several challenges that impede their commercial viability in comparison to traditional silicon solar cells. These challenges are both fundamental and practical, and include the operational stability of PSCs and the environmental compatibility of the perovskite composition. For instance, the widely studied $MAPbI_3$ perovskite is known to degrade when exposed to heat, moisture, and light in ambient air [75]. Additionally, the use of gold as an electrode increases the overall device cost, and the use of lead in leading PSCs raises environmental and health concerns due to its toxicity [76]. To tackle this issue, researchers are investigating substitute materials for lead, including Tin (Sn), germanium (Ge), rubidium (Rb), bismuth (Bi), and antimony (Sb). Although Sn-based PSCs initially had lower performance than Pb-based ones, they have demonstrated potential. However, Nishimura et al. [77] introduced a strategic substitution in the perovskite structure, leading to enhanced device stability and a record PCE of 13%. It is important to note that the oxidation process, transitioning Sn^{2+} to Sn^{4+}, can generate the hazardous by-product hydroiodic acid [78]. Ju et al. [79] stated that the fabrication of stable, lead-free perovskites can only be achieved once there is a thorough understanding of the degradation and toxicity mechanisms of current perovskites.

Achieving commercial viability necessitates a significant increase in the longevity of PSCs, with the aim of stable performance over years in real-world conditions. Recent advances have focused on modifications to the interface and optimization of charge transport layers. Min et al. [80] introduced an interface layer (IL) between the ETL and the absorber layer, resulting in a PCE of 25.5% with commendable operational stability. The Swiss Federal Institute of Technology Lausanne (EPFL) took a different approach, replacing the conventional ETL with quantum dots of Tin (Sn^{IV}) oxide, leading to a PCE of 25.7% [81]. This replacement addressed the limitations of the widely used mesoporous-TiO_2 ETL, which suffers from low electron mobility and susceptibility to negative photocatalytic events under ultraviolet illumination. The light trapping efficiency was improved and charge carrier recombination was reduced. Liang et al. [82] employed organic hydrophobic molecules, Benzylamine, with an appended side chain to bolster the performance of Formamidinium lead iodide ($FAPbI_3$) films, resulting in an increase in voltage from 1 V to 1.12 V and a remarkable improvement in stability, extending the lifespan from three days to four months. Krishna et al. [83] used a different surface passivation technique, depositing a thin layer of biphenyl-4 4'-dithiol on top

of $(FAPbI_3)_{0.97}(MAPbBr_3)_{0.03}$ perovskite film, leading to higher efficiencies (champion cell: 23.8%). One promising way to control the surface morphology of perovskite film is solvent engineering. For instance, Liu et al. demonstrated that a one-step film formation approach, when exposed to chlorobenzene, led to rapid crystallization, producing even and smooth perovskite layers [84, 85, 86]. Seok's group further optimized the formation of perovskite films by blending dimethylsulphoxide (DMSO) and g-butyrolactone followed by toluene drop-covering, resulting in smooth, tightly-packed large grains perovskite film.[87, 88, 89]. Tandem solar cells, which combine perovskite with other materials, have the potential to exceed the efficiency limits of single-junction cells [90, 91], as they are not constrained to Shockley-Quessier limit. The efficiency limit for a perovskite-silicon tandem solar cell is 47%, much higher than the 31% for single-junction. To achieve optimal efficiency in tandem cells, it is essential to utilize a wide bandgap perovskite material with a bandgap of 1.7 eV and a thickness of approximately 1 μm. However, producing high-quality, micron-thick perovskite of this bandgap remains a significant challenge. Perovskite-Si tandem cells have currently achieved a power conversion efficiency (PCE) of 33.7%, surpassing the performance of top-tier monocrystalline silicon cells [92]. Additionally, the integration of perovskite with second-generation material CIGS has reached a PCE of over 28% [93]. These advancements suggest a promising future with declining PV costs in the upcoming years. Two-dimensional (2D) perovskites, distinguished by their layered structures, offer improved stability over traditional 3D perovskites but at the cost of reduced efficiency [28]. The versatility of perovskites, especially their tunable bandgap, and flexibility, opens up applications beyond traditional solar panels, including in electric vehicles and building-integrated photovoltaics [94, 95]. In conclusion, the domain of perovskite solar cells is vibrant with research and innovations, holding immense promise for the future of sustainable energy. As the scientific community continues to address the existing challenges, PSCs stand at the forefront of revolutionizing the solar energy landscape.

1.3 Luminescence of perovskites solar cells

A deviation from thermal equilibrium can alter the number of electrons and holes in a semiconductor. An increase in temperature, for example, will cause the rate of thermally generated electrons and holes to rise, resulting in a change in their concentration until a new equilibrium is established. An external stimulus, such as light (photons), can also create electrons and holes, leading to a non-equilibrium state. In this thesis, we will only focus on light absorption as the stimuli to generate electron-hole pairs. Luminescence is when

material emits photons(light) to get back to equilibrium after excitation. The light coming out of the material can provide us with valuable information about quality, defects, efficiency, and stability. Luminescence when caused by to interaction of electrons with matter creating excess carriers is called cathodoluminescence [96]. When carriers are injected via electrical contacts, it is referred to as electroluminescence [97], and when light interacts with matter to excite carriers which emit photons back after relaxation is referred to as PL. For a high absorption and emission material such as perovskite, PL is most indicated for their study. It allows us to quantify key parameters such as decay times and transport properties. Kirchhoff's law of radiation is the fundamental justification for using the emitted light from the material as a tool for inspection. It states that: At thermal equilibrium, the absorptance and the emittance of a body per photon energy per angle should be equal [98].

1.3.1 Generation of charge carriers

Generation refers to the creation of electrons and holes through the absorption of light during photo-excitation. Recombination, on the other hand, is the process in which electrons and holes are annihilated. When the energy of a photon ($E_p = h\nu$) is greater than the energy

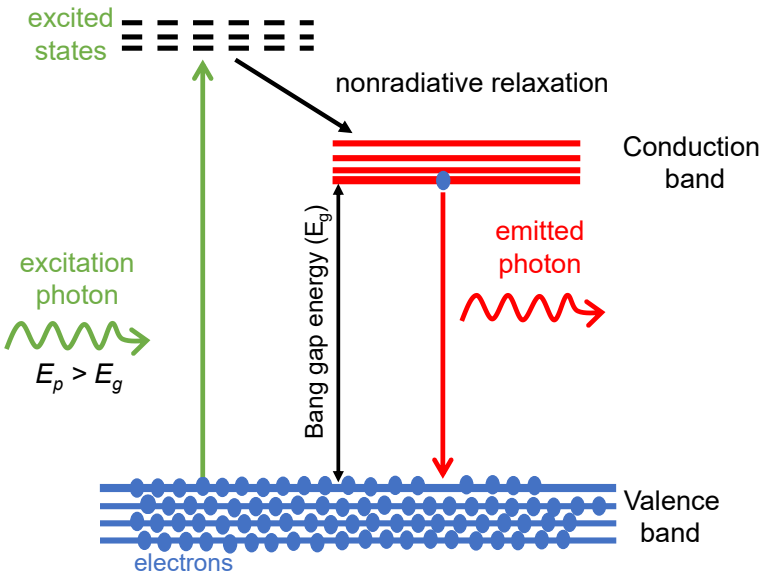

Figure 1.6: Generation of electron-hole pair from photon with energy $E_p > E_g$, where E_g is the band gap of the material. Electrons in the excited state relaxes down to the minimum of the conduction band and recombines with the hole present in the valence band leading to the emission of a photon equal to the band gap E_g

gap (E_g) of a semiconductor, the incoming photon can interact with a valence electron and excite it into the conduction band. The additional electrons and holes created are called

excess electrons and excess holes. The concentration of electrons in the conduction band and holes in the valence band increases above their thermal equilibrium value when there is an excess of electrons and holes.

$$\begin{aligned} n &= n_0 + \Delta n \\ p &= p_0 + \Delta p \end{aligned} \tag{1.9}$$

where Δn and Δp are the excess electron and hole concentration generated respectively. An important requirement of any solar cell is to absorb light (photons) as efficiently as possible. The light absorption of a material depends on its absorption coefficient (α in cm^{-1}) and the thickness of the material. The Lambert-Beer model (B.3) can be used to calculate the light intensity at any point in the device. The equation is given by $I = I_0 e^{-\alpha x}$, where α represents the absorption coefficient, which is an intrinsic property of the material. The variable x denotes the distance into the material, and I_0 represents the light intensity at the top surface. This equation implies that at the surface ($x = 0$), the intensity of incident light will be maximum and will exponentially decrease as we move deeper into the absorber material. Assuming that all incident photons are absorbed by the semiconductor material, we can correlate the number of incident photons with the generation of electron-hole pairs, meaning that each absorbed photon will produce an electron-hole pair. Thus, the generation G can be determined from the total absorbed light in the material as

$$G = \alpha \Phi e^{-\alpha x} \tag{1.10}$$

where Φ is the photon flux at the top surface. A steady-state generation of excess electrons Δn and excess holes Δp will not cause a continuous buildup of carrier concentration. As in the case of thermal equilibrium, an electron will relax down to the lower edge of the conduction band and recombine with the hole in the valence band as illustrated in figure 1.6. Generation can be categorized as internal generation G_{int} and external generation G_{ext}. External generation G_{ext} is the generation rate as a function of time and location of electron-hole pairs due to external illumination, whereas internal generation G_{int} is the generation rate where the photon emitted via radiative recombination is reabsorbed inside the material which is also referred to as photon recycling [99, 100, 101]. Charge carriers will undergo various processes once they are generated and the dynamics can be explained by writing the continuity equation for electrons and holes [102],

$$\begin{aligned} \frac{dn}{dt} &= G_{\text{ext}}(x,t) + G_{\text{int}}(x,t,n,p) - R(x,t,n,p) + D_n \frac{d^2 n(x,t)}{dx^2} + F\mu_n \frac{dn(x,t)}{dx} \\ \frac{dp}{dt} &= G_{\text{ext}}(x,t) + G_{\text{int}}(x,t,n,p) - R(x,t,n,p) + D_p \frac{d^2 p(x,t)}{dx^2} - F\mu_p \frac{dp(x,t)}{dx} \end{aligned} \tag{1.11}$$

x is the position from top surface of cell, t is the time, n and p are the electron and hole concentration, $D_{n/p} = \frac{\mu_{n/p} kT}{q}$ are the diffusion constants for electrons and holes, F is the electric field, $\mu_{n/p}$ are the electron and hole mobilities, R is the recombination rate, G_{ext} and G_{int} ate the external and internal generation rate. The last two terms in equation 1.11 are the diffusion and drift term respectively that governs the movement of charges. The above-mentioned equation does not consider the trapping and detrapping mechanism. These would require additional differential equations to be included in the continuity equation.

1.3.2 Recombination of excited charge carriers

When a material is excited, it reaches a state of non-equilibrium in thermodynamics, meaning that the distribution of electrons and holes is not stable and does not correspond to the lowest free energy of the system, hence the term "non-equilibrium." This state is transient, and the material seeks to revert to its ground state by losing its electron excitation energy. This return to equilibrium can occur through one of two primary pathways.

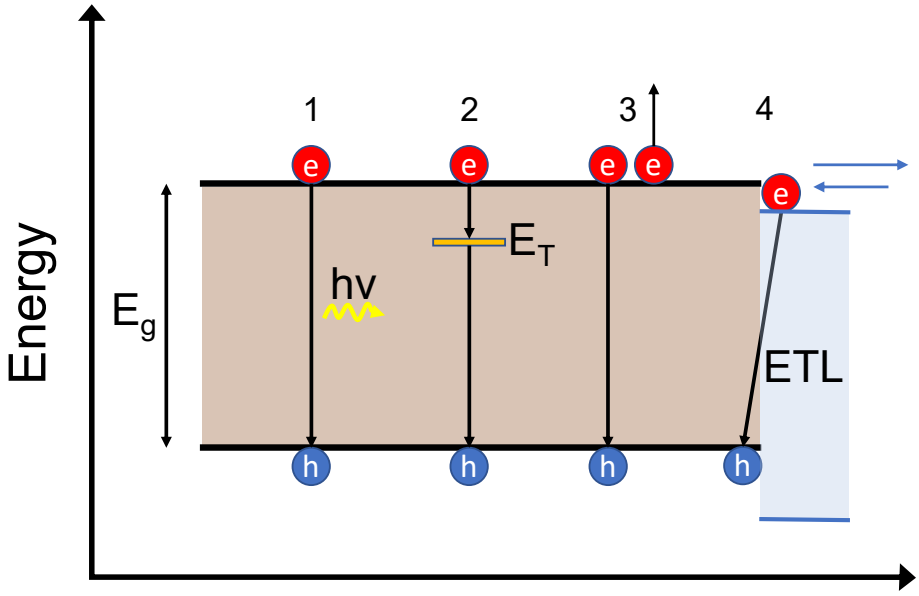

Figure 1.7: Types of recombination in the solar cell. 1) Radiative band-to-band recombination which emits a photon for each electron-hole pair annihilation. The energy released will be equal to the band gap of the absorber material E_g. 2) Non-radiative Shockley-Read-Hall recombination which is defect driven. E_T is the energy level of a defect and no photons are emitted in this type of recombination. 3) Auger recombination in which the photon is given off by band-to-band transition is reabsorbed by another electron in the conduction band pushing it higher in energy. 4) Interface recombination in which the electron in the ETL material recombines with the hole in the absorber layer.

The first pathway involves the emission of a photon, resulting in what is known as a radiative transition. This process typically occurs over a characteristic time denoted as τ_{rad}, also referred to as the radiative lifetime. Alternatively, the excited state may decay non-radiatively with a characteristic time termed as non-radiative lifetime. In such a scenario, the excess energy is dissipated as heat to the crystal lattice. This non-radiative transition usually happens over a time period τ_{nrad}, termed the non-radiative lifetime [103]. These processes are not only limited to energy transition but can also induce photochemical changes within the crystal matrix or lead to the formation of lattice defects. The inverse values of these times, τ_{rad}^{-1} and $\tau_{\mathrm{nrad}}^{-1}$, represent the probabilities per unit time of these transitions occurring. The probability of such a transition to a valence band is given by

$$\frac{1}{\tau} = \frac{1}{\tau_{rad}} + \frac{1}{\tau_{nrad}} \tag{1.12}$$

The significance of τ lies in its ability to describe the process of the excited-state level becoming empty in a collection of luminescence centers through both radiative and non-radiative transitions occurring simultaneously. The decrease in luminescence intensity after the excitation is terminated indicates the decay of the carrier population at the excited level. As a result, the time τ can be measured experimentally. Different ways that the excess charge carriers electrons in the conduction band can recombine with the holes in the valence band are illustrated in figure 1.7. Once recombined, a photon is emitted with the same energy or energy close to the band gap E_g of the solar cell absorber material, provided the transition is band-to-band. Not all recombination is radiative; defect-assisted recombination, also known as Shockley-Read-Hall recombination [104, 105], Auger recombination and interfaces recombination are all non-radiative. Hence three recombination mechanisms and rates are considered in semiconductors; radiative with recombination rate denoted as R_{rad}, defect-assisted SRH recombination with rate R_{SRH}, and Auger recombination with rate R_{aug}.

1.4 Recombination and charge carrier dynamics

1.4.1 Radiative recombination

In a state of thermal equilibrium, every microscopic process is in balance with its reverse process. This principle, known as detailed balance, is crucial for understanding the performance and limitations of different types of solar cells [106]. The amount of radiation absorbed by a body is equal to the amount emitted by the same body itself. Kirchhoff's law [107] expresses this relationship using extrinsic quantities, where the emitted photon flux ϕ_{em} is equal to the product of the absorptance (A) and the incident photon flux ϕ_{in}. Additionally, van Roos-

broeck and Shockley [108] provided a different perspective on the detailed balance approach by connecting intrinsic quantities. They discovered that the internal radiative recombination rate matches the absorption rate $\propto \alpha\phi_{bb}$ of a body in thermal equilibrium. Here, α is the absorption coefficient and ϕ_{bb} represents black body radiation. Consequently, an ideal solar cell should also function as an ideal LED. In the radiative limit, where radiative recombination is the only recombination process present, the maximum achievable open-circuit voltage V_{oc}^{rad} of a solar cell can be determined as [14, 109],

$$V_{\mathrm{oc}}^{\mathrm{rad}} = \frac{k_B T}{q} \ln\left(\frac{J_{sc}}{J_0^{\mathrm{rad}}} + 1\right) = \frac{k_B T}{q} \ln\left(\frac{\int_0^\infty Q_e \phi_{\mathrm{sun}}(E)\, dE}{\int_0^\infty Q_e \phi_{\mathrm{bb}}(E)\, dE}\right) \tag{1.13}$$

where J_{sc} is the short-circuit current density, J_0^{rad} is the radiative saturation current density, Q_e is the quantum efficiency defined as $Q_e(E) = \int_0^d g(x,E) f_c(x) dx$, where g is the generation rate and f_c is the collection efficiency. ϕ_{sun} is the solar spectrum. Direct band-to-band recombination of electrons and holes is radiative, meaning that they release energy as photons. The amount of luminescence we can get after exiting the material with a short laser pulse will depend on the doping density and the excess charge carrier generated by absorption. Thus $I_{PL}(t) = BN_A\Delta n(t)$ where B is the recombination coefficient which is also referred to as k_{rad} that has a dependence on the bandgap of the material. The rate of radiative recombination R_{rad} is a material characteristic that is determined by the radiative coefficient k_{rad} and the doping density. It can be expressed as:

$$R_{rad} = k_{rad}(1 - p_r)(np - n_i^2) \tag{1.14}$$

where p_r is the re-absorption probability.

1.4.2 Non-radiative recombination

Auger recombination: The emission of a photon outside the system is not always the result of a direct transition of an electron to recombine with a hole. In some cases, the emitted photon can be reabsorbed by another electron, causing it to be excited to a high energy level in the conduction band. The process of transferring kinetic energy to another electron during this transition is known as the Auger recombination mechanism. The relaxation of the carrier back to the band edge within the same energy band is referred to as thermalization, which leads to the emission of phonons. Auger recombination becomes relevant when the number of excess charge carriers generated is significantly larger than the doping density of the material. The Auger recombination rate is expressed as [102],

$$R_{Aug} = (C_n n + C_p p)(np - n_i^2) \tag{1.15}$$

where C_n and C_p are the Auger coefficients.

Shockley-Read-Hall recombination rate (trap-assisted): When recombination occurs via defects present within the bandgap of the material, they are referred to as Shockley-Read-Hall recombination. The charges that are generated get trapped at the trap energy level and are not able to recombine radiatively. The rate of non-radiative SRH recombination [102] is expressed as:

$$R_{SRH} = \frac{(np - n_i^2)}{(n + n_1)\tau_p + (p + p_1)\tau_n} \tag{1.16}$$

τ_n and τ_p are the SRH electron and hole lifetimes respectively with $\tau_{SRH} = \tau_n + \tau_p$. Here $n_1 = N_C \exp \frac{(E_T - E_C)}{kT}$ and $p_1 = N_V \exp \frac{(E_V - E_T)}{kT}$ are the electron densities at the trap where E_T is the energy of trap state. If the trap state is deep within the band gap (deep defect), then the SRH recombination rate is given as:

$$R_{SRH} = \frac{np - n_i^2}{n\tau_p + p\tau_n} \tag{1.17}$$

Surface and Interface recombination: The charge carrier dynamics in the bulk is determined by the Shockley-Read-Hall recombination, while recombination at the boundaries of the absorber is significantly influenced by defect states at the surfaces and interfaces. These defects occur due to discontinuities in the crystal lattice at the absorber's surfaces or when there is a mismatch in lattice constants with a different material at the interfaces. The defects at the surfaces and interfaces create localized states within the bandgap, which act as recombination centers for charge carriers [110]. Consequently, the rate of surface/interface annihilation can be considered a specific instance of Shockley-Read-Hall recombination that occurs near the absorber surface.

$$\frac{1}{\tau_{eff}} = \frac{1}{\tau_{bulk}} + \frac{1}{\tau_{surf+diff}} \tag{1.18}$$

Thus equation 1.18 provides with effective decay time with the sum of bulk contribution and surface contribution with transport included. The impact of diffusion will come into play for samples with larger thicknesses. Figure 1.8 shows that there are two interfaces where the surface recombination can take place. When determining the surface recombination velocity or lifetime, it is crucial to know the carrier concentration at each interface. The rate equation for bulk SRH (Shockley-Read-Hall) recombination does not consider surface recombination, making it a representation of the minimum defect-related bulk lifetimes. Calculating the surface recombination of a film on glass is usually simpler, as the back contact between glass and perovskite is considered inactive, and only the perovskite interface with the ambient is taken into account. However, this changes when the perovskite comes into contact with charge transport layers. In the presence of charge transport layers, the interface between the

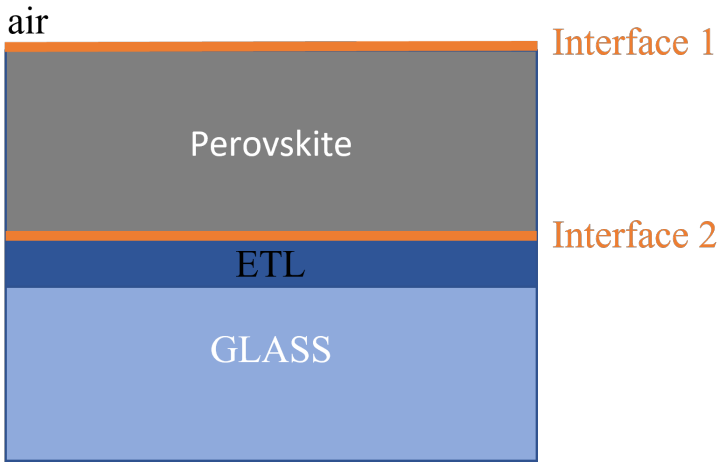

Figure 1.8: Schematic of two interfaces for perovskite on the ETL. The top surface has an interface with the ambient which can be air or nitrogen labeled as Interface 1 and Interface 2 is the back interface with the charge transport layer.

perovskite and transport layers is no longer inert and introduces additional interface defects. One approach to differentiate the surface recombination velocities at the two interfaces is to passivate one of the interfaces to reduce non-radiative recombination. Surface lifetime term τ_{surf} is of particular interest because it is dependent on the thickness of the absorber material. The equation that relates τ_{surf} to the thickness is expressed as [111];

$$\tau_{surf} = \frac{d}{2S_n} + \frac{d^2}{D_n \cdot \pi^2} \tag{1.19}$$

where S_n is the surface recombination velocity, d is the thickness of the absorber material, and D_n is the diffusion constant. Hence the first term is the surface recombination term and the other is the diffusion term. Equation 1.19 assumes that the velocities at both the interfaces are equal which may not be the case as different interfaces can exhibit different densities of defects and traps. Hence, in an extreme case, for estimation purposes, one can assume one of the interfaces is completely passivated which will provide the limiting condition for the defect-related lifetime. In such a case we can use equation [112];

$$\tau_{surf} = \frac{d}{S_n} + \frac{4d^2}{D_n \cdot \pi^2} \tag{1.20}$$

As diffusion can also occur laterally, the fact that the diffusion length will be smaller than the pixel size of the sensor, for the image acquired for most cases, the lateral diffusion concept need not be taken into account. In this thesis, we make use of two different geometries to understand the surface recombination velocities at the top and back interfaces via transient PL which will be discussed in detail in Chapter 4,5,6.

1.4.3 Low injection and High injection condition

Depending on the concentration the charge carriers are generated, there exist two situations; Low-Level Injection (LLI) and High-Level Injection (HLI). LLI occurs when the number of generated minority carriers (electrons in p-type and holes in n-type) is much smaller than the number of majority carriers (holes in p-type and electrons in n-type). HLI occurs when the number of injected or generated minority carriers is comparable to or greater than the majority carriers. In such a case (HLI), the excess generated carriers can alter the distribution of the electric field, change the recombination rate, and affect the mobility of carriers. For a p-type material at LLI, $n << p$ so $n = n_0 + \Delta n \approx \Delta n$ and $p \approx N_A$, Thus the recombination rate equation gets modified to,

$$\begin{aligned} R_{rad} &= k_{rad}(1 - p_r)(nN_A - n_i^2) \\ R_{SRH} &= \frac{(nN_A - n_i^2)}{(N_A + p_1 + n_1)\tau_n} \\ R_{aug} &= C_n n + C_p p(np - n_i^2) \end{aligned} \tag{1.21}$$

At HLI where $n = p$ the recombination rates get modified to:

$$\begin{aligned} R_{rad} &= k_{rad}(1 - p_r)(n^2 - n_i^2) \\ R_{SRH} &= \frac{(n^2 - n_i^2)}{(n + n_1 + p_1)(\tau_p + \tau_n)} \\ R_{aug} &= (C_n + C_p)n^3 \end{aligned} \tag{1.22}$$

The rate equation at HLI reveals that the radiative and Auger recombination rates have a quadratic and cubic dependence on n respectively, which means that they only become dominant when the excess generated charge carriers are in high densities. The sum of all the recombination rates, $R_{rad} + R_{SRH} + R_{aug}$, provides us with the total recombination rate, R_{tot}.

$$R_{tot} = \left(k_{rad}(1 - p_r) + \frac{1}{n\tau_p + p\tau_n} + C_n n + C_p p \right) (np - n_i^2) \tag{1.23}$$

At low-level injection in a p-type semiconductor N_A as bulk doping density, the above equation simplifies to

$$R_{tot} = \left(k_{rad}(1 - p_r)N_A + \frac{1}{\tau_n} + C_p N_A^2 \right) (n - n_0) := \frac{\Delta n}{\tau_{eff}} \tag{1.24}$$

The equilibrium concentration of electrons in the p-type semiconductor denoted as n_0, is determined by the formula $n_0 = \frac{n_i^2}{N_A}$. Here, n_i represents the intrinsic carrier concentration and N_A is the density of acceptor atoms. In this case, the hole density p_0 is approximately equal to N_A. By considering Equation 1.23, it can be concluded that the recombination dynamics can be summarized using an effective lifetime τ_{eff}, which is the inverse of

the first bracket term in Equation 1.24. To experimentally extract this τ_{eff}, the transient PL measurement under low-level injection would show mono-exponential decay and follow $\Delta n(t) = \Delta n(0) \exp(\frac{-t}{\tau_{eff}})$. To distinguish different recombination mechanisms, one needs to conduct transient PL measurement using an excitation condition that goes from LLI to HLI as the high-order mechanisms such as radiative and auger start becoming relevant due to their quadratic nature.

1.5 Steady state and Time-resolved transient photoluminescence of perovskites

1.5.1 Steady state Photoluminescence and imaging

The technique of steady-state PL imaging is capable of operating at various length scales, ranging from sub-nanoscale to large centimeter length scales. This wide dynamic range is significant because heterogeneity can exist at multiple length scales. At the nanoscale level, PL imaging has been employed to investigate the heterogeneity between individual grains to comprehend losses [113]. Steady-state PL can be used to check the transport layer for its ability to hold the high luminescence. The use of photoluminescence characterization plays a crucial role in the advancement of solar cells because it can predict or evaluate the open-circuit voltage of a device by comparing it to the quasi-Fermi level splitting determined from photoluminescence observations.

Further details regarding the application of imaging will be presented in the dedicated chapter on understanding the PL imaging system (Chapter 3). Here, I will briefly discuss the optoelectronic parameters that are crucial and can be mapped and spatially resolved by the imaging system.

1.5.2 Luminescence quantum yield

According to the fundamental principle of detailed balance in photovoltaic material, radiative recombination is the requirement as it is the inverse process of absorption [108]. To achieve a high and efficient photocurrent in a solar cell, it is crucial to have a high absorption coefficient. The figure of merit for recombination, however, does not solely depend on the measured long lifetime. Instead, it is determined by the ratio of the radiative recombination rate to the total recombination rate called internal luminescence quantum efficiency Q_i^{lum} [114, 115, 116, 117].

$$Q_i^{lum} = \frac{R_{rad}}{R_{rad} + R_{nrad}} = \frac{k_{rad} np}{k_{rad} np + R_{SRH} + R_{aug}} \tag{1.25}$$

In a steady-state PL experiment, it is not possible to measure the term Q_i^{lum} because not all photons are emitted solely into the hemisphere above (or below) the absorber layer. This is because some photons have a probability p_e of being emitted, while others have a probability p_r of being reabsorbed within the absorber layer itself. Additionally, there is a possibility that some photons may be reabsorbed by the other layers of the stack with a probability p_a [118]. Instead, a quantity that can be measured through experimentation, the external luminescence quantum efficiency Q_e^{lum} is defined as the ratio of the outgoing photon flux or emitted photons to the incoming photon flux or absorbed photons.

$$Q_e^{lum} = \frac{p_e R_{rad}}{(1-p_r)R_{rad} + R_{nrad}} \tag{1.26}$$

neglecting Auger recombination rate and approximating SRH recombination by $\frac{\Delta n}{\tau}$, where for high injection $\tau = \tau_n + \tau_p$ and for low injection τ would be τ_n or τ_p, equation 1.26 simplifies to

$$Q_e^{lum} = \frac{p_e k_{rad} np}{\frac{\Delta n}{\tau} + (p_e + p_a)k_{rad} np} \tag{1.27}$$

To establish a relationship between the Q_e^{lum} and the carrier lifetime, assumptions must be made about p_e, k_{rad}, and N_A. Multiple research groups have reported varying values of k_{rad} for their perovskite absorbers. Simulations by Kirchartz [102] in Figure 1.9 show that when the excess electron density Δn is small, the primary factor determining the effective lifetime is likely to be the low-order recombination mechanism. As the excess electron density increases, the dominant factor becomes the radiative lifetime $\tau_{rad} = (k_{ext} N_A)^{-1}$, leading to a decrease in the effective lifetime. Auger recombination only becomes significant when the excess electron density exceeds way above the doping density of perovskite.

1.5.3 Quasi Fermi level splitting

Fermi level describes the distribution of electrons in the conduction band and holes in the valence band. Generation of excess charge carriers leads to splitting of equilibrium Fermi level into electron Fermi level and hole Fermi level [98], the energetic position of each provides us information on the distribution of generated charge carriers. If we consider $E_{F,n}$ to be electron quasi fermi level and $E_{F,h}$ to be hole quasi fermi level, then the density of electrons in the conduction band will be,

$$n = N_C \exp\left(-\frac{E_C - E_{F,n}}{k_B T}\right) \tag{1.28}$$

Similarly, the density of holes will be given as,

$$p = N_V \exp\left(-\frac{E_{F,p} - E_V}{k_B T}\right) \tag{1.29}$$

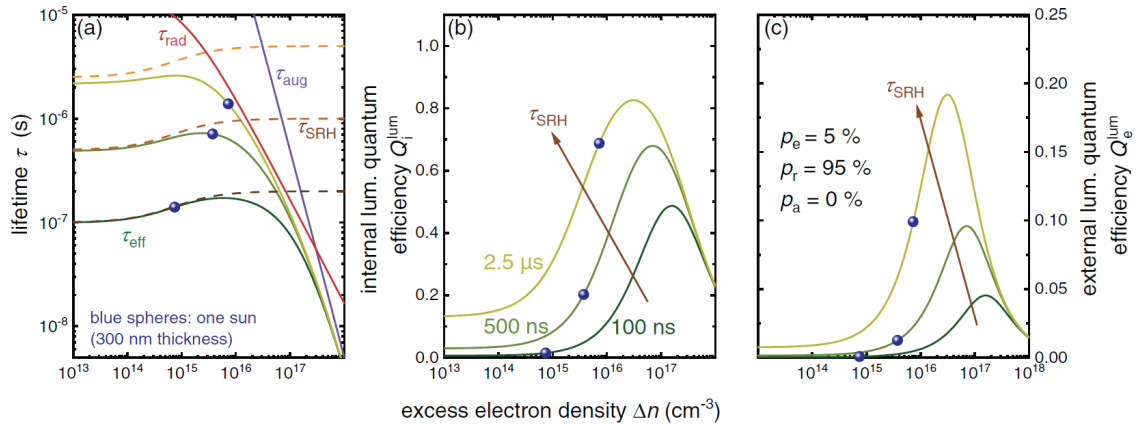

Figure 1.9: Simulation results by Kirchartz [102] illustrating a) The impact of different lifetimes on the effective lifetime (τ_{eff}) is examined. b) The quantum efficiencies of internal luminescence are analyzed for three SRH lifetimes. c) The quantum efficiencies of external luminescence are evaluated for different values of τ_p ($= \tau_n = 100\,\text{ns}, 500\,\text{ns}, 2.5\,\mu\text{s}$) and N_A ($= 10^{15}\,\text{cm}^{-3}$). This analysis emphasizes the transition from low- to high-level injection. Importantly, Auger recombination only affects τ_{eff} at densities greater than 1 sun

As band gap E_g is given as $E_C - E_V$, and by law of mass action $np = n_i^2$, we get

$$np = n_i^2 \exp\left(\frac{\mu_{qfls}}{k_B T}\right) \tag{1.30}$$

where μ_{qfls} is represented as quasi fermi level splitting. Under LLI, $n = n_0 + \Delta n$, $p \approx p_0 \approx N_A$ and $n_0 = \frac{n_i^2}{p_0}$. Using these in the equation and solving for μ_{qfls}, we get relation between the excess generated carriers and μ_{qfls} given as,

$$\Delta E_F = \mu_{qfls} = k_B T \ln\left(\frac{N_A \Delta n}{n_i^2}\right) \tag{1.31}$$

1.5.4 Time-resolved photoluminescence and Imaging

The experiments involving time-resolved photo-luminescence entail illuminating the sample with a light pulse and examining the luminescence intensity emitted by the sample over time. This technique allows for the investigation of different decay times of carriers within the absorber. Time-resolved measurements have been widely employed in the study of semiconductors, as documented in a review by Ahrenkiel in 1993 [110]. In most cases, the luminescence decay of materials exhibits a mono-exponential behavior, enabling the accurate determination of an effective lifetime parameter through fitting. However, in the case of lead halide perovskites, the decay is typically not mono-exponential. Consequently, researchers seek to understand the information that can be extracted from the time-resolved photo-luminescence decay of these materials. In the literature, two methods are mentioned

for interpreting the TRPL data. One is empirical fitting of the decay curve and the second is drift-diffusion modeling. For the empirical fitting method, the choice of function is solely based on the shape of the transient. It can be mono-exponential, bi-exponential [119] , stretched exponential [120, 121, 122] and sometime even tri-exponential [123]. The more sum of exponential is needed to fit the transient, the more complicated it gets to put physical meaning behind the recombination rate and lifetime values. The second method relies on modeling from drift-diffusion equations [124, 102, 125]. One can insert a set of values and parameters into the model to output the transient data that best fits with the experimentally measured transient. However, when there are too many unknowns, it becomes a time-consuming process. Lifetime is measured in a transient PL experiment which is a powerful technique sensitive to generated charge carrier carrier concentration. If we excite the semiconductor with a laser pulse, the excess charge carriers generated Δn start decaying with time via different recombination processes which we discussed earlier. The rate at which it decays follows the differential equation;

$$-\frac{dn}{dt} = \frac{n - n_0}{\tau_{eff}} \tag{1.32}$$

with a solution

$$\Delta n(t) = \Delta n_{(t=0)} \cdot \exp(\frac{-t}{\tau_{eff}}) \tag{1.33}$$

Even though it seems that measuring lifetime is easy, interpreting the transient and extraction of the true parameters is challenging. Differentiating between recombination mechanisms is only feasible when the excitation conditions are identified, and this differentiation varies depending on the level of injection, ranging from low to high. The term "charge-carrier lifetime" generally refers to how the concentration of electrons or holes changes over time after they are generated by a laser pulse. The recombination mechanisms are associated with lifetimes: τ_{rad} for radiative recombination, τ_{SRH} for Shockley-Read-Hall recombination, and τ_{Aug} for Auger recombination. These three processes form the bulk recombination lifetime τ_{bulk} as follows:

$$\frac{1}{\tau_{bulk}} = \frac{1}{\tau_{rad}} + \frac{1}{\tau_{SRH}} + \frac{1}{\tau_{Aug}} \tag{1.34}$$

Differential lifetime: As we discussed above, in most cases, transient data fit with the exponential decay functions based on their shape. The disadvantage of this method is that the higher the sum of exponential used for fitting, the harder it gets to make sense of the processes taking place in the sample. Particularly, this approach does not take into account the impact of non-linearities caused by accumulation of charges at the interface which will affect the transfer velocity, changes in band alignments, and also promotion of interface

recombination. Instead, Krogmeier et al. [126] defined the differential lifetime $\tau_{diff}(t)$ as the inverse negative slope of the logarithmically plotted photon flux ϕ_{PL};

$$\tau_{diff} = -\left(\frac{dln(\phi_{PL}(t)}{dt}\right)^{-1} \tag{1.35}$$

Transforming the experimental transient into a differential lifetime and plotting against

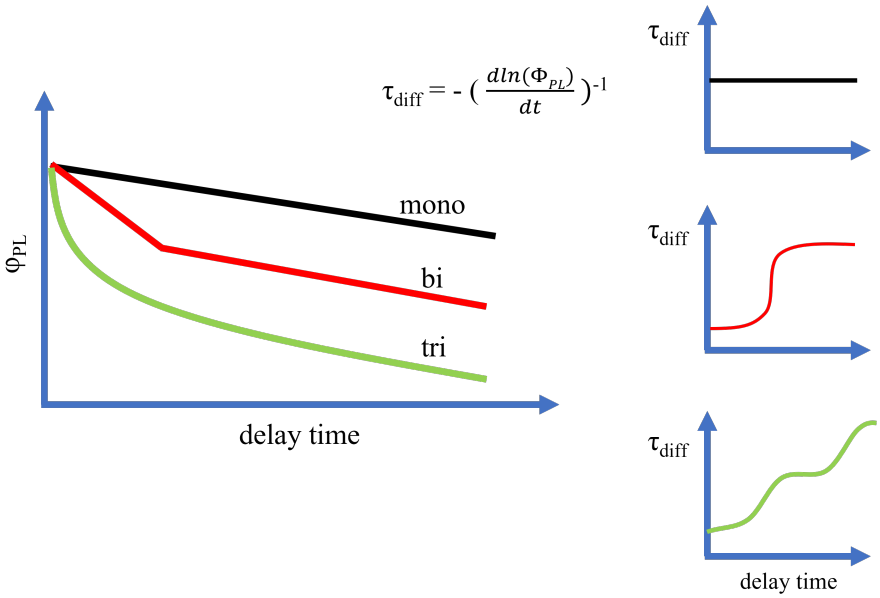

Figure 1.10: Schematic of how the differential lifetime plot would look depending on the transient PL data.

delay time has the advantage that every change of slope of the transient is preserved. Figure 1.10 shows how the experimentally acquired transients can be transformed into a differential lifetime. Several plateaus describe the number of recombination mechanisms that are taking place in the absorber. For example, if the decay is mono-exponential, there will be one dominant recombination taking place. For bi-exponential decay, there will be two plateaus, one at the small delay times and one at the longer delay times. Such a method of extracting decay life is more reliable as compared to traditional fitting using function. For low injection levels, the distinction between the process of charge transport and recombination can be easily seen from the plot of differential lifetime. However, at a high injection level, such distinction becomes difficult. In this thesis, I will use the differential lifetime approach to understand the processes taking place in perovskite when illuminated at low injection level and high injection level.

Transient PL imaging: For transient imaging, an imaging camera with a good shutter and gating speed can obtain images at all times of the transient decay. There are different types of time-resolved imaging systems, one where the sample is scanned line by line (a very

time-consuming process) and the other using snapshot ability where an image is taken of the entire surface with excellent spatial resolution. Imaging time-resolved PL has a lot of potential as a characterization tool not only for research but also for industries. As it is an imaging technique, its non-destructive, and no physical contact is needed with the sample to extract the data. In literature, many research groups have started using time-resolved PL imaging for the characterization of carrier diffusion [127], carrier transport across grain boundaries [128], 4D vertical charge transport [129]. Figure 1.11 shows the potential of the

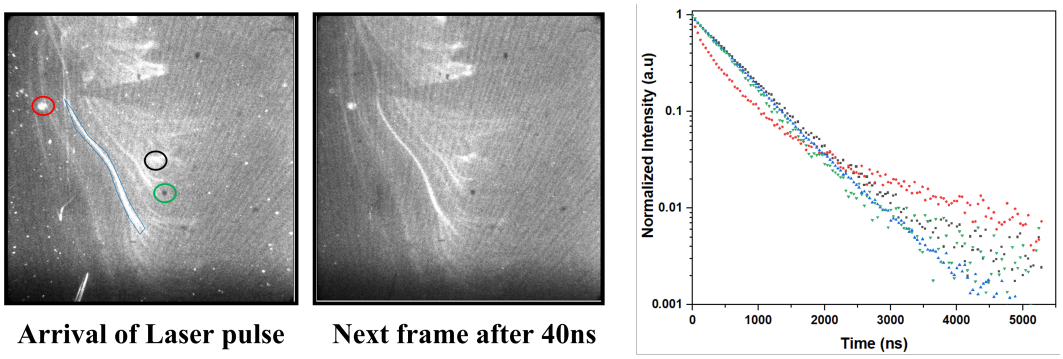

Figure 1.11: Example of ability of time-resolved PL imaging. The image on the left is the perovskite being illuminated by a short laser pulse and the image next to it is the image taken after $40ns$ of pulse arrival. The transient in the plot shows the data extracted from the marked region in the images. This shows how we can spatially map the decays of the features and identify their nature.

time-resolved transient PL imaging system. A perovskite excited with a short laser pulse and image was recorded at two time stamps; immediately after arrival of pulse and after $40ns$. The bright pattern on the PL image seen has no conclusive explanation so far but the possibility is vertical chemical heterogeneity where in some regions the chemical composition varies and shows variation in the optoelectronic properties. Nevertheless, the point here is that imaging gives us the flexibility to study any desired feature on the surface. The transient plotted for the color-marked feature on the surface shows different transient decay.

In this thesis, we will make use of our PL imaging system in both steady-state conditions as well as time-resolved conditions to study mixed halide as well as triple cation perovskite.

Chapter 2

Methodology

In this chapter, the perovskite samples used for study will be introduced. Apart from the sample stack itself, I will talk a little bit about storing the samples and characterization techniques used to measure and analyze the perovskites

2.1 Samples and storage

2.1.1 Perovskite from EPFL

The first perovskite that will be used in chapter 4,5 and partially 6 is a two-cation mixed halide perovskite $(FAPbI_3)_{0.97}(MAPbBr_3)_{0.03}$. For simplicity, I will refer to this perovskite as FAPIBr. The partial stack of this perovskite consists of Fluorine doped tin-oxide (FTO) glass substrate, a 20-40nm thick layer of compact TiO_2 applied by spray pyrolysis, a 100-150nm thick mesoporous (mp)-TiO_2 layer applied by spin-coating and then finally perovskite film deposited on mp-TiO_2 by spin-coating followed by annealing. One sample group is just the partial stack mentioned above and the other has a bifunctional aromatic ligand, biphenyl-4 4'-dithiol spin coated on the perovskite as a passivation layer. Thus the two sample groups will be referred to as unpassivated and passivated perovskite in this thesis. For a more detailed fabrication process and parameters, refer to Krishna et al. [83] who grew the samples at EPFL. The samples were then sent to me in a nitrogen-filled sealed box and were stored in a nitrogen-filled glovebox.

2.1.2 Perovskite from IPV Stuttgart

The perovskite that will be used to study in chapter 6 of this thesis is a tripe-cation mixed halide perovskite $Cs_{0.05}(MA_{0.17}FA_{0.83})_{0.95}Pb(I_{0.83}Br_{0.17})_3$. I will refer to this perovskite as CsFAMA in this thesis. An Indium-doped tin oxide (ITO) glass substrate was used as a

base to spin-coat perovskite followed by an annealing step. In this study, there will be a total 4 sample groups, First with bare perovskite surface which is referred to as unpolished, second will be perovskite with laser treatment which is referred to as polished, third will be unpolished perovskite with Spiro-OMeTAD and last will be polished perovskite with Spiro-OMeTAD layer on top. The laser used to polish the surface is a pulse, point-focused laser with a wavelength of 355nm and with pulse duration of 130ns. Complete details of the fabrication and treatment parameters can be found in Kedia et al. [130] who grew the samples and shipped them to me in nitrogen-sealed bags which were later stored in a nitrogen-filled glovebox.

2.2 Characterization techniques

This section will introduce all the characterization techniques used in this thesis to study the above-mentioned perovskites.

2.2.1 Photoluminescence Imaging

As this characterization technique has a dedicated separate chapter with full details (Chapter 3), I will skip this one here.

2.2.2 Profilometer

Brucker's DektakXT stylus profilometer is used in this thesis to measure the surface height variation of the FAPIBr perovskite as well as the mesoporous structure of the charge extraction layer. Contact profilometry sometimes also called stylus profilometry is a widely used method to map the surface geometry and roughness [131, 132]. It consists of a probe that applies a very small force on the surface and scans either a specified direction or line-by-line mapping. As the probe moves along the surface, a feedback loop measures the reaction force of the sample to the tip. An advantage of such a technique is its high-resolution height profile and ease of use. However, it also has limitations. As with all the probe techniques, there is always a possibility of breaking the probe or contaminating it which causes changes in the output. Not only probe but soft material or dusty surface can impact the tip radius making it effectively larger and reducing the resolution. Generally, the probe has a tip radius of approximately a few micrometers. The profilometer setup used for measurement in this thesis is shown in Figure 2.1.

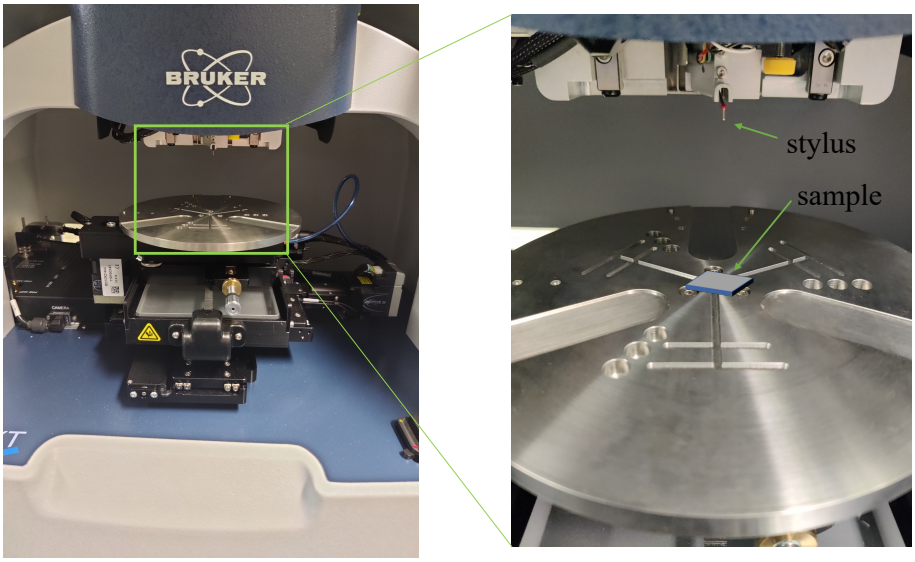

Figure 2.1: Profilometer setup. On the right is the measurement area where the sample is positioned and the stylus approaches the sample from the top.

2.2.3 Atomic Force Microscopy

The invention of Atomic Force Microscopy Atomic force microscopy (AFM) took place in 1989 by Binnig and Gerber [133] who measured the force between the tip and a sample. The forces between the tip and the sample can be classified as long-range force (van der Waals) and short-range force (repulsive or attractive). These two forces can be expressed by Lennard-Jones potential [134].

$$U(r) = 4\epsilon \left[\left(\frac{\sigma}{r}\right)^{12} - \left(\frac{\sigma}{r}\right)^{6} \right] \tag{2.1}$$

ϵ is the potential well depth, σ is the distance at which the $U_r = 0$ and r is the distance between two particle or atoms. When the tip which is mounted on a flexible cantilever approaches the sample surface, it first senses long-range force and will get attracted to the surface thus bending the cantilever towards the surface. As the distance gets closer and closer, repulsive forces start dominating bending the cantilever away from the surface. This deflection of the cantilever is monitored via the beam-deflection method where a laser beam is focused at the end of the cantilever. This laser then reflects off the cantilever on the photodiode measuring the variation of the signal intensity. The schematic of the operation of AFM as well as different modes is shown below; As there exists more than one force between the tip and sample depending on the distance between them, different modes of measurement exist when using AFM. Contact mode is perfect for soft materials such as polymers but still, there is a risk of damaging the tip as it is always in contact with the surface. Tapping mode is when the tip vibrates with some frequency, gently tapping the

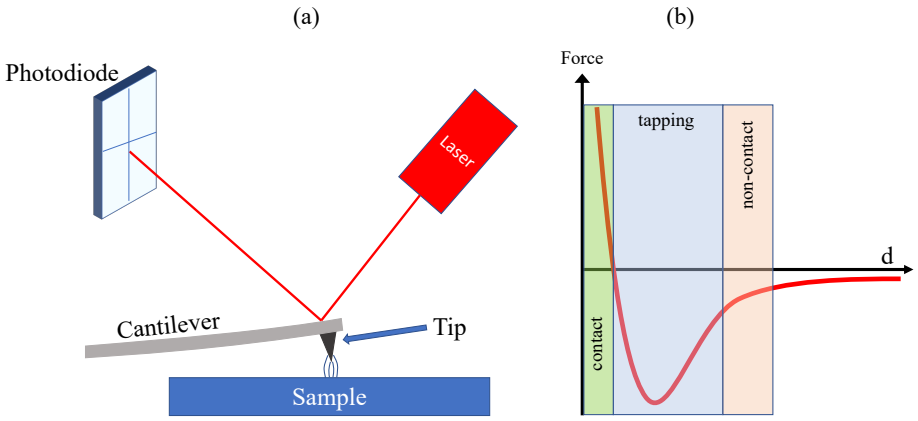

Figure 2.2: (a) General working principle of AFM measurement. (b) Force distance curve from the Lennard-Jones potential where d is the distance between tip and sample. The green region represents a repulsive regime where the tip and sample are brought in contact. The orange region represents an attractive regime where the tip and sample are not in contact. The middle blue region is where the tip taps the sample with some frequency and this mode is commonly referred to as tapping mode.

surface and the amplitude of the vibration then changes with the force between the tip and sample. This change is then recorded to determine the topography of the sample surface. As compared to contact mode, this mode is less destructive but still has the possibility of damage. Non-contact mode is not destructive as the tip and sample always have some distance between them i.e. they never touch. Interaction between the tip and sample can be thought of as that of a capacitor where the distance between the two plates affects the capacitance. The AFM cantilever is mechanically excited to its natural resonance frequency f_0 or close to it. This depends on the mass of the cantilever and its spring constant k. The resonant frequency f_0 is written as [135];

$$f_0 = \frac{1}{2\pi}\sqrt{\frac{k}{m}} \tag{2.2}$$

As the tip approaches the sample, the amplitude of the cantilever gets affected and this induces a change in spring constant k given as $k^{'} = k - \frac{\partial F}{\partial z}$ [135]. Thus the change in the resonance frequency Δf will be given as,

$$\Delta f = -\frac{f_0}{2k}\frac{\partial F}{\partial z} \tag{2.3}$$

Equation 2.3 says that the change in resonance frequency is caused by the force gradient along the vertical direction z. Using this formulation, non-contact mode AFM can work in either amplitude mode (AM) or Frequency mode (FM). In Amplitude modulation KPFM (AM-KPFM), the change in amplitude of the vibration is measured and the topography map

is constructed [136] whereas in Frequency modulation KPFM (FM-KPFM) the change in the frequency Δf itself is tracked [137] which has high accuracy and better lateral resolution [138].

2.2.4 Kelvin Probe Force Microscopy

With AFM, One can also measure the topography as well as the function of the sample simultaneously, if the WF of the tip is known. For Kelvin probe force microscopy (KPFM), an applied AC bias voltage is applied to the cantilever in addition to the mechanical oscillation that modulates the electrostatic force between the tip and sample [139]. Figure 2.3 illustrates

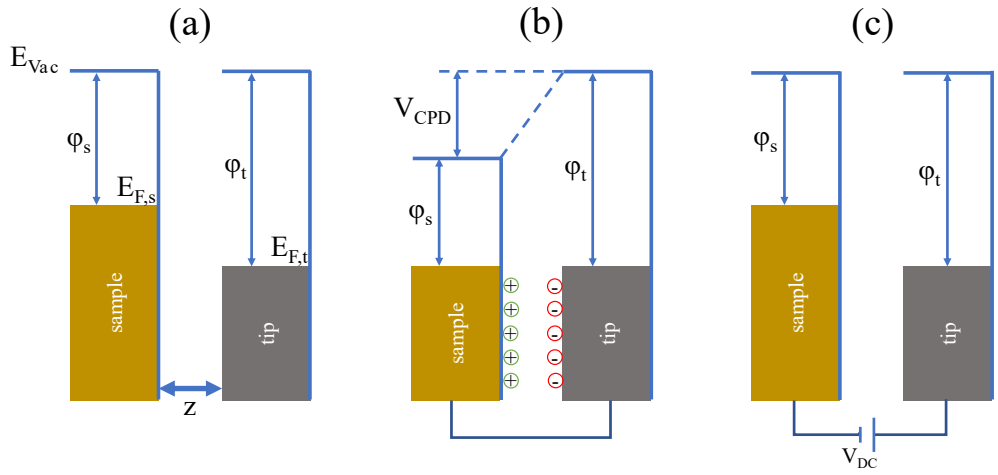

Figure 2.3: Model of KPFM working principle. (a) Sample and tip with the difference in their fermi energy at distance z between them. (b) The sample and tip are in contact with each other lowering the high fermi energy of the sample to align with the tip fermi energy thus lowering the vacuum energy by V_{CPD}. (c) External DC bias is applied to raise the E_{Vac} to the tip vacuum level or to nullify the generated V_{CPD}. The model is adapted from reference [139]

the process that occurs when the tip and sample come into contact. In this process, E_{Vac} represents the vacuum level of the system, $E_{F,s}$ and $E_{F,t}$ represent the fermi energy levels of the sample and tip, respectively, z represents the distance between the tip and sample, and V_{CPD} represents the Contact Potential Difference (CPD). When the tip and sample are in contact, electrons from the sample flow into the tip until their fermi energy levels align. This flow of charge leads to the CPD, which is proportional to the difference in WF between the tip and the sample. It can be expressed as [139]:

$$V_{CPD} = \frac{\phi_{sample} - \phi_{tip}}{e} \tag{2.4}$$

To nullify the CPD, an external DC bias is applied. This DC bias is then measured by the KPFM tool which is equivalent to the Contact potential difference (CPD). Similar to the two modes of AFM (AM and FM), KPFM can also be operated in these modes. In AM mode, the electrostatic force between the tip and sample is nullified, while in FM mode, the force gradient is nullified [140]. In this thesis, AFM/KPFM data was measured in FM mode, as it provides better lateral resolution for WF variation compared to AM mode [141]. Therefore, the measurable quantity for performing KPFM is the frequency variation Δf. By applying an additional AC bias to the cantilever, equation 2.3 for KPFM becomes:

$$\Delta f \approx \frac{\partial^2 C}{\partial z^2}(V_{DC} - V_{CPD} \cdot V_{AC} \sin \omega t) \tag{2.5}$$

Here, $\frac{\partial^2 C}{\partial z^2}$ represents the second derivative of the capacitance between the tip and sample, and the term $V_{AC} \sin \omega t$ represents the applied AC bias to the cantilever. From the equation, it can be observed that when the DC bias is equal to V_{CPD}, Δf becomes zero, indicating that the force gradient between the tip and sample has been nullified. A lock-in amplifier records Δf from the phase-locked loop (PLL) as input and continuously applies DC bias to maintain this change at zero.

As samples used in this thesis are perovskites on a glass substrate, to measure the CPD signal, an electrical contact is to be made between the surface and the sample mounting metal plate. To do this, I used conducting carbon glue. at the edges of the sample so that the surface and metal plate have a conducting path. This process was carried inside the glovebox to avoid exposure of perovskite to oxygen. Once the glue was dry, the sample was then sealed in a transfer box to bring it to the AFM/KPFM setup. The AFM/KPFM setup itself is enclosed in a thick glass box which provides the ability to fill it with nitrogen gas, thus measurements are conducted in the nitrogen environment. Once the topography and CPD data are acquired, further image processing is carried out using Gwyddion software[142]. As the CPD map does not directly provide information about the WF, if the WF of the tip is known, the WF of the sample can be calculated using CPD. I first use a freshly cleaved Highly-Oriented Pyrolitic Graphite (HOPG) sample to measure the CPD and calibrate the tip WF by using the HOPG WF of 4.60eV [143] using equation 2.4. Once the tip WF is known, the HOPG is then replaced by the perovskite sample to measure the topography and CPD. Using the same equation 2.4, the WF of the sample can be calculated.

2.2.5 Surface morphology and composition measurement techniques

To study the surface composition and inhomogeneities of the perovskite sample, I used Scanning Electron Microscope SEM, Energy-Dispersive X-ray Spectroscopy EDX as well as

Helium-Ion Microscope with Secondary Ion Mass Spectrometry HIM-SIMS. Measurement using these techniques was not personally performed by myself but with the help of experts with this equipment. Thus, here I will only provide a general working principle in short.

SEM: The technique known as Scanning Electron Microscopy (SEM) utilizes an electron beam that is focused onto the surface of a sample. This interaction between the beam and the sample produces secondary electrons, backscattered electrons, and characteristic X-rays. These particles are then detected by specific detectors and converted into an image. A SEM tool typically consists of an electron gun, a column containing electromagnetic lenses to focus and guide the beam onto the sample, several detectors to capture the emitted electrons, a sample chamber, and a computer unit. Two types of interactions occur: elastic and inelastic. In the inelastic interaction, low-energy secondary electrons are emitted from the sample. In the elastic interaction, the primary electrons are deflected by the cloud of electrons around the nucleus. The most commonly used signal for creating SEM surface maps is the secondary electron signal. The detection of these signals can provide information about the sample surface with a resolution of a few nanometers, depending on the energy of the incident electrons.

EDX: Energy-dispersive X-ray spectroscopy (EDX) is a technique used to determine the elemental composition of a sample using a scanning electron microscope (SEM). This involves exciting the atoms in the material with an electron beam and measuring the resulting characteristic X-rays. In this thesis, the EDX utilized is the Ultim Max 40 model, which is capable of both point and large-area mapping of chemical composition. EDX can detect elements with atomic numbers higher than that of Boron[144]. It has various applications, including mapping elemental distribution, detecting chemicals at specific locations, and conducting quality control. When electrons collide with the sample in the SEM, the sample emits characteristic X-rays that are unique to each element and transition. The primary beam's energy causes an electron in an atom's nucleus to become excited and be ejected from its energy level. Then, an outer shell electron fills the vacant position left by the ejected electron, releasing energy in the form of X-rays. The emitted X-rays consist of both continuum and characteristic X-rays, with the latter being used to identify the elements. From the energy position of the EDX spectra, one can refer to the library of elements and their respective energy to assign an element. EDX can be used for qualitative and quantitative analysis, enabling the identification and determination of the concentration of each element. By using the intensity of the EDX spectra, one can calculate the absolute composition of elements but this depends on many factors. The system needs to be calibrated by some standard pure

element with known composition. EDX spectra and mapping in this thesis on perovskite sample was achieved with an acceleration voltage of 20kV. This parameter is important as it determines the interaction depth of volume of the primary electron beam with the material. As I am using layer-stacked material, the elemental detection may go beyond the perovskite layer and to the layers under the perovskite.

HIM-SIMS: Helium-Ion Microscope with Secondary Ion Mass Spectrometry is an extremely powerful technique for analyzing surfaces with excellent sensitivity, high mass resolution, high dynamic range, and ability to differentiate between isotopes. The initial idea of the ion microscope was put forward by Knoll and Ruska in 1932 [145]. The working principle of a HIM consists of three stages, Helium ionization and acceleration, Beam formation and control, and Sample interaction. A stable ion source with high brightness and small virtual source size was realized by Ward, Notte, and Economou for use in microscope [146]. It is based on an emitter whose apex is shaped into a pyramid. Using Scanning Field Ion Microscopy (SFIM) the apex of the tip can be monitored and shaped using high fields that can ultimately remove weakly bound atoms from the apex. In this way, the configuration of the tip apex can be controlled at the atomic level. He ion beam is thus used to interact with the sample. As He has low mass, scattering is not very efficient at the very near surface. After the interaction, the signals that can be detected are secondary electrons, backscattered Helium as well as photons by a phenomenon called ionoluminescence. In this thesis, HIM is used in secondary electron mode to see the morphology of the perovskite.

About SIMS, two of the most common types of SIMS instruments used for imaging are time-of-flight SIMS (ToF-SIMS) and nanoscale SIMS (NanoSIMS). SIMS analysis generally creates images, where each pixel of the image contains a mass spectrum with chemical information of the sample. Hence, the spatial resolution is correlated to the incident ion beam diameter and pixel density. Previous studies have discussed methods of estimating the spatial resolution of SIMS by imaging the edges [147]. Mass resolution refers to the ability of the tool to distinguish between two adjacent masses [148]. In this thesis, 2D composition mapping was used to study the composition of the perovskite laterally.

For this measurement, the sample had to be exposed to air but for a very short time (less than a minute). The data treatment and analysis were carried out by me using Image processing software.

Chapter 3

The Hyperspectral Photoluminescence Imaging System

The book titled "La lumiére, ses causes et ses effets", published in 1867, compiles the 30 years of work by E. Becquerel in the field of PL [149]. This indicates that the study of PL dates back to the 1860s. In 1938, Gurney and Mott were the first to observe absorption and luminescence in solids [150, 151]. Shortly after, Johnson et al. observed luminescence using optical excitation [152] of Silicate, molybdate, and sulfide phosphors when excited by Hg 2536 Å radiation. The study of luminescence in solids and phosphors, as well as the investigation of luminescence decay and related phenomena, can be traced back to 1939 [153]. In the 1940s, William explored electrical properties and phenomena such as luminescence [154], while Randall et al. studied phosphorescence [155]. In the following decades, particularly in the late 1980s and 1990s, PL became a crucial tool for silicon characterization, particularly in photovoltaic (PV) applications. This progress was mainly driven by the research conducted by Peter Würfel's group at the University of Karlsruhe [156, 157, 158]. PL measurement technique has played a significant role in determining the optoelectronic properties of materials and provides insights into charge carrier recombination related to defects [159, 160, 102, 161]. Electroluminescence (EL) and PL imaging have become prominent in solar cell research due to their non-destructive nature, ease of use, and rapid analysis.

Hyperspectral PL imaging technique combines the established PL imaging with the spectrally resolved measurement providing detailed insight into the material properties [162, 163]. This technique has been applied to various materials, including Silicon [164, 165, 166, 167], GaAs [162], $Cu(In, Ga)Se_2$ [168], and Perovskites [169, 170]. It allows for precise spatial and spectral differentiation of luminescence signals, enabling the observation of properties such as the quasi-Fermi level split μ_{qfls} which indicates the maximum achievable open circuit voltage

(V_{oc}) of a solar cell [171, 172, 173], Urbach energy (E_U)[174, 63], PL quantum yield [102] and PL central wavelength. Hyperspectral imaging also helps to identify spatial inhomogeneities such as band gap variation, chemical heterogeneity [175], nature of grain boundaries [113], nano-scale trap clusters [176] at multiple length scales and many more that could affect solar cell efficiency. It is also less prone to artifacts compared to confocal configurations [168]. One of its major advantages is the capability to present luminescence intensity in absolute terms, unaffected by lateral carrier diffusion. Comparisons with electrical measurements have shown a consistent relationship between μ_{qfls} and V_{oc} across different devices, with deviations up to 20 meV [171, 172, 173].

In this chapter, I will introduce a hyperspectral PL imaging system I developed during this thesis. I will begin by providing a brief overview of the key components and their purpose in the imaging system. I will then move on to discussing the calibration method of the system for intensity and spectral correction which is crucial for the system to be able to accurately determine the absolute number of photons and to resolve them spectrally. Further, I will discuss how the data acquired by the system is processed. As the system captures image images in gray scale, it requires external image analysis to obtain quantitative optical parameters of the sample under study.

3.1 Design and components

Figure 3.1 shows the complete custom-built PL setup used for steady state and Time-resolved PL measurements. I will talk briefly about the essential components of the PL setup starting with the camera followed by a spectrometer, laser source, and homogenizer.

3.1.1 intensified Charge-Coupled Device Camera (iCCD)

The PI-Max4:1024i from Princeton Instruments is the central element of the imaging system. This sophisticated intensified charge-coupled device camera (iCCD) has a 1024 x 1024 interline CCD connected to intensifiers, offering remarkable sensitivity in the UV to NIR range from 200-900 nm. The pixel size is $12.8 \times 12.8\,\mu m$ ultimately corresponding to the sensor dimension of $13.1 \times 13.1\,mm$. The resolution limit of the camera is between 40-64 lp/mm (linepair per millimeter). CCD cameras are ideal for low-light applications due to the electron multiplication of the intensifier. Additionally, their rapid shutter speed of less than a nanosecond makes them suitable for fluorescent lifetime imaging microscopy. All the applications of the iCCD in various fields of studies can be found at *Princeton Instruments* research stories page [177].

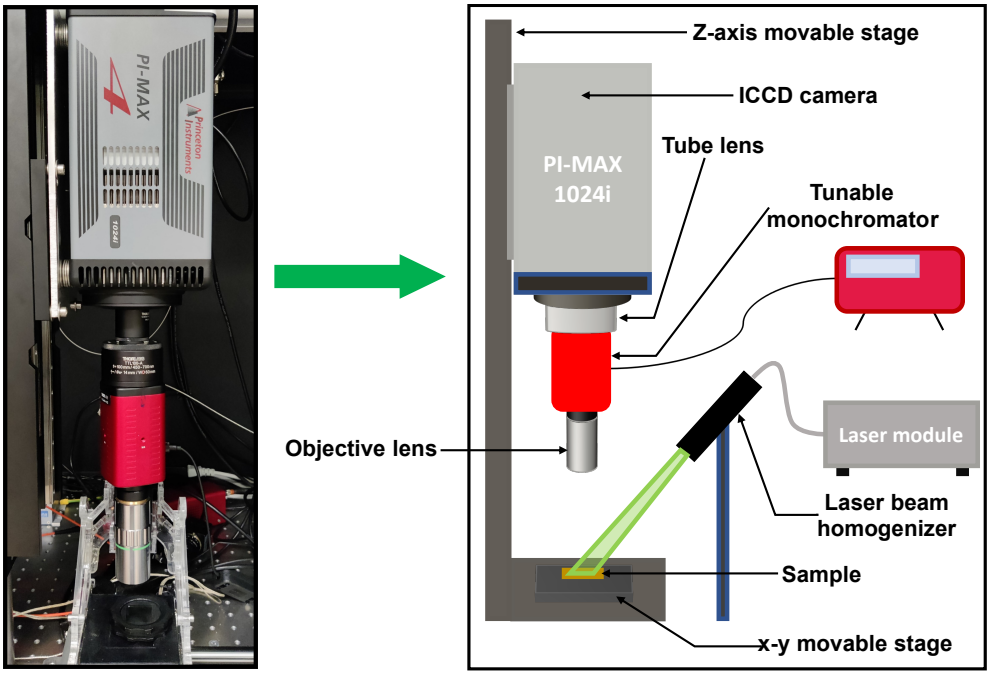

Figure 3.1: Picture of Hyperspectral PL imaging system in our lab used for steady state and Time-resolved PL measurements and imaging. The image on the right shows the schematic of the essential components that make up the system.

The intensifier is composed of three main components: a photocathode, a microchannel plate (MCP), and a phosphor screen on a fiber optic. Figure 3.2 shows the components of CCD inside the camera. When photons hit the photocathode, they are converted into photoelectrons, which are then accelerated to the MCP. This MCP is responsible for the multiplication of the photoelectrons, creating an electron cloud. This process is regulated by the camera's gain, which is managed by the MCP voltage. The electron cloud then strikes the phosphor fiber optic, transforming the electrons back into photons. The photons are then guided, through fiber-optic coupling, to the CCD array where the respective pixels become ultimately charged. At this point, the phosphor decays, and the accumulated charge is transferred to the serial register and converted to an analog voltage by an on-chip amplifier. This voltage is then digitally encoded and converted into gray values. Putting together all the voltages from the CCD array allows for the generation of a 1024x1024 pixels image (or frame), that is ultimately displayed on the Lightfield software. Thanks to the MCP's amplification, CCD detectors are highly sensitive, even capable of detecting single photons. The ultra-fast shutter speeds in iCCD detectors are enabled by the controlled voltage across the intensifier, allowing a gating process that prevents photons from reaching the CCD. To enhance the signal-to-noise ratio, certain parameters can be adjusted, such as the intensifier gain, gate width, and On-CCD accumulations. The intensifier gain is linked to the number

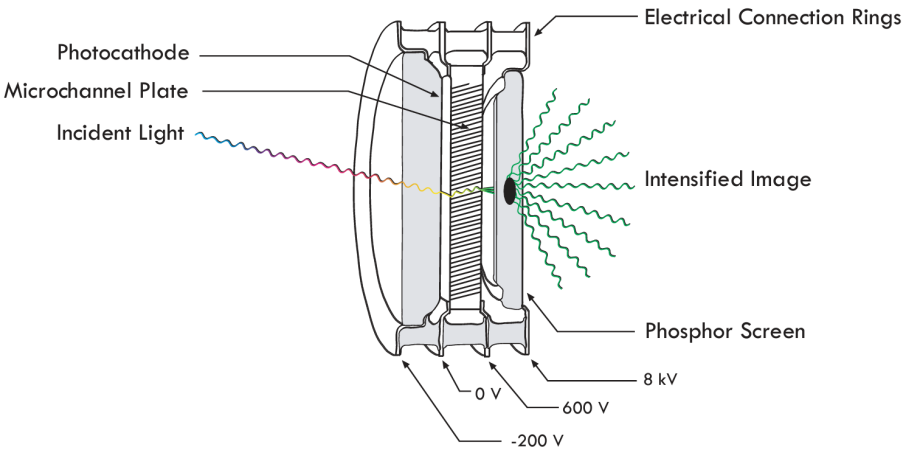

Figure 3.2: Schematic representation of the CCD sensor inside the camera. Incoming photons cause the emission of photo-electrons followed by signal intensification via microchannel plate. Further, these electrons excite a phosphor screen emitting photons towards the CCD chip. This schematic has been taken from *Princeton Instruments* [178].

of electrons generated per detected photon, so the higher the value, the more electrons are produced. The gate width is the period during which the intensifier is active, meaning that only photons that reach the camera within this time frame are detected. The number of On-CCD accumulations determines how many detection cycles (gate width intervals) are accumulated on the CCD array before they decay and form a frame. However, one must be careful to avoid saturating the CCD detectors. It is important to understand how these parameters affect the number of counts detected by the camera. The details of how different parameter affects the PL signal for this setup are reported in the Master thesis of Ricardo Poeira [179]. The use of CCD cameras in photovoltaics is widespread [177]. They can be used to analyze the PL of PV materials, providing insight into the quality of the layer, defect states, and charge recombination processes. The rapid gating of iCCD cameras allows researchers to investigate up to nano-second time scale charge carrier dynamics in materials, revealing the pathways of charge generation, separation, and recombination. Moreover, CCD cameras enable the spatial mapping of carrier dynamics across layers [180, 181], aiding in the optimization of fabrication processes. Additionally, CCD cameras could be used to address the stability issues of PV, particularly perovskites by combining them with controlled stress tests, allowing for the monitoring of degradation in real-time. In conclusion, iCCD cameras are invaluable tools for researchers studying PV, giving a better understanding of the material properties and behaviors that determine the efficiency and durability of these promising solar technologies.

3.1.2 Laser beam and source

This section introduces the pulsed laser light source from PicoQuant. This laser operates at a central wavelength of 532 nm, which falls under the visible region of the electromagnetic spectrum and is suitable for exciting a wide range of materials. This wavelength is chosen because the solar spectrum AM1.5G has a peak intensity at around 530nm, so using the 532nm laser for PL provides insights into the performance of perovskite solar cells under real-world operating conditions. The laser module is based on the Master Oscillator Fiber Amplifier concept with frequency conversion [182]. To ensure a uniform laser beam profile suitable for imaging applications, an optical fiber from the laser source was connected to a custom-built dynamic homogenizer (Bayerisches Laserzentrum GmbH). This homogenizer combines the principles of microlens arrays with a rotating disc. The microlens array splits the incoming laser beam into multiple smaller beamlets, which overlap to average out intensity variations. Figure 3.3 illustrates the optical ray diagram of the homogenizer working principle with the output laser beam. The rotating disc, with a diffusive surface, dynamically alters the phase

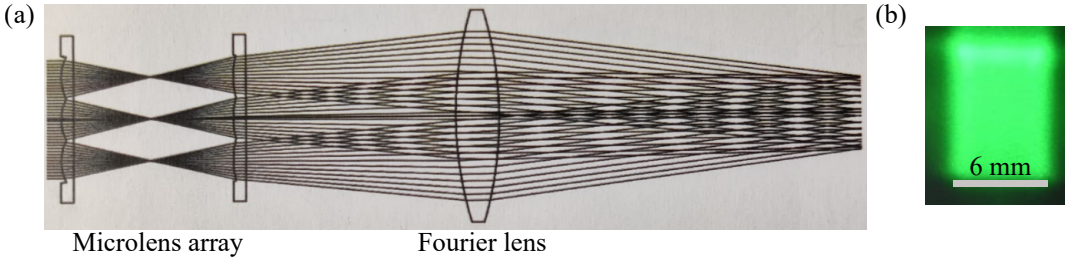

Figure 3.3: (a) Working principle of homogenizer consisting of the microlens array and a Fourier lens [183]. (b) the output laser beam from the homogenizer with a beam size of 6mm x 7mm.

and intensity distribution of the emerging beamlets, further aiding in the beam's homogenization. Indeed, using the rotating diffuser is a very efficient way of reducing the speckle of the laser but it does reduce the transmitted intensity to one third. The laser power without the homogenizer would be $14\,\mathrm{mW/cm^2}$ and with homogenizer would be $4.8\,\mathrm{mW/cm^2}$. The resulting beam, after passing through this system, is highly uniform, making it ideal for imaging applications that require uniform and consistency in illumination.

3.1.3 Spectrometer

The KURIOS-XE2 Liquid Crystal Tunable Bandpass Filter, manufactured by Thorlabs, is an indispensable component of our research arsenal when it comes to examining the properties of materials used in solar cells. This filter is specifically designed for multispectral or

hyperspectral imaging, making it an ideal choice for analyzing solar cell absorbers. It offers a tunable center wavelength (CWL) that can be adjusted within the range of 650 - 1100 nm. Additionally, the filter head is equipped with temperature control to ensure stability during experiments. The Full Width at Half Maximum (FWHM) of the CWL bandwidth is approximately 17 nm, and the maximum time required for switching from lowest to highest wavelength is less than < 250 ms. The filter's liquid crystal cells enable rapid tuning

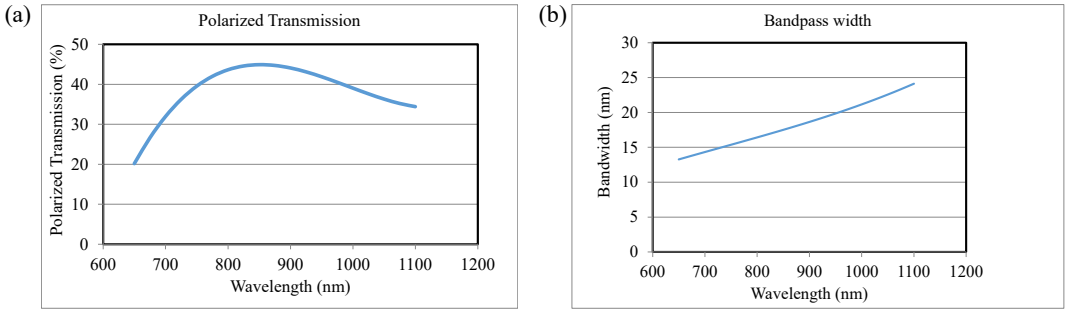

Figure 3.4: (a) Polarized transmission at the operation wavelength (650-1100 nm) of the spectrometer. (b) Bandwidth response of the spectrometer concerning center wavelength. The data for these plots is taken from Thorlabs [184]

and maximum transmission for linearly polarized input beams. The liquid crystal optics in Kurios filters are not sensitive to the direction of propagation, allowing the filter to be used in either direction. The included controller supports manual CWL control, programmable sequences, and synchronization with other devices. The CCD camera and the spectrometer communicate with each other by a trigger signal. The user first has to set the range of wavelength to be scanned, for example, 650 to 900nm at a step size of 5 nm. As the camera starts acquiring images, after each acquisition a trigger signal is sent to the spectrometer informing it to switch the wavelength to the next step. By this, we get images at every wavelength which can be then processed to get an average PL spectrum or spatially and spectrally resolved maps. This filter is indispensable for our hyperspectral PL studies of perovskite materials.

3.1.4 Other essential components

The imaging system is equipped with a micrometer precision x-y stage. The x-y stage, where the sample is placed, allows for precise adjustments in both the horizontal and vertical directions, allowing for specific regions of the sample to be targeted accurately or for a comprehensive scan to be conducted systematically. The z stage, which holds the camera, is responsible for controlling the vertical positioning of the camera, which is essential for

adjusting focus and capturing images at different depths, especially in materials with layered structures such as perovskite solar cells. The combination of these two stages provides three-dimensional control, ensuring that every aspect of the sample is thoroughly examined. For

Figure 3.5: Black pl box with rubber ring sealing and glass top

all the measurements performed in this thesis, the sample was placed in a box with a rubber ring sealing and a glass top. This action of sample placement and closing the box was carried out inside a glove box making sure that the sample was not exposed to the air and was always in N_2 environment. Due to the well-known sensitivity of perovskite absorber material to air and moisture, this is a step to get more reproducible quantitative data. Figure 3.5 shows the PL box used to place the sample in for all PL measurements unless mentioned.

3.2 Calibration of Imaging system

Calibration is essential for obtaining quantitative results from any system or instrument. It ensures that measurements are in line with established standards, guaranteeing accuracy, and consistency. Without proper calibration, even the most advanced equipment can produce inaccurate results, potentially compromising the integrity of research or applications. The main objective of the research project was to calibrate the hyperspectral PL imaging setup to obtain absolute photon numbers that represent the emission from the excited material as well as spectrally distinguish the emitted photons. The system's output is an image where each pixel corresponds to a specific number of counts measured by the camera's detector. Calibration is necessary for several reasons:

1. As a hyperspectral imaging system captures a wide spectrum of light at each pixel, spectral calibration will make sure that the spectral response is accurately mapped

to the correct wavelength, without this the wavelength recorded by the sensor will be misidentified. Also, different optical elements have varying responses to the same wavelength and calibration adjusts these discrepancies.

2. The camera counts are not absolute quantities, making them unsuitable for intensity-calibrated measurements. A more useful metric would be the number of detected photons emitted from the sample and this leads to a need for intensity calibration based on photon count rather than camera counts.

3. The laser's output power must be converted into the number of incident photons to determine the injection used during the measurement and to calculate a very important metric of a PV absorber which is PL Quantum Yield (Q_e^{lum}). This necessitates the need to measure power at each mode and convert it into several photons.

3.2.1 Spectral calibration

I begin with the spectral calibration method. This process ensures that the wavelengths measured by the sensor are indeed the correct representation of the photon wavelength emitted from the sample. This allows correct determination of material properties such as band gap energy and defect states. Furthermore, it ensures that data from different samples is comparable, and can be analyzed quantitatively. The emission spectrum that we measure from our sample does not precisely match the expected form of the true luminescence spectrum. The spectral response of our photo-detector is not consistent across all wavelengths, and the optical components such as the dispersing element, mirrors, and lenses have their wavelength-specific reflections and transmissions, which is the cause of this discrepancy and shifts the energy from its expected value. Thus, we perform a spectral calibration method. If we represent the light intensity as a function of wavelength $I(\lambda)$, the measured spectrum $I(\lambda)$ by the system will be equal to;

$$i(\lambda) = Q(\lambda)I(\lambda) \tag{3.1}$$

The spectral response of the entire detection system, denoted as $Q(\lambda)$, encompasses both the transmittance of the spectral device and the sensitivity of the detector. It is necessary to determine $Q(\lambda)$ experimentally for a specific system configuration. The process of spectral calibration is similar to measuring the PL of a sample, except that in this case, the light emitted from an Ulbricht sphere is measured instead of using a sample. The schematic of the setup used for spectral calibration can be seen in Figure 3.6 Instead of the sample, the light emitted by an integrating sphere is measured. This sphere is connected to a stabilized

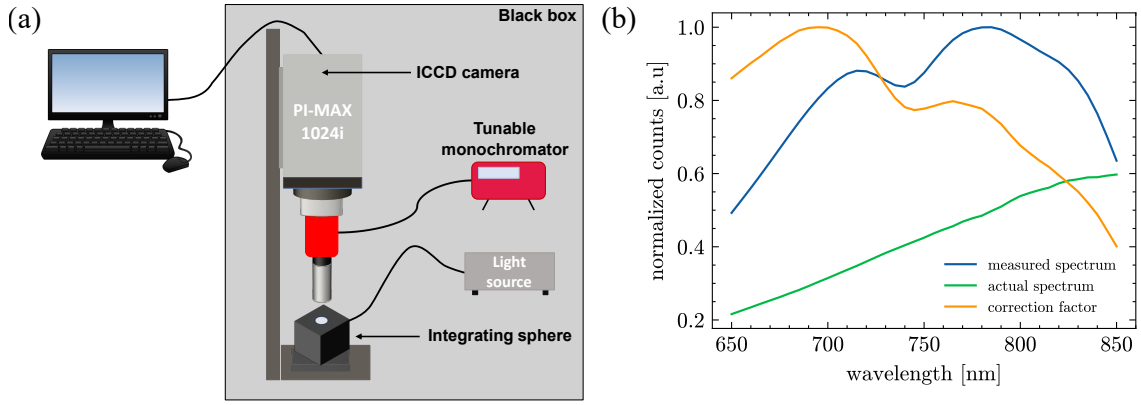

Figure 3.6: (a) PL setup schematic used for spectral calibrating the system. (b) plot of measured spectra (blue), actual spectra (green) which is provided by the manufacturer, and correction factor (orange) calculated from the equation 3.2. **Note:** As the ratio of the measured spectrum and actual spectrum give values above 1 for some range, the calculated correction factor has been normalized to represent all three plots in the same graph. The shape of the correction factor is not changed but only normalized.

light source, which remains stable over time and has a well-known calibrated spectrum. For our experiments, both components were sourced from Thorlabs: a 2-inch integrating sphere (IS200) and a stabilized tungsten IR light source (SLS202L/M) connected by a fiber patch cable. The camera's z-position was adjusted to focus on the sphere's aperture, and the white light spectrum was measured over a wavelength range of 900-650 nm with a step size of 5nm, with the light both ON for experimental data and OFF for background data. To generate a spectrum counts from background images were subtracted from measured counts from light sources (for each wavelength) and plotted against wavelength. This gave a background-corrected count plotted against wavelength, resulting in an experimentally measured spectrum $i(\lambda)$. Thorlabs provided the expected light source spectrum $I(\lambda)$. With both the experimentally observed and real spectra, the spectral correction factor $Q(\lambda)$ can be defined as the ratio of the experimentally measured spectrum to the actual light spectrum of the calibrated source, expressed in the equation;

$$Q(\lambda) = \frac{\text{measured spectrum}}{\text{actual spectrum}} = \frac{i(\lambda)}{I(\lambda)} \tag{3.2}$$

Figure 3.6b shows the spectral calibration factor that was obtained. Thus, to obtain the spectrally corrected curve, one must divide the measured spectrum of the sample by the calibration factor $Q(\lambda)$. In the discussed case, the correction factor can only be applied to the spectrum generated by averaging the images. To correct images at the pixel level, one must calculate pixel-by-pixel calibration factor $Q(\lambda)$ maps. This will enable the generation

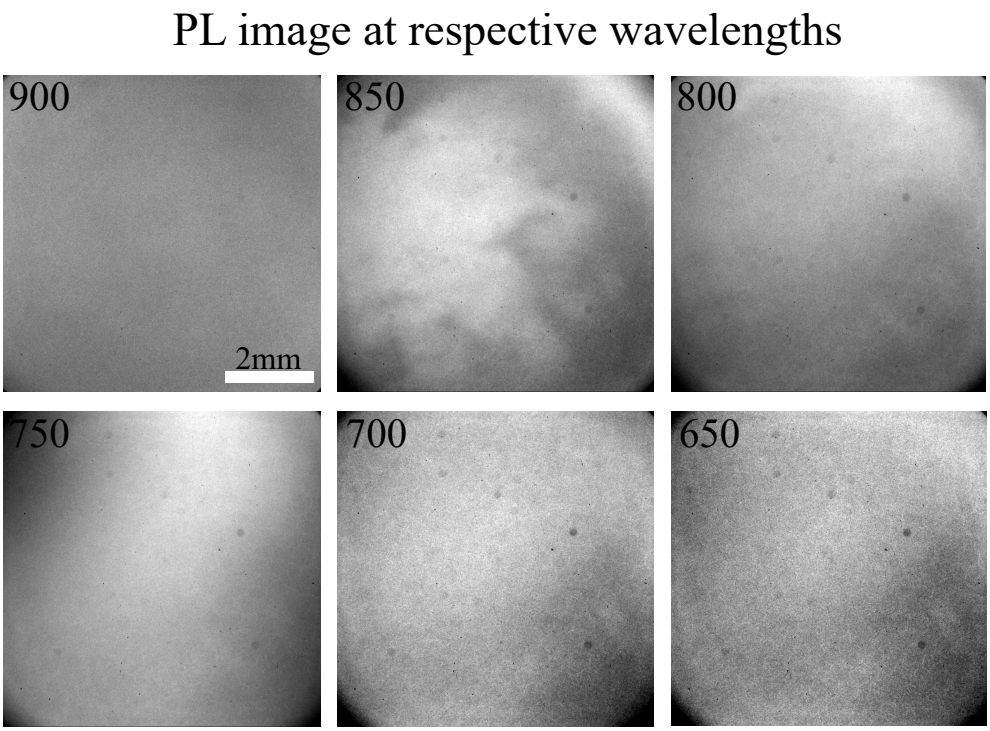

Figure 3.7: PL images were captured using a white light source that was connected to an integrating sphere. These images were obtained at various wavelengths (nm) and revealed variations in intensity across space. This observation suggests that there is a requirement for spatially resolved spectral correction.

of spatially resolved spectrally corrected PL peak position maps or simple PL peak position maps. Our system is an imaging system which means that the correction factor should be applied spatially. Figure 3.7 shows PL images taken at a few wavelengths that show intensity variation. The experimental setup remains the same, but the calculation of the calibration factor $Q(\lambda)$ maps is modified. Instead of taking the average of each image, we take the background subtracted pixel value detected by the sensor and divide it by the data provided by Thorlabs at its corresponding wavelength according to equation 3.2, and store the resulting images in an array that will serve as the correction factor for mapping. This completes the spectral calibration of the apparatus, allowing for intensity calibration next.

3.2.2 Intensity calibration

To carry out the intensity calibration, two distinct measurements are necessary. Firstly, the total number of counts detected by the camera sensor must be determined. Secondly, the total photon emission from the source must be measured. To do this, a 786 nm laser is used as the light source connected to the integrating sphere with an iris diaphragm at the top. A PL spectrum measurement is carried out and a plot of counts/sec as a function of

wavelength is recorded. The second measurement involves determining the power density at the position of the iris diaphragm, which is measured using a Thorlabs PM100D power meter and a Thorlabs S130C Si photodiode. The schematic of the measurement can be seen in Figure 3.8. For the first set of measurements, the spectra of the laser diode are measured as

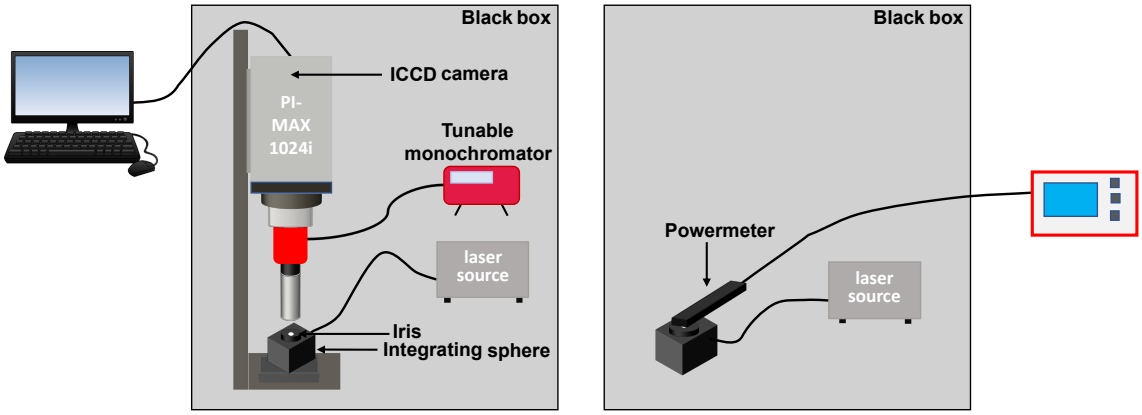

Figure 3.8: PL setup schematic used for intensity calibration. The integrating sphere that was used for spectral calibration was used here with a laser diode connected to it. On the right is the schematic of power measurement emitted by the laser diode from the integrated sphere opening

a function of wavelength. As discussed in the previous section, we would need to first apply a spectral correction factor to correct this spectrum. Then to convert the corrected intensity as a function of energy, we cannot simply change the x-axis wavelength into energy. Due to the inverse relationship between wavelength and energy, the intensity at the intervals dλ in the wavelength spectrum has to be multiplied by $\frac{\Delta\lambda}{\Delta E} = \frac{\lambda^2}{hc}$, which is known as Jacobian transformation [185]. This transformation scales the y-axis intensity accordingly such that the integrated PL spectra value remains the same after conversion from wavelength to energy. After multiplying the Jacobian transformation factor, the resultant PL spectra of the laser diode are represented in Figure 3.9. To get the total number of counts (N_{counts}) detected by the Camera sensor, a Gaussian function was used to fit the curve and integrated over the full range. Subsequently, without disturbing the setup, a power meter is placed right above the integrating sphere that measures the power emitted by the 786 nm laser. This measured power by the power meter is equivalent to the number of detected counts by the camera. The power is then divided by the area of the power meter detector to convert it into mW cm^{-2}. To convert the power density into the number of photons, I use the equation;

$$N_{photons} = \frac{\rho \times \lambda}{h \times c} \tag{3.3}$$

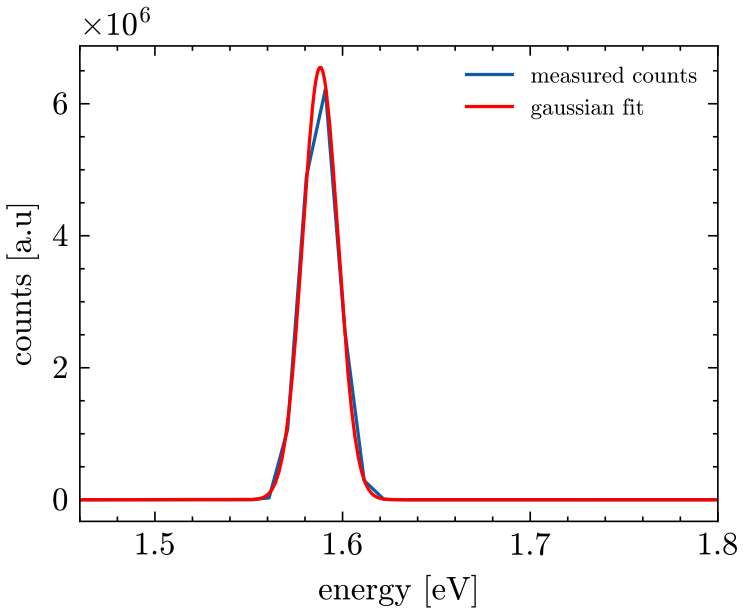

Figure 3.9: Intensity calibration measurement using the Ulbricht sphere and laser diode source. The laser diode has a wavelength of 786 nm. The red curve represents the Gaussian fit to the measured PL spectrum

where $N_{photons}$ is the number of photons/cm^2/sec ρ is the measured power density, λ is the wavelength of the laser diode used as the source, h is the Plank's constant and c is the speed of light in vacuum. Now that we have the total number of counts (N_{counts}) detected by the camera sensor and the total number of photons ($N_{photons}$) emitted from the integrated sphere, we can equate them and the result is the number of photons containing in a count detected by the camera sensor, by taking the ratio

$$C_{photons} = \frac{N_{photons}}{N_{counts}} \tag{3.4}$$

The equation 3.4 yields a conversion factor of 2.14×10^8 photons/cm^2/count which is an essential factor for quantitatively analyzing the sample. Thus, the y-axis of the measured spectra can now be converted into number of photons/cm^2/sec providing the correct way to represent the PL spectra of the sample. The final PL spectrum is then the plot of PL flux in photons/cm^2/sec/eV vs energy in eV. Considering that the sample measured will be placed in a PL box with a glass top, we also need to take into account the transmission of light through the (Poly methyl methacrylate) PMMA glass used in our sample box. Ricardo Poeira [179] carried a PL measurement of the sample placed in the PL box and without the PL box and showed that the intensity or counts decreased by 12%, which is in agreement with the transmission spectrum of the PMMA [186]. Integrating the spectrum in Figure 3.9 gives the total number of photons emitted by the sample and detected by the sensor

provided there were no losses in between. Dividing the total number of photons with the number of impinging photons on the sample (which is known from power measurements of laser), provides the PL quantum yield Q_e^{lum} which is an important parameter to track non-radiative recombination as well as the maximum achievable open-circuit voltage for the absorber material called quasi-fermi level splitting μ_{qfls}.

3.3 Data analysis methodology

So far, I discussed the key components of the PL imaging system and the necessary calibration methods required to claim it a hyperspectral PL imaging setup which is calibrated to absolute-photon number. Next comes the part where the acquired images need to be analyzed. We will discuss the methodology and steps taken to pull physics out of the experimental data from the imaging system.

3.3.1 PL spectra and PLQY

As the system is now spectrally and absolute photon number calibrated, the PL steady-state measurement now would have the y-axis represented as photon flux (PL_{flux}) which provides a better quantitative comparison of different samples. Once a PL measurement is carried out, the output from the system is a simple average count vs wavelength plot and set of images taken at every wavelength. To calculate the PL_{flux} I would then apply the spectral correction factor ($Q(\lambda)$), count to photon conversion factor ($C_{photons}$), and the Jacobian transformation ($\frac{hc}{E^2}$) to convert the wavelength dependence to energy dependence.

$$PL_{flux}(E) = \frac{\text{counts}}{GW \times Q(\lambda)} \times C_{photons} \times \frac{hc}{E^2} \tag{3.5}$$

I divide the counts with the gate width (GW) used during the measurement to ensure that the quantity counts are in units of counts/sec. Equation 3.5 thus gives us the PL_{flux} which is then plotted against the energy seen in Figure 3.10. Integrating this spectrum will give us the total number of photons emitted by the absorber after recombining radiatively. This then leads to defining a very important optical parameter of the photovoltaic absorber which is PL Quantum Yield (PLQY) or denoted as Q_e^{lum}. The efficiency of light emission in, for example, perovskite materials can be evaluated through PLQY measurements. This can help us to comprehend the effect of defects or processing conditions on the luminescence properties and, in turn, the power generation of solar cell absorber material. Q_e^{lum} is defined as the ratio of the number of photons emitted by the absorber $N_{emitted}$ to the number of

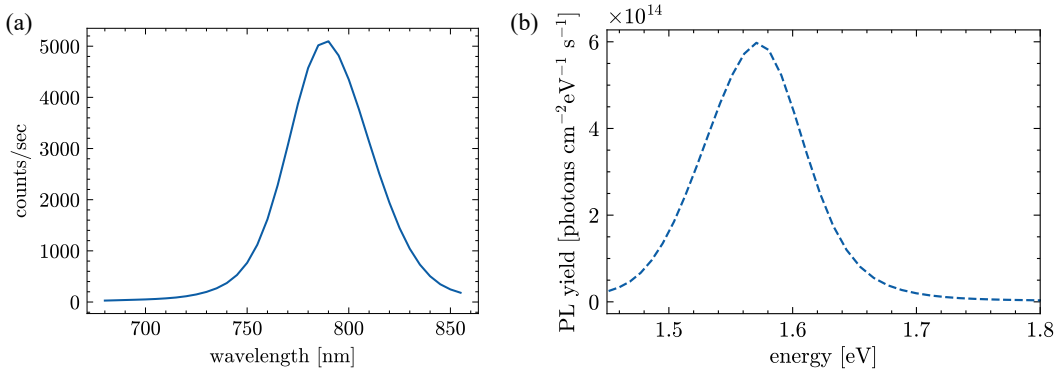

Figure 3.10: Plot (a) is the unprocessed PL spectrum that I get as an average output data file of camera software. It is simply a plot of counts/sec vs wavelength in nm. Plot (b) is the processed PL spectra with the y-axis representing PL_{yield} after the application of all calibration factors and transformations. the x-axis has changed from wavelength to energy thus the spectrum is inverted due to the inverse relation between wavelength and energy.

photons absorbed or injected on the absorber $N_{absorbed}$ as shown in the equation,

$$Q_e^{lum} = \frac{N_{emitted}}{N_{absorbed}} = \frac{\int PL_{yield}(E)dE}{N_{absorbed}} \tag{3.6}$$

Under open-circuit conditions, the external charge extraction is zero. The variable Q_e^{lum} denotes the proportion of radiative recombination compared to the total of radiative and non-radiative recombination. A high value of Q_e^{lum} suggests that a significant amount of the absorbed light by the perovskite absorber material has been transformed into luminescence.

3.3.2 Quasi-fermi level splitting extraction

Quasi-fermi level splitting (μ_{qfls}) is the splitting of the quasi-fermi level into electron and hole quasi-fermi levels under illumination. When the material is illuminated, the concentrations of electrons and holes in the semiconductor change, leading to shifts or splitting into their respective Fermi levels. The difference between these two Fermi levels is the μ_{qfls}. For just an absorber material on glass, the μ_{qfls} values are generally high provided their Q_e^{lum} is high. As more and more layers are added, interface losses reduce the μ_{qfls} value and the value then measured practically on the complete device is the V_{oc}. This the quantity μ_{qfls} represents the upper limit of the achievable V_{oc}. Generally high Quasi-fermi level splitting indicates that the charge carriers are separated efficiently and significant potential difference is created for hole and electron transport. μ_{qfls} and Q_e^{lum} are closely related as the latter defines the extent of non-radiative recombination reducing the μ_{qfls} value. Factors that will influence this relationship are defects in the material and composition variations. Experimentally once

the PL peak position and Q_e^{lum} is measured, one can analytically estimate the value of μ_{qfls} using equation [187],

$$\mu_{qfls} = E_g - kT \cdot ln(kT \cdot g \cdot \frac{E_g^2}{\phi_{abs}}) + kT \cdot ln(Q_e^{lum}) \tag{3.7}$$

where E_g is the PL peak position or estimated band gap of the absorber in eV, g is a constant, kT is the thermal energy, ϕ_{abs} are the number of photons injected or absorbed and Q_e^{lum} is the PLQY. This allows us to estimate the value of μ_{qfls}. The derivation of equation 3.7 will be shown in Appendix A.1. From the PL spectrum, as the quantitative data we extract is the average of the large length scale region, I can use equation 3.7 to construct the map of μ_{qfls} using the PL peak position and Q_e^{lum} extracted from every pixel. Such a map will provide us with valuable information about the spatial heterogeneity and variation in charge carrier separation.

3.3.3 PL Image processing and analysis

The imaging setup we discussed generates output in the form of a data cube A.2, which consists of images representing the PL intensity map of a sample at different wavelengths. This allows us to analyze any desired region of the sample at any wavelength. Instead of averaging each image at its corresponding wavelength, as we did in the previous section to obtain average spectra, we now use counts per second at each pixel of an image. This enables us to plot the PL spectrum for each pixel. Before plotting the PL spectrum for each pixel, all the images undergo the corrections and transformations discussed in the previous section. To handle the large amount of data and the image processing calculations involved, I have developed a Python script that takes the raw data as input, performs corrections, and outputs spatial maps of PL photon flux, PL peak position, Q_e^{lum}, μ_{qfls}, and decay time from transient PL imaging measurements. For each pixel, the PL spectrum is extracted from the hyperspectral data cube, and the total number of emitted photons is calculated by integrating each PL spectrum. This number is then divided by the number of absorbed photons to generate a spatially resolved map of Q_e^{lum}. Since our laser has a broad beam and is homogenized, the injection at each region of the illuminated sample is uniform. The laterally resolved Q_e^{lum} map provides information about the variation in the luminescence efficiency of the sample, as well as the detection of defects or impurities. It also serves as a measure of the efficiency of the absorber in converting absorbed light into emitted light. In addition to Q_e^{lum}, we can also create a spatially resolved map of the PL peak position, which closely estimates the band gap of the material. The energy difference between the valence and conduction bands, known as the band gap, is of great significance as it determines the optical

and electronic characteristics of the material. Spatially resolved PL peak measurements of semiconductor absorber materials are important for understanding material heterogeneity, as they can reveal variations in composition or different phases across the film. This detailed insight can be used to optimize fabrication processes and identify regions with high defect density or poor crystallization. Such in-depth characterization can contribute to improving material selection, device design, as well as device performance and stability. Taking it a step further, we can also construct a map of μ_{qfls}, displaying the variation in charge carrier separation efficiency across the large sample region. An increased μ_{qfls} indicates reduced non-radiative recombination, implying better material quality and fewer defect states.

3.3.4 Time-resolved PL and Imaging analysis

The iCCD camera that we discussed has a very high shutter speed and internal timer that enables it to measure time-resolved PL. During the TRPL measurement, the spectrometer is removed to have a better signal. When a laser pulse is sent to the sample, it excites the charge carriers in the absorbers, which then recombine and emit photons. The emitted photons are then captured by the camera sensor and stored in the form of a histogram as a function of time. The working principle of the TRPL measurement using an iCCD camera is shown below. When the software initiates the recording process, a signal is sent

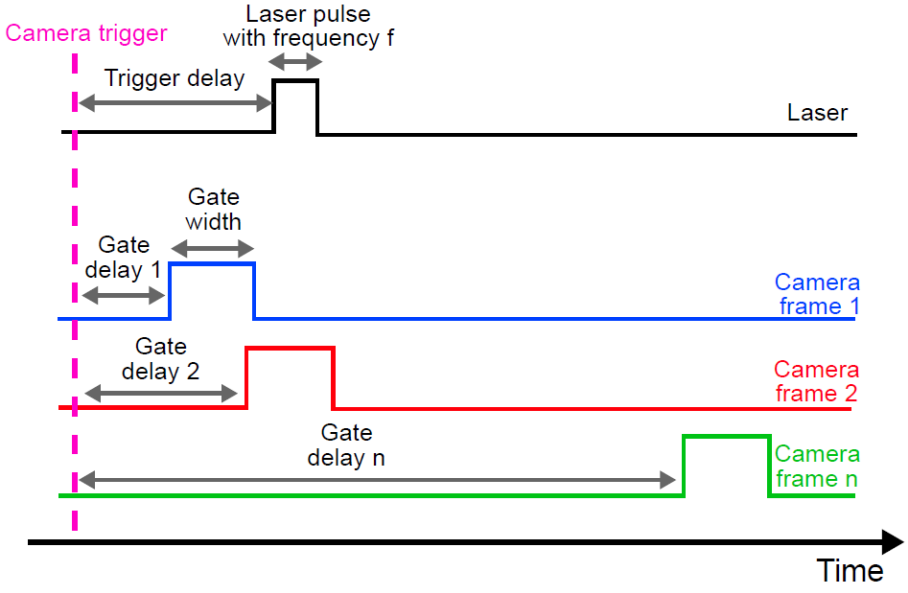

Figure 3.11: Synchronization of times for time-resolved PL measurement using imaging system

to both the camera and laser. Following a delay known as the trigger delay, a laser pulse is emitted. This laser pulse also triggers the camera to start capturing PL after a specific gate

delay and for a certain duration referred to as the gate width. The gate width determines the intensity of the signal, with a longer gate width resulting in higher intensity but lower resolution of the TRPL transient. By increasing the gate delay, the acquisition of the PL during relaxation can be shifted from before the laser pulse to after the excitation and before the next laser pulse. This process can be repeated multiple times for different gate delays and then averaged to improve statistical accuracy and resolution. The collected data is subsequently processed externally by plotting the measured intensity against time and fitting it with exponential functions. If a single exponential decay is observed, it suggests the presence of one predominant recombination mechanism. On the other hand, multiple exponential decays indicate the existence of multiple processes or a range of lifetimes. In this thesis, a novel method called differential lifetime is employed for calculating the lifetime. The conventional approach involves fitting the TRPL transient with an exponential function to extract the lifetime τ, but this method is only reliable for simple systems such as an absorber layer on glass with a low injection level. As the complexity of the material increases by adding more layers, fitting the data with multi-exponential functions does not provide meaningful information about the lifetime or identification of recombination mechanisms [102, 188, 126]. Therefore, the calculated differential lifetime, defined as the inverse negative slope of the logarithmically plotted PL intensity in equation 1.35, is used instead. This approach retains all the information about how the decay changes over time. With the time-resolved imaging capability of our system, it is possible to obtain images at any desired delay time of the transient decay. Different regions of the sample may emit light at different wavelengths and exhibit different rates of decay. Our time-resolved capability using an iCCD acquisition generates a data cube consisting of N images for N moments in time before and after the laser pulse strikes the sample. As mentioned earlier, the spectrometer needs to be removed to improve the signal quality, resulting in the emitted light from the sample is not spectrally resolved. To process the time-resolved data, a separate Python script is developed which takes the time-resolved transient PL raw data as an input, performs background subtraction, and fits the transient by a defined decay function. However, single-pixel transients often suffer from poor signal-to-noise ratio. To address this issue, a software binning method is implemented, which groups 4×4 pixels and averages their values to reduce noise. Once this is done, the transient from the grouped pixel is fitted with an appropriate decay function to extract τ, thereby generating a decay time map. Time-resolved PL imaging has significant potential as a characterization tool for both research and industrial purposes. It provides direct insight into the spatial variation of lifetime across the sample, aiding in

the identification of local losses. Not only decay time, but it can also reveal variation in the charge transport properties [181] in the presence of transport layers as well as map the charge diffusion process [127].

3.4 Conclusions

In this chapter, we have extensively discussed the development and application of a custom-made hyperspectral PL imaging system for advanced solar cell research. The main focus was on the system's design, key components, and rigorous calibration methods that enable precise measurements of absolute photon numbers. The CCD camera, which has a wide spectral range and fast shutter speed, serves as the core of the system, capturing detailed luminescent data that is crucial for understanding the optoelectronic properties of photovoltaic materials. Through a combination of spectral and intensity calibration techniques, the system has been finely tuned to provide accurate insights into the PL characteristics of various solar cell materials, including perovskites. This calibration not only corrects for spectral response but also quantifies photon emission, which is essential for precise measurements of PL quantum yield (PLQY). The outlined data analysis methodology offers a comprehensive approach to extracting meaningful insights from the acquired images. By analyzing the PL spectra and generating spatially resolved maps of PLQY (Q_e^{lum}) and quasi-Fermi level splitting (μ_{qfls}), we can observe variations in material efficiency and quality. This spatial resolution is crucial for identifying defects or inconsistencies in the solar cell materials, which play a vital role in improving solar cell performance. Furthermore, the incorporation of time-resolved PL imaging adds another dimension to our analysis, allowing us to investigate the dynamics of charge carriers within these materials. In conclusion, the hyperspectral PL imaging system that we have designed and calibrated is a powerful tool for solar cell research. It offers a multifaceted approach to characterize and comprehend the intricate details of photovoltaic materials, which is indispensable for the advancement of solar cell technology. The system's ability to provide detailed and spatially resolved data makes it an invaluable asset in the ongoing pursuit of developing more efficient and reliable solar cells.

Chapter 4

Heterogeneity in mixed halide perovskite and its charge carrier dynamics

In the previous chapter, I presented a comprehensive introduction to the hyperspectral PL imaging setup, highlighting its capabilities and potential applications in the field of material science. This chapter delves deeper into the implementation of this technique, aiming to understand the perovskite stack, their recombination mechanisms, charge carrier decay times, and charge dynamics at both the top interface as well as back interface.

Sample used in this chapter: $(FAPbI_3)_{0.97}(MAPbBr_3)_{0.03}$ spin-coated on TiO_2 ETL. It will be referred to as FAPIBr.

The goal here in line with the theme of the thesis is to use a PL imaging setup to study the inhomogeneities in FAPIBr perovskite. First I will begin by answering a question: Can I use a pulsed laser to acquire steady-state PL data? How is it comparable with the continuous laser source? This question is important to me as the laser source employed in our PL imaging setup is a pulsed source and generally for steady-state PL measurement, a continuous laser source is used. Then I begin with an in-depth analysis of heterogeneity from the steady-state PL imaging results obtained from FAPIBr absorbers. This section will thoroughly examine the spectrally resolved PL maps, providing a visual representation of the spatial variation in the PL across the sample. Critical to our understanding is the analysis of the Quasi-fermi level splitting (μ_{qfls}), which offers insight into the energy levels within the absorber material. Additionally, the PL quantum yield (Q_e^{lum}) maps will be discussed, offering a quantitative measure of the efficiency of PL processes for the sample. Moving forward, the chapter will then transition to a discussion centered around temporal studies.

This section is pivotal in understanding the dynamic behavior of charge carriers, particularly in the presence of the electron extraction layer. Through these studies, I aim to unravel the processes governing the movement and recombination of charge carriers, which are critical for optimizing device efficiency. I utilize the hyperspectral PL imaging setup to develop laterally resolved decay time maps. These maps are instrumental in identifying local regions within the sample where charge extraction is efficient as well as the location of the non-radiative recombination center. By analyzing these regions, I can infer valuable information about the effectiveness of the charge extraction layer, leading to potential improvements in the design and fabrication of perovskite-based devices.

4.1 Optical heterogeneity study of FAPIBr perovskite

4.1.1 CW vs pulsed laser illumination

The hyperspectral PL imaging setup is equipped with a pulsed laser source. Before discussing the results from the imaging results, we should first be familiar with the type of source used for illumination. In the community, the choice of the laser source to perform steady-state and time-resolved PL has been a topic of considerable interest [189]. It is common that for time-resolved measurement, one should use the pulsed laser as the aim is to study the decay of the generated charge carriers after excitation by a laser pulse. However, Is it possible that the pulsed laser used at a high repetition frequency rate outputs the same result as the Continuous wave (CW) illumination? Traditionally for steady-state PL, CW light or laser is used. With a steady light source, excess carriers are continuously generated and the concentration is stable over time. As the generation rate is equal to the recombination rate in the steady state, the excess carrier concentration strongly depends on the minority carrier lifetime τ [19]. As in my case, I have a pulsed laser, I will show that pulsed laser when used at high repetition frequency is very similar to the CW illumination. A pulsed light source generates a train of short pulses at a certain repetition frequency f_{rep}. In this case, every pulse generates the excess carrier in the sample which then recombines when the light is off or before the next pulse arrives. It is a good practice to always represent photon flux incident per pulse which then translates to the amount of charge carriers generated per pulse. For Figure 4.1, I used a mixed halide perovskite to see how different sources affect the optical properties. For CW measurement, a 637 nm red laser was used as an illumination source with an absolute-photon calibrated PL setup. PL spectra, with laser flux equivalent to 0.5 sun and 1 sun, were acquired and integrated to get the PL Yield. Following this, an

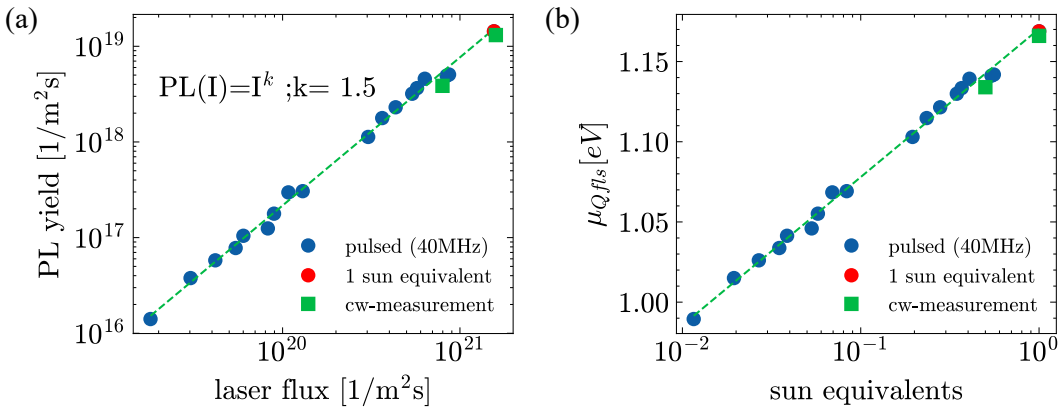

Figure 4.1: (a) Integrated PL yield as a function of incident photon flux using a pulsed laser (solid blue circles) at 40 MHz repetitive frequency of 532 nm wavelength with pulse width of < 1 ns. The solid red circle represents the value calculated from 1 sun equivalent photon injection and solid green squares are the measurements using cw laser carried out with 637 nm wavelength. (b) Quasi-fermi level splitting μ_{qfls} as a function of sun equivalent photon density from pulsed and CW laser.

independent absolute-photon calibrated PL setup with a pulsed laser source of wavelength 532 nm was used to measure the PL spectra at different laser fluxes, and PL yield was extracted similar to the previous case. From the plot figure 4.1a, I can see that the PL yield is linear on log-log scale with the laser flux with the optical diode factor $k = 1.5$ and the measurement conducted at 0.5 sun and 1sun equivalent from both the CW and pulsed laser align very nicely. The integrated PL yield values then were converted into Q_e^{lum} using equation 3.6. The measured Q_e^{lum} was then used to estimate the quasi-fermi level by the equation;

$$\mu_{qfls} = \mu_{qfls}^{rad} + kT \cdot ln(Q_e^{lum}) \tag{4.1}$$

with μ_{qfls}^{rad} being the radiative limit of the fermi level splitting at a given photon flux. The results here conclude that the pulsed laser source, if used at a significantly high repetition frequency, will yield results very close to the CW laser source measurements and can be considered quasi-static. This makes sense as the carrier lifetime in perovskites (which will be discussed in upcoming sections) is much longer as compared to the time between two pulses (25 ns for 40 MHz). Thus, I will continue using the pulsed laser for our steady-state PL imaging measurements.

4.1.2 Quasi steady state PL of FAPIBr perovskite

Heterogeneity in halide perovskite materials can be observed at various length scales. At the smallest scale (< 100 nm), grains contain sub-grain features such as crystallites and twin domains, which may be impacted by local strain fields. These features can influence electron and ion diffusion pathways [190, 191, 192]. At intermediate scales (from >100 nm to <10 μm), the 3D distribution of grain interfaces can affect non-radiative recombination events, ion migration, and the infiltration of elements like oxygen and moisture [193, 194]. Long-range disorder, which can be tens of micrometers or larger, is often caused by nano-scale and meso-scale heterogeneities, but can also be due to not optimized fabrication processes [195], sub-optimal interfaces [196], or inadequate heat-transfer management, leading to strain or wrinkling. These issues are also seen in vertical grain morphology and can negatively affect device performance, resulting in electrical hysteresis. Our focus will be to study the heterogeneity at a larger length scale (≥500 μm). I use the ability of our hyperspectral PL setup to understand the impact of inhomogeneity on the optoelectronic behavior of the mixed halide perovskite. Almost all of the PL measurements are performed with the sample kept under N_2 in a black box with a glass top and rubber sealing shown in figure 3.5. This ensures that the perovskite is not exposed to the ambient environment during PL measurement. The PL intensity map of FAPIBr measured using a 532nm laser is displayed in Figure 4.2.

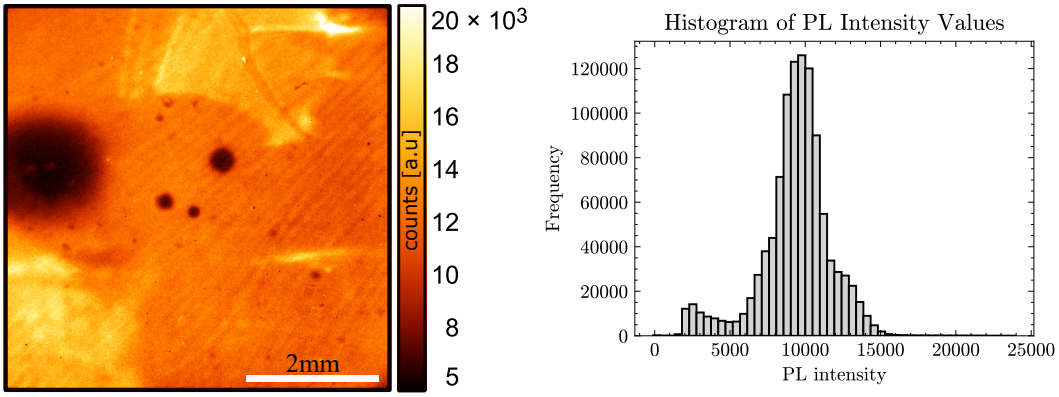

Figure 4.2: PL image of FAPIBr perovskite. The image size is $6 \times 6\,\mathrm{mm}^2$. On the right is the distribution of the luminescence intensity of perovskite.

The perovskite layer is spin-coated on mesoporous-TiO_2 serving as an electron extraction layer. The heterogeneity (variation in emitted light intensity) across the perovskite film can be attributed to several factors, as evidenced by the three distinct peaks from the intensity distribution plotted as a histogram in Figure 4.2. The first peak in the range 0 to 5000 counts (intensity) represents the average intensity of the dark circular regions. Possible causes of

these regions include defects such as vacancies, interstitials, and/or impurities, which can lead to the degradation of the perovskite and act as non-radiative recombination centers, reducing the PL in localized areas. The core of these dark circles has very low intensity (almost zero) compared to the surrounding dark region, suggesting the presence of pinholes. The formation of pinholes can lead to localized alterations in material properties, such as changes in crystal structure, and increase recombination activity, contributing to increased non-radiative recombination. Pinhole edges provide additional surface area which increases the surface-to-volume ratio locally and enhances the surface recombination. Carriers (electrons and holes) generated in the perovskite film tend to diffuse before recombining. The presence of a pinhole can act as a sink for carriers, leading to their non-radiative recombination at the pinhole edges. This can result in a reduction of carriers available for radiative recombination in the surrounding region, leading to a darker area in the PL image. The histogram's primary peak at 10000 counts, which is attributed to a good quality film of uniform FAPIBr perovskite material. A close examination of the PL intensity map revealed a periodic striped pattern which will be discussed in chapter 5. The primary peak of the histogram has a right shoulder which is due to the bright patches seen in Figure4.2. The cause of these patches is still not fully understood, but they are indeed present in the perovskite bulk and are much brighter than the average intensity. Uneven solvent evaporation due to a temperature gradient during the annealing step may be the cause of such a region as this region is present on multiple samples that are spin-coated. This also points towards chemical inhomogeneity in the bulk of the perovskite. The PL peak position of FAPIBr was plotted by capturing

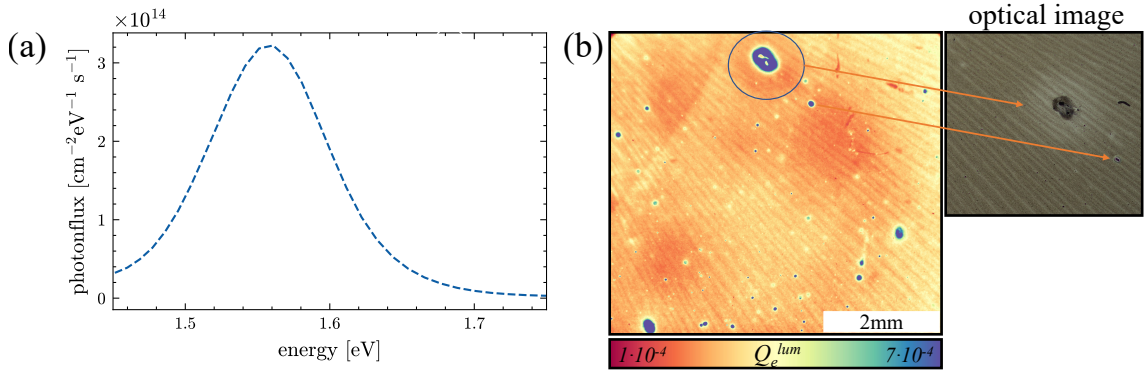

Figure 4.3: (a) PL spectrum of mixed halide perovskite indicating peak position at 1.56 eV. (b) Q_e^{lum} map of the perovskite sample showing regions of low luminescence as well as local heterogeneities. On the right is the optical image taken of the perovskite region showcasing the defect.

PL intensity images at different wavelengths from 900nm to 650nm in steps of 5nm. After

analyzing the hyperspectral cube, the average photon number for each image was extracted and plotted against the energy, as shown in Figure 4.3. The PL intensity peaked at 1.56 eV with a standard deviation of 44 meV after a Gaussian fit. The PL spectrum appears to be symmetrical around the peak energy and does not have any shoulders, suggesting that the structure and composition of the perovskite film are uniform with no evidence of phase segregation. However, it is important to note that the spectrum is an average of a large length scale region around 6.2 mm x 6.2 mm area of the film. By averaging such a large area, one assumes that the full sample indeed is homogeneous but it is not the case as we saw from the intensity image of Figure 4.2. This averaging process masks the local variations in the PL intensity as well as their peak position. To gain insight into these local variations, I implement pixel-by-pixel analysis to generate a Q_e^{lum} map as seen in Figure 4.3(b). The average Q_e^{lum} of $4.2 \cdot 10^{-4}$ is measured at 0.68 sun illumination. The large dark patches (orange color) indicate low Q_e^{lum} and hence increased non-radiative recombination activity. Local bright dots suggest the presence of crystal residues that is the consequence of incomplete perovskite formation during the annealing process, meaning that the precursor solution used to spin coat the perovskite did not completely crystallize to perovskite but rather leave few residues of the precursor on the surface after the annealing step. From the optical image of this perovskite, Figure4.3(b)outset, I see that the surface is covered with a lot of black dots some of which are large and develop a whitish region surrounding the feature. Comparing this with the Q_e^{lum} map, I see that this whitish region shows a slight reduction in Q_e^{lum}. I also compared the optical properties of the region by constructing a correlation map. A map of PL peak position and a map of Q_e^{lum} were used as input to perform pixel-by-pixel correlation. If there is a positive correlation, the value would be close to 1. If there is anti-correlation then the value would be close to -1. value of 0 means there is no linear correlation between two variables. Figure 4.4 shows the PL flux image of the unpassivated perovskite and the correlation map where the two input variables were the image dataset. Pearson correlation method was utilized to construct the map [197].

$$r = \frac{\sum_{i=1}^{n}(x_i - \overline{x})(y_i - \overline{y})}{\sqrt{\sum_{i=1}^{n}(x_i - \overline{x})^2}\sqrt{\sum_{i=1}^{n}(y_i - \overline{y})^2}} \tag{4.2}$$

The first variable was the map of the PL peak position whereas the second variable was the Q_e^{lum} map. Just looking at the PL flux map does not help in understanding the nature of the inhomogeneity, for this reason, I constructed a map of correlation. Such a map helps tremendously to visualize the relationship between the two variables as well as their spatial location on the surface. To understand these types of inhomogeneities on perovskite, I used 20x objective on the PL imaging system to have a closer look. Figure 4.5 features the PL

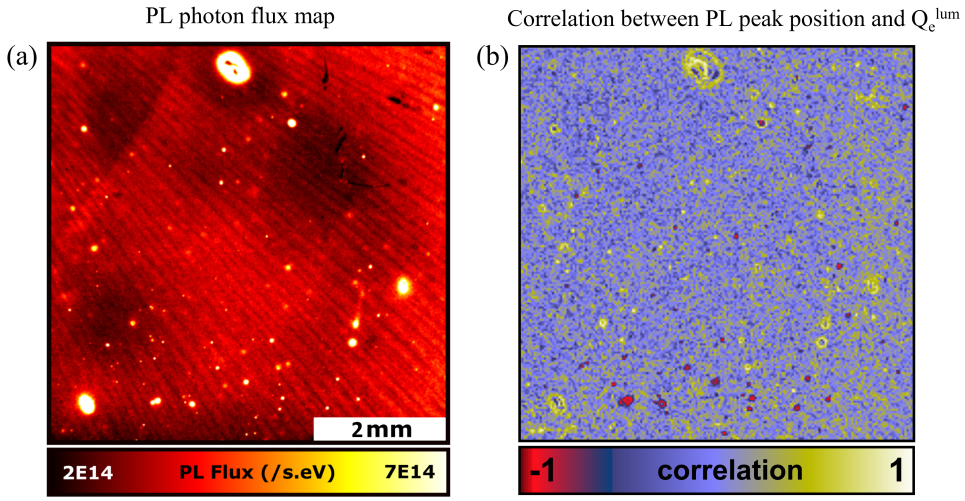

Figure 4.4: (a) Photon flux image of a large length scale area for unpassivated perovskite demonstrating several features. (b) pixel-by-pixel Pearson correlation map constructed between the PL peak position map of (a) and Q_e^{lum} map

imaging performed on one of the defective regions on the perovskite. I observe a possible pinhole that has first a bright ring surrounding it followed by a broad dark circular patch indicating low Q_e^{lum} from the average. Interestingly not all of the pinholes show the bright ring surrounding them. Some simply have the darker region surrounding them which is either poor quality of perovskite from the beginning itself or degraded perovskite since its growth. This already hints that the growth process still needs optimization to make sure of

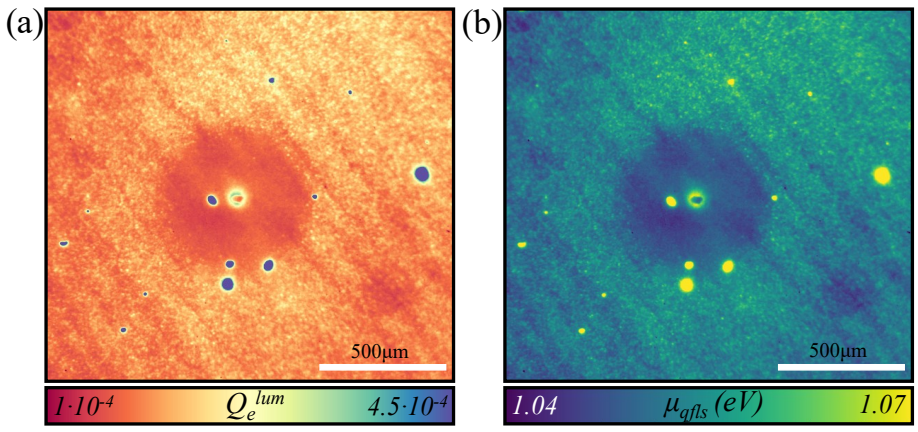

Figure 4.5: PL imaging measurement on the dark region. (a) Q_e^{lum} map featuring a possible pinhole surrounded by the bright ring and then by a dark circular patch. (b) μ_{qfls} map featuring the variation in the charge separation efficiency in the dark region.

the uniform coating of the absorber material together with uniform temperature annealing. With the average Q_e^{lum} and the PL peak position, I used equation 4.1 to estimate the value of

the Quasi-fermi level splitting, μ_{qfls}. μ_{QFL} represents the upper limit or maximum achievable V_{oc} of that absorber and here I calculate the value of 1.067 eV under 0.68 sun corresponding to 1.15×10^{17} photons/cm^2/s. In solar cells, a larger μ_{qfls} can result in a higher V_{oc}. The total non-radiative recombination losses can be determined by subtracting the μ_{qfls} from the Shockley Queisser limit V_{oc} (1.291 eV) calculated from PL peak position resulting in 224 meV loss. Another way of confirming this is to simply use the measured Q_e^{lum} and calculate the term $kT \cdot ln(Q_e^{lum})$ as this term in equation 4.1 represents the non-radiative recombination losses and turn out to be -201 meV where negative sign indicates loss or decrease from the radiative limit.

4.2 Surface chemical heterogeneity of FAPIBr perovskite via EDX and SIMS

4.2.1 EDX

The heterogeneity that I have observed so far is purely optical and at a relatively large length scale, i.e. milli-meter. To understand the chemical nature of the surface, I used SEM together with the EDX to get an idea of local chemical changes, if any, present on the surface that may explain the optical heterogeneities that I observed using PL. Figure 4.6 shows an

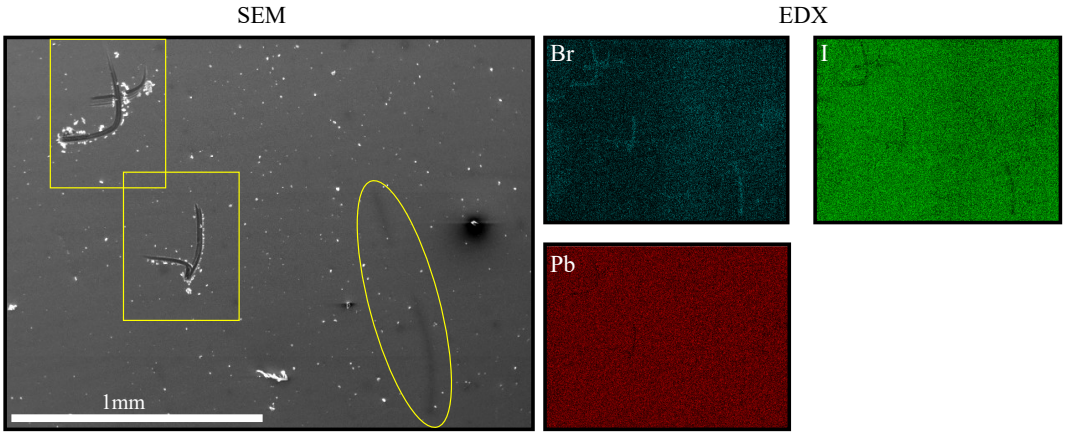

Figure 4.6: SEM surface map of FAPIBr perovskite at large length scale featuring inhomogeneities. Corresponding EDX chemical maps of Br, I, and Pb of the same region show the elemental distribution across the surface.

SEM image as well as EDX chemical distribution map of the FAPIBr perovskite surface. The region marked in yellow boxes are the scratches that must have been made while handling the perovskite stack. Proof of this is shown in the optical image of this sample in B.1. Looking at the chemical distribution, the scratch shows a high level of Br and a low level

(a)

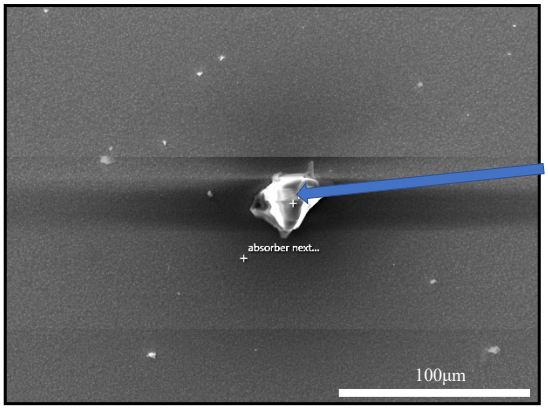

Feature	Atomic %
C	4.93
O	68.25
Si	26.01
Ti	0.00
Br	0.52
Sn	0.19
I	0.08
Pb	0.03
Total	100.00

(b)

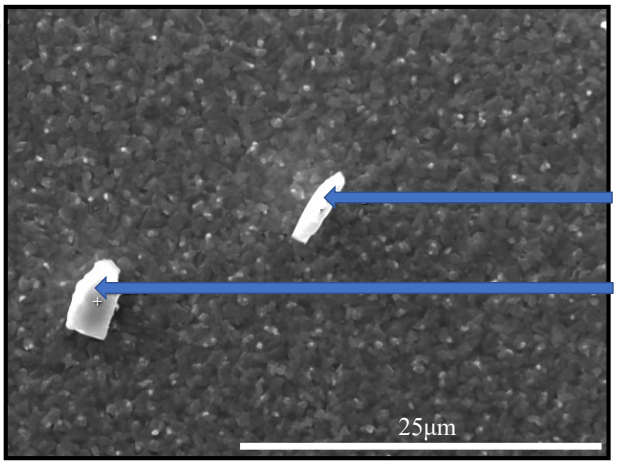

Bright feature 1	Atomic %
Ti	5.24
Br	5.90
Sn	9.43
I	55.49
Pb	23.95
Total	100.00

Bright feature 2	Atomic %
Ti	0.89
Br	3.19
Sn	0.40
I	66.31
Pb	29.21
Total	100.00

Figure 4.7: (a) SE image of a feature observed on the FAPIBr perovskite surface where point EDX spectrum measurement was conducted. The outset shows the atomic percentage distribution of elements at this spot. (b) SE image of two other bright features observed on FAPIBr perovskite surface and their atomic percentage distribution shown at the outset.

of I. This is possible if one assumes that the scratch exposed the underlying fresh layer that was rich in Br as compared to the surface. This is consistent as both the scratched areas show high Br. Another interesting feature is the one marked in yellow oval which is not the scratch but seems to exist from processing itself. This feature shows a different contrast in the optical image, however, the chemical distribution trend is the same; high Br and low I. The distribution of Pb seems to be quite uniform. Zooming onto the surface, I see a high density of bright dots in the SEM image for which I used point EDX spectra on these features to get the chemical percentage. With prior information of the expected chemical elements that should be present in the stack, EDX point spectra will help in determining the dominant species at these spots. From Figure 4.7(a), the feature shows a high percentage of oxygen and silicon which is coming from the glass substrate. One may argue that it could be from TiO_2 or FTO but there was no Ti or Sn detected. This means that the feature

has no perovskite and an exposed glass layer. The EDX spectra of this feature as well as a point next to it representing a pristine perovskite spot are shown in B.2. From Figure 4.7(b), both features show a high percentage of iodine and lead indicating that this may be lead iodide species. The feature on the left is thicker than the right based on the fact that the right feature shows signs of Ti and Sn which is possible if the electron beam penetrates the features and goes deeper into the perovskite towards TiO_2 and FTO layer. Both of these signals are significantly lower on the left feature.

4.2.2 HIM-SIMS

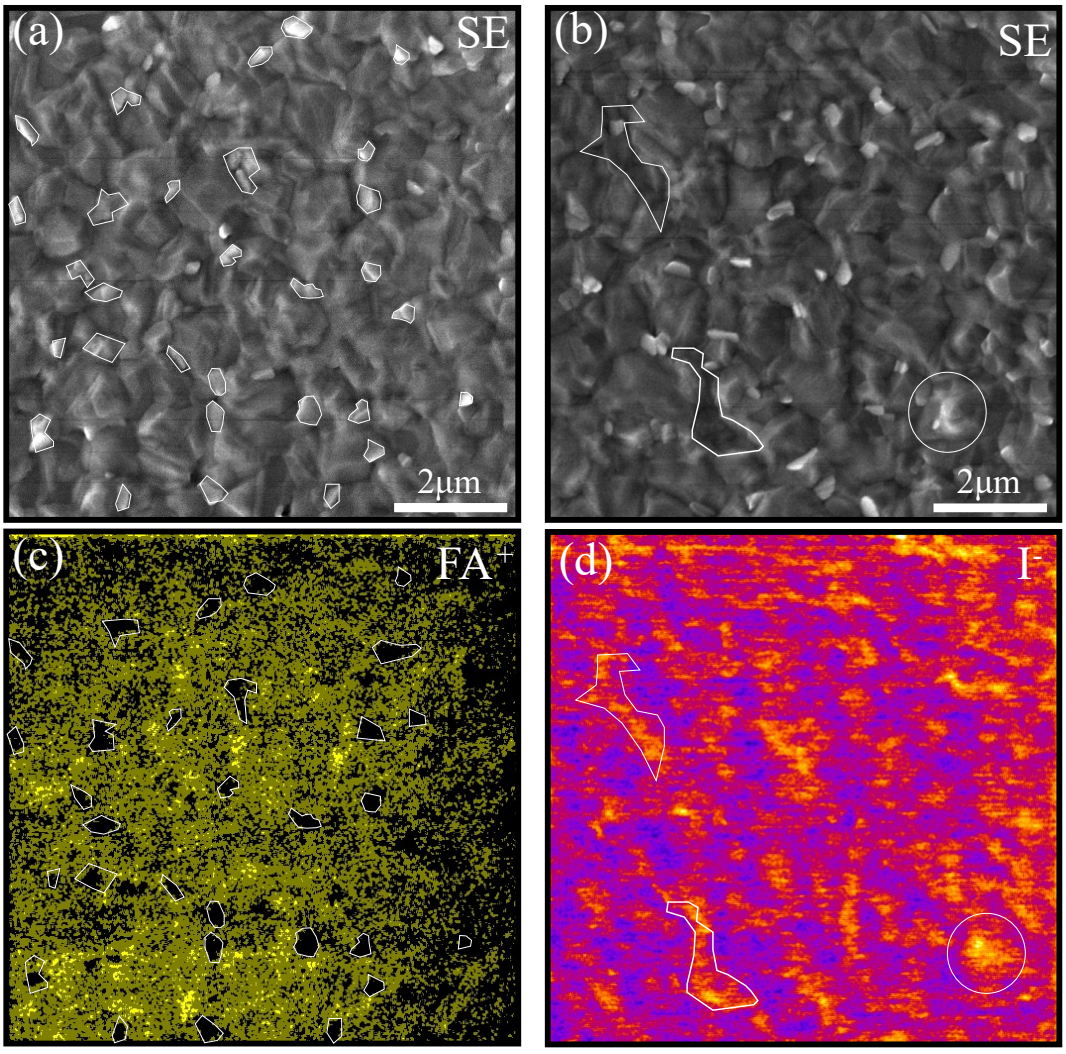

Figure 4.8: HIM-SIMS measurement on FAPIBr surface showing bright features distributed across the surface. (a,b) Secondary electron image of surface. (c) SIMS chemical distribution map of organic part FA and (d) I. Note: These measurements were done by a colleague but the sample is from the same group as was used for PL measurement.

The spot EDX spectra do help in getting an idea of what the chemical species is present

on the surface, but what would be more interesting and impact-full is the high-resolution SE image and chemical distribution which is achieved from a very powerful surface-sensitive technique called HIM-SIMS. Measurement from this technique revealed surface morphology and chemical heterogeneity on the perovskite surface. Here, as the penetration depth of the primary ion beam is up to $\approx$ *tens* of nm, I expected true surface chemical distribution as compared to the EDX where a high energy electron beam penetrates much deeper. Figure 4.8 illustrates a measurement where a helium ion beam was utilized to map the surface of the perovskite to generate a secondary electron image. The secondary electron image reveals small domains exhibiting bright contrast, which can be compared with the SIMS map of FA. Interestingly, these domains do not exhibit the presence of the organic group FA. In addition to FA, variations in the distribution of Iodine can also be observed. Taking into account the low amount of FA and Br, and the presence of Pb in these high contrast domains shown by Hieulle et al. [198], the interpretation of the presence of PbI_2 is considered. The contrast in the secondary electron image is related to the work function of the material [199, 200]. Therefore, the bright contrast observed must be a species with a high work function, and PbI_2 is known to have a high work function. As the perovskite was grown with an excess of PbI_2 to optimize the efficiency, there needs to be care taken regarding these domains of PbI_2 as they act as the degradation center. Hieulle et al. [198] showed that when exposed to light, these domains trigger the degradation reaction forming granular grains. In conclusion to the chemical heterogeneity, mixed-halide perovskite shows variation in the chemical species at a small length scale as well as a relatively larger length scale, and tackling this makes it a necessity for improvement.

4.3 Transient photoluminescence of FAPIBr perovskite

In steady state measurement that I discussed previously, the generation and recombination of charge carriers is continuous as long as the laser is incident on it. I want to study the dynamics of the charge carrier generated inside the mixed-halide perovskite in contact with the charge extraction layer. The best tool for this purpose is the time-resolved transient PL.

4.3.1 Transient photoluminescence measurement

A pulsed laser source was used for this purpose with incident energy per pulse of $2.0\,\mathrm{nJ/cm^2}$, corresponding to photon density per pulse of $5.1 \times 10^{14}\,\mathrm{cm^{-3}}$ with an absorption coefficient of $1 \times 10^{5}\,\mathrm{cm^{-1}}$. Figure 4.9(a) shows the result of transient PL data acquired for a perovskite on the electron charge extraction layer. The transient is fitted by the sum of three exponential

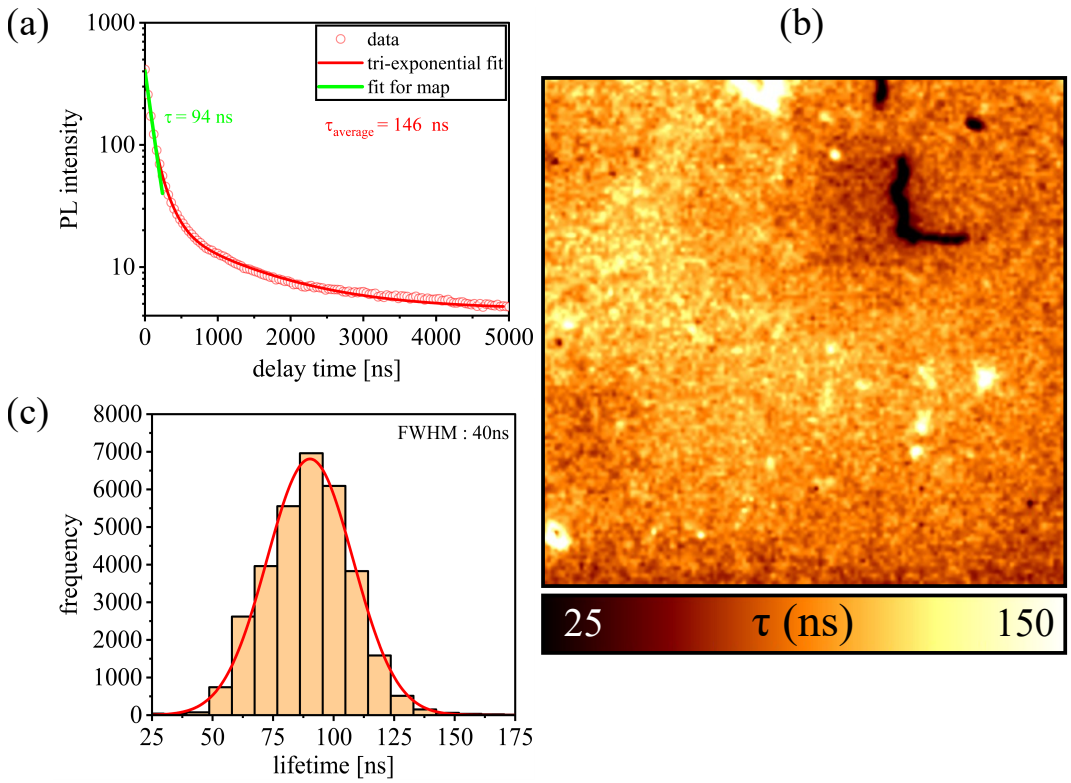

Figure 4.9: Time-resolved photoluminescence measurement for the FAPIBr perovskite. (a) transient PL of the FAPIBr perovskite stack. The green fit line represents the data fitting range used to construct the lifetime map in (b). (b) $5 \times 5\ mm^2$ map of decay time developed by fitting mono-exponential function to every pixel transient for the range seen in (a) green line. τ was thus extracted from each pixel. (c) Distribution of decay time with FWHM of approximately 40ns. Injection: $2.0\,\mathrm{nJ/cm^2}$

decay functions shown in a solid red line. The choice of three exponential was made purely based on the shape of the transient together with the trial-error method starting with mono, bi, and then tri-exponential decay function which showed the best fit. With that said, there must be three recombination mechanisms taking part in the decay. Before talking about which recombination process is happening, one should know the injection level used during the measurement as this impacts the recombination rates. For this, I estimated the bulk doping density in the order of $1 \times 10^{15}\,\mathrm{cm}^{-3}$ which is a generally accepted order of magnitude in literature for perovskites. This is just an estimation, thus the absolute value may fluctuate but not by order of magnitude. Using this estimated bulk doping and the photon density per pulse, I can safely assume that the measurement was conducted under LLI. At LLI, the decay should be proportional to the excess generated minority carrier density (Δn) and all recombination mechanisms should be linear with Δn with decay constant giving the effective lifetime. But as I observe in Figure 4.9, the FAPIBr perovskite on TiO_2 sample does not show

clear linear behavior even under LLI possibly due to very bad front surface. The average decay time $\tau_{average} \approx 146\ ns$ was extracted from the fit using the equation;

$$\tau_{\text{average}} = \frac{A_1\tau_1 + A_2\tau_2 + A_3\tau_3}{A_1 + A_2 + A_3} \tag{4.3}$$

where A is the amplitude and τ is the decay time extracted from fit. The average decay time that I observe is the contribution of the surface lifetime, both front and back as well as bulk lifetime by relation;

$$\frac{1}{\tau_{average}} = \frac{1}{\tau_{surf+diff}} + \frac{1}{\tau_{bulk}} \tag{4.4}$$

Surface recombination as well as diffusion of generated charge carriers is a fast process taking place within a few tens of nanoseconds after the laser pulse. Surface recombination reduces the number of electrons by non-radiative recombination. To understand the influence of surface recombination and diffusion, I need to assume that the back interface recombination velocity is negligible. In this case Sproul et al. [111] in 1994 showed that surface lifetime part τ_{surf} is approximated by $\frac{L}{S_{top}} + \frac{4}{D} \times (\frac{L}{\pi})^2$. The first term is the top surface recombination where L is the thickness of the absorber layer and S_{top} is the top surface recombination velocity. The second term is the diffusion related term where D is the diffusion coefficient.

To distinguish different recombination processes, one would need to vary the injection level from low to high which I will do later on. First what I am interested in is the lateral variation of the decay time across the FAPIBr absorber. To achieve this, I need to extract the decay time from transient data acquired by grouped pixels (4×4) to have reduced noise. As the transient on single pixels is very noisy, I will only fit the data where the signal-to-noise ratio is high. I have fitted the mono-exponential function to the first 400 ns of delay time after the laser pulse and extracted the decay time of $94 \pm 7\ ns$ for this range. The fit can be seen in figure 4.9(a) in solid green. I use this same range to fit every transient from every grouped pixel and generate a map of extracted τ seen in figure 4.9(b). The fast recombination process takes place after the laser pulse which then at a longer delay time beyond 1000 ns becomes slower and longer, usually attributed to trap-assisted recombination (SRH). Overall in the measured region, the distribution shows an FWHM value of $40ns$ and standard deviation $\sigma = 17\ ns$ indicating a deviation from the average value of $94ns$ extracted from a small delay time fit. Due to the perovskite being unpassivated at the surface, there are a lot of surface defects, dangling bonds, and inhomogeneities that I discussed in previous sections that contribute to the recombination rate. By fitting the first 400 ns delay time, what I am observing can be interpreted to be a surface recombination mechanism. Surface recombination is a mechanism of recombination that is non-radiative and leads to a decrease in the intensity signal of PL. In the continuity equation, the electron and hole concentrations

are subject to the boundary condition of surface recombination. Specifically, for the electron, this boundary condition can be expressed as follows:

$$\pm D_n \frac{dn}{dx} = \frac{np - n_i^2}{\frac{n}{S_p} + \frac{p}{S_n}} \tag{4.5}$$

where x varied from 0 to d and S_n and S_p are the surface recombination velocities for electrons and holes. This means that if electron concentration decreases towards the back interface at $x = d$, this will lead to a positive rate of recombination at that interface. It is thus important to know the carrier concentration at the surface or interface. As long as I am in a low injection regime, the system should be easy to interpret for simple systems such as the absorber layer on glass. Assuming that I have a p-type absorber layer, equation 4.6 becomes,

$$\pm D_n \frac{dn}{dx} = S_n n \tag{4.6}$$

To understand this, I need to consider that once charges are generated, they need some time to diffuse into the bulk. The time that it takes to diffuse depends on the thickness of the sample. *Cho et al.* [129] recently provided a rough approximation of the time ($\approx 80ns$) needed for the charge carrier to travel across the thickness of 600 nm FAPI perovskite. Using this 80 ns, vertical diffusivity $D_{n,verti}$ can be estimated by $D_{n,verti} \propto \frac{d^2}{80ns}$, where d is the thickness of absorber layer. Using this diffusion time and thickness, the diffusivity of $0.011\,\mathrm{cm}^2/\mathrm{sec}$ is estimated. The perovskite in our case has a similar thickness of $\approx 600 \pm 50$ nm so an assumption is that it will take charges $\approx 80 \pm 10$ ns to travel to the back interface. Hence the fact that I fitted the low delay time < 300 ns, I can assume that between this delay time, I have a diffusion process in combination with surface recombination playing simultaneously. As the diffusion mechanism will try to distribute the charges in the entire bulk of perovskite, at the same time, electrons will be lost at the surface due to non-radiative recombination reducing the PL significantly. Putting D=$0.011\,\mathrm{cm}^2/\mathrm{sec}$ with a thickness of 600 nm, the diffusion contribution in equation 4.4 is $\tau_{diffusion} = \frac{1}{D}\left(\frac{L}{\pi}\right)^2 \approx 33\ ns$. Heterogeneity in vertical diffusion can occur and produce variation in the decay rate as shown by *Cho et al.* [129]. When it comes to imaging, one has to consider the possibility of variation both in vertical as well as lateral directions. This makes quantitative analysis of transient imaging tricky as in most cases the PL signal detected by the camera is depth average. Nevertheless, I can still extract transient images at the desired timestamp to understand the variation. From the transient PL image taken immediately after laser pulse arrival, (Figure 4.10(a), I observe some bright features highlighted in red circles that decay very fast as compared to the surrounding average. However, these particular spots also show high Q_e^{lum}

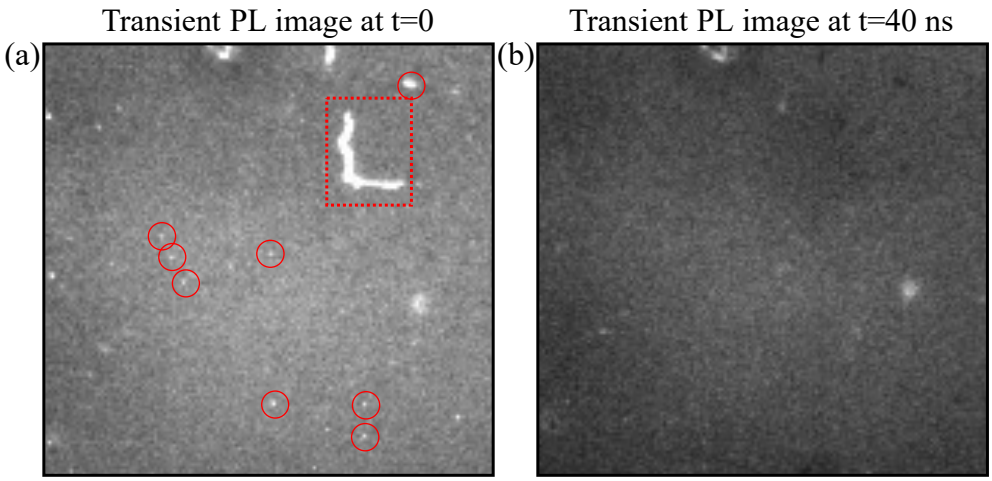

Figure 4.10: Transient PL image ($2.5mm \times 2.5\ mm$) taken immediately after the arrival of the laser pulse at (a) t=0 ns and (b) t=40 ns. A red rectangle and solid red circles mark the features that show a high PL signal immediately after pulse arrival but drop 77% after 40 ns as compared to an average PL drop of 38%.

values in quasi-steady state measurement when compared with Figure4.3(b). The L-shape bright contrast feature initially shows high luminescence at the laser pulse arrival but decays after $40ns$. From the decay time map in Figure 4.10(b), the region around this L-shaped feature has low τ in positive correlation with low Q_e^{lum} value observed in Figure 4.3 indicating the region is simply poor quality perovskite. The FAPIBr perovskite that is being studied has an active back interface with the TiO_2 ETL, hence next section will focus on the charge transfer mechanism and fluence dependence on the transient PL.

4.3.2 Insights into electron transfer into electron transport layer

In the scientific community, very few papers question the interpretation of the transient decay of the absorber material when in contact with the charge extraction layer. Some notable groups that tackled this question were Thomas Kirchartz and Uwe Rau's group [188, 201]. At high laser fluence, there is not much difference between the decays of full devices, partial stacks, or thin film on glass. However, at low fluence, an effect due to the extraction layer and built-in electric field can modify the shape of the transient. High accumulation of charges at the interface slows down or in extreme cases stops the transfer process due to repulsive force, however, it takes part in the interface recombination due to Coulomb attraction. *Krogmeier et.al* [126] simulated the charge dynamics of the perovskite in contact with the extraction layer using low laser fluence and high laser fluence for different surface recombination velocity, Figure 4.11. Simulation results indicate that to differentiate between

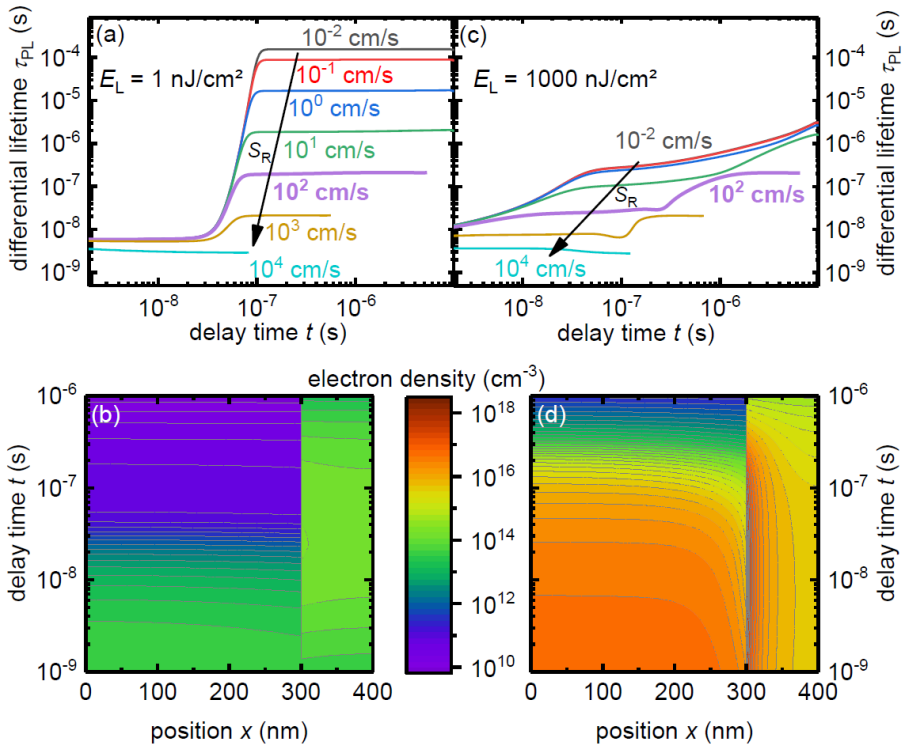

Figure 4.11: Simulation from *Krogmeier et al.*[126]. (a) Simulated differential lifetime at a low laser fluence of 1 nJ/cm^2 for ranging surface recombination velocity S showing two plateaus, first dominated by transfer and second by recombination. (b) Map of electron density for S =100 cm/sec for fluence of 1 nJ/cm^2 indicating how electron density increases inside the extraction layer. (c) Simulated differential lifetime at a high laser fluence of 1000 nJ/cm^2 showing no obvious plateaus due to multiple processes like transfer, recombination as well as charge accumulation at interface occurring at the same timescale. (d) Map of electron density for S =100 cm/sec for fluence of 1000 nJ/cm^2 indicating accumulation of electrons at the interface.

transfer and recombination processes, transient PL measurements should be conducted at LLI. At High level injection (HLI), the system becomes more complex due to the high density of charge carriers accumulating at the interface, which impedes further charge extraction. When the surface recombination velocities are lower, the recombination in the bulk is more significant compared to the interfacial recombination. The dependence of the two plateaus observed in Figure 4.11(a) on the surface recombination velocity (S) is evident and pronounced, especially at LLI. Initially, the electron density is evenly distributed as seen in Figure 4.11(b), but over time, electron transfer reduces the density in the bulk and increases it in the extraction layer. As the electron has nowhere to go beyond the extraction layer, it can either recombine with the hole in the bulk, leading to interface recombination or reinject

itself back into the perovskite bulk and participate in bulk recombination. The first scenario occurs when the interface recombination velocities are high and the conduction band offsets are large, while the second scenario occurs when there are low recombination velocities and small conduction band offsets. After a while, the electron density inside the ETL will start decreasing due to interface recombination and the bulk electron density decreases slowly due to bulk recombination. When transitioning to HLI in figure 4.11(b), the two plateaus become indistinguishable due to the influence of charge accumulation. The influence of charge accumulation is most significant for low values of S since recombination at the interface will diminish the accumulation of charges. In this case, the accumulation of electrons at the interface is seen in Figure 4.11(d).

In my study, I will utilize the fact that immediately after the laser pulse, the distribution of charge carriers will be governed by a Lambert-Beer distribution and the number of excess carriers generated near the surface will be highest compared to the inner regions of the material. To investigate this, I will employ two different geometries to examine the two interfaces of the partial perovskite stack. The first interface is the top surface of the perovskite, denoted as Perovskite side (PS), while the second interface is the back interface of perovskite/TiO_2, referred to as Glass side (GS). This technique allows for the examination of surface recombination and interface recombination by considering the Lambert-Beer model.

4.3.3 Low Fluence transient PL and its effect on charge extraction

As I have a partial stack as Glass/FTO/c-TiO_2/mp-TiO_2/perovskite, using our custom PL setup, I can illuminate from perovskite surface, in which more charge carriers are generated close to the surface as compared to the back interface which is $\approx 600\ nm$ deep, and exponentially decreases as I go deeper into the layer according to the Lambert-beer model shown in appendix of this thesis B.3. Another geometry is where I flip the sample 180° and illuminate the backside to probe the perovskite/TiO_2 interface in which the charges are now generated more at the back interface as compared to the top surface. The schematic to clear the above-mentioned information is shown in fig4.12. The reason behind such a measurement is to see the effect of the electron extraction layer when carriers are generated in close vicinity to it. I am aware of the fact that after generation, the charges diffuse within a few tens of nanoseconds inside the bulk, distributing itself homogeneously, but here I will be looking at processes happening within the first 100 nanoseconds which is the time I assume the diffusion dynamics are still in play. Figure 4.13 shows transient PL measured in two scenarios indicated in figure 4.12. From transient PL from PS and GS, the initial decay of the PL

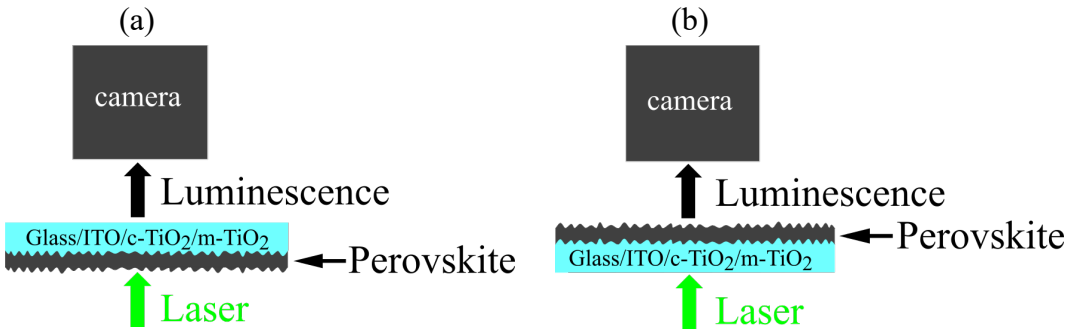

Figure 4.12: Two measurement geometry used to understand the process of charge transfer. A collimated laser beam with a Gaussian profile illuminates, (a) the perovskite surface, referred to as the PS, and (b) back interface of perovskite/TiO_2, referred to as the GS. The transient measurement is performed here in transmission mode.

intensity is larger when illuminated from GS i.e. when a generation of charges is closer to the interface. The measurements here are performed in transmission mode and air due to technical challenges of the setup. The laser spot is no longer broad beam homogenized but a collimated laser beam was used to illuminate the sample at 750 khz frequency. The photon density per pulse was measured to be $2.4 \times 10^{14}\,\mathrm{cm}^{-3}$ for an absorption coefficient approximated as $1 \times 10^{5}\,\mathrm{cm}^{-1}$. The transient is fitted by a sum of three exponential functions. Here

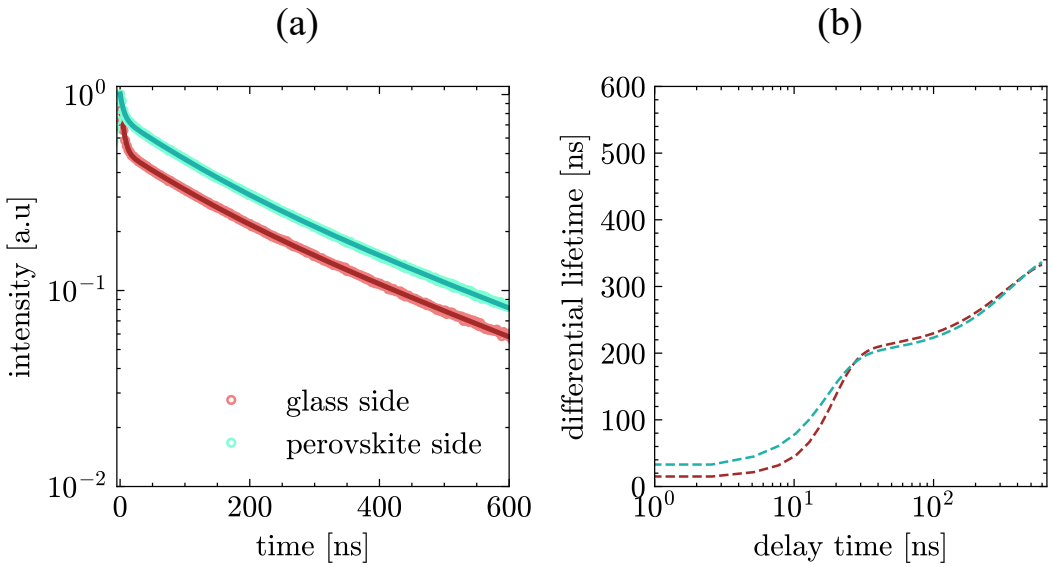

Figure 4.13: Transient PL (left side) and differential lifetime plot (right side) of perovskite sample. (a) unpassivated perovskite illuminated from GS(brown) and PS(aquamarine). (b) Differential lifetime plot from the fit acquired from (a). The laser injection in all cases was $1.2\,\mathrm{nJ/cm^2}$.

the purpose of the fit is not to extract the decay time or lifetime from the function but to

have data that best fits or aligns with the experimental data. Alternative to this, one can use heavy Gaussian smoothing. This is because I use differential lifetime to extract the decay time $\tau_{diff}(t)$ and the derivative of the experimental data is very sensitive to small changes, so I first fit the data to a decay function model, which helps to have smooth data and reduce the noise. I make sure that the fit aligns well with the experimental data, and then use the fit data as my transient to calculate the differential lifetime from equation 4.4. This technique is more resilient to the shape of the PL transient and can take into account the effects of non-linearities. By differentiating the PL transient, I can retain all the information about how the decay changes over time, which is essential for studying phenomena such as charge accumulation and charging that do not display simple exponential or power-law behavior. At low laser fluences, the two plateaus observed in the differential lifetime plot resulting from charge transfer and interfacial recombination are easily distinguishable, but they become less distinguishable at higher laser fluences due to stronger charge accumulation at the interface [126]. When unpassivated perovskite is illuminated via the two geometries that I showed in Figure 4.12, the initial drop in luminescence intensity is observed in both cases. The drop is greater in the case of GS illumination because there are more excess carriers generated close to the charge extraction layer in this geometry. *Krogmeier et.al* [126] showed that the charge carrier transfer to the extraction layer will cause a reduction in the PL signal early which is not caused by recombination. What I observe is very similar and can be used to quantify the extraction as the *np* product at the interface, is changed.

I have already defined surface lifetime τ_{surf} in equation 1.19 with an assumption that the surface recombination velocities are the same on both interfaces ($S_{top} = S_{back} = S$). To analyze this quantitatively, I first calculated the differential lifetime of these transients, shown in Figure 4.13(b), then I estimated the surface recombination velocity using the differential lifetime τ_{diff}. Differential lifetime $\tau_{diff}(t)$ is the inverse negative slope of the logarithmically plotted PL photon flux Φ_{PL} [110](eq. 174). Differential lifetime is expressed as:

$$\tau_{\mathrm{diff}}(t) = \frac{m}{-\left|\frac{d}{dt}\ln\Phi_{\mathrm{PL}}(t)\right|} \tag{4.7}$$

where m relating to the injection level used using measurement; $m = 1$ for LLI and $m = 2$ for HLI.

Ahrenkiel et al. [110] calculated the PL decays with varying surface recombination velocities that provided a good estimation of surface lifetime for the fast decay near $t = 0$. If I use τ_{diff} at $t = 0$ when I am probing the perovskite surface (illuminating from PS, I can

get an estimation of Surface recombination velocity S using;

$$S = \frac{1}{\alpha}\left(\frac{1}{\tau_{\text{diff}}(t=0)} - \frac{1}{\tau}\right) \tag{4.8}$$

where the absorption coefficient is defined as α and τ in this refers to the bulk decay time, which in this case is the SRH decay time. The SRH decay time is taken to be the second plateau value of the differential lifetime, $\tau \approx 220\ ns$ for the equation. τ_{diff} at delay time $t = 0$ was measured to be 35 ns for PS illumination. Plugging these values into an equation 4.8 and using $\alpha = 1 \cdot 10^5\ cm^{-1}$, the surface recombination velocity for unpassivated perovskite from PS illumination is calculated to be 240 cms^{-1}. As electron-hole pair generation is higher at the surface as compared to the back interface, the surface recombination will dominate as compared to the backside interface recombination, as the concentration of excess charge carriers Δn is high at the surface and relatively low at the back interface at smaller delay time after the laser pulse. Whereas, the opposite will occur when illuminated from the back interface (GS). Δn will be higher close to the extraction layer as compared to the front surface and thus charge transfer and interface recombination will be dominant compared to the surface recombination. This is evident from the two varying transient decay that I measured in Figure 4.13. By using the calculated S for PS, the surface lifetime can be estimated using equation 1.19. Here, an assumption needs to be made that one of the interfaces is perfectly passivated or has negligible recombination velocity. Let's say the back interface of /perovskite/TiO_2 is passivated or inactive. It will provide a limiting condition for defect-related lifetime. The dominant recombination processes will be surface and bulk. I then use equation 1.20 and estimate the surface lifetime τ_{surf} of 250 ns for the perovskite surface. This τ_{surf} of 250 ns is very close to the SRH lifetime τ_{bulk} of 220 ns. If one assumes that the recombination velocity at both the front and the back interface is the same, the estimated S would come out to be 125 ns which is lower than the long decay time. To conclude, when the PS is illuminated, the initial drop in the luminescence for the unpassivated case is attributed to the high surface recombination velocity due to defects and the high density of traps. When the laser pulse arrives from GS of the stack, the transient that is measured shows faster initial decay as compared to the PS. As mentioned above, this is because high concentrations of electrons are being extracted into the TiO_2 layer reducing the PL relatively fast within the first tens of nanoseconds. From the differential lifetime plot I see that once the charge transport process has finished, the decay continues as the bulk recombination evidenced by the same position of the second plateau of the two discussed transients. In the next section, I see how different fluence impacts the shape of the transient when illuminated from the PS and GS.

4.3.4 Fluence dependence of transient PL and its effect on charge extraction

Previously I talked about LLI transient PL for FAPIBr perovskite in contact with the ETL (mp-TiO_2) layer. At HLI, recombination such as radiative and Auger starts showing significant contribution. Nevertheless, so far our study is on a non-passivated perovskite on charge extraction layer, the trap-assisted recombination from surface and bulk will also come into play. This already gives an idea of the complexity involved in interpreting the transient PL data. The transient PL in this section has been conducted by an independent calibrated Time-correlated Single Photon Counting (TCSPC) setup with a 655nm pulsed laser source. Figure 4.14 shows fluence-dependent transient PL on FAPIBr perovskite sample grown on

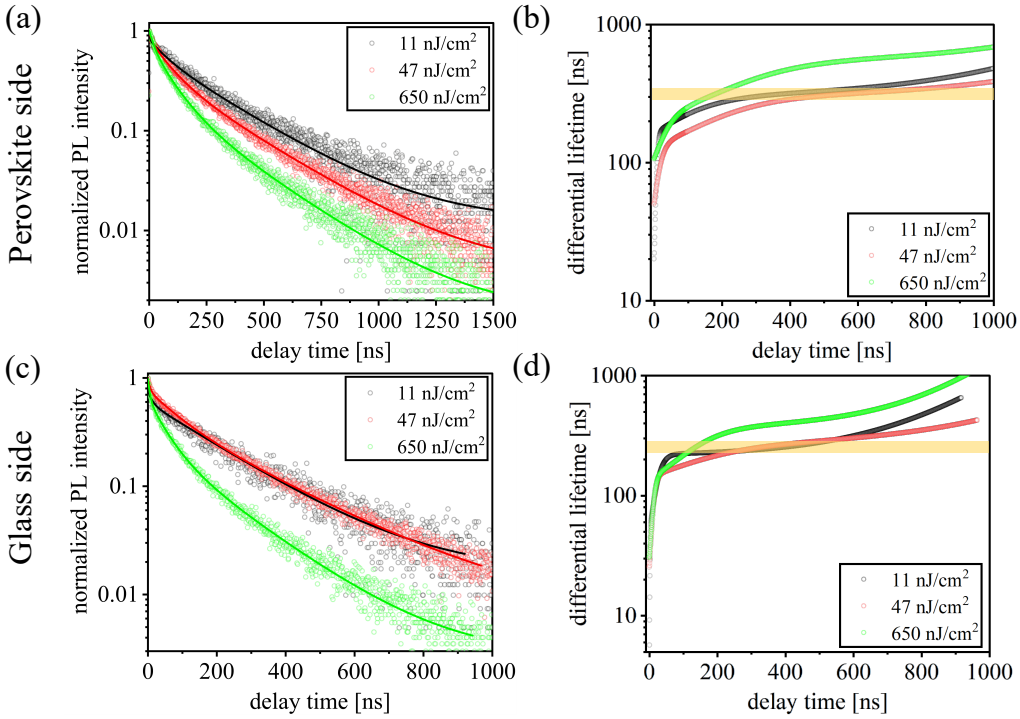

Figure 4.14: Fluence dependent measurement of FAPIBr perovskite using three laser fluences. (a) Transient PL is acquired when the stack is illuminated from the PS. (b) The plot of a differential lifetime for PS transient was calculated from the fit data of (a) using equation 4.7. (c) Transient PL is acquired when the stack is illuminated from the GS. (d) The plot of a differential lifetime for GS transient was calculated from the fit data of (c) using equation 4.7. The yellow-shaded level of differential lifetime marks the plateau for fluence 11 nJ/cm^2 and 47 nJ/cm^2.

TiO_2 ETL layer, where three fluences were used; 11 nJ/cm^2, 47 nJ/cm^2, 650 nJ/cm^2. For PS illumination, I use the same argument of generation of charged carriers as used previously for

respective geometries. In such a case, the surface recombination mechanism will dominate initially followed by the bulk recombination at a longer delay time. As the sample is unpassivated, the majority of the density of excess carriers generated at the surface will likely take part in the surface recombination and the relatively less excess carrier will be extracted by the extraction layer. This is evident from the absence of an initial PL drop in the transient. I observe from the transients in Figure 4.14(a) that as fluence increases, the overall transient decay rate becomes faster. To understand the transient data at HLI of $650\,\mathrm{nJ/cm^2}$, I make use of the quasi fermi level splitting estimated by equation [202, 188] at HLI,

$$\mu_{qfls} = k_b T \ln\left(\frac{\Delta n^2}{n_i^2}\right) \tag{4.9}$$

n_i is taken to be $8 \times 10^4\,\mathrm{cm^{-3}}$. $650\,\mathrm{nJ/cm^2}$ corresponds to the photon density per pulse of 2.1×10^{12} per pulse. With this, I calculated the absorbed photon density for the thickness of 600 nm and the Lambert-Beer model to be $3.5 \times 10^{16}\,\mathrm{cm^{-3}}$. Using this as Δn in equation, the maximum $\Delta E_{F,max} \approx 1.33\ eV$. Similarly, I used quasi fermi level splitting equation at LLI for fluence $11\,\mathrm{nJ/cm^2}$ given as;

$$\mu_{qfls} = k_b T \ln\left(\frac{\Delta n}{n_0}\right) \tag{4.10}$$

In equation 4.10, $n_0 \approx \frac{n_i^2}{N_A}$, where N_A is assumed to be $1 \times 10^{15}\,\mathrm{cm^{-3}}$ as bulk doping density. The estimated $\Delta E_{F,max} \approx 1.15eV$

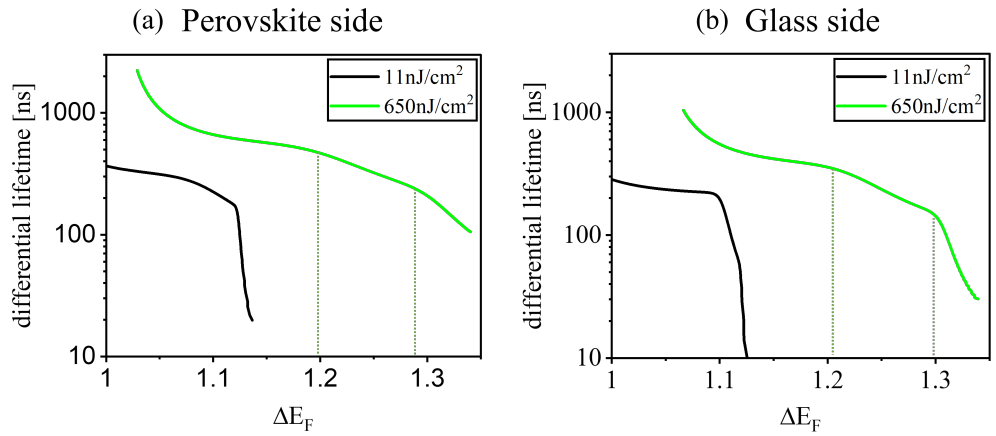

Figure 4.15: Differential lifetime plotted against quasi-fermi level splitting calculated from equation 4.9 for HLI and equation 4.10 for LLI. (a) Illumination from the perovskite side. (b) Illumination from the glass side. The dotted line marked for high fluence represents the change in the slope of the curve.

Figure 4.15 shows the differential lifetime plotted against the quasi fermi level splitting calculated using equation 4.9 and 4.10. For high fluence, I observed a fast closing of the fermi

levels with two inflection points marked at 1.29 eV and 1.2 eV. These may be occurring due to the accumulation of charges at the interface. Various factors such as the band offset of the ETL with the perovskite, the thickness of the ETL, the interface recombination velocity, and the fluence can affect the transient decay when in contact with the ETL. The data presented here is purely experimental. To extract parameter dependence, one needs to run a simulation by varying the parameters mentioned above and find the set of parameters that best match the shape with the experimental data. Nevertheless, just from experimental data, I still see how the quasi-fermi level splitting changes at different rates going from low decay time to longer decay time.

4.4 Conclusion

This chapter presents a thorough investigation of the PL behavior in FAPIBr mixed-halide perovskites, focusing on quasi-steady state and transient measurements. A comparative analysis of CW and pulsed laser illumination reveals that high repetition rate pulsed lasers closely mimic the steady-state behavior observed under CW illumination. This finding is significant as it validates the use of pulsed lasers in steady-state PL studies of perovskites, particularly when operated at high repetition frequency. The study also explores the optical and chemical heterogeneity of FAPIBr perovskite and identifies variations in PL intensity attributed to different long-length scale disorders. Specifically, the analysis of the FAPIBr perovskite shows a PL peak position at 1.56 eV with a standard deviation of 44 meV. The heterogeneity within the perovskite film is further assessed quantitatively through the distribution of luminescence intensity, revealing distinct peaks in the range of 0 to 5000 counts and a significant peak at 10000 counts. This indicates areas of both high and low PL activities due to underlying defects and material inhomogeneities. SEM mapping, EDX map as well as point spectra helper in recognizing the chemical species present on the surface that act as a source of inhomogeneity. Additionally, the study investigates the charge carrier dynamics within the perovskite structure through transient PL measurements under different illumination geometries. The average decay time $\tau_{average}$, calculated to be approximately 146 ns using weighted averaging of the τ's from the sum of 3 exponential function fit, is found to be influenced by both surface, bulk as well as interface lifetimes. At low injection for unpassivated perovskite, the requirement of such a function to fit the data already tells you that the perovskite has a lot of surface traps and non-radiative recombination mechanisms taking place. Differential lifetime plots at low-level injection provided insights into charge transfer mechanisms and interface recombination dynamics when different illumination ge-

ometries were implemented. I observed initial PL decay within the first 50 ns of laser pulse arrival which I attributed to the interplay of surface recombination as well as diffusion. I mentioned that it will take time for the generated carrier to be transported to the back interface and this needs to be considered when interpreting transient PL data. Notably, under high fluence transient PL measurements, different decay rates are observed at varying laser fluences, reflecting the complex interplay of charge carrier dynamics at different injection levels. Furthermore, the calculated Quasi-Fermi level splitting values under different fluences and plotted against differential lifetime provided insight into the charge accumulation at the interface experimentally observed by the plateau formation. The formation of the plateau becomes more pronounced as the laser fluence increases. For relatively low fluence, I only see one plateau. Overall, this chapter contributes to the fundamental understanding of PL behavior in mixed-halide perovskites and highlights the importance of illumination type and experimental conditions. The detailed insights into heterogeneity and carrier dynamics have significant implications for the development and optimization of perovskite-based optoelectronic devices.

Chapter 5

Stripes: Exploring Optoelectronic variations in Spin-Coated Perovskite on TiO_2

5.1 Stripe formation and characteristics

Previously, I noticed a stripe-like pattern in the optical image of the FAPIBr perovskite stack as well as in the PL intensity map. These stripes, also known as striations, have been seen in studies where perovskite absorbers were spin-coated on TiO_2 double layers [169, 83]. I will refer to these striation defects as stripes. What is the primary cause of the formation of these stripes? Are they due to the perovskite or the TiO_2? To answer these questions, I will explore the cause and effect of these stripes. I will start by discussing the deposition process, as it is the main cause of the formation of the stripes. Then, I will move on to the optoelectronic effect of these stripes on the perovskite absorber.

5.1.1 Role of spin coating

Spin coating is a process in which a colloidal suspension is applied to a stationary or slowly rotating substrate, which is then accelerated to a predetermined rotation rate. This causes the majority of the suspension to be flung off the substrate, leaving behind a thin film that continues to thin due to radial outflow and solvent evaporation. The process of spin coating can be divided into four distinct stages, each with its time frame [203]. The schematic can be seen in Figure 5.1. The first stage is the deposition stage, in which the coating solution spreads over the substrate due to gravitational force, surface tension, and centrifugal force (if the substrate is rotating). The second stage is spin-up shown in Figure 5.1 step 2, which starts

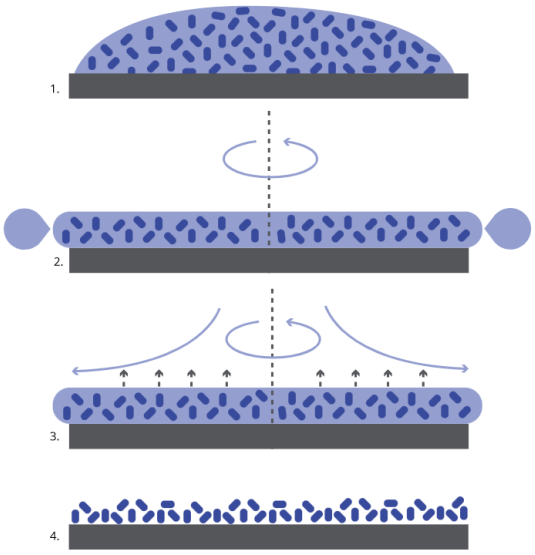

Figure 5.1: Spin coated process divided into 4 main steps. (1) Deposition, (2) Spin up, (3) Spin down, and (4) Evaporation. This schematic has been taken from Ossila webpage [203]

with the acceleration of the substrate to its terminal velocity. This acceleration rate does not always have to be rapid; for example, when spin coating large diameter substrates, the inertia of the disk prevents rapid acceleration. The rotation of the disk induces a centrifugal pump action in the overlying gas phase, which increases evaporation, although at this stage the contribution of evaporation to film thinning is usually small. Inertial forces, in addition to centrifugal forces, are significant during spin-up. The third stage is spin-off shown in Figure 5.1 step 3, which corresponds to the decrease of inertial forces other than centrifugal. During spin-off, the film thins due to centrifugal force and evaporation. As the film thins, the coating solution viscosity rises (as a result of solvent evaporation), and viscous forces become increasingly important, thus effectively ceasing centrifugal thinning. The final stage is drying, which involves the film thinning only by evaporation. The mass of suspended or non-volatile material in the film at the beginning of the drying stage ultimately determines the final film thickness. Any imperfections in the film that may have occurred and persisted during the previous three stages of spin coating are now frozen into the film.

The author Burkitt et al.[204] states that when the TiO_2 layer is spin coated, it results in the formation of radial striation defects[205]. These defects serve as the foundation for the subsequent deposition of perovskite, hence perovskite deposition also shows stripes. These linear features are aligned with the direction of spin. The source of these striations is likely to be evaporative convection[206], with the main driving force being a surface tension gradient,

or the Marangoni effect. Therefore, when the perovskite solution is spin-coated on top of these stripes, the perovskite layer takes on the striped pattern as the underlying TiO_2 layer.

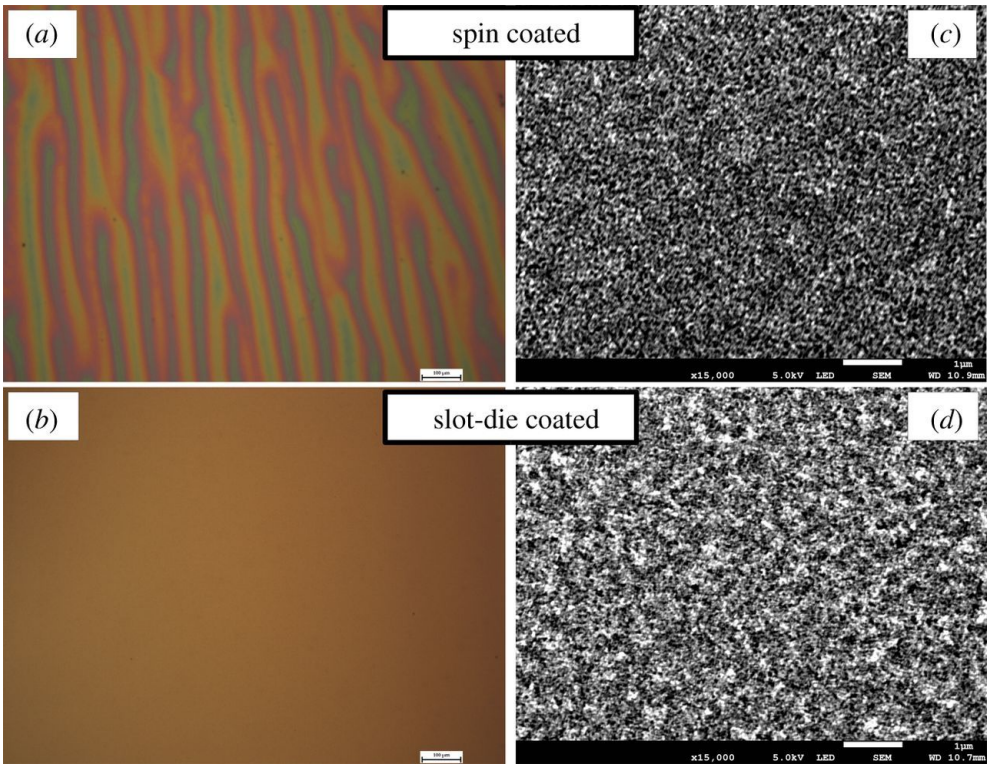

Figure 5.2: Optical microscope (a,b) and SEM (c,d) images of titanium dioxide scaffold layer. It shows that even though both the spin-coated and sloth-die-coated technique creates a mesoporous layer (evident from SEM), the stripes or striations are only formed when TiO_2 is spin-coated. This figure has been taken from Burkitt et al.[204]

Figure 5.2 from Burkitt et al. shows the optical and SEM image of the TiO_2 that is spin-coated(a,c) and slot-die coated(b,d). The stripes are only formed in the sample that was spin-coated, while the film is very homogeneous when using the slot-die method. This suggests that either the spin coating procedure and/or the volatility of the solvent used in the solution is the primary cause of the formation of stripes. To avoid these striation defects or stripes, one can choose slot-die or spray-coating methods to yield a homogeneous and porous TiO_2 film. In this thesis, I are more interested in the effect of the spin-coated TiO_2 on the optoelectronic properties of the perovskite, as the spin-coating is still a widely used process for both TiO_2 and perovskite deposition. Therefore, I will discuss the morphology of the stripes first and its impact on charge dynamics structures in more detail in the following sections.

5.1.2 Morphological features of stripes via profilometer

As discussed and concluded in the previous section, the origin of the stripes is due to the spin coating process of TiO_2 solution. To study the morphological features of these structures, I implement the profilometer technique which is already discussed in brief in Chapter 2. Due to the sample architecture being Glass/FTO/c-TiO_2/mp-TiO_2/perovskite, I measured the morphology on the surface of the perovskite followed by the mp-TiO_2.

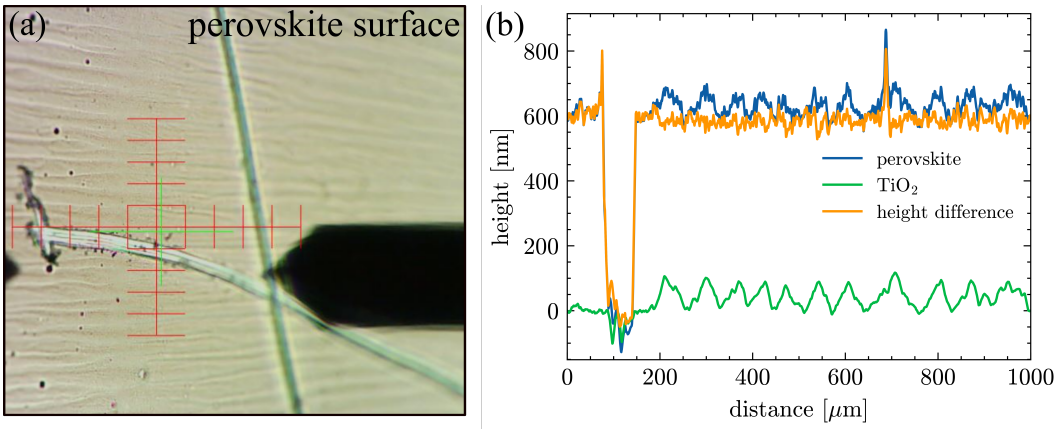

Figure 5.3: Profilometer measurement on perovskite surface and mp-TiO_2. (a) Perovskite surface scanned with profilometer tip and scan direction (vertically up. (b) Line profile across the scratch on, the perovskite surface (blue) and mp-TiO_2 (green). The orange curve is the difference between perovskite and mp-TiO_2 profile, representing the remaining corrugation of the perovskite.

A scratch was made on the perovskite sample, as seen in Figure 5.3(a), to serve as a guide for measuring the same spot. The tip of the profilometer was then scanned through the scratch for a distance of 1 mm. The line profile (blue) plot in Figure 5.3(b) reveals that the surface of the perovskite is corrugated with an average period of $\approx$80 μm and a height of $\approx$100 nm for the hill and valley features. The perovskite layer was then removed by dipping the sample in Dimethyl-formamide (DMF), allowing us to measure the corrugation of the mesoporous-TiO_2 at the same spot and along the same line. After measuring the surface of the mp-TiO_2, the hill and valley pattern aligned very well with the perovskite profile. This concludes that the corrugation on the perovskite surface was caused by the underlying corrugation of the mp-TiO_2. By measuring the perovskite and mp-TiO_2 profile, I was able to determine roughly the perovskite thickness to approximately 600 ± 50 nm. To check if there exists any significant thickness variation of the perovskite absorber layer with the mp-TiO_2, I simply subtracted the two profiles and observed that the thickness of the perovskite layer from the surface of the mp-TiO_2 layer is uniform and the average RMS-roughness is 30 nm.

5.2 Optoelectronic properties of perovskite in the presence of stripes

5.2.1 Impact on photoluminescence

The stripes created by spin coating TiO_2 have a major impact on the PL yield of the perovskite film, yet this has not been thoroughly studied. The stripes may lead to an uneven interface, impeding charge transfer, and may also contain more trap states and/or areas of poor contact, which can affect the PL. Additionally, the thickness variation between the compact and the mesoporous TiO_2 that must be formed due to spin coating could be another potential cause.

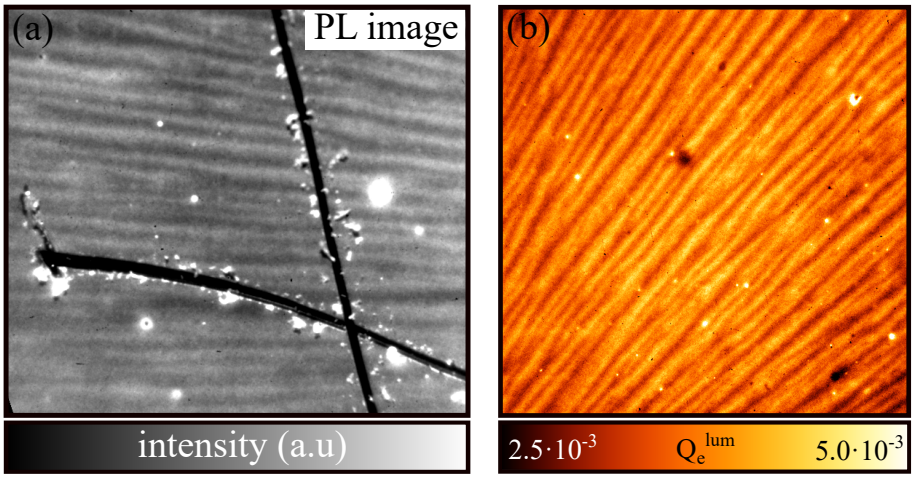

Figure 5.4: PL intensity and Q_e^{lum} map of the stripes defects. (a) region of the perovskite where profilometer measurement was performed in figure 5.3 as confirmed from the scratch and stripes. (b) A 6×6 mm^2 Q_e^{lum} variation map of perovskite showing stripes pattern. The two images are not the same area of the sample.

Figure 5.4(a) shows a PL image of the area that was measured with a profilometer 5.3(a). The scratch and corrugated pattern are visible, confirming that it is the same area. Interestingly, the hill and valley features influence luminescence intensity; the hill has a high PL signal and the valley has a low signal, even though the perovskite thickness concerning the mesoporous layer is mostly homogeneous (Figure 5.3). I previously concluded that the striped pattern is derived from the underlying mp-TiO_2, so the PL intensity variation is also a result of the TiO_2 corrugation or one can say the interface of perovskite/TiO_2. This suggests that the PL intensity is determined not only by recombination in the perovskite layer but also by the charge carrier dynamics from the perovskite layer through the ETL interface. The variation in the PL signal then translates to Q_e^{lum} variations as seen in Figure 5.4(b). I

performed cross-section SEM of the perovskite stack to check if the mesoporous TiO_2 layer has varying thickness with its compact layer. Figure 5.5 shows a cross-section SEM image

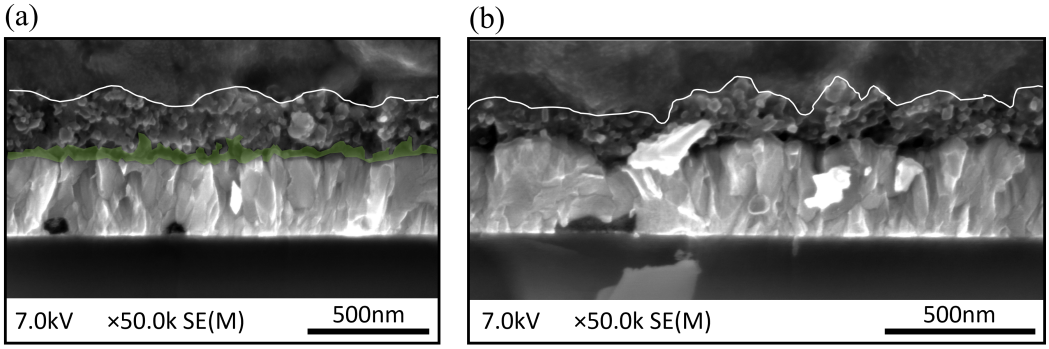

Figure 5.5: Cross section SEM image of the FAPIBr perovskite of the same sample taken at two different regions. Green highlighted region shows the compact-TiO_2 layer and the white marked line shows the interface of perovskite with the mesoporous TiO_2.

taken at two different locations of the same perovskite stack sample. The thickness of the mesoporous layer (corrugated layer in SEM image) on spot1 (Figure 5.5(a)) is different as compared to (Figure 5.5(b)). At some local regions, the mesoporous layer is observed to be thin enough that there is a possibility that perovskite is in direct contact with the compact-TiO_2. Such variation of the mesoporous layer with the compact layer can significantly affect the optoelectronic properties of the sample. This Q_e^{lum} variation would not exist if the TiO_2 layer was coated by the slot-die method or any other process that produces uniform and planar surfaces without the striation defects [204]. To further investigate the Q_e^{lum} variation and confirm the charge extraction mechanism in detail, I make use of local transient PL imaging on the stripes where I separate the transient PL data of the hills and valley and study them independently to see if there is any difference in their decay rate indicating the variation in dynamics.

5.2.2 Local transient PL on hills and valleys

The time-resolved photoluminescence (TRPL) of the perovskite sample was studied to investigate the influence of the corrugation and to assess how the charge extraction efficiency and carrier dynamics are affected by the inhomogeneous TiO_2. In literature, a similar study was conducted by *Yamashita et.al* [207] on MAPI perovskite using microscopic PL and photocurrent (PC) imaging. From their study, they found a positive correlation between PL intensity and PL lifetime and a negative correlation between the PL and PC intensities. This means high PL intensity regions will have a longer lifetime but decreased photocur-

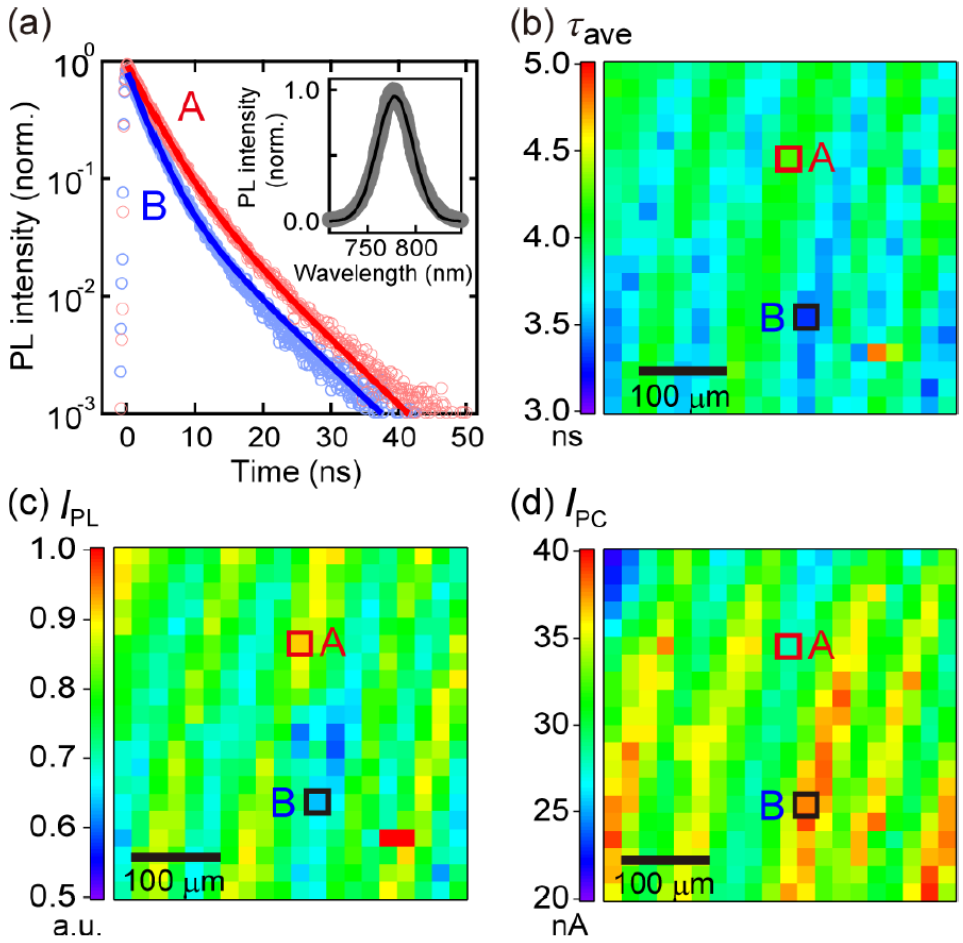

Figure 5.6: (a) PL decay curve measured at points A and B of (b). (b) Map of average PL lifetime. (c) time-integrated PL intensity map. (d) photo-current intensity map. Reprinted with permission from [207] Copyright 2023 American Chemical Society.

rent. As the MAPI used in their study was also grown on mesoporous TiO_2 just like our sample, they also observed a strip pattern in their PL imaging. Figure 5.6(a,b,c) taken from *Yamashita et.al* shows that the transient taken at the top of the high PL region (hills) and bottom of the low PL region (valley) is different at with longer lifetime observed for the one at the hill. For our time-resolved measurement, as the injection conditions are low, the signal at a pixel level is very faint, making it hard to extract the transients with a good signal-to-noise ratio. Thus to separate the hills from valleys, I used image processing to better visualize the transient signal. I employed a two-dimensional Fast Fourier Transform (2D-FFT) to separate the TRPL image into two parts, hills and valleys. The regularity of the stripe pattern enabled us to single out the distinct frequency of the stripes. I began by extracting the PL intensity image at $15ns$ after the laser pulse arrived. This was chosen as the optimal time to clearly distinguish between hills and valleys. In this PL image shown

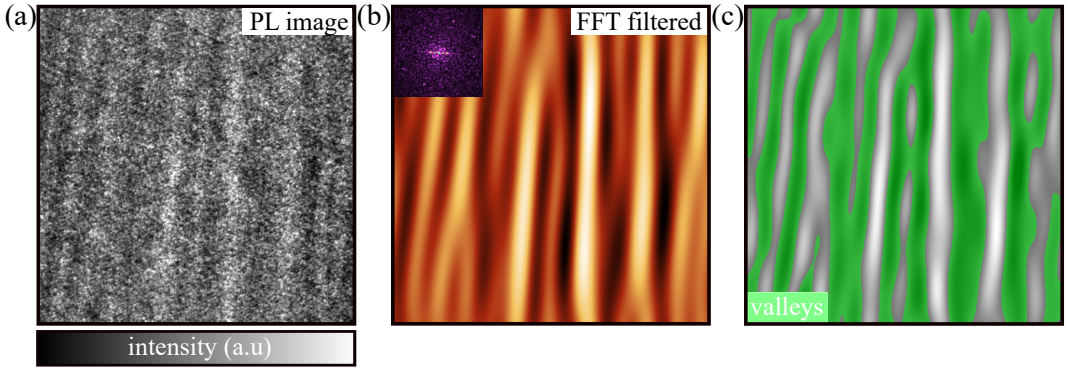

Figure 5.7: Transient PL of hills and valley. (a) a $1 \times 1\ mm^2$ transient PL image at $t =$ 15ns after laser pulse. The stripe pattern is visible. (b) 2D-FFT filtered image of (a), with an inset showing the dominant frequencies. The image enhances the visualization of the stripe pattern on the sample. (c) Applied threshold and mask (green) the valley region to distinguish between hill and valley.

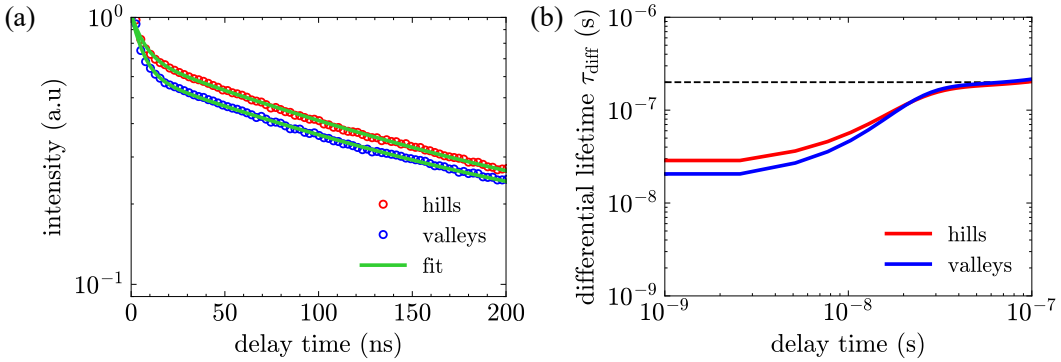

Figure 5.8: (a) Time-resolved PL transients and (b) differential lifetime plot of the hills and valley. The black dotted line represents the bulk differential lifetime τ_{bulk} of 200ns.

in Figure 5.7(a), I already see the variation in the PL intensity at $t = 15\ ns$ after the laser pulse. To reduce the pixelation of the image, a 2-pixel Gaussian filter was applied. I then used a 2D-Fast Fourier Transform to identify the frequency from the FFT image, as seen in the inset of Figure 5.7(b). This allowed us to reconstruct the filtered image, which enabled us to isolate the hills and valleys. Finally, I used an intensity threshold to mask the image and cover the valley region with a green mask, creating a binary image of the mask. This mask was then used as a stencil on the raw data of the time-resolved PL images to extract transients from the hills and valleys. I employed a GS illumination geometry of the perovskite stack to observe the charge transfer process as more carriers are formed near the charge extraction layer considering Lambert-Beer's law. The plotted transients can be seen in Figure 5.8(a). Since the injection that I am using for the transient data is $1.2\,\mathrm{nJ/cm^2}$,

the photon density per pulse is $2.4 \times 10^{14}\,\mathrm{cm}^{-3}$. This is less than the bulk doping density N_A that I estimated as $1 \times 10^{15}\,\mathrm{cm}^{-3}$, thus as $\Delta n < N_A$, I am in the low injection regime, which is better for distinguishing the transfer and interface recombination lifetime [126]. At high laser fluence, the effect of charge accumulation at the interface will be strong due to the high density of excess charge carriers generated. I observed that the two lifetimes are distinguishable as seen from two plateaus in the differential lifetime plot in Figure 5.8(b) and observe that $\tau_{diff,hills}$ is higher than that of $\tau_{diff,valleys}$. At longer delay time ($< 100\ ns$) the two transients coincide with the SRH bulk lifetime of $\tau_{SRH} = 200 \pm 20\ ns$. These results are in agreement with the conclusion from *Yamashita et.al* [207]. I observe that the intensity

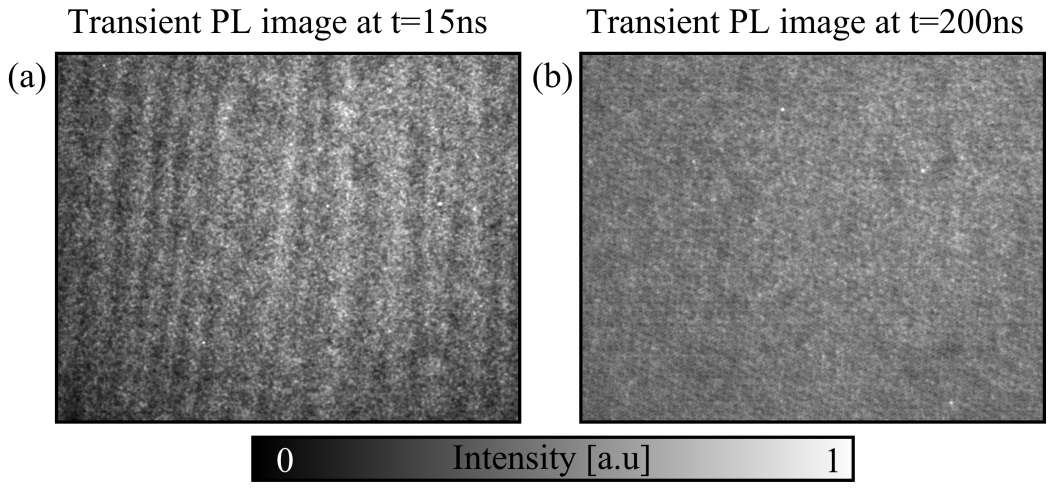

Figure 5.9: (a) Transient PL image taken at $t = 15ns$ after laser pulse. The image is cropped from the full-scale image and is $2 \times 1.5\ mm^2$.
(b) Transient PL image taken at $t = 200\ ns$ after the laser pulse. The first image shows the stripes distinguishable whereas beyond after 100 ns of pulse arrival, the stripe pattern is not observed.

variation due to stripes is visible at $t = 15\ ns$ as seen from the transient PL image taken at that delay time. However, for delay time beyond $t = 100\ ns$, the variation vanished and the PL intensity is more homogeneous. If it was some recombination mechanism, I would have seen the pattern to the end of the transient which I do not. This is another evidence that the process happening within the first tens of nanoseconds is the electrons injecting into the mp-TiO_2 and this injection efficiency is changing due to the stripe pattern. After these few tens of ns, electrons can no longer take part in transporting themselves to the extraction layer and SRH bulk recombination then dominates homogeneously everywhere.

5.2.3 Charge carrier dynamics in striped region

Under open-circuit conditions, which is the case for steady-state PL, there will be no net flow of carriers and consequently no constant drain of electrons from the perovskite to the TiO_2. But in transient measurement, as I am keeping track of the carrier concentration after the laser pulse, it becomes easy to look for processes such as transfers and recombination. The literature suggests that the thickness of the TiO_2 layer may have a significant impact on the efficiency of charge extraction [208]. However, in most cases, the average thickness of the mesoporous TiO_2 layer is considered, and the variations caused by spin coating are often overlooked. Thicker layers offer more surface area for charge extraction, but they also increase the distance that charges need to travel to reach the electrode. This could potentially lead to electron re-injection into the perovskite and contribute to recombination after a longer delay [188]. The presence of striations or stripes in the layer creates variations in thickness compared to the compact TiO_2 layer, resulting in variations in charge extraction. Therefore, optimizing not only overall thickness but also the uniformity of the TiO_2 is crucial for improving power conversion efficiency in perovskite solar cells. The differences between the hills and valleys can be attributed to slight changes in the conduction and valence bands, as well as a shift in the recombination rate at the interface. Previous studies have demonstrated that Li-doping can effectively lower the conduction band [70]. In our case, Li-TFSI is used to reduce trap density and enhance charge extraction. However, due to the mesoporous nature of the TiO_2 layer together with the striations formed due to spin coating, the deposition of Li-TFSI may not be uniform, resulting in further variations in electrical properties and extraction of carriers. Another approach to eliminate these variations is to modify or optimize the deposition method. For example, slot-dye coating has been shown to produce a homogeneous and stripe-free mesoporous TiO_2 layer [204]. If the mesoporous TiO_2 layer is free of stripes, spin coating the perovskite would result in an even more uniform layer, eliminating variations and ultimately improving device parameters.

5.3 Conclusion

In this detailed analysis, I have delved into the stripe formation in perovskite solar cells, primarily focusing on the role of the spin coating process used for TiO_2 layer deposition and its profound impact on the optoelectronic properties of the subsequent perovskite layer. My findings suggest that the stripe-like patterns or striations originate from the TiO_2 layer and significantly affect the morphology and function of the overlying perovskite layer.

Morphological Analysis and Stripe Formation: The profilometer measurements on the perovskite surface revealed a corrugation pattern with an average period of approximately 80 μm and a height differential of about $100nm$ between the peaks (hills) and troughs (valleys). The correlation between the corrugation on the perovskite and the underlying mesoporous-TiO_2 confirms that the striations originate from the TiO_2 layer. The perovskite thickness was estimated to be around 600 ± 50 nm, with an average RMS-roughness of 30 nm, indicating significant texture imparted by the TiO_2 layer.

PL Variations: PL imaging demonstrated that the stripe patterns significantly influenced luminescence intensity. Notably, areas corresponding to the hills displayed higher PL intensity compared to the valleys, despite a mostly uniform perovskite thickness relative to the mesoporous layer. This variation in PL signal was attributed to the corrugation in the TiO_2 layer, suggesting an inhomogeneous interface affecting charge transfer and the presence of trap states. The observed variations in the PL intensity and the Q_e^{lum} map further indicated that these morphological features significantly impact the charge extraction efficiency across the perovskite layer.

Transient Photoluminescence (TRPL) Analysis: Time-resolved transient studies provided deeper insights into the charge dynamics influenced by the stripe pattern. The differential lifetime plots showed that the initial lifetimes for hills ($\tau_{diff,hills}$) were longer than those for valleys ($\tau_{diff,valleys}$), with a bulk differential lifetime (τ_{bulk}) of approximately 200 ns. This variation in τ_{diff} highlighted the inhomogeneity in charge extraction efficiency across the striped regions.

Implications for Solar Cell Performance: The inhomogeneity in the TiO_2 layer, manifested as stripes, has significant implications for solar cell performance. The variations in charge extraction can lead to localized areas of inefficiency, potentially reducing the overall power conversion efficiency of the cell. Moreover, the striations introduce additional pathways for non-radiative recombination, further impacting device performance. If the TiO_2 layer is made homogeneous, either by optimizing the spin coating process itself or replacing spin coating with another alternative deposition process, I can expect an improvement in the power conversion efficiency. This improvement was also demonstrated by [204] where spin coating and slot-die coating methods were compared

Recommendations for Improved Fabrication: To mitigate these issues, alternative deposition techniques such as slot-die coating are recommended. These methods can produce more uniform and planar TiO_2 layers, thereby eliminating the striation defects and leading to a more homogeneous perovskite layer. Such improvements in layer uniformity are crucial

for enhancing the overall efficiency and reliability of perovskite solar cells.

In conclusion, the study emphasizes the critical role of the TiO_2 deposition process in determining the morphological and optoelectronic properties of perovskite solar cells. By optimizing this process and reducing the formation of striations, it is possible to significantly enhance the performance and efficiency of these photovoltaic devices.

Chapter 6

Strategies for Enhancing Uniformity in Mixed Halide Perovskites

The research field of PSC has grown significantly, with PCEs surpassing 25% [15]. However, there is still a gap between this and the theoretical optimum PCE of 31% for a band gap of 1.56eV given by the Shockley–Queisser limit [209]. Additionally, their stability is not comparable to that of silicon-based solar cells. This can be attributed to many factors such as the mobile ions, migration of vacancy defects [210, 211], sensitivity to the external environment like oxygen, moisture, defects at grain boundaries as well as at interfaces that trigger the degradation of perovskite [212, 213] has put a limit to further improvements in efficiency and stability [214]. To increase the PCE of PSC, it is necessary to reduce nonradiative recombination processes and prevent the quenching of carriers within the photo-active layer and at the interfaces, while simultaneously promoting balanced charge transport and collection [215, 216, 217, 218]. Defects in charge transport layers, perovskite films, and their interfaces have a major impact on the optoelectronic properties, the growth dynamics of polycrystalline perovskite films, and the transport properties of electrons and holes. To tackle the problem of instability, several approaches have been devised to stabilize the crystal phase and manage defects in PSC. These include interface engineering via surface passivation and charge compensation with metal oxides, additive engineering to enlarge the dimensions of perovskite grains and increase crystallinity, and the use of small molecules or polymers [219, 220, 72, 221]. Figure 6.1 illustrates the strategies that are constantly being applied by different research groups to improve perovskite solar cells.

6.1 What are different ways to improve the perovskite homogeneity?

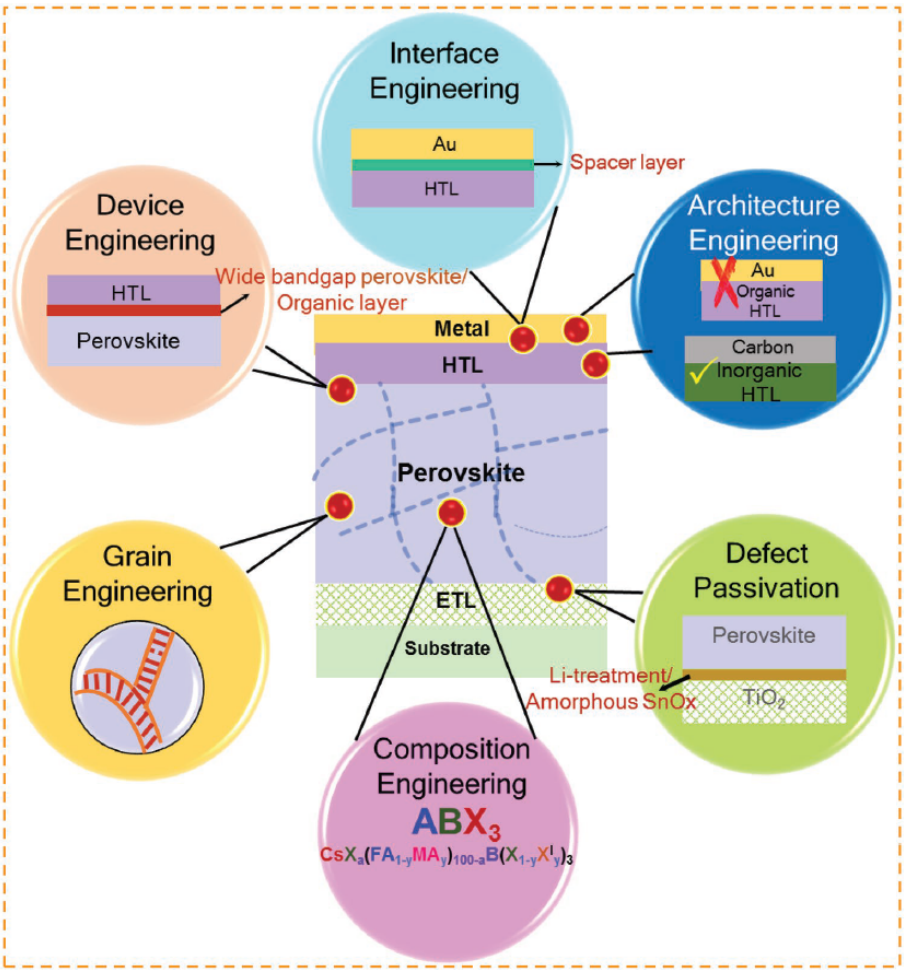

Figure 6.1: Different strategies to improve the perovskite solar cell. The figure has been taken from *Akin et. al* [222] with permission from John Wiley and Sons and Copyright Clearance Center with License number: 5710691048922.

As demonstrated in Figure 6.1, there are a variety of methods to improve the quality, optoelectronic response, and charge extraction efficiency of each layer and its interface with the adjacent layer. Every layer of a solar cell is essential and must be optimized. Starting from ETL on the substrate, the choice and the hunt to find an ideal ETL is never-ending research and there are a lot of candidates to choose from, including a variety of self-assembled monolayers (SAMs) [223, 224], polymers or some fullerene derivatives [225]. ETL as well as HTL need to fulfill some criteria, namely providing low recombination at their interface with the absorber layer which can be achieved by passivation [226, 227, 63], provide proper band alignment to the absorber layer for allowing efficient extraction of one type of carrier

while blocking the other which is achieved by selectivity [228] as well as minimize resistive and optical loses. Next comes the absorber layer which has been engineered and modified chemically, at all the length scales from nano-meters to millimeters. Grain boundary (GB) engineering, GB passivation, absorber doping, composition engineering, band gap tuning, and surface treatments using lasers are a few of the methods used by researchers to improve the absorber layer. Following is the HTL which is then deposited on the absorber layer. This makes it a requirement that the surface of the perovskite needs to be with low or no defects or trap density so that the HTL can be deposited homogeneously and aid in efficient hole extraction. As it goes for ETL, the choice of HTL is also a challenge and continuous research is ongoing to look for an ideal HTL layer. The solar cell ends with the metal contact which again needs to be a conducting material. Therefore, every layer of the solar cell consists of optimization, and additional layers mean ever more research and optimization. A full detailed overview of the optimization and research consisting of each layer and interface can be found in *Akin et al.* [222]

In the following section, I will take a closer look at two specific passivation techniques, one involving the passivation of the surface with a thin layer of an organic molecule and the other being a more recent approach to treat perovskite using a low-energy UV laser to cure the surface.

6.2 Enhancing material performance with chemical layer surface passivation

Surface passivation is a promising approach to address the issues discussed. It can reduce the number of nonradiative recombination centers, which capture charge carriers and reduce the PCE of PSC, as well as enhance the uniformity of the perovskite absorber layer. Chemical passivation involves the utilization of Lewis base molecules to attach to the surface defects of the perovskite absorber layer. Perovskite thin film deposited using solution processing is full of surface defects because of chemical heterogeneities, as well as grain boundaries at the surface that are exposed to ambient [229, 230, 231]. These defects lead to multiple non-radiative recombination traps, which cause local band bending and phase segregation, resulting in voltage losses [232, 233]. To improve the efficiency and stability of PSC, it is essential to reduce defect densities by passivating the interface. Various chemical strategies, for example, Lewis acid or base additives, 2D layers, and polymers, have been widely studied to reduce non-radiative recombination and achieve high-efficiency PSC. [234, 235, 222, 236,

237]. Fullerene C_{60} and its derivatives (PCBM) have demonstrated their effectiveness as passivation agents in high-efficiency PSCs [225]. The study by *Shao et al.* was the first to identify the potential of PCBM, which is C_{60} modified with phenyl butyric acid methyl ester, as a highly efficient passivation molecule. It enhances device performance by reducing the presence of both shallow and deep traps. There exist 100s of chemicals that can be used for passivating the perovskite and the hunt for the ideal passivator is still ongoing. In this section, I will explore how passivating the surface of the perovskite affects the optoelectronic properties via PL as well as the overall improvement of the PSCs. The perovskite that I discussed in the previous Chapter, (4,5) is now passivated with bifunctional aromatic ligand biphenyl-4 4'-dithiol[83], which can bind to perovskite via non-covalent interactions.

Note: The perovskite studied in this Chapter has been received from different research groups and was grown or treated there. I received the FAPIBr perovskite stack to study the optoelectronic properties of the perovskite after surface passivation (from EPFL) and laser treatment (from Stuttgart). However, the study is extended by using PL imaging and transient PL imaging equipment to understand their effect deeply. Respective mention will be given to avoid confusion.

6.2.1 Characterization of surface passivated perovskite

In Chapters 4 and 5, I discussed the impact of inhomogeneities on the optoelectronic properties of an unpassivated mixed halide perovskite. This was done through the use of quasi steady-state and transient PL imaging techniques as well as other complementary techniques. In the following section, I will be focusing on a surface passivated perovskite and comparing its effects to those of an unpassivated surface. The passivated layer is deposited on the perovskite surface with a thickness of a few nanometers. For more detailed information about the molecule and its deposition process, please refer to the work by Krishna et.al [83]. Here the main interest lies in examining the optoelectronic response of the perovskite after it has been passivated and checking the inhomogeneities observed on the optical images via chemical characterization techniques such as EDX and SIMS. From Figure 6.2(b), the average Q_e^{lum} (4×10^{-3}) due to passivation of the surface has increased by almost an order of magnitude as compared to unpassivated perovskite surface (4.2×10^{-4}) as shown in Figure 4.3(b). Nevertheless, the strip pattern is still visible which I already discussed in detail in Chapter 5. A tenfold increase in Q_e^{lum} suggests the possibility of surface defects being passivated by the organic layer leading to reduced non-radiative recombination. In addition to the possible surface defects passivation, the organic layer leads to passivation of surface halide vacancy

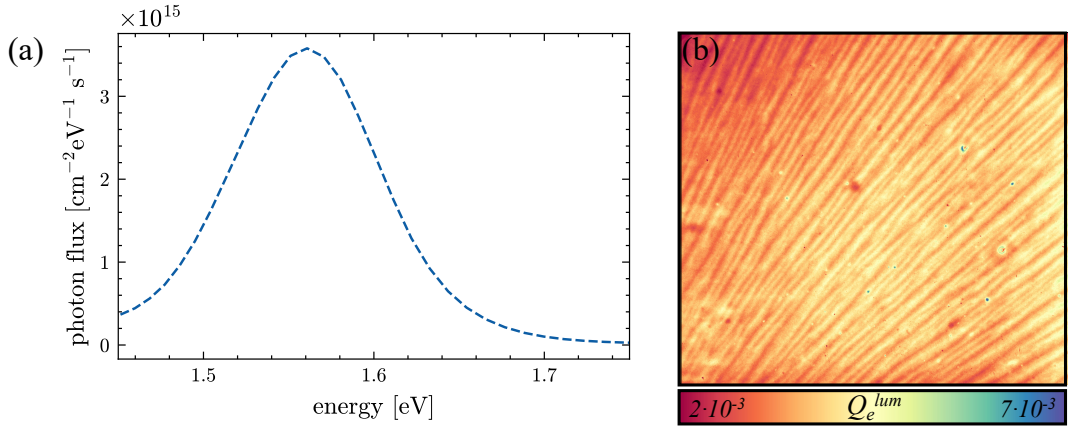

Figure 6.2: Quasi steady-state PL on FAPIBr perovskite whose surface is passivated by a thin layer of organic molecule. (a) PL spectrum measured at 0.68sun showing peak position at 1.56 eV. (b) $6 \times 6\ mm^2$ Map of Q_e^{lum} constructed from integrated PL spectra of each pixel and divided by the total absorbed photons.

reducing the loss of surface Iodine and organic component FA, thus overall reducing defect concentration as shown by Krishna et al. [83]. Using the average Q_e^{lum} of 4×10^{-3} and PL peak position of 1.56 eV, the quasi-fermi level splitting μ_{qfls} is estimated to be $1.135eV$ at 0.68 sun using equation 3.7. The non-radiative loss using $kT \cdot \ln Q_e^{lum}$ comes out to be 143 meV when illuminated at 0.68sun which is a good improvement from an unpassivated sample that showed a loss of 201 meV under the same illumination. Even though only the surface is passivated, I observe variation in the Q_e^{lum} between the stripe pattern. I used a 20x objective lens to further have a detailed insight into the perovskite which is shown in appendix C.1. As the passivation layer is very thin ($\approx 1 - 2\ nm$) and spin-coated, passivation is likely not uniform everywhere. Besides the passivation layer, the FAPIBr perovskite still shows inhomogeneities which I will study using EDX. Figure 6.3(a) displays the optical image of the passivated FAPIBr obtained from the confocal setup. Upon initial observation of the optical image, it is evident that there are numerous dark dots distributed throughout the sample. Figure 6.3(b) presents the secondary electron image of a perovskite section, revealing contrast in the dots, which can appear either bright or dark. Additionally, besides the dots, there are features present on top of the perovskite that have not crystallized into the perovskite matrix. The secondary electron image and EDX spectra of these features can be found in the appendix C.2.1. Some of these bright features show a high Br level whereas some show a high Sn level coming from the FTO. This is only possible if the thickness of the perovskite is not uniform evident from the chemical signal coming from deep layers with the same accelerating voltage of 20 keV.

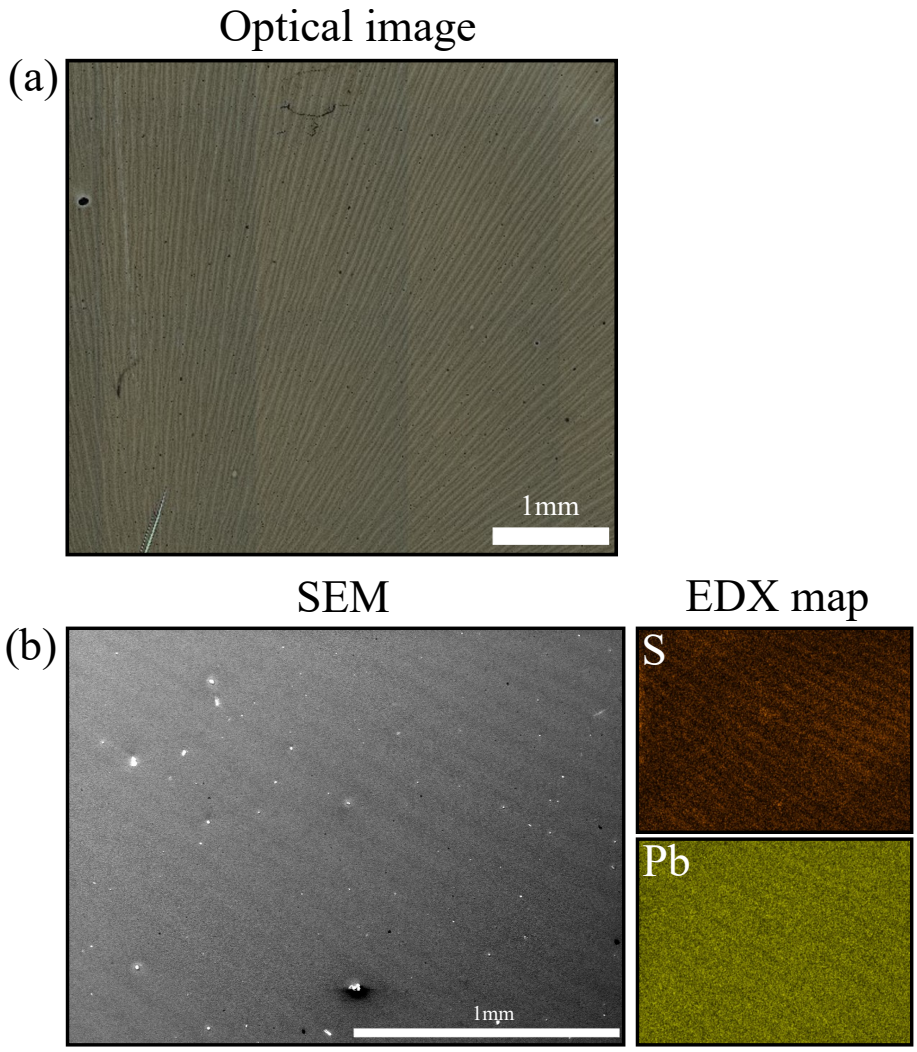

Figure 6.3: (a) Con-focal optical image of passivated perovskite. (b) SEM image of the passivated perovskite taken with an acceleration voltage of 20 kV with simultaneous EDX mapping highlighting Sulfur and Lead distribution on the surface.

The EDX map in Figure 6.3(b) specifically highlights sulfur and lead, as the passivator compound contains sulfur [83]. Notably, despite the passivation layer having a thickness of $1-2\ nm$, EDX was able to detect the sulfur signal from the surface. The passivation layer seems to exhibit a stripe pattern, with higher sulfur concentration on the hills compared to the valleys. If the assumption that the passivation layer reduces surface defects holds true, this may explain why the hills exhibit higher photoluminescence (PL) compared to the valleys. However, it should be noted that the sulfur and lead (Mα) peaks in the EDX spectra are very close to each other (at $\approx 2.3\ eV$), which could potentially lead to misinterpretation of the sulfur to lead signal or vice versa. In this case, considering the prior knowledge that the passivator contains sulfur, I consider the EDX map to indicate sulfur distribution. One advantage of EDX is that it allows for the selection of specific points or features on the surface

to obtain information about the chemical content. Given the inhomogeneity of the perovskite in the form of bright and dark dots. All the aforementioned discussion pertains to a large length scale, specifically at the millimeter scale. However, the passivation must certainly have an effect at the small length scale as well. To analyze the surface morphology, AFM and high-resolution secondary electron images were utilized and are shown in the appendix C.3.1.

Following, I show from the transient PL data that enhancement in the Q_e^{lum} is supported by the reduction in surface recombination velocity.

6.2.2 Transient PL and lifetime mapping of surface passivated perovskite

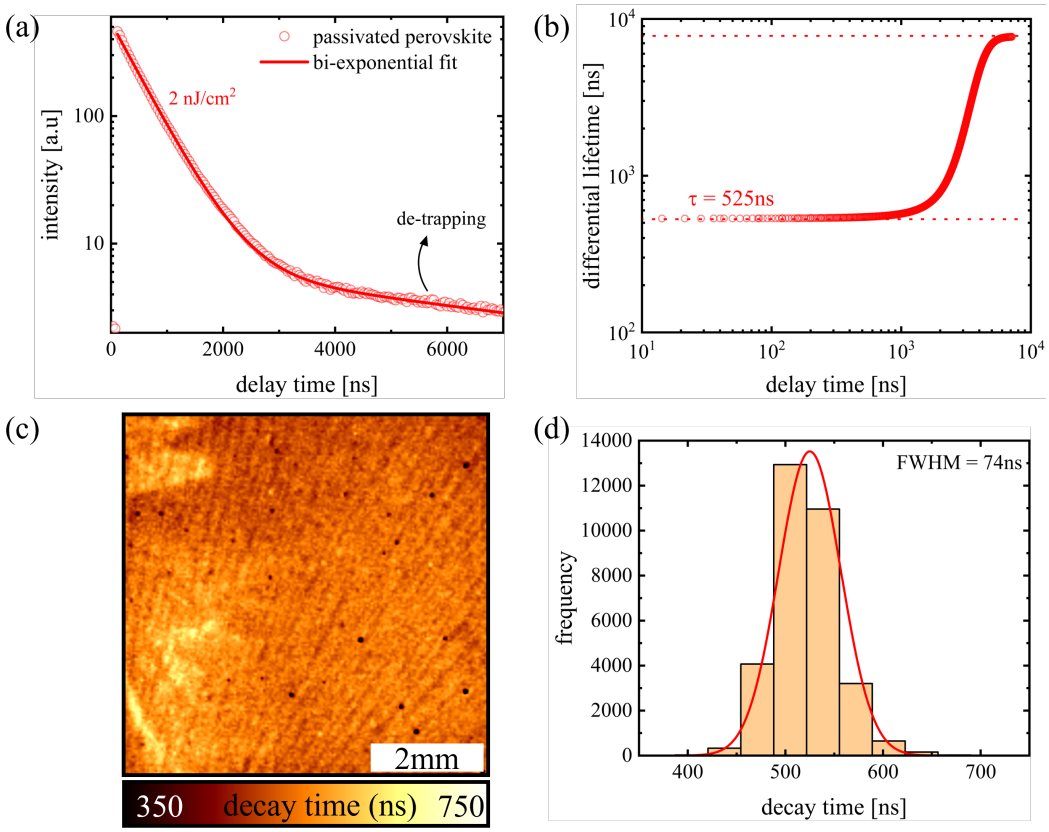

Figure 6.4: Time-resolved transient PL on surface passivated perovskite. (a) Transient decay curve measured with fluence $2\,\mathrm{nJ/cm^2}$ (photon density per pulse of $5 \times 10^{14}\,\mathrm{cm^{-3}}$) fitted with a bi-exponential decay function. (b) Differential lifetime plot calculated from the fit data from the plot (a) using equation 1.35. (c) Map of decay time extracted by fitting transients from each pixel by mono-exponential decay function within the delay time range of 0 to $1500ns$. (d) Distribution of decay time fitted with Gauss function and FWHM of 74ns

To study the charge dynamics of the surface passivated perovskite, I measured transient

PL with laser fluence of $2\,\mathrm{nJ/cm^2}$ shown in Figure 6.4(a). The transient shows two slopes, first within the delay time range of 0 to 2000 ns and second with the delay time beyond $3\mu s$. Hence, the transient is fitted by a bi-exponential decay function that outputs two values of τ, 525 ns, and $> 7\mu s$. These two τs can also be seen in the differential lifetime plot in Figure 6.4(b). As the surface is passivated, I assume surface recombination to be negligible and thus consider the decay time of 525 ns as the bulk recombination decay time. The slow decay time of < 7 μs, I consider to be a de-trapping mechanism [125]. As charges get trapped at the trap state present within the energy gap of absorber material, they can de-trap after some time followed by recombination, and thus occurrence of this detrapping and recombination mechanism takes place at a longer delay time. Figure 6.4(c) shows the map of decay time that was extracted by fitting the mono-exponential decay function of single pixel transient. This helped me to spatially visualize the variation in the decay time that ranges from $> 100ns$ for dark dots to 750 ns for bright features. I do not currently have an explanation of the bright features showing longer lifetime but my intuition says it has to do with vertical composition gradient from surface to bulk. But the dark dots that I see are very fast decay species on the surface of the perovskite and decay within 100 ns. Even though the average transient yields a single value of τ, spatial mapping shows that τ is not uniform and shows variation between the range 75 ns *to* 750 ns as shown from the histogram. Figure 6.4(d) shows a histogram of the decay time distribution with FWHM of 74 ns. The standard deviation from the Gauss fit to the distribution comes out to be 33 ns thus the average decay time for the first slope is represented as 525 ± 33 ns. Using this decay time, I can estimate the bulk doping density of the perovskite by using equation 1.27 with some assumptions; Considering a p-type semiconductor, N_A would represent doping density in bulk. At LLI, product $np = \Delta n N_A$. Taking $\tau = 525ns$, $p_e = 0.1$, k_{rad} $=6 \times 10^{-11}\,\mathrm{cm^3/sec}$ [112], measured Q_e^{lum} $=4 \times 10^{-3}$ and ignoring p_a, equation 1.27 modifies to;

$$\frac{1}{N_A} = \tau p_e k_{rad} \cdot \left(\frac{1}{Q_e^{lum}} - 1 \right) \tag{6.1}$$

After inserting the values stated above, N_A is estimated to be $1.2 \times 10^{15}\,\mathrm{cm^{-3}}$. This estimated value is higher than the photon density per pulse used during the transient measurement ($5 \times 10^{14}\,\mathrm{cm^{-3}}$), thus $\Delta n < N_A$, and the measurement regime is in low-level injection.

6.3 Low injection level transient PL on surface passivated mixed-halide perovskite

To understand the recombination mechanism, I apply the same methodology that I did for unpassivated perovskite in chapter 4 where I illuminate the stack from the PS (this time passivated perovskite) and GS which is represented in figure6.5. The transient is fitted by a sum of two exponential functions. Even though it might look like the PS transient is mono-exponential decay, the bi-exponential function provided a better fit and covered the initial decay that gets reflected in the differential plot. This is also because the resolution here is much better than the transient in the previous section. Just for a reminder, I am only using fitting functions to have noise-free data so that our differential lifetime plot is clean. Let us first discuss the illumination from the PS. By comparing the transient of

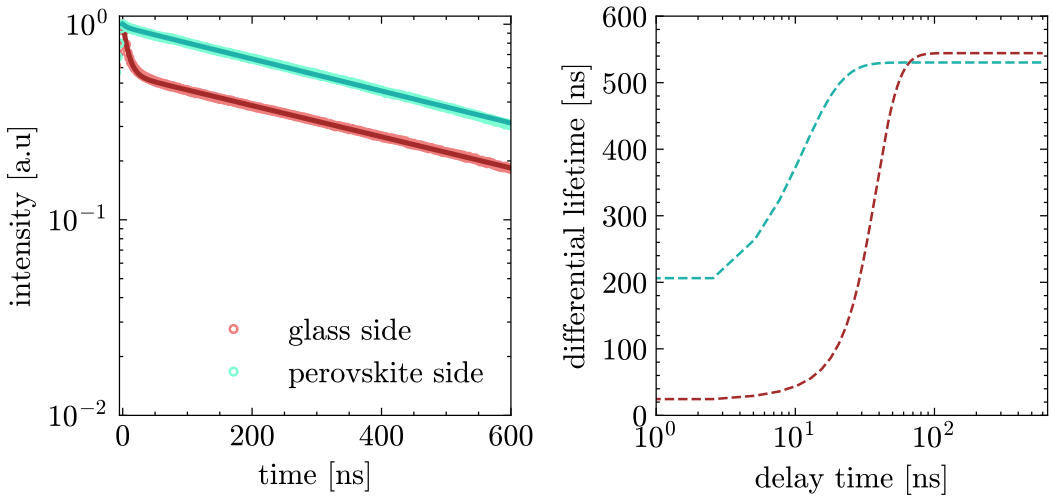

Figure 6.5: Transient PL measurement from two geometries. (left) Transient decay is acquired from illuminating passivated PS (cyan) and GS (brown) illuminating back interface. On the right is the differential lifetime plotted from the fit decay extracted from transients. Laser fluence used for this acquisition is 1.2 nJ/cm^2.

unpassivated perovskite (shown in Figure 4.13) with the transient here, I observe that the initial drop in PL mentioned in Chapter 4 is no longer present. This is because the surface has been passivated, leading to a reduction in non-radiative surface recombination and allowing carriers to recombine radiatively. After calculating the differential lifetime from the fitted data obtained from the transient (plotted on the right side of Figure 6.5), I observe that at a delay time of $t = 0$ ns, a differential lifetime of approximately 200 ns is observed. At longer delay times, the differential lifetime levels off at 530 ns, which I attribute to bulk recombination and which also matches the value from the previous section. I can use this

differential lifetime at delay time $t = 0$ to get an estimate of surface recombination velocity at the passivated surface. Assuming that the distribution of excess charge carrier generation follows Lambert-Beer model and the interface recombination velocity at the back interface of the perovskite/mp-TiO_2 is negligible, I estimate the surface recombination velocity at the passivated PS to be approximately 30 cm/sec, using Equation 4.8. Comparing this value with the surface recombination velocity obtained from the unpassivated surface (240 cm/sec under the same assumption), I can see that the thin layer of the organic molecule has passivated the surface states, resulting in a reduction in the surface recombination velocity translating into longer charge carrier decay. Referring to the illumination from the GS, the transient demonstrates an initial rapid decay within the first 50 ns after the laser pulse, followed by a decay time ($\tau = 540$ ns) associated with bulk and interface at longer delay times. Since the charge carriers Δn are present at a high density at the interface of perovskite/mp-TiO_2 due to illumination geometry and Lambert-Beer model, I can expect electrons to be injected into the TiO_2 layer for delay times $< 100ns$. The differential lifetime plot agrees with the TCAD simulation conducted by Krogmeier [126] where they showed that if the injection is lower than bulk doping, the distinction between the charge extraction mechanism and recombination mechanism becomes clear. Therefore, I attribute the first plateau to the charge transfer process to the delay time from, which is consistent with the simulation by Krogmeier. The slope at which differential lifetime climbs to the second plateau occurs is determined by the charge transfer velocity, thus higher the slope, the faster the transfer [126]. Once the second plateau is reached, it indicates the end of the charge transfer process and the dominance of trap-assisted non-radiative recombination. Since the mp-TiO_2 in our perovskite stack is doped with Li, I can anticipate that the charge carriers will distribute themselves evenly in the TiO_2 layer but eventually come back at the interface or in perovskite as they have nowhere to go.

6.4 Fluence dependent transient PL on surface passivated mixed-halide perovskite

In Chapter 4 I saw how the fluence affects the transient PL when measured on unpassivated perovskite. For a perovskite on charge extraction layer, the interplay of multiple processes such as surface recombination, charge transfer into the extraction layer, interface recombination, SRH bulk recombination as well as Auger and radiative recombination at high fluence is present. Thus it becomes very difficult to analyze and interpret the transient PL for such

a system. The charge carrier dynamics of passivated perovskite were investigated using the

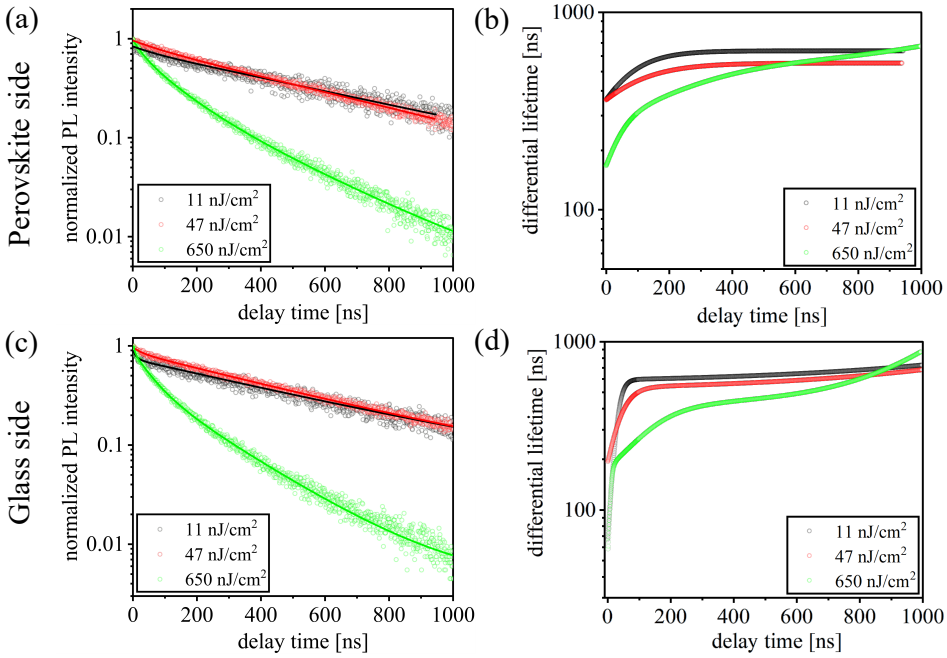

Figure 6.6: Fluence dependent transient PL measurement on passivated perovskite from PS and GS. The three fluence used are 11 nJ/cm^2, 47 nJ/cm^2, 650 nJ/cm^2. (a) Transient PL decay curves acquired when illumination is from PS, fitted using a bi-exponential function for 11 nJ/cm^2, 47 nJ/cm^2 and tri-exponential function for 650 nJ/cm^2. (b) The plot of a differential lifetime for PS transient was calculated from the fit data of (a) using equation 4.7. (c) Transient PL decay curves acquired with illumination from the GS for the same three fluences. (d) The plot of a differential lifetime for GS transient was calculated from the fit data of (c) using equation 4.7

same laser fluences as in Chapter 4 for unpassivated perovskite. Figure 6.6 displays the transient decays and differential lifetime plots. When analyzing the transient on the PS, it can be observed that at fluences of 11 nJ/cm^2 and 47 nJ/cm^2, the decay is nearly mono-exponential, in contrast to the high fluence of 650 nJ/cm^2 which exhibits a higher order decay. The continuous change in slope observed in the transient at this high fluence can be attributed to a higher order recombination mechanism, where the dependence is no longer on Δn but on Δn^2 [238]. The differential lifetime was calculated using equation 4.7 with m=2 for high injection and m=1 for low injection. Independent of the side of illumination, I see a plateau forming at around 600 *ns* which is then close to the value I measured from the imaging setup. Fermi-level splitting values were estimated using equation 4.9 for HLI, assuming an intrinsic carrier concentration on the order of $8 \times 10^4\,\mathrm{cm}^{-3}$ [112]. The estimated value for

low fluence PS illumination, using equation 4.10, comes to be 1.145 eV whereas for HLI, using equation 4.9 comes to be 1.34 eV. It is important to note that although the intrinsic carrier concentration is assumed, the exponential relationship between the quasi-Fermi level splitting and the PL flux, i.e., $\Phi_{PL} \propto \exp \frac{\Delta E_F}{k_B T}$, ensures that the shape of the plot remains unchanged, although the values of x-axis may shift. The shape of the plot indicates the rate at which the quasi-Fermi level comes together after separation, to go back to the equilibrium Fermi-level energy. At a high laser fluence of 650 nJ/cm^2, two inflection points are observed

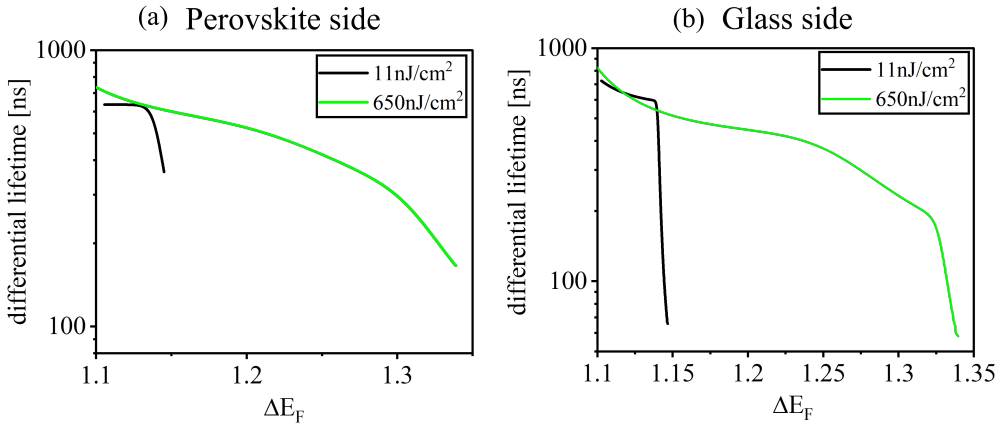

Figure 6.7: Differential lifetime plotted against quasi-fermi level splitting calculated from equation 4.9 for HLI and equation 4.10 for LLI. (a) Illumination from the passivated perovskite side. (b) Illumination from the glass side. Only 11 nJ/cm^2 and 650 nJ/cm^2 fluence is shown

where ΔE_F changes slope, observed in Figure 6.7. Explanation of this first plateau has been attributed to the charge accumulation in the extraction layer [188]. The more the energy offset of the absorber layer and extraction layer, severe the charge accumulation in the extraction layer will take place. As ΔE_F depends on Δn, the change of slope would represent a changing recombination rate. This effect is more distinguishable when illuminated from the GS as the generation of carriers close to the back interface of perovskite/TiO_2 is high. It would be reasonable to take the value of effective lifetime to be the value where differential lifetime saturates at low ΔE_F, i.e. 600 ns consistent with illumination from both sides (PS and GS). This value will change considering the thickness of the extraction layer; the thicker the layer, the longer will it take for an electron to come back into the perovskite provided the band offset is small.

In conclusion, I studied the effect of surface passivating the perovskite on the optical properties of perovskites as well as charge dynamics. The increase of Q_e^{lum} to an order of magnitude and reduction of the surface recombination velocity when compared with the

unpassivated perovskite is proof that a thin layer of passivating molecule provided benefit in improving the absorber layer. In the next section, I will see a different approach to treating the surface of the perovskite using a UV laser.

6.5 Use of laser to combat heterogeneity in perovskite layer

Although countless studies have demonstrated the benefits of chemical passivation, adding yet another solvent-based processing step poses challenges for scalability and reliability. In addition, due to the increasing variety of chemical passivation, there is a lack of agreement on the final result, which may necessitate tailored approaches for each perovskite composition. Recently, attempts have been made to achieve interface passivation of perovskite films without the use of chemicals. For instance, techniques such as adhesive tape peeling and mechanical polishing have been employed to enhance the interfaces with the charge transport layer [239]. Alternatively, near-infrared lasers have been utilized to crystallize perovskite films and microplates or to remove a thin layer of perovskite surface [240, 241, 242, 243]. This promotes the development of more convenient, solvent-free, and high throughput processes using lasers. Since lasers are already employed in various industries for cutting, drilling, annealing, and patterning, their integration into the perovskite field would not require additional infrastructure. In this section, I will explore how lasers have been utilized to enhance perovskite uniformity, utilizing PL imaging and surface-sensitive techniques to analyze the results.

Reminder: The perovskite under study in the next section has been grown and treated by *Kedia et. al.*[130] and I received the sample in a nitrogen-filled bag. I used the PL imaging setup to study the effect of laser treatment and image the homogeneity of Spiro-OMeTAD coverage before and after laser treatment.

6.5.1 Photoluminescence Imaging on laser polished CsFAMA perovskite

The perovskite under investigation is a CsMAFA perovskite that consists of three cations. To polish the top surface of the perovskite, a pulsed UV laser with a wavelength of 355 nm was employed. The laser was moved in a raster pattern along the XY direction. Following the treatment, the sample was sealed in a N_2 bag and sent to me for PL imaging and AFM/KPFM analysis to examine changes in the WF and morphology. It is crucial to carefully control the energy of the laser pulses to prevent any damage to the perovskite absorber. Given the high absorption coefficient of perovskite thin films in the UV region, it is expected that the laser will penetrate the material to a depth of a few tens of nanometers. This laser treatment

has the potential to alter the surface morphology. Laser-based post-treatment processes on materials are traditionally categorized based on their effects on the material surface, which include ablation (removal of material above the surface roughness), recrystallization (redistribution of material through melting of the removed material to form a new surface), and polishing (smoothing within the surface depth profile). This study aims to investigate the impact of laser polishing on the optical properties of the perovskite.

To see if the laser polishing has enhanced the uniformity of perovskite, I acquired images from our imaging setup. Figure 6.8 shows the PL imaging results of the unpolished and laser-polished perovskite on glass. From the map of the PL peak position, there is a small redshift

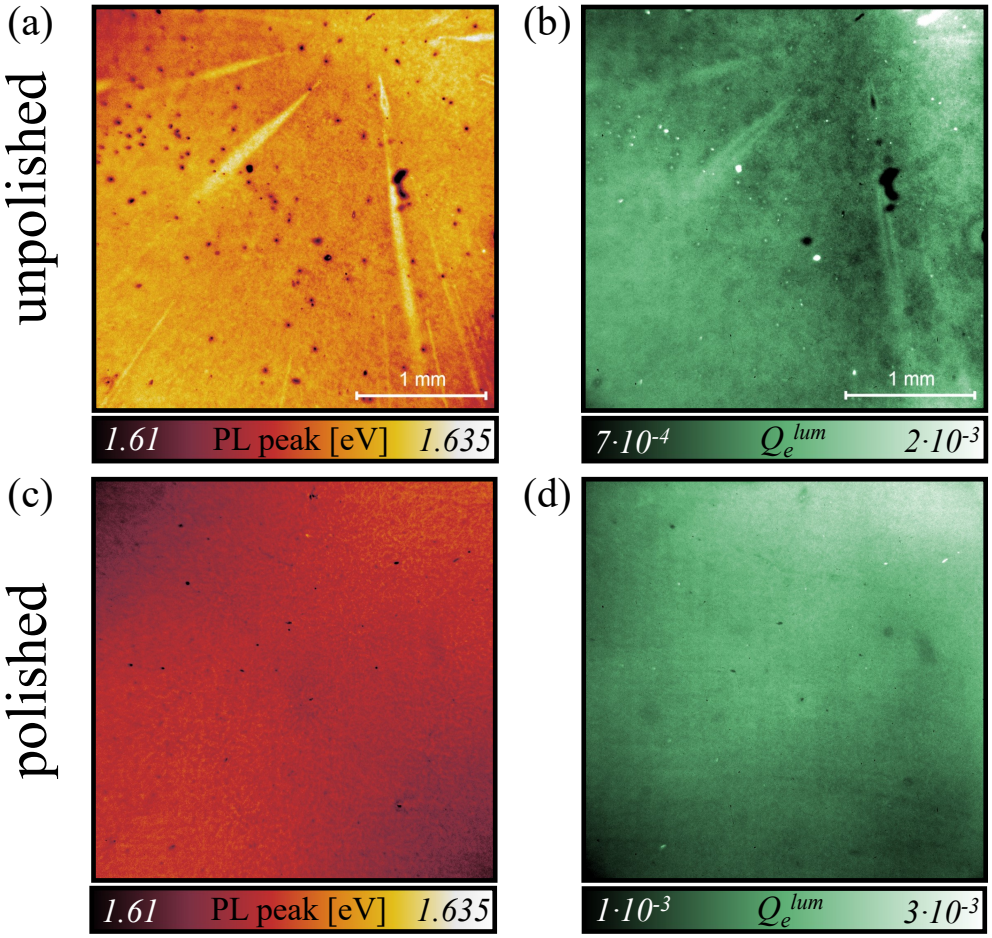

Figure 6.8: PL imaging result of triple cation perovskite. (a,c) Map of PL peak position of unpolished and laser-polished perovskite. (b,d) Q_e^{lum} map of unpolished and laser polished sample obtained by integrating single pixel PL spectrum and dividing by injection value.

of average of $\approx 10\ nm$ after laser treatment which was difficult to observe on the average PL spectrum. In the unpolished case, I observe some variation of the PL peak position from the average value of 1.63 eV. The extended bright features are known to be a consequence of the spin coating process [244] and are possibly perovskite with different compositions or

phases. Because of the absence of EDX measurement in this region, I cannot be sure of different compositions or phases but it's the likely scenario. The literature mentions that the presence of inhomogeneities in the form of ions is influenced not only by phase segregation but also by the preparation process and solution concentration [245, 246, 247]. Fedeli et al. [245] and Sadhanala et al. [246] demonstrated that mixed halide perovskites may not exhibit homogeneous halide distribution after preparation, and this strongly depends on the halide ratio in the solution. Regions with a higher iodine content tend to emit at lower energy sites, while regions with a higher bromine content shift towards higher energy. Although it is challenging to observe such iodine or bromine phases due to their large size in my case, it is not impossible. From the XPS analysis conducted by Kedia et al. (who grew and provided the sample), the unpolished perovskite showed a high Br/Pb ratio (0.96) which was two times higher than in the perovskite precursor mix (0.51). This means that the surface is bromine rich and no wonder a slight high energy PL peak position is observed. After laser polishing, this ratio goes down to (0.46), much closer to the precursor mix. Large crystal particles, or intermediate crystal phases, from the precursor solution, can remain on the surface even after the spin coating and annealing process, and their low emission peak suggests that they are likely iodine-based. Rehermann [248] extensively investigated this heterogeneity using an in situ setup to study the formation process of mixed halide perovskites during spin coating and thermal annealing. In Figure 6.9, the bright dots, which are encircled in blue, exhibit a peak

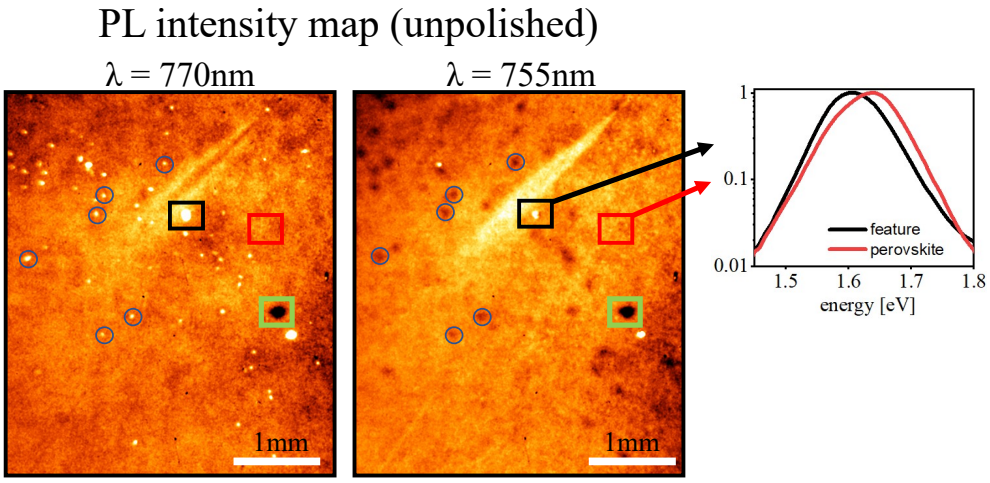

Figure 6.9: PL image taken at two wavelengths, 770 nm and 755 nm highlighting inhomogeneities in the form of bright spots at 770 nm that turn dark at 755 nm. Outset shows the PL spectrum of one of the bright spots (black) plotted together with the perovskite region.

at a wavelength of 770 nm, while the surrounding perovskite peaks at 760 nm. To illustrate the distinction, I have plotted the PL spectrum of a specific feature in a black rectangle,

along with the neighboring clean perovskite, and observed a shift of 10nm in the PL peak position (as shown in the outset of Figure 6.9). Although the PL peak position map in Figure 6.8(a) for the unpolished sample reveals a darker contrast for these dots (indicating a lower PL peak energy of 1.60 eV), it is important to note that not all of them possess the same characteristics. There are other dark spots with weaker luminescence signals (indicated by the green box), which can be attributed to the poor quality of the perovskite in that region. Despite exhibiting the PL peak position of the average perovskite, the luminescence in this dark region is significantly weaker, suggesting a poor quality of perovskite.

The average Q_e^{lum} exhibits a slight increase after laser polishing, indicating that the laser treatment has modified the top surface of the perovskite by reducing surface defects. By scanning the surface, the UV laser locally heats the region, thereby modifying the surface and the near-surface layer of the perovskite. This heat is utilized by the inhomogeneities present on the surface to recrystallize into the perovskite matrix. Consequently, the perovskite luminescence becomes uniform, without any noticeable bright or dark features, following laser polishing. Although there is a slight shift in the PL peak to lower energy after laser polishing, the small increase in Q_e^{lum} will result in a small increase in μ_{qfls}. By considering the measured PL peak position of 1.63 eV for both the unpolished and polished samples (ignoring the small shift), along with their respective average Q_e^{lum} values of 9×10^{-4} and 2×10^{-3}, I observe a small increase in μ_{qfls} of approximately 20 meV. It is important to note that, although the values are not significantly larger, the main objective of treating the surface with the laser is to reduce the inhomogeneities, thereby enabling the uniform deposition of the HTL with reduced interface defects and facilitating efficient hole transport mechanism. Hence, I will compare the PL images of the unpolished and polished samples after depositing the Spiro-OMeTAD layer on top.

6.5.2 Effect of Spiro-OMeTAD deposition on untreated and laser-treated perovskite

Laser treating the triple cation perovskite indeed improved the surface of the perovskite. But the question is, how does this affect the deposition of the Spiro-OMeTAD layer which goes on the top of it? I observe that on the unpolished sample, the deposited Spiro-OMeTAD shows a lot of inhomogeneity in the form of dark and bright dots with PL peak position significantly shifted to lower energy. Figure 6.10 shows the PL peak position map of unpolished and polished perovskite after the Spiro-OMeTAD layer was deposited. I observe that on unpolished perovskite the Spiro-OMeTAD deposition is very inhomogeneous and it

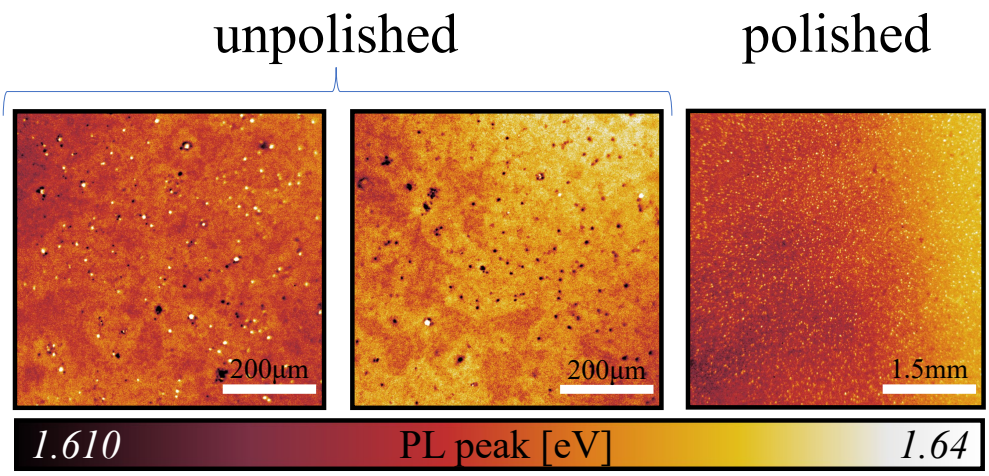

Figure 6.10: Map of PL peak position variation for unpolished and polished perovskite after deposition of Spiro-OMeTAD. The two maps for unpolished are taken on the same sample but on different regions

reacts with the surface perovskite. The two PL peak position maps of the unpolished sample show coverage of features showing either a shift towards high energy or low energy. If I look at the left image, some bright dots features have a peak position at 1.65 eV whereas the same measurement is taken on the same sample but at different regions revealing that there are dark dots present on the surface that have a PL peak position at 1.61 eV. Such heterogeneity of Spiro-OMeTAD deposition on untreated perovskite surface may cause inefficiency in hole transport. Considering the measured average PL peak position of the region to be 1.63 ± 0.01 eV, these feature shows a discrepancy of 20 meV from the average on either side which is significant. Such a fluctuation in the PL peak position can affect the open-circuit voltage as shown by Rau et al. [109]. The fact that on the same sample, two inhomogeneous regions and features exist calls for the need to treat the surface as well as optimize the Spiro-OMeTAD deposition mechanism. After laser polishing the surface, the PL peak position shows heavy coverage of bright dots on the surface which is most likely Spiro-OMeTAD, showing the peak position of 1.64 eV (bright dots). Considering that the average PL peak position of perovskite itself is 1.63 eV the discrepancy here is only 10 meV. But, the Spiro-OMeTAD looks uniformly covered on the perovskite. This proves the effect of laser polishing the surface of the perovskite for better coverage of the Spiro-OMeTAD layer as compared to unpolished perovskite. The next question in terms of optical properties is how stable is the polished perovskite under continuous laser illumination as photo-induced halide segregation is well known in mixed halide perovskites and does the surface or the perovskite morphology change due to light-induced degradation? To answer this I illuminate

the unpolished and polished perovskite sample under 532 nm laser for 8 hours and track the luminescence signal.

6.5.3 Stability check of perovskite before and after laser polishing

The stability of the perovskite absorber layer is a crucial requirement for the long-term viability and commercialization of solar cells. A study on metal halide perovskite solar cells demonstrated that encapsulated MAPI thin films could withstand 1000 hours of AM1.5 irradiation without any noticeable degradation, as confirmed by absorption spectra analysis [249]. Numerous other studies have also shown stability over extended periods of light exposure. However, it is important to note that the absence of observable changes in the solar cell's photocurrent and absorption does not necessarily imply the absence of photo-induced changes. Several studies have focused on investigating the degradation or changes in perovskite films caused by light [250, 35, 251, 252]. It is worth mentioning that photo-induced changes are not always detrimental for thin-film materials. For instance, in CIGS solar cells, light soaking induces metastable defect reactions with the generated charge carriers, leading to improvements in open circuit voltage, fill factor, and conductivity [253, 254]. Similar effects have also been reported in perovskite solar cells [250, 251]. A comprehensive discussion on the photo-induced changes and their effect on the stability of perovskite solar cells is reported in Boyd et al. [255]. In this study, a low-energy UV laser was used to polish the perovskite, but it only treated or modified the top surface. Therefore, I aim to investigate whether this treatment affects the perovskite bulk as well in terms of luminescence under continuous illumination of a 532nm laser. Initially, the unpolished perovskite was illuminated for 8 hours continuously, and luminescence images were captured every hour. This experimental setup allowed us to observe the state of the perovskite under constant laser exposure. Figure 6.11(a) presents the PL intensity image taken at time $t = 0$ and at $t = 8$ hours. The sample was kept in a nitrogen-filled PL box during the measurements to avoid oxygen + light-induced heterogeneity. Overall, a decrease in the average intensity was observed, dropping from 15000 to 6000 units, indicating that the perovskite is undergoing degradation due to constant laser exposure. The unpolished perovskite initially showed some dark features in the PL image, some of them are pinholes marked by blue circles, but after 8 hr of exposure to the laser, the optical morphology seems to have changed. I observe bright dots spread all over the sample caused by photo-induced effect, a bright ring formed around the pinhole marked by a blue rectangle, and a few bright dots that stayed the same as seen from the PL image at $t = 0$, indicating that these are reflection coming off a residue

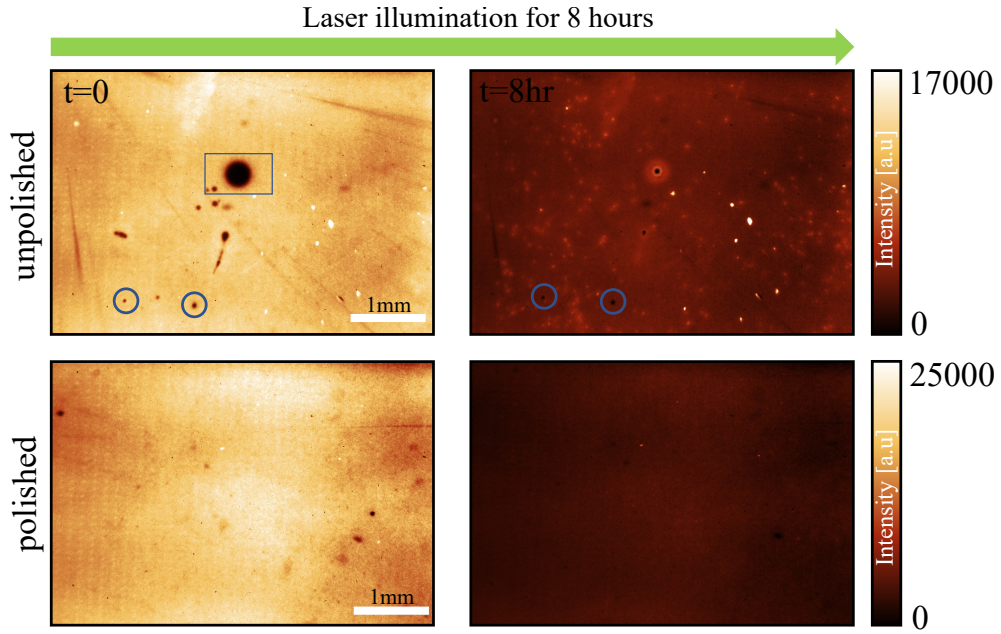

Figure 6.11: PL degradation study of unpolished and laser polished sample when exposed continuously for 8 hr by 532 nm laser. PL intensity map of unpolished perovskite (top row) at time $t = 0$ on the left and after $t = 8$ hours on the right (bottom row). Blue circles enclosed pinholes. PL intensity image of polished perovskite at time $t = 0$ on the left and $t = 8$ hours on the right. The color bar unit is arbitrary indicating the background subtracted intensity signal detected by the sensor.

present on the surface. On the other hand, if I compare the PL image in Figure 6.11(b) at $t = 0$ and $t = 8$ hours, I see that polished perovskite has uniform luminescence. Even though the bulk is the same for both the perovskite, the surface treatment has improved the uniformity. Nevertheless, the average intensity for polished perovskite drops from 22000 to 9000 units which is a drop of approximately 61% as compared to 60% for unpolished. This means that the rate of degradation is the same for both the unpolished and polished samples under constant laser light. Interestingly, the evolution of the dark spot and the luminescence increase around it caught my attention. Figure 6.12 highlights the dark circular spot that I observe in the PL image of Figure 6.11(a) with the line profile plotted through this spot at $t = 0$ and $t = 8$ hours. From the line profile, I see that this dark spot consists of a dark core which I attribute to a pinhole, and poor perovskite around it. The perovskite in the region around the dark core has a level of luminescence intensity very close to the one measured after 8 hours. This means that the perovskite surrounding the pinhole had a very slow rate of degradation. In fact, after 8 hours of light illumination, the region surrounding the dark core showed an increase in luminescence. This suggests that the quality of perovskite

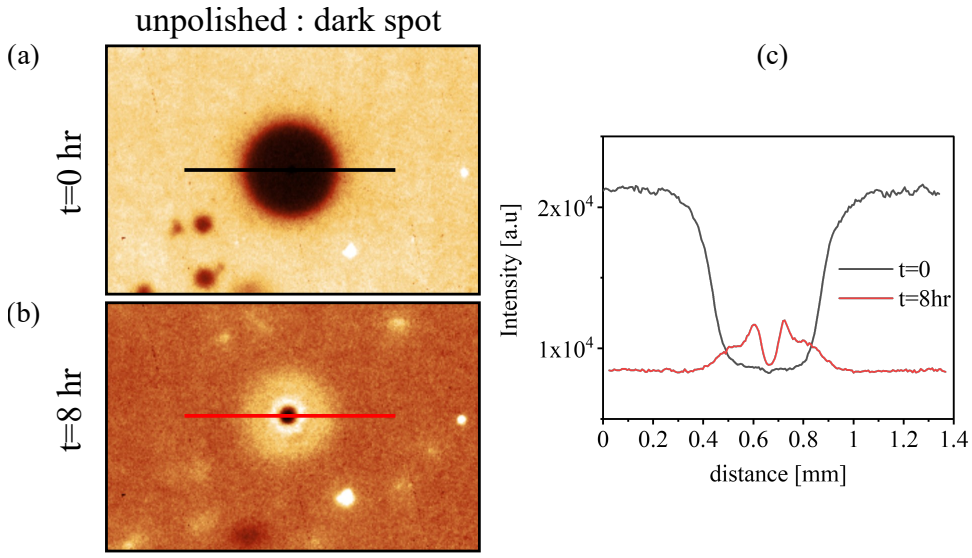

Figure 6.12: Quasi steady-state PL image of dark region observed on unpolished CsFAMA perovskite. (a) PL image at $t = 0\ hr$, (b) PL image at $t = 8\ hrs$ of continuous laser (532nm) illumination. (c) The line profile is drawn across the dark region on images (a) and (b).

here is either bad from the beginning (after processing/growth) or the presence of a dark core acted as a degradation catalyst. Light-induced effects are well known in the perovskite community, processes such as ion-distribution, halide segregation, and cation segregation are possible and discussed in Boyd et al. [255]. Careful interpretation of the line profile shows that the luminescence signal around the pinhole has increased by 17% after 8 hours of laser exposure. Such heterogeneities are not seen on polished samples because of laser scanning and local heat from laser curing the surface. One needs to be careful that laser treatment will not get rid of pinhole as pinhole is a simple absence of perovskite exposing the underlying layer. A small model that explains the two types of pinhole that I see on unpolished perovskite is shown in figure 6.13.

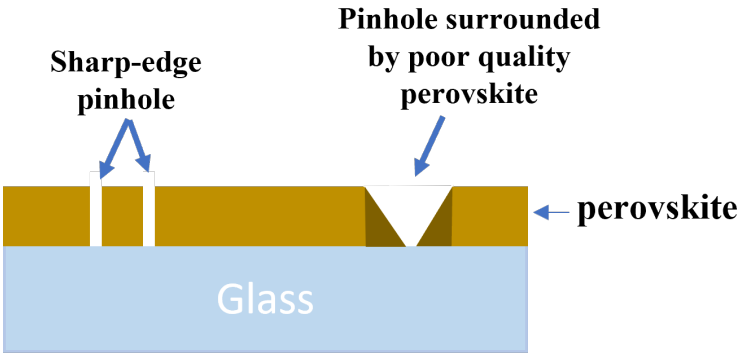

Figure 6.13: Model highlighting type of pin-hole at large scale observed on unpolished perovskite

6.5.4 Effect of laser polishing on perovskite surface revealed via AFM/KPFM

The impact of laser polishing is primarily observed on the surface, while the bulk of the material remains not significantly affected. To assess any changes in the electrical properties of the surface, Atomic Force Microscopy (AFM) and Kelvin Probe Force Microscopy (KPFM) measurements were conducted in a nitrogen environment to avoid exposure to air. The topography was obtained using Amplitude Modulation (AM), while the KPFM signal was acquired using Frequency Modulation. A HOPG (graphite) with the WF of $4.6eV$ was utilized to calibrate the WF of the tip, which facilitated the determination of the perovskite's surface WF based on the contact potential difference value using the equation [139],

$$V_{CPD} = \frac{\phi_{sample} - \phi_{tip}}{e} \tag{6.2}$$

Figure 6.14(a),(b) depicts the AFM topography of the unpolished and laser-polished perovskite surface. Laser polishing reduced the root-mean-square roughness value from 33 nm

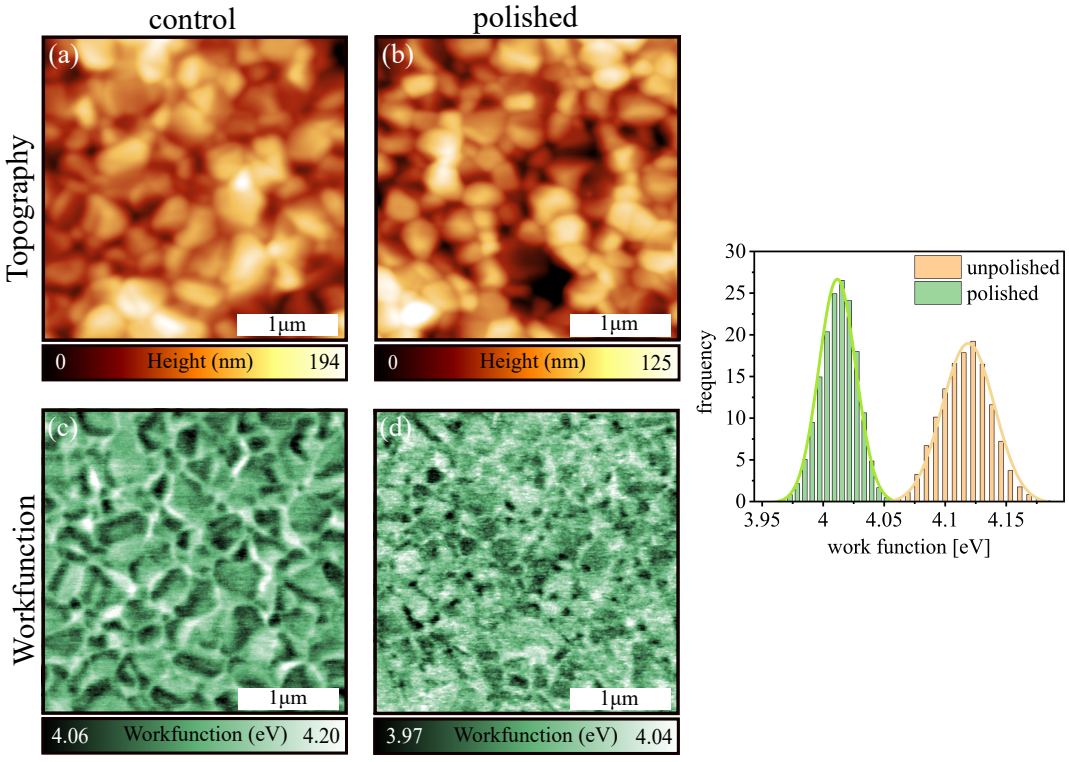

Figure 6.14: AFM/KPFM measurements on unpolished and laser polished sample to understand the effect of laser on WF. (a,b) Topography map of unpolished and polished samples respectively showing grains and grain boundaries. (c,d) WF map measured simultaneously with topography data showing a decrease in the WF after treatment. On the right is the distribution of WF for the two perovskites.

to 24 nm. Two scenarios can occur when polishing with laser; first, the laser energy can

be absorbed by the perovskite and the heat from it can facilitate the recrystallization of the residues present on the surface or second the laser etch away a very thin layer from the top of the perovskite thus revealing the fresh layer free from residues. If the latter is true, then thickness reduction would be observed which in this case was within the error bar limit [130]. From topography, the average grain size remained unchanged in both unpolished and polished perovskite. Simultaneous KPFM measurements, as shown in Figure 6.14(c),(d), revealed that the average WF after laser polishing decreased by 130 meV. Moreover, the Full Width at Half Maximum (FWHM) of the WF distribution decreased from 50 meV for the unpolished surface to 35 meV for the polished surface, indicating that the homogenization of the WF across the sample was a result of laser polishing. This homogeneous WF then helps the HTL to bind with the perovskite surface with reduced non-radiative recombination regions.

Everything I discussed above for the laser polishing benefits comes under the category that the UV laser is either recrystallizing the surface residues or removing a very thin layer of the surface. Additionally what laser can also do is ablation (means removal of material) where continuous line scanning of the perovskite by sufficiently controlled laser power removes layer thus reducing the thickness. This then pushes towards the direction of using a laser to achieve the desired thickness which traditionally is achieved by playing with spin coating parameters. Thus in the next short section, I will show how laser ablation affects the optoelectronic property or CsMAFA perovskite when compared with spin coated sample.

6.6 Effect of laser ablation on photoluminescence of CsMAFA perovskite

Reminder: The perovskite under study in this section has been grown and laser ablated at the Institute for Photovoltaics at the University of Stuttgart. I received the sample in the nitrogen-filled bag to avoid exposure to air and moisture.

I used our PL imaging setup to study the optical response of the CsMAFA perovskite whose thickness was reduced using laser ablation. The laser used for ablation is the same as that used for polishing but with a slightly higher power. Two perovskite samples, both with a thickness of 200 nm but one was spin-coated whereas the other was laser ablated. To be clear, initially, the sample was spin-coated to 450 nm and then the laser was used to remove two layers down to the thickness of 200 nm. Figure 6.15 shows PL imaging measurements of the spin-coated vs laser-ablated perovskite. The thickness of spin-coated

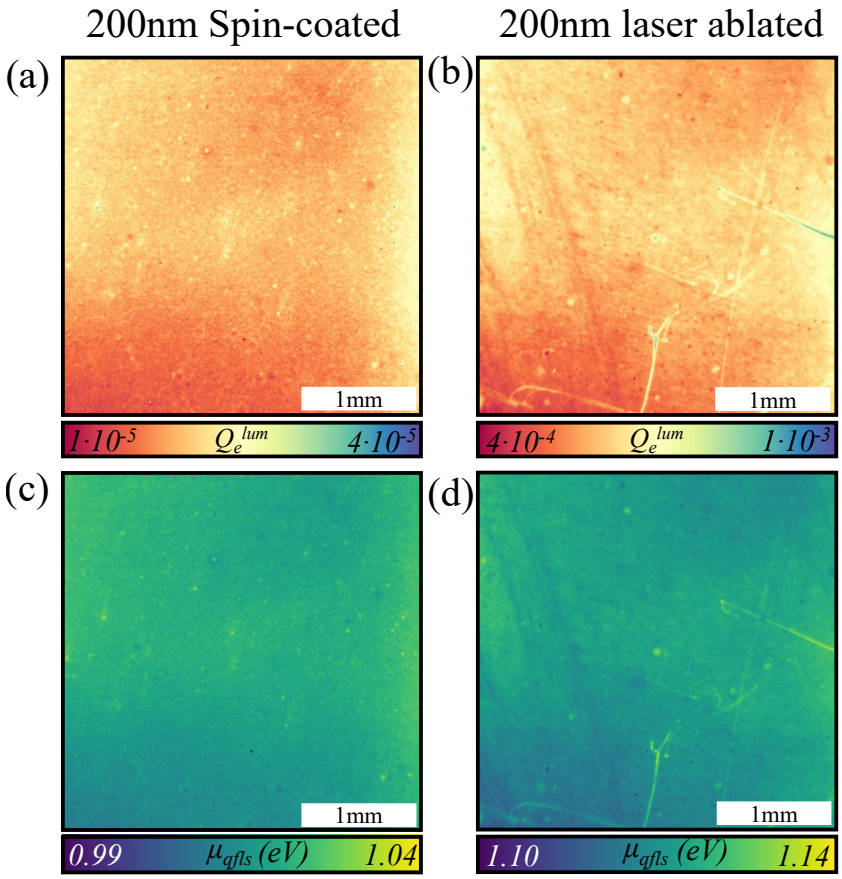

Figure 6.15: PL imaging of 200 nm thick spin coated and laser ablated perovskite. (a) Map of Q_e^{lum} with an average value of 2×10^{-5} for spin-coated perovskite. (b) Map of Q_e^{lum} with an average value of 5.5×10^{-4} for laser ablated perovskite. (c) Map of μ_{qfls} constructed using PL peak position of 1.64 eV and the Q_e^{lum} values from the map. The average μ_{qfls} of 1.02 eV was measured. (d) Map of μ_{qfls} constructed using PL peak position of 1.65 eV and the Q_e^{lum} values from the map. The average μ_{qfls} of 1.125 eV was measured for laser ablates perovskite.

perovskite (200 nm) is achieved by changing the molar concentration of the solution and the thickness of laser ablated sample was achieved by scanning line by line using laser removing layer by layer till 200 nm thickness was reached. I observe an improvement in the Q_e^{lum} by one order of magnitude when measured under the same illumination. This shows that using a laser to tune the thickness has its benefits as compared to the spin coating. From the average PL spectrum, both the samples showed a peak position at 1.64 ± 0.01 eV. Using this peak position and the measured Q_e^{lum}, I calculated the μ_{qfls} using equation 3.7 of 1.02 eV for spin-coated perovskite and 1.125 eV for laser ablated perovskite.

This study is fairly new and concrete conclusions are yet to be made in support of the data measured from other techniques. However, using the power of PL imaging, I can

for sure conclude that the use of laser polishing or ablation is beneficial in improving the optoelectronic properties of the perovskite at least for the thickness reduction up to 200 nm. Application of laser on a light absorbing material such as perovskite will for sure have some changes taking place on the very surface as well as in the bulk with some optimization. There will be a threshold up to which laser can be used to scrap away the layers and too-thin perovskite layers may enter the realm of quantum confinement. This is something yet to be understood in the present system.

6.7 Conclusion

To conclude this chapter, I recognized the importance of surface treatments using chemical passivation as well as polishing the surface by UV laser. Chemical passivation with an organic molecule significantly boosted the PL quantum yield by almost tenfold as compared to when the surface was not passivated. This provided proof of passivation working. Not only increase in PL quantum yield but the surface recombination velocity was reduced as evidenced by our transient PL measurements. I used our PL imaging setup to plot the average PL spectrum as well as construct a map of Q_e^{lum} revealing spatial variation. By employing confocal microscopy, secondary electron imaging, and Energy-Dispersive X-ray Spectroscopy (EDX), the passivated FAPIBr sample has been thoroughly examined, leading to valuable insights regarding its surface morphology and chemical composition. The optical image displays a pattern of dark dots scattered throughout the sample. Upon closer examination using secondary electron imaging, these dots exhibit different contrasts, appearing either bright or dark. This variation, combined with the presence of non-crystallized characteristics on top of the perovskite matrix, indicates an uneven surface. Moreover, the detection of varying levels of bromine (Br) and tin (Sn) in different features suggests inconsistencies in the thickness of the perovskite layer. The sensitivity of the EDX map is demonstrated by its ability to detect sulfur on the surface, even though the passivation layer is very thin (1-2nm). This indicates the presence of a passivator compound that contains sulfur. The passivation layer exhibits a stripe pattern, where the hills have a higher concentration of sulfur compared to the valleys. This suggests that the passivation process may selectively reduce surface defects in the elevated regions, which may be related to the areas of higher photoluminescence (PL). Our Low injection and High injection dependent transient measurement on the surface passivated perovskite showed insight into the charge transfer and charge accumulation process. The initial fast decay that I observe at low injection when laser illuminated from the GS shows a clear distinction between the charge transfer process and the non-radiative recombination

mechanism. Whereas the low injection PS illumination reveals the effect of passivating the surface traps and defects by lowering the surface recombination velocity when compared to the unpassivated sample. Under high-level injection, I observe high-order recombination such as radiative and auger becoming dominant and reducing the PL. With few assumptions and estimation, I calculated the quasi-fermi level splitting plotted against differential lifetime that showed the rate at the quasi-fermi level closes towards equilibrium and the change of this rate correlates with the recombination rate of the generated charge carriers. At high quasi-fermi level splitting, the change of slope I observe under high injection is attributed to the charge accumulation at the interface of the perovskite/TiO_2 layer which is more pronounced when illuminated from the GS as compared to the PS. Apart from the chemical passivation method, I also studied CsMAFA perovskite whose surface was polished using a UV laser. PL imaging revealed features present on unpolished perovskites showing variation in the PL peak position in both high and low energy directions. Such inhomogeneity was cured using laser polishing. As the aim of laser polishing is to cure the surface for the coming Spiro-OMeTAD layer, I checked the coverage of this layer by PL imaging setup. I showed that Spiro-OMeTAD is very non-uniform on the unpolished sample and reacts with the surface residues to form bright and dark dots with varying PL peak positions. Dark dots present on the surface have a PL peak position at 1.61 eV whereas the bright dots have a PL peak position at 1.65 eV, The average PL peak position of the sample is 1.63 eV. After polishing the surface of perovskite with laser and then depositing Spiro-OMeTAD, the coverage has improved significantly with reduced discrepancy in the PL peak position. Then the stability of the perovskite under light illumination was studied using the PL imaging setup where the unpolished and polished sample was illuminated by a 532nm laser for 8 hours continuously and capturing PL intensity images every 1 hour. Images revealed that no emergence of bright or dark features occurs after laser polishing which is not true for the unpolished perovskite. In the end, I used a surface-sensitive technique (AFM/KPFM) to reveal the change in the WF of the surface after laser polishing. I observed a decrease in the RMS roughness from 33 nm to 24 nm evident from the AFM topography maps and reduced WF by 130 meV after laser treatment.

Chapter 7

Summary

Here, I summarize the thesis with key findings and conclusions. Later on, I will give an idea of the next research focus that could follow the work.

7.1 Overall summary

Most of the work in this thesis is based on the characterization of perovskite thin film using a hyperspectral PL imaging system. The custom build setup is a powerful technique allowing large-length scale measurements of the sample under uniform illumination. I talked about the essential components of the imaging system and how they play a role in the measurement process. The methodology for calibrating the system spectrally and to absolute photon number was defined to have quantitative data extraction from the sample used for the study. I then used this PL imaging system to study a state-of-the-art mixed halide perovskite on the electron transport layer. The goal was to understand the optical response improvement of the mixed halide perovskite when its surface is unpassivated (Chapter 4) vs when the surface was passivated using a thin layer of organic molecule ligand (Chapter 5). I observed that the PL quantum yield (Q_e^{lum}) of the perovskite under 0.68 sun uniform illumination of $532nm$ wavelength laser was improved after passivation. One benefit of the imaging measurement is that you can observe the lateral changes or variations from the spectrally resolved images of the perovskite. I saw how the unpassivated sample consist of a lot of inhomogeneities on the surface in the form of microcrystal clusters, degraded perovskite, and chemical dust that shows variation in the luminescence intensity. After passivation, most of these inhomogeneities were reduced evident from Q_e^{lum} map of passivated perovskite. Another interesting observation was that due to the electron transport layer being spin-coated followed by perovskite spin coating, the stripe features were observed on both the passivated as well as

unpassivated samples. I discussed the origin and its effect on the luminescence properties in Chapter 5. As the perovskite is in contact with the electron transport layer, the dynamics of the charge carrier are complicated to define due to phenomena such as charge extraction, charge accumulation, and interface recombination. I used the rapid shutter and gating speed ability of the PL imaging system for transient PL imaging measurement where I could image the perovskite at any desired timescale after the laser pulse, thus visualizing the decay dynamics. I used low-level injection illumination to measure the transient of the unpassivated and passivated perovskite to study the effect of charge extraction. I measured using two geometries, illumination from the perovskite side and glass side that allowed me to distinguish the surface recombination mechanism from charge extraction and interface recombination mechanism. I also measured fluence-dependent transient on this perovskite which helped me in recognizing the charge accumulation process at the interface of the perovskiteTiO_2 layer. Passivation not only improved the Q_e^{lum} but also reduced the surface recombination velocity as I saw from the transient PL measurement.

A detailed study of the striped pattern that I observe in the optical image as well as the PL image of the perovskite is presented in Chapter 5. I studied the morphology of the perovskite surface as well as the mesoporous-TiO_2 surface using a profilometer. I observed that the hill and valley exhibit different PL decay. I used the 2D-FFT frequency isolation and masking method to separate the transient data of hills and valleys to have a noise-free average decay profile in those two regions. I found that they have a difference in differential lifetime at low delay time which later saturates to the non-radiative bulk recombination. The observation of the hills and valleys for low delay time in transient PL image after pulse laser excitation indicates the process generated electrons being transported to the extraction layer.

I dedicated Chapter 6 to the study of enhancing the uniformity as well as optoelectronic properties of the perovskite by chemical method i.e. surface passivation by organic molecule and laser polished surface of the perovskite. The perovskite that went under passivation was the mixed halide perovskite (MAFA) whereas for laser polishing the perovskite was tripecation halide perovskite (CsMAFA). Using our PL imaging system I showed how the two strategies worked in providing uniformity and reducing the inhomogeneities from the surface. I also discussed, in short, an ongoing study where a laser was used to ablate the layer of the perovskite to bring down its thickness from $450nm$ to $200nm$. I observed an increase in the Q_e^{lum} when the laser was used to reach the thickness of 200nm against the spin-coating method. This provides a new way to manipulate the thickness of the perovskite thin film

while at the same time curing the surface.

7.2 What more can be done?

My next interest is to learn TCAD simulation to obtain accurate derived parameters for the transient data presented in this thesis. This will greatly enhance my understanding of the extraction and recombination mechanism. Additionally, the PL imaging setup now includes a green LED with a wide beam, which, once calibrated, can deploy 1sun illumination. By using this setup on perovskite devices with contacts, I can measure the quantum efficiency as a function of bias voltage, similar to the work done by Wagner [169]. I also have a 100x objective lens that enables the resolution of features in the tens of micrometers range for PL measurement. Although achieving a stable focus has been a technical challenge so far, it is expected to be possible in the future, allowing for the continuation of inhomogeneity studies on a sub-micrometer scale. This will also help direct the correlation of the PL spatial maps with the chemical distribution map as they will be more or less on the same length scale. Furthermore, I am highly interested in collaborating with the University of Stuttgart to further explore the use of a UV laser to modulate thickness and see if it helps in pushing the efficiency of the PSC further or improving some aspects of the absorber layer when compared to absorber grown by spin coating process.

Appendix A

Appendix Chapter 3

A.1 Derivation of analytical equation for quasi-fermi level splitting

An equation that relates the externally emitted PL yield (Y_{PL}) to the absorptivity $a(E)$ and μ_{qfls} within the sample was introduced by Würfel [156],

$$Y_{PL}(E) = \frac{2\pi}{h^3c^2}\frac{a(E)E^2}{\exp\left(\frac{E-\mu_{qfls}}{kT}\right)-1} \approx g\frac{a(E)E^2}{\exp\left(\frac{E}{kT}\right)-1}\exp\left(\frac{\mu_{qfls}}{kT}\right)$$

where T is the temperature of the photoexcited charge carriers which is assumed to be in thermal equilibrium with the lattice, c is the speed of light and h is the Plank's constant. g is the constant given by $\frac{2\pi}{h^3c^2}$.

Ross [114] proposed the prediction of open-circuit voltage by subtracting the non-radiative losses given by Q_e^{lum} from the radiative limited voltage by equation,

$$\mu_{qfls} = \mu_{qfls}^{rad} + kT \cdot \ln Q_e^{lum}$$

where μ_{qfls}^{rad} is the quasi-fermi-level splitting if only radiative recombination occurs. We start with the Plank's generalized law. External quantum efficiency under white light condition is expressed as,

$$Q_e^{lum} = \frac{\int_0^\infty Y_{PL}(E)dE}{\int_0^\infty \phi_S(E)a(E)dE} = \frac{g}{\phi_{abs}(E)} \cdot \int_0^\infty \frac{E^2a(E)dE}{\exp\left(\frac{E-\mu_{qfls}}{k_BT}\right)-1}$$

where ϕ_S is the sun spectrum and $\phi_{abs}(E)$ is the absorbed number of photons. Using Boltzmann approximation, the above equation can be rearranged to solve for μ_{qfls},

$$\mu_{\text{qfls}} = kT\ln Q_e^{lum} - kT\ln\left(\frac{g}{\phi_{\text{abs}}}\int_0^\infty \frac{E^2a(E)}{\exp\left(\frac{E}{k_BT}\right)}dE\right)$$

In ideal case, the absorptivity $a(E)$ can be expressed as a high energy side step function at the bandgap, which allows to solve the above equation analytically [256, 50] to give,

$$\mu_{qfls} \approx E_g - kT \cdot ln(kT \cdot g \cdot \frac{E_g^2}{\phi_{abs}}) + kT \cdot ln(Q_e^{lum}) \tag{A.1}$$

This equation contains the bandgap E_g of the material which can be measured by taking the PL spectrum. The peak position of the PL spectrum is used as bandgap as for perovskite material the absorption edge is very close to the PL peak position. Equation A.1 is the one used in the python script to generate the μ_{qfls} map what I showed in the thesis. I used the PL peak position that I measured from the average PL measurement and the Q_e^{lum} calculated by knowing the number of incident photons.

A.2 Hyperspectral data cube methodology

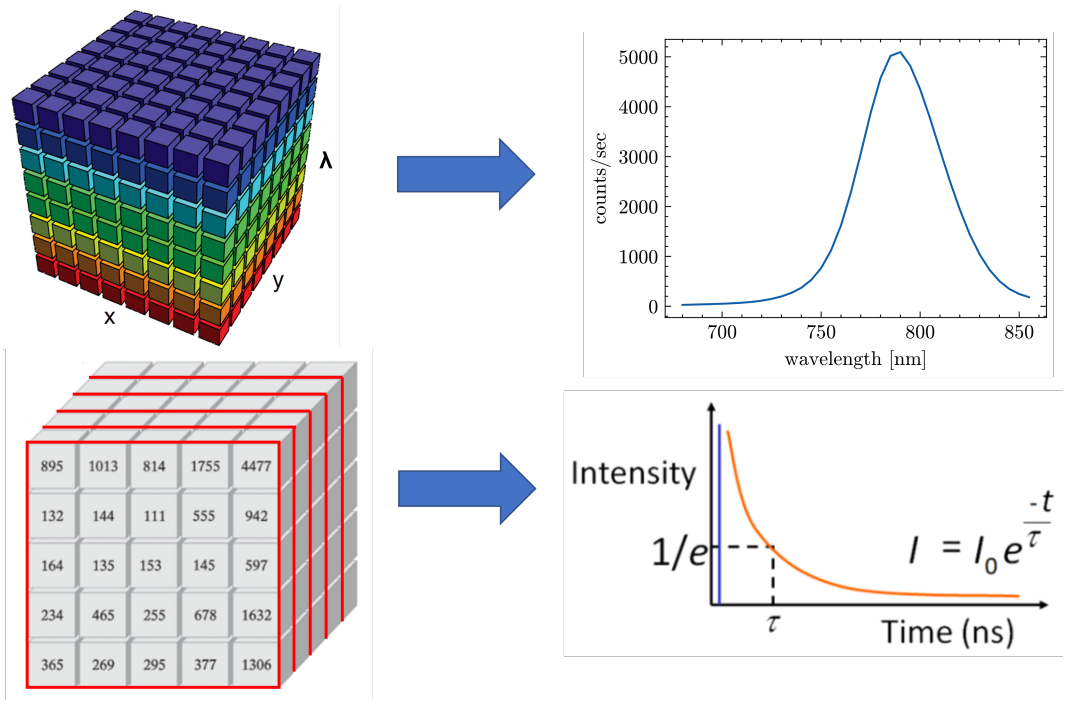

Figure A.1: Hyperspectral data cube generated by the PL imaging setup as a result of a measurement. It then requires external processing to be able to analyze the PL data for steady state as well as time-resolved.

Appendix B

Appendix Chapter 4

B.1 Optical microscope image of perovskite

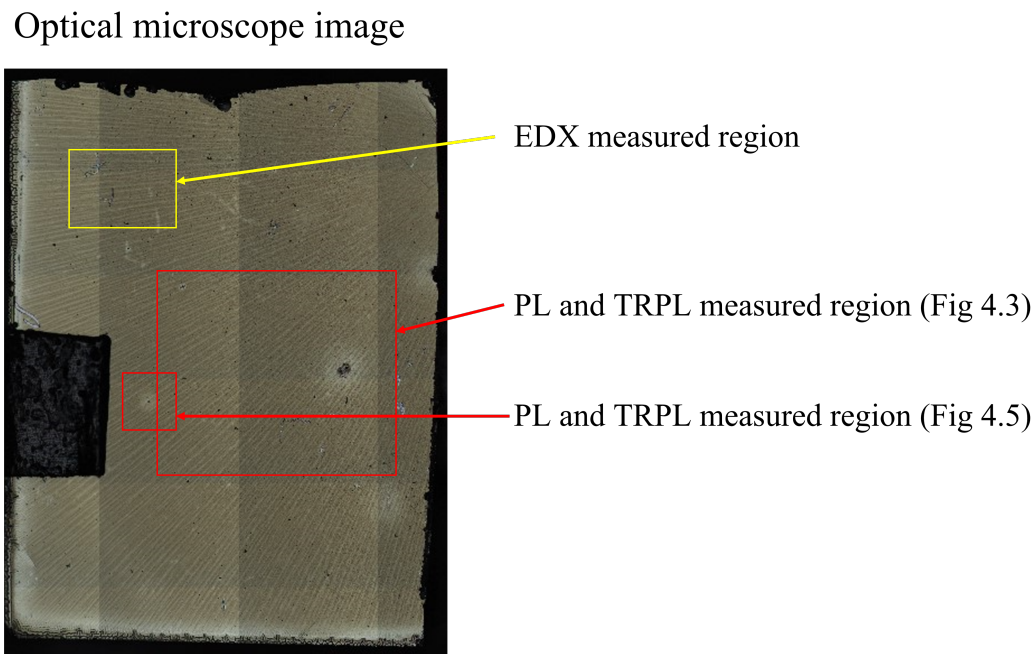

Figure B.1: Optical microscope image taken of FAPIBr perovskite.

From the Optical image, there is no homogeneity. There are scratches, stripes, bright regions, and dark spots. The yellow box highlights the region where EDX map was measured whereas red boxes show the region where PL imaging was taken. The black rectangle on the right covering the perovskite is the conductive carbon tape that was used using the EDX measurement.

B.2 EDX spectra

As discussed in Figure 4.7, EDX spectra of the two features are shown here, the glass-exposed features show a high percentage of silicon and oxygen. whereas the pristine perovskite region shows all the components of perovskite. One can see the chemical signature of Sn and Ti which is mainly coming from the layers underneath the perovskite.

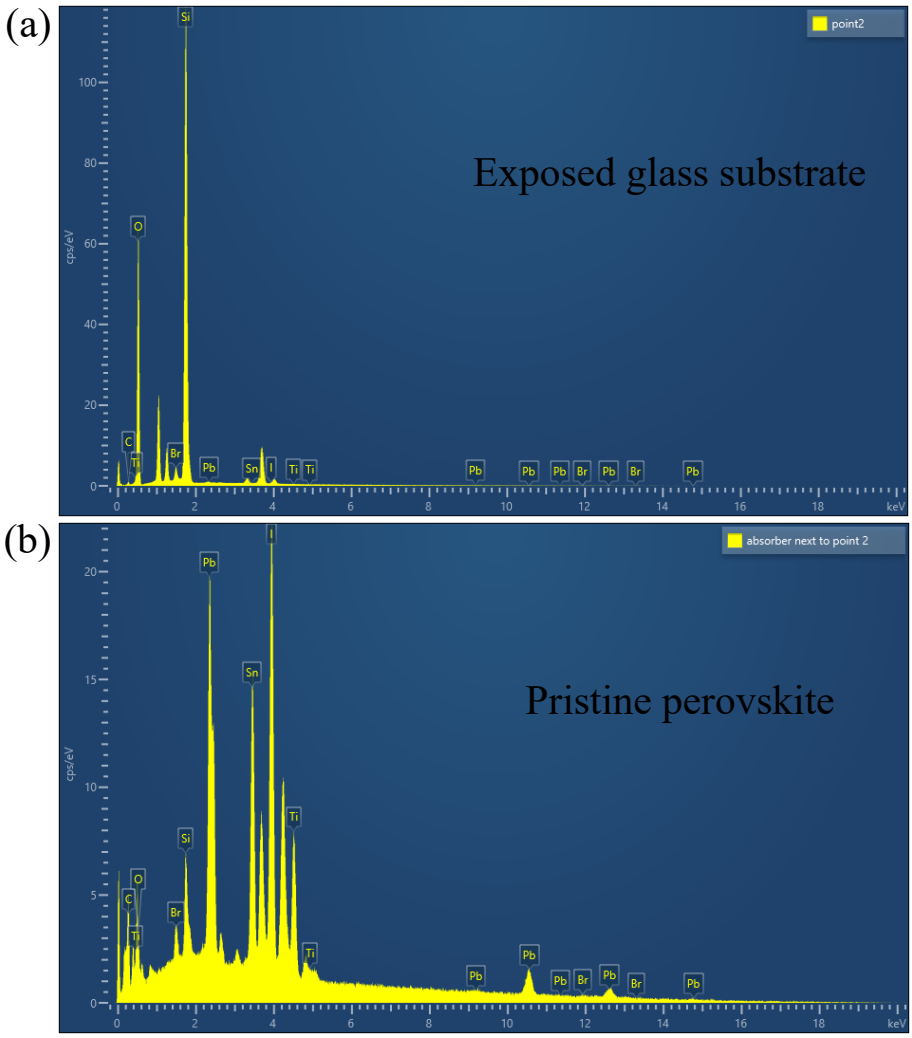

Figure B.2: EDX spectra from the region in Figure 4.7(a) where (a) here is the glass exposed feature and (b) is the point next to it featuring pristine perovskite region.

B.3 Lambert-beer profile

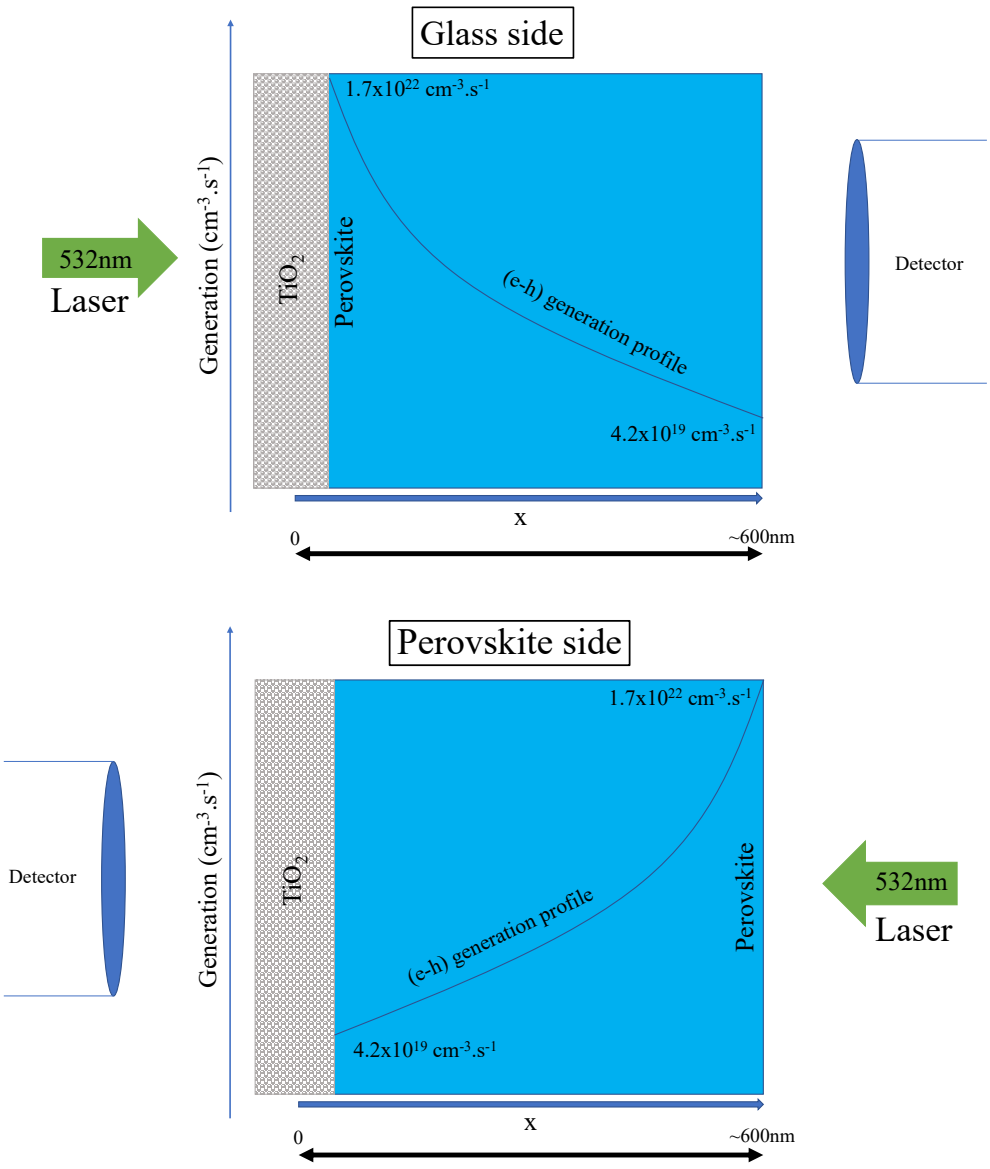

Figure B.3: Lambert-Beer model based schematic of electron-hole pair generation for 600nm thick sample. Glass side means that the laser is coming from the back interface and the detection is done in transmission mode. Perovskite means that the surface of the perovskite is facing the laser.

The photogeneration process in a photovoltaic material is governed by the Lambert-Beer model for absorption, given as

$$G(x) = \int_{\lambda_{\min}}^{\lambda_{\max}} \phi(\lambda)\alpha(\lambda)e^{-\alpha(\lambda)x}d\lambda \tag{B.1}$$

For simplicity, we take the absorption coefficient to be $1 \times 10^5\,\mathrm{cm}^{-1}$ and the bandgap of $1.56eV$ resulting in the absorbed photon flux of $\approx 1.7 \times 10^{17}\,\mathrm{cm}^2/\mathrm{sec}$. Assuming that every

absorbed photon generates an electron-hole pair, we can replace absorbed photons with generated photons. Hence according to Lambert-Beer law, the initial generation at $x = 0$ will be equivalent to $1.7 \times 10^{22}\,\mathrm{cm}^3/\mathrm{sec}$ and will exponentially decrease. Taking $x = 600nm$, we estimated that the generation at the back interface in our case will be $4.2 \times 10^{19}\,\mathrm{cm}^3/\mathrm{sec}$

Appendix C

Appendix Chapter 6

C.1 20x PL imaging of passivated perovskite variation

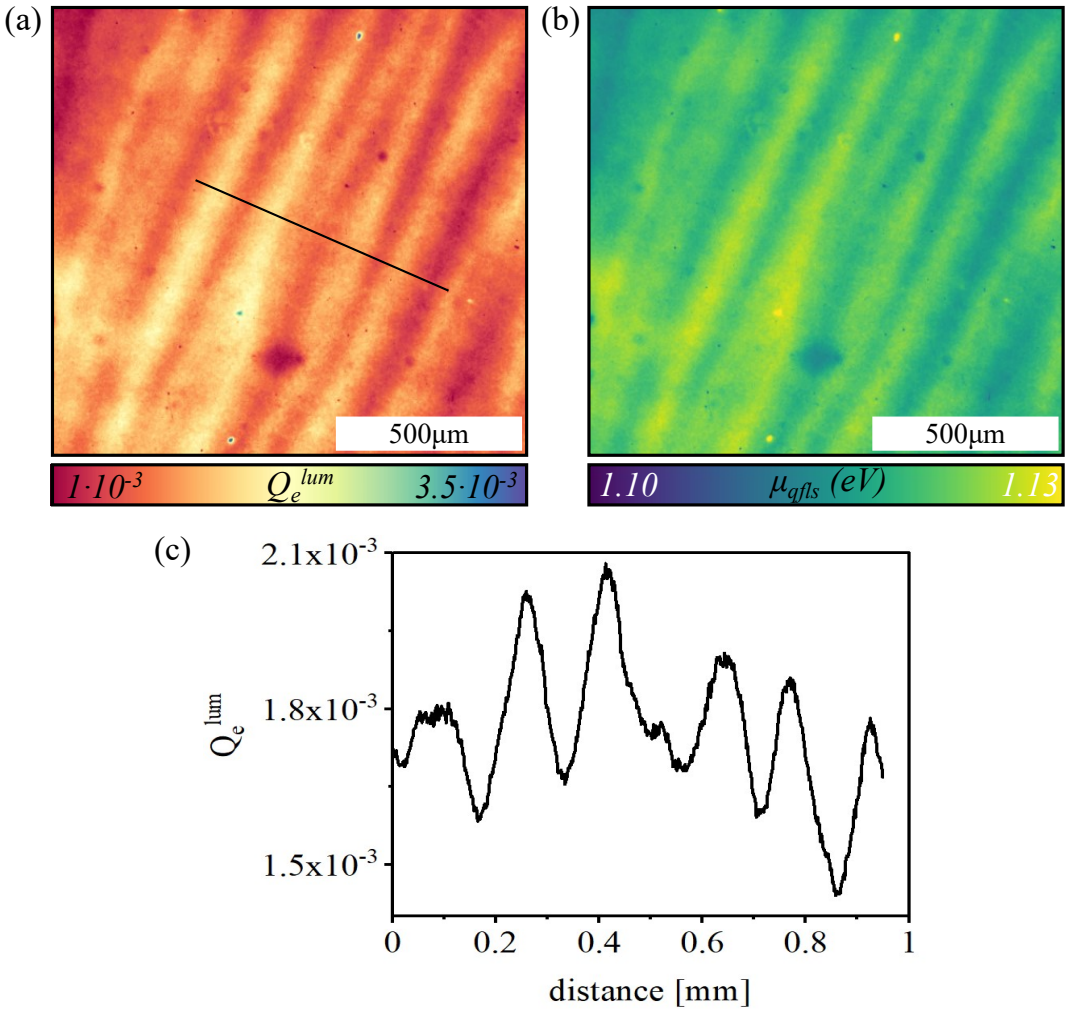

Figure C.1.1: PLQY variation and lineprofile on Q_e^{lum} amp.

As we discussed passivated perovskite in Chapter 6, Figure C.1.1 shows PL imaging mea-

surement of the FAPIBr perovskite taken at 20x objective. This allows for better resolution of the stripes. A line profile along the stripes shows variation in the Q_e^{lum} and this variation gets reflected in the quasi-fermi level splitting μ_{qfls} calculated using equation 3.7 taking $1.56eV$ as peak position.

C.2 EDX analysis

Figure C.2.1(a) shows EDX point spectra performed on three features observed in the secondary electron image. The feature on the right marked as 1 is bright in contrast, 2 is dark in contrast and seems to have no perovskite and 3 is the pristine perovskite point. From

(a)

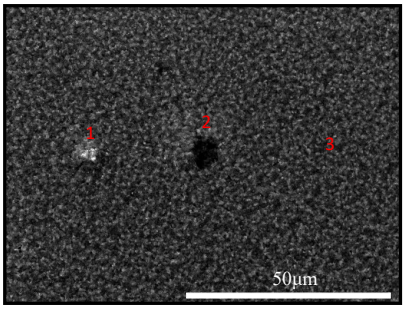

Atomic % (arb.)

Spectrum Label	Spectrum 1	Spectrum 2	Spectrum 3
Ti	43.47	15.13	11.63
Br	1.72	2.55	3.29
Sn	6.24	29.43	28.20
I	34.95	38.93	42.18
Pb	13.62	13.96	14.71
Total	100.00	100.00	100.00

(b)

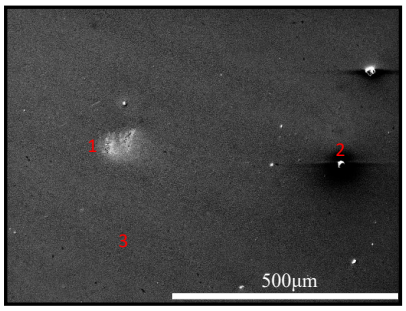

Atomic % (arb.)

Spectrum Label	Spectrum 1	Spectrum 2	Spectrum 3
Ti	11.55	0.31	13.80
Br	3.58	95.15	2.92
Sn	27.67	0.00	24.09
I	42.02	2.93	42.98
Pb	15.18	1.60	16.21
Total	100.00	100.00	100.00

Figure C.2.1: EDX point spectra on features on the surface of the passivated perovskite with their atomic percentage of elements present in the layered stack.

their respective atomic percentage, feature 1 shows a high level of TiO_2 together with I and Pb indicating that either this spot has an exposed charge extraction layer or very thin perovskite is present on it. The atomic percentage of spectrum 2 and 3 does not show a lot of difference in their atomic content. Figure C.2.1(b) shows the different areas on the perovskite sample with another set of inhomogeneities marked by a number. Particularly interesting the the spectrum 2 because this spot shows a very high level of Br. Spot 1 shows a bright contrast as compared to Spot 3 which is a pristine region of the perovskite, but not a different distribution of elements. One needs high-resolution spectra of these spots to have a quantitative distribution of the chemical content. The goal of this thesis is just to see the different chemical species in these regions that reflect the contrast in PL measurements.

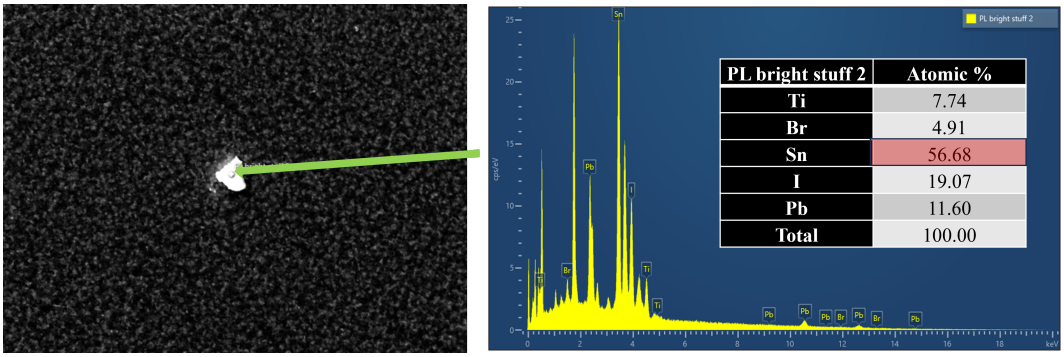

PL bright stuff 2	Atomic %
Ti	7.74
Br	4.91
Sn	56.68
I	19.07
Pb	11.60
Total	100.00

Figure C.2.2: EDX point spectra performed on a bright feature that shows a high level of Tin coming from the FTO. This means that this is an FTO-exposed region on the perovskite and can be considered as a pinhole.

C.3 Surface sensitive characterization of passivated perovskite

Figure C.3.1 illustrates the application of surface-sensitive characterization techniques on the passivated FAPIBr perovskite to investigate its chemical and morphological heterogeneity at the micrometer scale. In Figure C.3.1(a), an AFM topography map is presented, which was obtained under a nitrogen environment. In addition to the grains, numerous small granular structures can be observed throughout the sample surface, which are attributed to the presence of the passivation layer. These specific regions are indicated by the white color. The corresponding secondary image, displayed in Figure C.3.1(b), exhibits similar features, even though the AFM measured region and the SE image region are not identical. Upon conducting SIMS analysis on this region, it was noted that the organic component FA^+ and the element Br were absent from these features. Conversely, the presence of Pb and I in this region suggests the potential existence of PbI species. The elemental distribution maps derived from secondary ion mass spectrometry are presented in Figure C.3.1(c,d), and have been superimposed onto the secondary electron image to emphasize the features and the absence of the aforementioned elements.

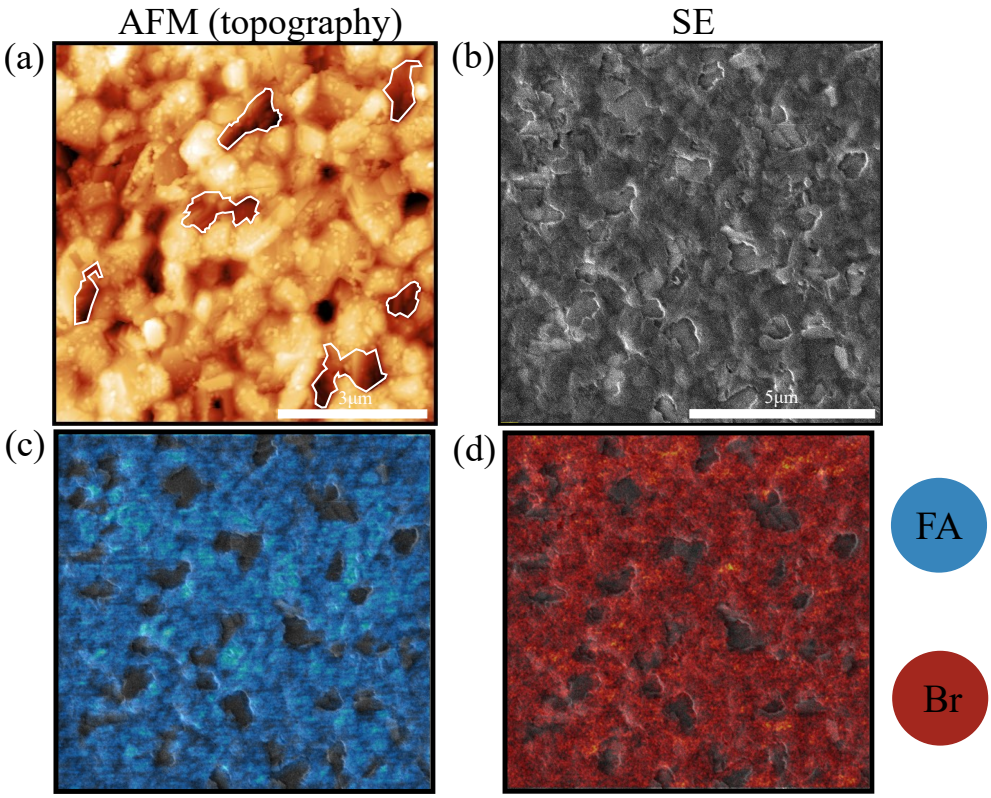

Figure C.3.1: (a)AFM topography map of surface passivated FAPIBr perovskite. Topography shows domains that are marked with sharp edges and seem to have less amount of the passivation layer, the passivation layer is indicated by the small granular spots that are spread across the surface. (b) Secondary electron image of the passivated perovskite (not the same region as of AFM map) showing similar domains with sharp borders with edges showing a bit high contrast. (c,d) are the chemical spatial distribution of FA^+ and Br showing that the sharp border domains observed in AFM as well as SEM image have these chemicals absent

Publications and Presentations

List of publications

First author

1. **H. Phirke**, S. Gharabeiki, A. Singh, A. Krishna, S. Siebentritt, A. Redinger; Quantifying recombination and charge carrier extraction in halide perovskites via hyperspectral time-resolved photoluminescence imaging. APL Energy 1 March 2024; 2 (1): 016111.

Supporting author

1. Krishna, Anurag, Viktor Skorjanc, Mathias Dankl, Jeremy Hieulle, **Himanshu Phirke**, Ajay Singh, Essa A. Alharbi et al. "Mitigating the heterointerface driven instability in perovskite photovoltaics." ACS Energy Letters 8, no. 8 (2023): 3604-3613.

2. Kedia, Mayank, Monika Rai, **Himanshu Phirke**, Clara A. Aranda, Chittaranjan Das, Vladimir Chirvony, Stephan Boehringer et al. "Light makes right: laser polishing for surface modification of perovskite solar cells." ACS Energy Letters 8 (2023): 2603-2610.

3. Elizabeth, Amala, Sudhir K. Sahoo, **Himanshu Phirke**, Tim Kodalle, Thomas D. Kühne, Jean-Nicolas Audinot, Tom Wirtz et al. "Surface Passivation and Detrimental Heat-Induced Diffusion Effects in RbF-Treated Cu (In, Ga) Se2 Solar Cell Absorbers." ACS Applied Materials and Interfaces 14, no. 29 (2022): 34101-34112.

4. Singh, Ajay, Jeremy Hieulle, Joana Ferreira Machado, Sevan Gharabeiki, Weiwei Zuo, Muhammad Uzair Farooq, **Himanshu Phirke**, Michael Saliba, and Alex Redinger et al. "Coevaporation Stabilizes Tin-Based Perovskites in a Single Sn-Oxidation State." Nano Letters 22, no. 17 (2022): 7112-7118.

5. Hieulle, Jeremy, Anurag Krishna, Ariadni Boziki, Jean-Nicolas Audinot, Muhammad Uzair Farooq, Joana Ferreira Machado, Marko Mladenović, **Himanshu Phirke**, Ajay Singh, Tom Wirtz, Alexandre Tkatchenko, Michael Graetzel, Anders Hagfeldt and Alex

Redinger et al. "Understanding and decoupling the role of wavelength and defects in light-induced degradation of metal-halide perovskites." Energy and Environmental Science 17, no. 1 (2024): 284-295.

6. Boumenou, Christian Kameni, **Himanshu Phirke**, Jonathan Rommelfangen, Jean-Nicolas Audinot, Shiro Nishiwaki, Tom Wirtz, Romain Carron, and Alex Redinger et al. "Nanoscale Surface Analysis Reveals Origins of Enhanced Interface Passivation in RbF Post Deposition Treated CIGSe Solar Cells." Advanced Functional Materials (2023): 2300590.

7. Lanzoni, Evandro Martin, Omar Ramírez, **Himanshu Phirke**, Amala Elizabeth, Harry Mönig, and Alex Redinger et al. "Impact of metallic potassium post-deposition treatment on epitaxial Cu (In, Ga) Se2." Thin Solid Films 741 (2022): 139002.

List of presentations

1. **Himanshu Phirke**, Ajay Singh, Jeremy Hieulle, Alex Redinger, and Anurag Krishna. "Inhomogeneities in lead halide perovskite absorbers revealed by quantitative Photoluminescence Imaging." 14th International Conference on Hybrid and Organic Photovoltaics (HOPV nanoGe), Valencia, Spain 2022. Oral presentation.

2. **Himanshu Phirke**, C. K. Boumenou, J. N. Audinot, T. Wirtz, A. Redinger, "Effect of Post-Deposition Treatment on optical, electrical and compositional properties of Cu(In,Ga)Se2 thin film solar cell", MASEENA 2021, Luxembourg, Poster presentation.

3. **Himanshu Phirke**, Sevan Gharabeiki, Ajay Singh, Anurag Krishna, Susanne Siebentritt, and Alex Redinger, "Quantifying recombination and charge carrier extraction in halide perovskites via hyperspectral time resolved photoluminescence imaging", PSCO 2023, Oxford, UK Poster presentation.

Acknowledgments

The successful completion of this dissertation would have been unattainable without the valuable contributions and unwavering support of numerous individuals. I am profoundly grateful for their assistance and would like to take a moment to express my heartfelt appreciation.

Foremost, my deepest gratitude goes to the coolest supervisor/mentor, Prof. Alex Redinger. His guidance in the Scanning Probe Microscopy (SPM) laboratory was instrumental. Throughout the four years of our collaboration, Prof. Redinger provided not only his expertise but also his time, engaging in extensive discussions about my research and beyond, despite his demanding schedule. His support and encouragement were pivotal in the fruition of this project, and for that, I owe him a debt of gratitude. Prof. Redinger's exceptional mentorship is something every Ph.D. candidate craves to have, and I am very fortunate to have experienced it firsthand. I would like to extend my gratitude to all the Jury member who took out some of their valuable time for me. Collaboration has been a cornerstone of this journey. I am thankful to Dr. Anurag Krishna from EPFL (now at imec, Belgium) and Mayank Kedia from the University of Stuttgart who provided me with state-of-the-art perovskite samples without which this thesis would not have been possible. I am truly grateful for their collaborative spirit. My experience at the Luxembourg Institute of Science and Technology (LIST) was greatly enriched by Dr. Jean-Nicolas Audinot who helped me with HIM-SIMS measurements. His readiness to assist is highly appreciated. Not only Dr. Audinot but other colleagues at LIST helped me a lot in measuring complementary characterization techniques such as SEM and EDX which played an important role. Dr. Michel Melchiorre for his contributions in measuring very nice high-quality field emission SEM of my perovskite sample providing good insight into the layers. My colleagues played an important role in providing me with social support and helping me survive this journey with ease. My family and friends have been my pillars of strength, offering constant encouragement and support throughout this journey. Lastly, but most importantly, my heartfelt appreciation goes to my beloved wife, your understanding, love, and unwavering support

have been the backbone of this journey. I love you profoundly.

Bibliography

[1] bp. Accessed: 2023-08-17. 2023. URL: https://www.bp.com/content/dam/bp/business-sites/en/global/corporate/pdfs/energy-economics/statistical-review/bp-stats-review-2022-full-report.pdf.

[2] Centre for Global Development. *Electricity Consumption and Development Indicators*. 2023. URL: https://www.cgdev.org/media/electricity-consumption-and-development-indicators.

[3] Copernicus Climate Change Service. *Global temperature record July*. 2023. URL: https://climate.copernicus.eu/july-2023-sees-multiple-global-temperature-records-broken.

[4] Phebe Asantewaa Owusu and Samuel Asumadu-Sarkodie. "A review of renewable energy sources, sustainability issues and climate change mitigation". In: *Cogent Engineering* 3 (1 Dec. 2016). Ed. by Shashi Dubey. doi: 10.1080/23311916.2016.1167990, p. 1167990. ISSN: null. DOI: 10.1080/23311916.2016.1167990. URL: https://doi.org/10.1080/23311916.2016.1167990.

[5] N. L. Panwar, S. C. Kaushik, and Surendra Kothari. "Role of renewable energy sources in environmental protection: A review". In: *Renewable and Sustainable Energy Reviews* 15 (3 Apr. 2011), pp. 1513–1524. ISSN: 1364-0321. DOI: 10.1016/J.RSER.2010.11.037.

[6] *Largest desert in the world*. accessed on 2023-12-10. 2023. URL: http://geology.com/records/largest-desert.shtml.

[7] Martin A Green. *Photovoltaic principles*. 2002. URL: www.elsevier.com/locate/physe.

[8] Académie des sciences (France) and Centre national de la recherche scientifique (France). *Comptes rendus hebdomadaires des séances de l'Académie des sciences*. Vol. t.9 (1839). https://www.biodiversitylibrary.org/bibliography/4466. Paris, publiés avec le con-

cours du Centre national de la recherche scientifique par MM. les secrétaires perpétuels, -1965, 1839, p. 920. URL: https://www.biodiversitylibrary.org/item/20576.

[9] Max Planck. "The theory of heat radiation". In: *Entropie* 144.190 (1900), p. 164.

[10] Huashan Li et al. "Solar constant values for estimating solar radiation". In: *Energy* 36 (3 2011), pp. 1785–1789. ISSN: 03605442. DOI: 10.1016/j.energy.2010.12.050.

[11] Gregory H Wannier. *The Structure of Electronic Excitation Levels in Insulating Crystals*. 1937.

[12] Tze Chien Sum and Nripan Mathews. *Advancements in perovskite solar cells: Photophysics behind the photovoltaics*. 2014. DOI: 10.1039/c4ee00673a.

[13] William Shockley and Hans J. Queisser. "Detailed balance limit of efficiency of p-n junction solar cells". In: *Journal of Applied Physics* 32 (3 1961), pp. 510–519. ISSN: 00218979. DOI: 10.1063/1.1736034.

[14] Tom Tiedje et al. *Limiting Efficiency of Silicon Solar Cells*. 1984.

[15] NREL. *Solar cell effciency chart*. Accessed: 2023-08-17. 2023. URL: https://www.nrel.gov/pv/interactive-cell-efficiency.html.

[16] Ye Xu et al. *Efficient charge generation at low energy losses in organic solar cells: A key issues review*. Aug. 2020. DOI: 10.1088/1361-6633/ab90cf.

[17] *Understanding Energy Loss in Organic Solar Cells: Toward a New Efficiency Regime*. Jan. 2018. DOI: 10.1016/j.joule.2017.09.020.

[18] S. M. Sze and Kwok Kwok Ng. *Physics of semiconductor devices*. Wiley-Interscience, 2007, p. 815. ISBN: 0471143235.

[19] Donald A. Neamen. *Semiconductor physics and devices : basic principles*. McGraw-Hill, 2012, p. 758. ISBN: 9780073529585.

[20] Hugh Jenkyns. "S IMMS , M. J., C HIDLAW , N., M ORTON , N. & P AGE , K. N. 2004. British Lower Jurassic Stratigraphy . Geological Conservation Review Series Volume 30. xvi+458 pp. Peterborough: Joint Nature Conservation Committee; distributed by NHBS Ltd, 2–3 Wills Road, Totnes, Devon TQ9 5XN, UK. Price £55.00 (hard covers). ISBN 1 86107 484 0". In: *Geological Magazine* 142 (3 May 2005), pp. 303–303. ISSN: 0016-7568. DOI: 10.1017/s0016756805210774.

[21] *Perovskite Mineral Data*. Accessed: 2023-08-17. URL: https://webmineral.com/data/Perovskite.shtml.

[22] P. Lemmens M. Johnsson. *Handbook of Magnetism and Advanced Magnetic Materials*. John Wiley & Sons, 2007. ISBN: 9780470022184.

[23] OIST. *Perovskite crystal structure*. Accessed on 2023-11-23. 2022. URL: https://www.oist.jp/image/perovskite-crystal-structure.

[24] Chonghea Li et al. "Formability of ABX 3 (X = F, Cl, Br, I) halide perovskites". In: *Acta Crystallographica Section B: Structural Science* 64 (6 2008), pp. 702–707. ISSN: 01087681. DOI: 10.1107/S0108768108032734.

[25] V M Goldschmidt. "Die Gesetze der Krystallochemie". In: *Naturwissenschaften* 14 (21 1926), pp. 477–485. ISSN: 1432-1904. DOI: 10.1007/BF01507527. URL: https://doi.org/10.1007/BF01507527.

[26] Gregor Kieslich, Shijing Sun, and Anthony K. Cheetham. "Solid-state principles applied to organic–inorganic perovskites: New tricks for an old dog". In: *Chemical Science* 5 (12 Oct. 2014), pp. 4712–4715. ISSN: 20416539. DOI: 10.1039/c4sc02211d.

[27] Zehua Li et al. "Ink Engineering of Inkjet Printing Perovskite". In: *ACS Applied Materials and Interfaces* 12 (35 Sept. 2020), pp. 39082–39091. ISSN: 19448252. DOI: 10.1021/acsami.0c09485.

[28] Zhen Li et al. *Scalable fabrication of perovskite solar cells*. Mar. 2018. DOI: 10.1038/natrevmats.2018.17.

[29] Yang Yang et al. "Low-temperature solution-processed perovskite solar cells with high efficiency and flexibility". In: *ACS Nano* 8 (2 Feb. 2014), pp. 1674–1680. ISSN: 19360851. DOI: 10.1021/nn406020d.

[30] K. Xerxes Steirer et al. "Defect Tolerance in Methylammonium Lead Triiodide Perovskite". In: *ACS Energy Letters* 1 (2 Aug. 2016), pp. 360–366. ISSN: 23808195. DOI: 10.1021/acsenergylett.6b00196.

[31] Jun Kang and Lin Wang Wang. "High Defect Tolerance in Lead Halide Perovskite CsPbBr3". In: *Journal of Physical Chemistry Letters* 8 (2 Jan. 2017), pp. 489–493. ISSN: 19487185. DOI: 10.1021/acs.jpclett.6b02800.

[32] Samuel D. Stranks et al. "Electron-hole diffusion lengths exceeding 1 micrometer in an organometal trihalide perovskite absorber". In: *Science* 342 (6156 2013), pp. 341–344. ISSN: 10959203. DOI: 10.1126/science.1243982.

[33] Weihua Ning et al. "Long Electron–Hole Diffusion Length in High-Quality Lead-Free Double Perovskite Films". In: *Advanced Materials* 30 (20 May 2018). ISSN: 15214095. DOI: 10.1002/adma.201706246.

[34] David P McMeekin et al. “A mixed-cation lead mixed-halide perovskite absorber for tandem solar cells”. In: *Science* 351.6269 (2016), pp. 151–155.

[35] Eric T Hoke et al. “Reversible photo-induced trap formation in mixed-halide hybrid perovskites for photovoltaics †”. In: (2015). DOI: 10.1039/c4sc03141e. URL: www.rsc.org/chemicalscience.

[36] Michael Saliba et al. “Cesium-containing triple cation perovskite solar cells: Improved stability, reproducibility and high efficiency”. In: *Energy and Environmental Science* 9 (6 June 2016), pp. 1989–1997. ISSN: 17545706. DOI: 10.1039/c5ee03874j.

[37] Tongle Bu et al. “A novel quadruple-cation absorber for universal hysteresis elimination for high efficiency and stable perovskite solar cells”. In: *Energy and Environmental Science* 10 (12 Dec. 2017), pp. 2509–2515. ISSN: 17545706. DOI: 10.1039/c7ee02634j.

[38] Kevin A. Bush et al. “Compositional Engineering for Efficient Wide Band Gap Perovskites with Improved Stability to Photoinduced Phase Segregation”. In: *ACS Energy Letters* 3 (2 Feb. 2018), pp. 428–435. ISSN: 23808195. DOI: 10.1021/acsenergylett.7b01255.

[39] Haizhou Lu et al. “iScience Compositional and Interface Engineering of Organic-Inorganic Lead Halide Perovskite Solar Cells”. In: (2014). DOI: 10.1016/j.isci. URL: https://doi.org/10.1016/j.isci..

[40] Luis K. Ono, Emilio J. Juarez-Perez, and Yabing Qi. *Progress on Perovskite Materials and Solar Cells with Mixed Cations and Halide Anions*. Sept. 2017. DOI: 10.1021/acsami.7b06001.

[41] Felix Ochieng Saouma et al. “Multiphoton Absorption Coefficients of Organic-Inorganic Lead Halide Perovskites CH3NH3PbX3 (X = Cl, Br, I) Single Crystals”. In: *Chemistry of Materials* 29 (16 Aug. 2017), pp. 6876–6882. ISSN: 15205002. DOI: 10.1021/acs.chemmater.7b02110.

[42] Rohit Prasanna et al. “Band Gap Tuning via Lattice Contraction and Octahedral Tilting in Perovskite Materials for Photovoltaics”. In: *Journal of the American Chemical Society* 139 (32 Aug. 2017), pp. 11117–11124. ISSN: 15205126. DOI: 10.1021/jacs.7b04981.

[43] Yoshihiko Kanemitsu and Taketo Handa. *Photophysics of metal halide perovskites: From materials to devices*. Sept. 2018. DOI: 10.7567/JJAP.57.090101.

[44] Priyanka Roy et al. "A review on perovskite solar cells: Evolution of architecture, fabrication techniques, commercialization issues and status". In: *Solar Energy* 198 (2020), pp. 665–688.

[45] Kunwu Fu et al. *Perovskite solar cells: technology and practices*. CRC Press, 2019.

[46] Edward J.W. Crossland et al. "Mesoporous TiO 2 single crystals delivering enhanced mobility and optoelectronic device performance". In: *Nature* 495 (7440 Mar. 2013), pp. 215–219. ISSN: 00280836. DOI: 10.1038/nature11936.

[47] Joseph S. Manser, Jeffrey A. Christians, and Prashant V. Kamat. *Intriguing Optoelectronic Properties of Metal Halide Perovskites*. Nov. 2016. DOI: 10.1021/acs.chemrev.6b00136.

[48] "Design Rules for Heterostructure Solar Cells and Modules". In: John Wiley Sons, Ltd, 2011, pp. 129–174. ISBN: 9783527633708. DOI: https://doi.org/10.1002/9783527633708.ch3. URL: https://onlinelibrary.wiley.com/doi/abs/10.1002/9783527633708.ch3.

[49] Uwe Rau and Thomas Kirchartz. "Charge carrier collection and contact selectivity in solar cells". In: *Advanced materials interfaces* 6.20 (2019), p. 1900252.

[50] Valerio Sarritzu et al. "Optical determination of Shockley-Read-Hall and interface recombination currents in hybrid perovskites". In: *Scientific reports* 7.1 (2017), p. 44629.

[51] Laura M Herz. "Charge-carrier mobilities in metal halide perovskites: fundamental mechanisms and limits". In: *ACS Energy Letters* 2.7 (2017), pp. 1539–1548.

[52] Adrien Bercegol et al. "Slow diffusion and long lifetime in metal halide perovskites for photovoltaics". In: *The Journal of Physical Chemistry C* 122.43 (2018), pp. 24570–24577.

[53] Yevgeny Rakita et al. "Mechanical properties of APbX3 (A= Cs or CH3NH3; X= I or Br) perovskite single crystals". In: *Mrs Communications* 5.4 (2015), pp. 623–629.

[54] Stefania Cacovich et al. "Light-induced passivation in triple cation mixed halide perovskites: interplay between transport properties and surface chemistry". In: *ACS applied materials & interfaces* 12.31 (2020), pp. 34784–34794.

[55] Davide Raffaele Ceratti et al. "Self-healing inside APbBr3 halide perovskite crystals". In: *Advanced Materials* 30.10 (2018), p. 1706273.

[56] Riley E Brandt et al. "Identifying defect-tolerant semiconductors with high minority-carrier lifetimes: beyond hybrid lead halide perovskites". In: *Mrs Communications* 5.2 (2015), pp. 265–275.

[57] Riley E Brandt et al. "Searching for "defect-tolerant" photovoltaic materials: combined theoretical and experimental screening". In: *Chemistry of Materials* 29.11 (2017), pp. 4667–4674.

[58] H Jin. "E. debroye, M. Keshavarz, IG Scheblykin, MBJ Roeffaers, J. Hofkens and JA Steele". In: *Mater. Horiz* 7 (2020), p. 397.

[59] Yevgeny Rakita, Igor Lubomirsky, and David Cahen. "When defects become 'dynamic': halide perovskites: a new window on materials?" In: *Materials Horizons* 6.7 (2019), pp. 1297–1305.

[60] Thomas Kirchartz et al. "Impact of small phonon energies on the charge-carrier lifetimes in metal-halide perovskites". In: *The Journal of Physical Chemistry Letters* 9.5 (2018), pp. 939–946.

[61] Pabitra K Nayak et al. "Impact of Bi3+ heterovalent doping in organic–inorganic metal halide perovskite crystals". In: *Journal of the American Chemical Society* 140.2 (2018), pp. 574–577.

[62] Philip Schulz, David Cahen, and Antoine Kahn. "Halide perovskites: is it all about the interfaces?" In: *Chemical reviews* 119.5 (2019), pp. 3349–3417.

[63] Stefania Cacovich et al. "Imaging and quantifying non-radiative losses at 23% efficient inverted perovskite solar cells interfaces". In: *Nature communications* 13.1 (2022), p. 2868.

[64] Akihiro Kojima et al. "Organometal halide perovskites as visible-light sensitizers for photovoltaic cells". In: *Journal of the American Chemical Society* 131 (17 May 2009), pp. 6050–6051. ISSN: 00027863. DOI: 10.1021/ja809598r.

[65] In: *Scientific Reports* 2 (2012). ISSN: 20452322. DOI: 10.1038/srep00591.

[66] Henry J. Snaith. *Perovskites: The emergence of a new era for low-cost, high-efficiency solar cells*. Nov. 2013. DOI: 10.1021/jz4020162.

[67] Martin A. Green, Anita Ho-Baillie, and Henry J. Snaith. *The emergence of perovskite solar cells*. 2014. DOI: 10.1038/nphoton.2014.134.

[68] Julian Burschka et al. "Sequential deposition as a route to high-performance perovskite-sensitized solar cells". In: *Nature* 499 (7458 2013), pp. 316–319. ISSN: 00280836. DOI: 10.1038/nature12340.

[69] Jeong Hyeok Im et al. "Growth of CH3 NH3 PbI3 cuboids with controlled size for high-efficiency perovskite solar cells". In: *Nature Nanotechnology* 9 (11 Nov. 2014), pp. 927–932. ISSN: 17483395. DOI: 10.1038/nnano.2014.181.

[70] Fabrizio Giordano et al. "Enhanced electronic properties in mesoporous TiO2 via lithium doping for high-efficiency perovskite solar cells". In: *Nature Communications* 7 (Jan. 2016). ISSN: 20411723. DOI: 10.1038/ncomms10379.

[71] In: *Nature Energy* 1 (10 Oct. 2016). ISSN: 20587546. DOI: 10.1038/nenergy.2016.142.

[72] Ruo Xi Yang et al. "Spontaneous octahedral tilting in the cubic inorganic cesium halide perovskites CsSnX3 and CsPbX3 (X = F, Cl, Br, I)". In: *Journal of Physical Chemistry Letters* 8 (19 Oct. 2017), pp. 4720–4726. ISSN: 19487185. DOI: 10.1021/acs.jpclett.7b02423.

[73] PV. Accessed: 2024-03-13. 2023. URL: https://www.pv-magazine.com/2023/05/24/oxford-pv-sets-28-6-efficiency-record-for-full-size-tandem-cell/.

[74] Hui Seon Kim, Anders Hagfeldt, and Nam Gyu Park. "Morphological and compositional progress in halide perovskite solar cells". In: *Chemical Communications* 55 (9 2019), pp. 1192–1200. ISSN: 1364548X. DOI: 10.1039/c8cc08653b.

[75] Taame Abraha Berhe et al. *Organometal halide perovskite solar cells: Degradation and stability*. Feb. 2016. DOI: 10.1039/c5ee02733k.

[76] Jiupeng Cao and Feng Yan. "Recent progress in tin-based perovskite solar cells". In: *Energy and Environmental Science* 14 (3 Mar. 2021), pp. 1286–1325. ISSN: 17545706. DOI: 10.1039/d0ee04007j.

[77] Kohei Nishimura et al. In: *Nano Energy* 74 (Aug. 2020). ISSN: 22112855. DOI: 10.1016/j.nanoen.2020.104858.

[78] Aslihan Babayigit et al. *Toxicity of organometal halide perovskite solar cells*. Feb. 2016. DOI: 10.1038/nmat4572.

[79] Ming Gang Ju et al. *Toward Eco-friendly and Stable Perovskite Materials for Photovoltaics*. July 2018. DOI: 10.1016/j.joule.2018.04.026.

[80] Hanul Min et al. In: *Nature* 598 (7881 Oct. 2021), pp. 444–450. ISSN: 14764687. DOI: 10.1038/s41586-021-03964-8.

[81] SANDRA ENKHARDT. *Quantum Dot Layer Pushes Perovskite Solar Cell Efficiency Up to 25.7%.* Accessed: 2023-08-23. 2022. URL: https://www.pv-magazine.com/2022/01/24/quantum-dot-layer-pushes-perovskite-solar-cell-efficiency-up-to-25-7/.

[82] Guangbao Wu et al. *Surface Passivation Using 2D Perovskites toward Efficient and Stable Perovskite Solar Cells.* Feb. 2022. DOI: 10.1002/adma.202105635.

[83] Anurag Krishna et al. "Mitigating the Heterointerface Driven Instability in Perovskite Photovoltaics". In: *ACS Energy Letters* 8 (8 2023), pp. 3604–3613. DOI: 10.1021/acsenergylett.3c01029. URL: https://doi.org/10.1021/acsenergylett.3c01029.

[84] Xuewen Liu, Chongyang Xu, and Eun Cheol Lee. "Chlorobenzene-Mediated Control of Crystallization in Perovskite Films for High-Performance Solar Cells". In: *ACS Applied Energy Materials* 3 (12 Dec. 2020), pp. 12291–12297. ISSN: 25740962. DOI: 10.1021/acsaem.0c02342.

[85] Gizachew Belay Adugna, Seid Yimer Abate, and Yu Tai Tao. "High-Efficiency and scalable Solution-Sheared perovskite solar cells using green solvents". In: *Chemical Engineering Journal* 437 (June 2022). ISSN: 13858947. DOI: 10.1016/j.cej.2022.135477.

[86] Weihua Hong et al. "New insights in construction of three-dimensional donor/acceptor interface for high performance perovskite solar cells: The preparation of wolf tooth stick-like TiO2". In: *Colloids and Surfaces A: Physicochemical and Engineering Aspects* 646 (Aug. 2022). ISSN: 18734359. DOI: 10.1016/j.colsurfa.2022.128958.

[87] Min Wang et al. "A Universal Strategy of Intermolecular Exchange to Stabilize α-FAPbI3 and Manage Crystal Orientation for High-Performance Humid-Air-Processed Perovskite Solar Cells". In: *Advanced Materials* 34 (23 2022), p. 2200041. DOI: https://doi.org/10.1002/adma.202200041. URL: https://onlinelibrary.wiley.com/doi/abs/10.1002/adma.202200041.

[88] Nam Joong Jeon et al. "Solvent engineering for high-performance inorganic-organic hybrid perovskite solar cells". In: *Nature Materials* 13 (9 2014), pp. 897–903. ISSN: 14764660. DOI: 10.1038/nmat4014.

[89] Qiuju Liang et al. "Enhancing the crystallization and optimizing the orientation of perovskite films via controlling nucleation dynamics". In: *Journal of Materials Chemistry A* 4 (1 Nov. 2015), pp. 223–232. ISSN: 20507496. DOI: 10.1039/c5ta08015k.

[90] Andrew S Brown and Martin A Green. *Detailed balance limit for the series constrained two terminal tandem solar cell*. 2002. URL: www.elsevier.com/locate/physe.

[91] S P Bremner, M Y Levy, and Christiana B Honsberg. "Analysis of tandem solar cell efficiencies under AM1.5G spectrum using a rapid flux calculation method". In: *Progress in Photovoltaics: Research and Applications* 16 (3 2008), p. 225233. DOI: 10.1002/pip.799. URL: http://dx.doi.org/10.1002/pip.799.

[92] EMILIANO BELLINI. *KAUST claims 33.7% efficiency for perovskite/silicon tandem solar cell*. Accessed: 2023-08-23. 2023. URL: https://www.pv-magazine.com/2023/05/30/kaust-claims-33-7-efficiency-for-perovskite-silicon-tandem-solar-cell/.

[93] Xinxing Liu et al. "Over 28% efficiency perovskite/Cu (InGa) Se 2 tandem solar cells: highly efficient sub-cells and their bandgap matching". In: *Energy & Environmental Science* 16.11 (2023), pp. 5029–5042.

[94] Aritra Ghosh and Brian Norton. "Optimization of PV powered SPD switchable glazing to minimise probability of loss of power supply". In: *Renewable Energy* 131 (Feb. 2019), pp. 993–1001. ISSN: 18790682. DOI: 10.1016/j.renene.2018.07.115.

[95] Aritra Ghosh. "Possibilities and challenges for the inclusion of the electric vehicle (EV) to reduce the carbon footprint in the transport sector: A review". In: *Energies* 13 (10 May 2020). ISSN: 19961073. DOI: 10.3390/en13102602.

[96] Thomas Bidaud. "Characterization of nanomaterials by cathodoluminescence for photovoltaic applications". PhD thesis. Université Paris-Saclay, 2021.

[97] Daniel Ory, Nicolas Paul, and Laurent Lombez. "Extended quantitative characterization of solar cell from calibrated voltage-dependent electroluminescence imaging". In: *Journal of Applied Physics* 129.4 (2021).

[98] Peter Würfel and Uli Würfel. *Physics of Solar Cells*.

[99] P Asbeck. "Self-absorption effects on the radiative lifetime in GaAs-GaAlAs double heterostructures". In: *Journal of Applied Physics* 48.2 (1977), pp. 820–822.

[100] Julian Mattheis, Jürgen H Werner, and Uwe Rau. "Finite mobility effects on the radiative efficiency limit of p n junction solar cells". In: *Physical Review B* 77.8 (2008), p. 085203.

[101] Julian Mattheis. *Mobility and homogeneity effects on the power conversion efficiency of solar cells*. 2008.

[102] Thomas Kirchartz et al. *Photoluminescence-Based Characterization of Halide Perovskites for Photovoltaics*. July 2020. DOI: 10.1002/aenm.201904134.

[103] Yasuhiro Yamada et al. "Photocarrier recombination dynamics in perovskite CH3NH3PbI3 for solar cell applications". In: *Journal of the American Chemical Society* 136.33 (2014), pp. 11610–11613.

[104] WTRW Shockley and WT Read Jr. "Statistics of the recombinations of holes and electrons". In: *Physical review* 87.5 (1952), p. 835.

[105] Re N Hall. "Electron-hole recombination in germanium". In: *Physical review* 87.2 (1952), p. 387.

[106] Thomas Kirchartz. *Generalized detailed balance theory of solar cells*. Vol. 38. Forschungszentrum Jülich, 2009.

[107] Gustav Kirchhoff. "Über das Verhältnis zwischen dem Emissionsvermögen und dem Absorptionsvermögen der Körper für Wärme und Licht". In: *Von Kirchhoff bis Planck: Theorie der Wärmestrahlung in Historisch-kritischer Darstellung* (1978), pp. 131–151.

[108] W Van Roosbroeck and William Shockley. "Photon-radiative recombination of electrons and holes in germanium". In: *Physical Review* 94.6 (1954), p. 1558.

[109] U. Rau and J. H. Werner. "Radiative efficiency limits of solar cells with lateral band-gap fluctuations". In: *Applied Physics Letters* 84 (19 May 2004), pp. 3735–3737. ISSN: 00036951. DOI: 10.1063/1.1737071.

[110] Richard K. Ahrenkiel. "Chapter 2 Minority-Carrier Lifetime in III–V Semiconductors". In: *Semiconductors and Semimetals* 39 (C Jan. 1993), pp. 39–150. ISSN: 0080-8784. DOI: 10.1016/S0080-8784(08)62594-6.

[111] A. B. Sproul. "Dimensionless solution of the equation describing the effect of surface recombination on carrier decay in semiconductors". In: *Journal of Applied Physics* 76 (5 1994), pp. 2851–2854. ISSN: 00218979. DOI: 10.1063/1.357521.

[112] Florian 1986- Staub and Universität Duisburg-Essen. *Time-resolved photoluminescence on perovskite absorber materials for photovoltaic applications*. ISBN: 9783958065031.

[113] Elizabeth M. Tennyson, Tiarnan A.S. Doherty, and Samuel D. Stranks. *Heterogeneity at multiple length scales in halide perovskite semiconductors*. Sept. 2019. DOI: 10.1038/s41578-019-0125-0.

[114] Robert T. Ross. "Some thermodynamics of photochemical systems". In: *The Journal of Chemical Physics* 46 (12 1967), pp. 4590–4593. ISSN: 00219606. DOI: 10.1063/1.1840606.

[115] G Smestad and H Ries. *Solar Energy Materials and Solar Cells Luminescence and current-voltage characteristics of solar cells and optoelectronic devices*. 1992.

[116] Uwe Rau et al. "Efficiency Potential of Photovoltaic Materials and Devices Unveiled by Detailed-Balance Analysis". In: *Physical Review Applied* 7 (4 Apr. 2017). ISSN: 23317019. DOI: 10.1103/PhysRevApplied.7.044016.

[117] Uwe Rau. "Reciprocity relation between photovoltaic quantum efficiency and electroluminescent emission of solar cells". In: *Physical Review B - Condensed Matter and Materials Physics* 76 (8 Aug. 2007). ISSN: 10980121. DOI: 10.1103/PhysRevB.76.085303.

[118] Uwe Rau, Ulrich W Paetzold, and Thomas Kirchartz. "Thermodynamics of light management in photovoltaic devices". In: *Physical Review B* 90.3 (2014), p. 035211.

[119] Dae-Yong Son et al. "Self-formed grain boundary healing layer for highly efficient CH3NH3PbI3 perovskite solar cells". In: *Nature Energy* 1.7 (2016), pp. 1–8.

[120] Dane W de Quilettes et al. "Impact of microstructure on local carrier lifetime in perovskite solar cells". In: *Science* 348.6235 (2015), pp. 683–686.

[121] Takumi Yamada et al. "Photon emission and reabsorption processes in CH 3 NH 3 PbBr 3 single crystals revealed by time-resolved two-photon-excitation photoluminescence microscopy". In: *Physical Review Applied* 7.1 (2017), p. 014001.

[122] Jian Wang et al. "Reducing surface recombination velocities at the electrical contacts will improve perovskite photovoltaics". In: *ACS Energy Letters* 4.1 (2018), pp. 222–227.

[123] Meng Zhang et al. "Composition-dependent photoluminescence intensity and prolonged recombination lifetime of perovskite CH 3 NH 3 PbBr 3- x Cl x films". In: *Chemical Communications* 50.79 (2014), pp. 11727–11730.

[124] Richard K Ahrenkiel and Mark S Lundstrom. *Semiconductors and semimetals*. Academic Press, 1993.

[125] Matthias Maiberg and Roland Scheer. "Theoretical study of time-resolved luminescence in semiconductors. I. Decay from the steady state". In: *Journal of Applied Physics* 116.12 (2014).

[126] "Quantitative analysis of the transient photoluminescence of CH 3 NH 3 PbI 3 /PC 61 BM heterojunctions by numerical simulations". In: *Sustainable Energy and Fuels* 2 (5 2018), pp. 1027–1034. ISSN: 23984902. DOI: 10.1039/c7se00603a.

[127] Wenhao Li et al. "Direct Characterization of Carrier Diffusion in Halide-Perovskite Thin Films Using Transient Photoluminescence Imaging". In: *ACS Photonics* 6 (10 Oct. 2019), pp. 2375–2380. ISSN: 23304022. DOI: 10.1021/acsphotonics.9b00778.

[128] Jordan M. Snaider et al. "Ultrafast Imaging of Carrier Transport across Grain Boundaries in Hybrid Perovskite Thin Films". In: *ACS Energy Letters* 3 (6 June 2018), pp. 1402–1408. ISSN: 23808195. DOI: 10.1021/acsenergylett.8b00560.

[129] Changsoon Cho et al. "Efficient vertical charge transport in polycrystalline halide perovskites revealed by four-dimensional tracking of charge carriers". In: *Nature Materials* 21 (12 Dec. 2022), pp. 1388–1395. ISSN: 14764660. DOI: 10.1038/s41563-022-01395-y.

[130] "Light Makes Right: Laser Polishing for Surface Modification of Perovskite Solar Cells". In: *ACS Energy Letters* 8 (6 June 2023), pp. 2603–2610. ISSN: 23808195. DOI: 10.1021/acsenergylett.3c00469.

[131] Kazuhisa Miyoshi. *Surface Characterization Techniques: An Overview NASA*. Tech. rep. TM-2002-211497, 12–22, 2002.

[132] S Mahovic Poljacek et al. "Comparison of fractal and profilometric methods for surface topography characterization". In: *Applied Surface Science* 254.11 (2008), pp. 3449–3458.

[133] Gerd Binnig, Calvin F Quate, and Ch Gerber. "Atomic force microscope". In: *Physical review letters* 56.9 (1986), p. 930.

[134] Bert Voigtländer. *Atomic force microscopy*. Springer, 2019.

[135] Ricardo Garcıa and Ruben Perez. "Dynamic atomic force microscopy methods". In: *Surface science reports* 47.6-8 (2002), pp. 197–301.

[136] Yves Martin, Clayton C Williams, and H Kumar Wickramasinghe. "Atomic force microscope–force mapping and profiling on a sub 100-Å scale". In: *Journal of applied Physics* 61.10 (1987), pp. 4723–4729.

[137] Thomas R Albrecht et al. "Frequency modulation detection using high-Q cantilevers for enhanced force microscope sensitivity". In: *Journal of applied physics* 69.2 (1991), pp. 668–673.

[138] Th Glatzel, S Sadewasser, and M Ch Lux-Steiner. "Amplitude or frequency modulation-detection in Kelvin probe force microscopy". In: *Applied surface science* 210.1-2 (2003), pp. 84–89.

[139] Wilhelm Melitz et al. *Kelvin probe force microscopy and its application*. 2011. DOI: 10.1016/j.surfrep.2010.10.001.

[140] Sascha Sadewasser and Thilo Glatzel. *Kelvin probe force microscopy*. Vol. 48. Springer, 2012.

[141] Evandro Martin Lanzoni et al. "The impact of Kelvin probe force microscopy operation modes and environment on grain boundary band bending in perovskite and Cu (In, Ga) Se2 solar cells". In: *Nano Energy* 88 (2021), p. 106270.

[142] Gwyddion contributors. *Gwyddion – A data visualization and processing tool*. Version 2.59. Available at http://gwyddion.net/. 2023.

[143] Wilford N Hansen and Galen J Hansen. "Standard reference surfaces for work function measurements in air". In: *Surface science* 481.1-3 (2001), pp. 172–184.

[144] J S Heslop-Harrison. "Energy Dispersive X-Ray Analysis". In: ed. by John F Linskens Hans-Ferdinand and Jackson. Springer Berlin Heidelberg, 1990, pp. 244–277. ISBN: 978-3-642-83611-4. DOI: 10.1007/978-3-642-83611-4_9. URL: https://doi.org/10.1007/978-3-642-83611-4_9.

[145] Max Knoll and Ernst Ruska. "Das elektronenmikroskop". In: *Zeitschrift für physik* 78 (1932), pp. 318–339.

[146] Bill W Ward, John A Notte, and Nicholas P Economou. "Helium ion microscope: A new tool for nanoscale microscopy and metrology". In: *Journal of Vacuum Science & Technology B: Microelectronics and Nanometer Structures Processing, Measurement, and Phenomena* 24.6 (2006), pp. 2871–2874.

[147] Mathias Senoner et al. "BAM-L002—a new type of certified reference material for length calibration and testing of lateral resolution in the nanometre range". In: *Surface and Interface Analysis: An International Journal devoted to the development and application of techniques for the analysis of surfaces, interfaces and thin films* 36.10 (2004), pp. 1423–1426.

[148] F Hillion. "A new high performance instrument: The Cameca Nano-SIMS50". In: *Proceedings of the 9ˆ¡ th¿ SIMS conference, 1993*. 1993.

[149] Ed Becquerel. *La lumière, ses causes et ses effets*. Vol. 1. Firmin Didot frères, fils et cie, 1867.

[150] F H Spedding, R W Gurney, and N F Mott. *LUMINESCENCE IN SOLIDS*. 1938. DOI: https://doi.org/10.1039/TF9393500069.

[151] J T Randall. *SOME RECENT EXPERIMENTS IN LUMINESCENCE*. 1938. DOI: https://doi.org/10.1039/TF9393500002.

[152] R P Johnson and W L Davis. *Luminescence During Intermittent Optical Excitation*. 1949. DOI: https://doi.org/10.1364/JOSA.29.000283.

[153] W De Groot. *LUMINESCENCE DECAY AND RELATED PHENOMENA*.

[154] Ferd E Williams. *Review of the Interpretations of Luminescence Phenomena*. 1949. DOI: https://doi.org/10.1364/JOSA.39.000648.

[155] "Phosphorescence and electron traps - I. The study of trap distributions". In: *Proceedings of the Royal Society of London. Series A. Mathematical and Physical Sciences* 184 (999 Nov. 1945), pp. 365–389. ISSN: 0080-4630. DOI: 10.1098/rspa.1945.0024.

[156] P Würfel, S Finkbeiner, and E Daub. "Generalized Planck's radiation law for luminescence via indirect transitions". In: *Applied Physics A* 60 (1995), pp. 67–70.

[157] K Schick et al. "Verification of a generalized Planck law for luminescence radiation from silicon solar cells". In: *Applied Physics A* 54 (1992), pp. 109–114.

[158] P. Wurfel and U. Wurfel. *Physics of solar cells: from basic principles to advanced concepts*. John Wiley & Sons, 2016. ISBN: 9783527413096.

[159] Susanne Siebentritt et al. "How photoluminescence can predict the efficiency of solar cells". In: *Journal of Physics: Materials* 4.4 (2021), p. 042010.

[160] Martin C Schubert et al. "Spatially resolved performance analysis for perovskite solar cells". In: *Advanced Energy Materials* 10.26 (2020), p. 1904001.

[161] Anh Dinh Bui et al. "Electrical properties of perovskite solar cells by illumination intensity and temperature-dependent photoluminescence imaging". In: *Progress in Photovoltaics: Research and Applications* 30.8 (2022), pp. 1038–1044.

[162] Amaury Delamarre. "Characterization of solar cells using electroluminescence and photoluminescence hyperspectral images". In: *Journal of Photonics for Energy* 2 (1 July 2012), p. 027004. ISSN: 1947-7988. DOI: 10.1117/1.jpe.2.027004.

[163] Gilbert El-Hajje et al. "Quantification of spatial inhomogeneity in perovskite solar cells by hyperspectral luminescence imaging". In: *Energy and Environmental Science* 9 (7 July 2016), pp. 2286–2294. ISSN: 17545706. DOI: 10.1039/c6ee00462h.

[164] T Trupke et al. “Photoluminescence imaging of silicon wafers”. In: *Applied Physics Letters* 89.4 (2006).

[165] E. Olsen and A. S. Flø. “Spectral and spatially resolved imaging of photoluminescence in multicrystalline silicon wafers”. In: *Applied Physics Letters* 99 (1 July 2011). ISSN: 00036951. DOI: 10.1063/1.3607307.

[166] M P Peloso et al. *Evaluating the electrical properties of silicon wafer solar cells using hyperspectral imaging of luminescence*. 2011.

[167] T Trupke et al. “Fast photoluminescence imaging of silicon wafers”. In: *2006 IEEE 4th World Conference on Photovoltaic Energy Conference*. Vol. 1. IEEE. 2006, pp. 928–931.

[168] Amaury Delamarre et al. “Quantitative luminescence mapping of Cu(In, Ga)Se2 thin-film solar cells”. In: *Progress in Photovoltaics: Research and Applications* 23 (10 Oct. 2015), pp. 1305–1312. ISSN: 1099159X. DOI: 10.1002/pip.2555.

[169] Lukas Wagner et al. “Revealing fundamentals of charge extraction in photovoltaic devices through potentiostatic photoluminescence imaging”. In: *Matter* 5.7 (2022), pp. 2352–2364. ISSN: 25902385. DOI: 10.1016/j.matt.2022.05.024.

[170] Christof Schultz et al. “Hyperspectral Photoluminescence Imaging for Spatially Resolved Determination of Electrical Parameters of Laser-Patterned Perovskite Solar Cells”. In: *Solar RRL* (Nov. 2023). ISSN: 2367198X. DOI: 10.1002/solr.202300538.

[171] Gordon Lasher and Frank Stern. “Spontaneous and Stimulated Recombination Radiation in Semiconductors”. In: *Phys. Rev.* 133 (2A 1964), A553–A563. DOI: 10.1103/PhysRev.133.A553. URL: https://link.aps.org/doi/10.1103/PhysRev.133.A553.

[172] Berndt Feuerbacher and P Wurfel. “Verification of a generalised Planck law by investigation of the emission from GaAs luminescent diodes”. In: *Journal of Physics: Condensed Matter* 2.16 (1990), p. 3803.

[173] P Wurfel. *The chemical potential of radiation*. 1982.

[174] Max Hilaire Wolter et al. “How band tail recombination influences the open-circuit voltage of solar cells”. In: *Progress in Photovoltaics: Research and Applications* 30.7 (2022), pp. 702–712.

[175] Juan-Pablo Correa-Baena et al. “Homogenized halides and alkali cation segregation in alloyed organic-inorganic perovskites”. In: *Science* 363.6427 (2019), pp. 627–631.

[176] Kyle Frohna et al. "Nanoscale chemical heterogeneity dominates the optoelectronic response of alloyed perovskite solar cells". In: *Nature Nanotechnology* 17 (2 Feb. 2022), pp. 190–196. ISSN: 17483395. DOI: 10.1038/s41565-021-01019-7.

[177] *Teledyne Princeton Instrument*. Accessed: 2023-12-30. URL: https://www.princetoninstruments.com/products/pi-max-family/pi-max/featured-published-research.

[178] *Teledyne Princeton Instrument*. Accessed: 2023-12-22. URL: https://www.princetoninstruments.com/products/pi-max-family/pi-max.

[179] R. Poeira. *"Growth of organic inorganic perovskite methylammonium lead triiodide by co-evaporation technique"*. Master's Thesis, University of Luxembourg. 2020.

[180] Adrien Bercegol et al. "Investigation of in-depth transport and absorption properties of various perovskite materials using luminescence imaging". In: *2018 IEEE 7th World Conference on Photovoltaic Energy Conversion (WCPEC)(A Joint Conference of 45th IEEE PVSC, 28th PVSEC & 34th EU PVSEC)*. IEEE. 2018, pp. 2540–2542.

[181] Guillaume Vidon et al. "Mapping Transport Properties of Halide Perovskites via Short-Time-Dynamics Scaling Laws and Subnanosecond-Time-Resolution Imaging". In: *Phys. Rev. Appl.* 16 (4 2021), p. 044058. DOI: 10.1103/PhysRevApplied.16.044058. URL: https://link.aps.org/doi/10.1103/PhysRevApplied.16.044058.

[182] R. Paschotta. *Field Guide to Optical Fiber Technology*. SPIE, 2010. ISBN: 9780819480903.

[183] Simon Schwarz et al. "Compact Beam Homogenizer Module with Laser-Fabricated Lens-Arrays". In: *Applied Sciences* 11 (3 2021). ISSN: 2076-3417. DOI: 10.3390/app11031018. URL: https://www.mdpi.com/2076-3417/11/3/1018.

[184] *Thorlabs Liquid crystal tunable filter*. accessed on 2023-12-30. URL: https://www.thorlabs.com/thorproduct.cfm?partnumber=KURIOS-XE2/M.

[185] Jonathan Mooney and Patanjali Kambhampati. *Get the basics right: Jacobian conversion of wavelength and energy scales for quantitative analysis of emission spectra*. Oct. 2013. DOI: 10.1021/jz401508t.

[186] Václav Prajzler et al. "Flexible polymer planar optical waveguides". In: *Radioengineering* 23.3 (2014), pp. 776–782.

[187] Thomas Unold Alex Redinger Marquez Jose. "Quantitative Imaging of Non-radiative losses in Thin film solar cells".

[188] Lisa Krückemeier et al. “Understanding Transient Photoluminescence in Halide Perovskite Layer Stacks and Solar Cells”. In: *Advanced Energy Materials* 11 (19 May 2021). ISSN: 16146840. DOI: 10.1002/aenm.202003489.

[189] Igal Levine et al. “Can we use time-resolved measurements to get steady-state transport data for halide perovskites?” In: *Journal of Applied Physics* 124.10 (2018).

[190] Mathias Uller Rothmann et al. “Direct observation of intrinsic twin domains in tetragonal CH3NH3PbI3”. In: *Nature communications* 8.1 (2017), p. 14547.

[191] Keith P McKenna. “Electronic properties of {111} twin boundaries in a mixed-ion lead halide perovskite solar absorber”. In: *ACS Energy Letters* 3.11 (2018), pp. 2663–2668.

[192] Yongtao Liu et al. “Chemical nature of ferroelastic twin domains in CH3NH3PbI3 perovskite”. In: *Nature materials* 17.11 (2018), pp. 1013–1019.

[193] Nga Phung and Antonio Abate. “The Impact of Nano-and Microstructure on the Stability of Perovskite Solar Cells”. In: *Small* 14.46 (2018), p. 1802573.

[194] John M Howard et al. “Humidity-induced photoluminescence hysteresis in variable Cs/Br ratio hybrid perovskites”. In: *The Journal of Physical Chemistry Letters* 9.12 (2018), pp. 3463–3469.

[195] Michael Saliba et al. “Perovskite solar cells: from the atomic level to film quality and device performance”. In: *Angewandte Chemie International Edition* 57.10 (2018), pp. 2554–2569.

[196] Bart Roose, Qiong Wang, and Antonio Abate. “The role of charge selective contacts in perovskite solar cell stability”. In: *Advanced Energy Materials* 9.5 (2019), p. 1803140.

[197] Israel Cohen et al. “Pearson correlation coefficient”. In: *Noise reduction in speech processing* (2009), pp. 1–4.

[198] Jeremy Hieulle et al. “Understanding and decoupling the role of wavelength and defects in light-induced degradation of metal-halide perovskites”. In: *Energy and Environmental Science* (Dec. 2023). ISSN: 17545706. DOI: 10.1039/d3ee03511e.

[199] Jacques Cazaux. “Material contrast in SEM Fermi energy and work function effects”. In: *Ultramicroscopy* 110.3 (2010), pp. 242–253.

[200] Yangbo Zhou et al. “Quantitative secondary electron imaging for work function extraction at atomic level and layer identification of graphene”. In: *Scientific reports* 6.1 (2016), p. 21045.

[201] Lisa Krückemeier et al. "Consistent Interpretation of Electrical and Optical Transients in Halide Perovskite Layers and Solar Cells". In: *Advanced Energy Materials* 11 (46 Dec. 2021). ISSN: 16146840. DOI: 10.1002/aenm.202102290.

[202] Thomas Kirchartz. "High open-circuit voltages in lead-halide perovskite solar cells: experiment, theory and open questions". In: *Philosophical Transactions of the Royal Society A* 377.2152 (2019), p. 20180286.

[203] Ossila. *Spin coating schematic*. Accessed: 2023-10-09. 2023. URL: https://www.ossila.com/pages/spin-coating.

[204] Daniel Burkitt, Justin Searle, and Trystan Watson. "Perovskite solar cells in N-I-P structure with four slot-die-coated layers". In: *Royal Society Open Science* 5 (5 May 2018). ISSN: 20545703. DOI: 10.1098/rsos.172158.

[205] Timothy J Rehg and Brian G Higgins. *Spin Coating of Colloidal Suspensions*. 1992. DOI: https://doi.org/10.1002/aic.690380403.

[206] Timothy Rehg and Brian Higgins. "Evaporative Convection in Spin Coating". In: (Oct. 2014).

[207] Daiki Yamashita et al. "Charge Injection at the Heterointerface in Perovskite CH3NH3PbI3 Solar Cells Studied by Simultaneous Microscopic Photoluminescence and Photocurrent Imaging Spectroscopy". In: *Journal of Physical Chemistry Letters* 7 (16 Aug. 2016), pp. 3186–3191. ISSN: 19487185. DOI: 10.1021/acs.jpclett.6b01231.

[208] Dong Geon Lee et al. "Effect of TiO2 particle size and layer thickness on mesoscopic perovskite solar cells". In: *Applied Surface Science* 477 (May 2019), pp. 131–136. ISSN: 01694332. DOI: 10.1016/j.apsusc.2017.11.124.

[209] Sven Rühle. "Tabulated values of the Shockley-Queisser limit for single junction solar cells". In: *Solar Energy* 130 (June 2016), pp. 139–147. ISSN: 0038092X. DOI: 10.1016/j.solener.2016.02.015.

[210] Hamid Shahivandi, Majid Vaezzadeh, and Mohammadreza Saeidi. "Theory of light-induced degradation in perovskite solar cells". In: *Solar Energy Materials and Solar Cells* 208 (May 2020). ISSN: 09270248. DOI: 10.1016/j.solmat.2019.110383.

[211] Saivineeth Penukula, Rodrigo Estrada Torrejon, and Nicholas Rolston. "Quantifying and Reducing Ion Migration in Metal Halide Perovskites through Control of Mobile Ions". In: *Molecules* 28 (13 July 2023). ISSN: 14203049. DOI: 10.3390/molecules28135026.

[212] Yanbo Wang et al. *Stabilizing heterostructures of soft perovskite semiconductors*. URL: http://science.sciencemag.org/.

[213] Sai Bai et al. "Planar perovskite solar cells with long-term stability using ionic liquid additives". In: *Nature* 571 (7764 July 2019), pp. 245–250. ISSN: 14764687. DOI: 10.1038/s41586-019-1357-2.

[214] Feng Wang et al. *Defects engineering for high-performance perovskite solar cells*. Dec. 2018. DOI: 10.1038/s41528-018-0035-z.

[215] Tejas S. Sherkar et al. "Recombination in Perovskite Solar Cells: Significance of Grain Boundaries, Interface Traps, and Defect Ions". In: *ACS Energy Letters* 2 (5 May 2017), pp. 1214–1222. ISSN: 23808195. DOI: 10.1021/acsenergylett.7b00236.

[216] Jiangjian Shi et al. *From Ultrafast to Ultraslow: Charge-Carrier Dynamics of Perovskite Solar Cells*. May 2018. DOI: 10.1016/j.joule.2018.04.010.

[217] M. Ibrahim Dar et al. "High photovoltage in perovskite solar cells: New physical insights from the ultrafast transient absorption spectroscopy". In: *Chemical Physics Letters* 683 (2017), pp. 211–215. ISSN: 00092614. DOI: 10.1016/j.cplett.2017.04.046.

[218] Neha Arora. "Intrinsic and Extrinsic Stability of Formamidinium Lead Bromide Perovskite Solar Cells Yielding High Photovoltage". In: (2016). DOI: 10.17863/CAM.9023. URL: https://www.researchgate.net/publication/316374906.

[219] Yi Yang et al. "Bi-functional additive engineering for high-performance perovskite solar cells with reduced trap density". In: *Journal of Materials Chemistry A* 7 (11 2019), pp. 6450–6458. ISSN: 20507496. DOI: 10.1039/c8ta11925b.

[220] Wanchun Xiang et al. "Europium-Doped CsPbI 2 Br for Stable and Highly Efficient Inorganic Perovskite Solar Cells". In: *Joule* 3 (1 Jan. 2019), pp. 205–214. ISSN: 25424351. DOI: 10.1016/j.joule.2018.10.008.

[221] Yang Bai, Xiangyue Meng, and Shihe Yang. *Interface Engineering for Highly Efficient and Stable Planar p-i-n Perovskite Solar Cells*. Feb. 2018. DOI: 10.1002/aenm.201701883.

[222] Seckin Akin et al. *New Strategies for Defect Passivation in High-Efficiency Perovskite Solar Cells*. Apr. 2020. DOI: 10.1002/aenm.201903090.

[223] Artiom Magomedov et al. "Self-Assembled Hole Transporting Monolayer for Highly Efficient Perovskite Solar Cells". In: *Advanced Energy Materials* 8 (32 Nov. 2018), p. 1801892. ISSN: 1614-6840. DOI: 10.1002/AENM.201801892. URL: https://onlinelibrary.wiley.com/doi/full/10.1002/aenm.201801892%20https://onlinelibrary.wiley.com/doi/abs/10.1002/aenm.201801892%20https://onlinelibrary.wiley.com/doi/10.1002/aenm.201801892.

[224] Amran Al-Ashouri et al. "Conformal monolayer contacts with lossless interfaces for perovskite single junction and monolithic tandem solar cells". In: *Energy & Environmental Science* 12.11 (2019), pp. 3356–3369.

[225] Zhifa Liu et al. "Interface Optimization via Fullerene Blends Enables Open-Circuit Voltages of 1.35V in CH3NH3Pb(I0.8Br0.2)3 Solar Cells". In: *Advanced Energy Materials* 11 (16 Apr. 2021), p. 2003386. ISSN: 1614-6840. DOI: 10.1002/AENM.202003386. URL: https://onlinelibrary.wiley.com/doi/full/10.1002/aenm.202003386%20https://onlinelibrary.wiley.com/doi/abs/10.1002/aenm.202003386%20https://onlinelibrary.wiley.com/doi/10.1002/aenm.202003386.

[226] KO Brinkmann et al. "Perovskite–organic tandem solar cells with indium oxide interconnect". In: *Nature* 604.7905 (2022), pp. 280–286.

[227] Martin Stolterfoht et al. "The impact of energy alignment and interfacial recombination on the open-circuit voltage of perovskite solar cells". In: ().

[228] Hao Chen et al. "Quantum-size-tuned heterostructures enable efficient and stable inverted perovskite solar cells". In: *Nature Photonics* 16.5 (2022), pp. 352–358.

[229] Mónica Lira-Cantú. *Perovskite solar cells: Stability lies at interfaces*. July 2017. DOI: 10.1038/nenergy.2017.115.

[230] Wanchun Xiang, Shengzhong Liu, and Wolfgang Tress. *Interfaces and Interfacial Layers in Inorganic Perovskite Solar Cells*. Dec. 2021. DOI: 10.1002/anie.202108800.

[231] Jionghua Wu et al. "Quantifying the Interface Defect for the Stability Origin of Perovskite Solar Cells". In: *Advanced Energy Materials* 9 (37 Oct. 2019). ISSN: 16146840. DOI: 10.1002/aenm.201901352.

[232] Hao Hu et al. "Surface Band Bending Influences the Open-Circuit Voltage of Perovskite Solar Cells". In: *ACS Applied Energy Materials* 2 (6 June 2019), pp. 4045–4052. ISSN: 25740962. DOI: 10.1021/acsaem.9b00060.

[233] Wan Jian Yin, Tingting Shi, and Yanfa Yan. "Unusual defect physics in CH3NH3PbI3 perovskite solar cell absorber". In: *Applied Physics Letters* 104 (6 Oct. 2014). ISSN: 00036951. DOI: 10.1063/1.4864778.

[234] Xiaopeng Zheng et al. "Defect passivation in hybrid perovskite solar cells using quaternary ammonium halide anions and cations". In: *Nature Energy* 2 (7 June 2017). ISSN: 20587546. DOI: 10.1038/NENERGY.2017.102.

[235] Dexin Yang et al. *Toward Stable and Efficient Perovskite Light-Emitting Diodes*. Feb. 2022. DOI: 10.1002/adfm.202109495.

[236] Efrain Ochoa-Martinez et al. "Physical Passivation of Grain Boundaries and Defects in Perovskite Solar Cells by an Isolating Thin Polymer". In: *ACS Energy Letters* 6 (7 July 2021), pp. 2626–2634. ISSN: 23808195. DOI: 10.1021/acsenergylett.1c01187.

[237] Lusheng Liang et al. "Efficient Perovskite Solar Cells by Reducing Interface-Mediated Recombination: a Bulky Amine Approach". In: *Advanced Energy Materials* 10 (14 Apr. 2020). ISSN: 16146840. DOI: 10.1002/aenm.202000197.

[238] Florian Staub et al. "Beyond Bulk Lifetimes: Insights into Lead Halide Perovskite Films from Time-Resolved Photoluminescence". In: *Physical Review Applied* 6 (4 Oct. 2016). ISSN: 23317019. DOI: 10.1103/PhysRevApplied.6.044017.

[239] Shangshang Chen et al. "Identifying the Soft Nature of Defective Perovskite Surface Layer and Its Removal Using a Facile Mechanical Approach". In: *Joule* 4 (12 Dec. 2020), pp. 2661–2674. ISSN: 25424351. DOI: 10.1016/j.joule.2020.10.014.

[240] Milena P. Arciniegas et al. "Laser-Induced Localized Growth of Methylammonium Lead Halide Perovskite Nano- and Microcrystals on Substrates". In: *Advanced Functional Materials* 27 (34 Sept. 2017). ISSN: 16163028. DOI: 10.1002/adfm.201701613.

[241] Wenchi Kong et al. "Enhancing Perovskite Solar Cell Performance through Femtosecond Laser Polishing". In: *Solar RRL* 4 (7 July 2020). ISSN: 2367198X. DOI: 10.1002/solr.202000189.

[242] Monika Rai, Lydia Helena Wong, and Lioz Etgar. "Effect of Perovskite Thickness on Electroluminescence and Solar Cell Conversion Efficiency". In: *Journal of Physical Chemistry Letters* 11 (19 Oct. 2020), pp. 8189–8194. ISSN: 19487185. DOI: 10.1021/acs.jpclett.0c02363.

[243] Xueyan Shan et al. "Flash Surface Treatment of CH3NH3PbI3 Films Using 248 nm KrF Excimer Laser Enhances the Performance of Perovskite Solar Cells". In: *Solar RRL* 3 (7 July 2019). ISSN: 2367198X. DOI: 10.1002/solr.201900020.

[244] Lucija Rakocevic et al. "Loss Analysis in Perovskite Photovoltaic Modules". In: *Solar RRL* 3 (12 Dec. 2019). ISSN: 2367198X. DOI: 10.1002/solr.201900338.

[245] Paolo Fedeli et al. "Influence of the Synthetic Procedures on the Structural and Optical Properties of Mixed-Halide (Br, I) Perovskite Films". In: *Journal of Physical Chemistry C* 119 (37 Sept. 2015), pp. 21304–21313. ISSN: 19327455. DOI: 10.1021/ACS.JPCC.5B03923.

[246] Aditya Sadhanala et al. "Preparation of single-phase films of CH3NH3Pb(I 1- xBrx)3 with sharp optical band edges". In: *Journal of Physical Chemistry Letters* 5 (15 Aug. 2014), pp. 2501–2505. ISSN: 19487185. DOI: 10.1021/JZ501332V/SUPPL_FILE/JZ501332V_SI_001.PDF. URL: https://pubs.acs.org/doi/full/10.1021/jz501332v.

[247] C Rehermann et al. "Role of solution concentration in formation kinetics of bromide perovskite thin films during spin-coating monitored by optical in situ metrology." In: *RSC advances* 12 (50 Nov. 2022), pp. 32765–32774. ISSN: 2046-2069. DOI: 10.1039/d2ra06314j. URL: http://www.ncbi.nlm.nih.gov/pubmed/36425710%20http://www.pubmedcentral.nih.gov/articlerender.fcgi?artid=PMC9664315.

[248] Carolin Rehermann et al. "Origin of Ionic Inhomogeneity in MAPb(IxBr1- x)3 Perovskite Thin Films Revealed by In-Situ Spectroscopy during Spin Coating and Annealing". In: *ACS applied materials interfaces* 12 (27 July 2020), pp. 30343–30352. ISSN: 1944-8252. DOI: 10.1021/ACSAMI.0C05894. URL: https://pubmed.ncbi.nlm.nih.gov/32510922/.

[249] Michael M Lee et al. "Efficient hybrid solar cells based on meso-superstructured organometal halide perovskites". In: *science* 338.6107 (2012), pp. 643–647.

[250] Amanda J Neukirch et al. "Geometry distortion and small polaron binding energy changes with ionic substitution in halide perovskites". In: *The journal of physical chemistry letters* 9.24 (2018), pp. 7130–7136.

[251] Hsinhan Tsai et al. "Light-induced lattice expansion leads to high-efficiency perovskite solar cells". In: *Science* 360 (6384 2018), pp. 67–70. ISSN: 10959203. DOI: 10.1126/SCIENCE.AAP8671. URL: https://www.science.org.

[252] Dane W. DeQuilettes et al. "Photo-induced halide redistribution in organic-inorganic perovskite films". In: *Nature Communications* 7 (May 2016). ISSN: 20411723. DOI: 10.1038/ncomms11683.

[253] Jean-François Guillemoles et al. “Stability issues of Cu (In, Ga) Se2-based solar cells”. In: *The Journal of Physical Chemistry B* 104.20 (2000), pp. 4849–4862.

[254] F-J Haug et al. “Light soaking effects in Cu (In, Ga) Se2 superstrate solar cells”. In: *Thin solid films* 431 (2003), pp. 431–435.

[255] Caleb C. Boyd et al. *Understanding Degradation Mechanisms and Improving Stability of Perovskite Photovoltaics*. Mar. 2019. DOI: 10.1021/acs.chemrev.8b00336.

[256] Julian Mattheis, Uwe Rau, and Jürgen H Werner. “Light absorption and emission in semiconductors with band gap fluctuations—A study on Cu (In, Ga) Se2 thin films”. In: *Journal of applied physics* 101.11 (2007).